

Gyrokinetic Particle-In-Cell Global Simulations of Ion-Temperature-Gradient and Collisionless-Trapped-Electron-Mode Turbulence in Tokamaks

THÈSE N° 4326 (2009)

PRÉSENTÉE LE 27 FÉVRIER 2009
À LA FACULTE SCIENCES DE BASE
CRPP ASSOCIATION EURATOM
PROGRAMME DOCTORAL EN PHYSIQUE

ÉCOLE POLYTECHNIQUE FÉDÉRALE DE LAUSANNE

POUR L'OBTENTION DU GRADE DE DOCTEUR ÈS SCIENCES

PAR

Sébastien JOLLIET

acceptée sur proposition du jury:

Prof. O. Schneider, président du jury
Prof. L. Villard, directeur de thèse
Dr X. Garbet, rapporteur
Dr A. Pochelon, rapporteur
Dr F. Zonca, rapporteur



ÉCOLE POLYTECHNIQUE
FÉDÉRALE DE LAUSANNE

Suisse
2009

Version abrégée

Le but de la fusion thermonucléaire est de construire des centrales électriques qui seront capables de produire un gigawatt d'électricité. Parmi les différentes méthodes pour produire la fusion, le tokamak, basé sur le confinement magnétique, est le moyen le plus prometteur. Un gaz est chauffé jusqu'à cent millions de degrés et se transforme en plasma, qui est maintenu - ou confiné - dans une chambre torique par des lignes de champ magnétique hélicoïdales. Puis, du deutérium et du tritium sont injectés et fusionnent, créant une particule alpha et un neutron énergétique. Pour avoir un bilan de puissance favorable, la puissance dégagée par les réactions de fusion doit excéder la puissance nécessaire au chauffage du plasma additionnée aux pertes. Ceci peut-être traduit dans une expression très simple qui stipule que la multiplication de la densité, de la température et du temps de confinement de l'énergie doit être plus grande qu'une certaine valeur donnée. Malheureusement, les tokamaks actuels ne sont pas capables d'atteindre cette condition, notamment à cause de la turbulence dans les plasmas. Ce phénomène accroît les pertes de chaleur et dégrade le temps de confinement de l'énergie, qui ne peut pas être prédit par des théories analytiques telles que la théorie dite "néoclassique", dans laquelle les pertes de chaleur sont provoquées par les collisions Coulombiennes. Par conséquent, des simulations numériques sont développées pour modéliser la turbulence dans les plasmas, principalement due aux instabilités de gradient de température ionique et d'électrons piégés. L'état du plasma est décrit par une fonction de distribution, dont l'évolution est régie par l'équation de Vlasov. Les champs électromagnétiques créés par les particules sont calculés de façon consistante au travers des équations de Maxwell. Le système ainsi obtenu, appelé système Vlasov-Maxwell est grandement simplifié en utilisant la théorie gyrocinétique, qui consiste, par un "ordering" approprié, à éliminer le mouvement rapide (comparé aux fréquences typiques des instabilités considérées) de gyration autour des lignes de champ. Néanmoins, il est toujours extrêmement difficile de résoudre ce système numériquement, dû à la grande gamme d'échelles spatiales et temporelles impliquées. Dans cette thèse, le système Vlasov-Maxwell est résolu de façon globale dans la limite électrostatique et non-collisionnelle à l'aide du code "Particle-In-Cell" ORB5 pour une géométrie de type tokamak. Cette approche de type Monte-Carlo est affectée par la présence de bruit statistique qui dégrade inévitablement la qualité de la simulation. Par conséquent, la première partie de ce travail a été consacrée à l'optimisation du code en

vue de réduire le bruit numérique. Le code a été réécrit dans un nouveau système de coordonnées qui utilise l'anisotropie de la turbulence, qui est principalement alignée avec les lignes de champ magnétique. Le résultat global de l'optimisation est que pour une précision donnée, le temps CPU a décréu d'un facteur deux mille, la mémoire totale a été réduite d'un facteur dix et le bruit numérique a été réduit d'un facteur deux cents. De plus, le scaling du code en fonction de la taille du plasma est à présent optimal, ce qui laisse présager que ORB5 pourra calculer le transport de chaleur des futurs installations de fusion telles que ITER. La deuxième partie de cette thèse présente la validation du code au travers de différents tests de convergence ainsi que des comparaisons linéaires (y compris des relations de dispersion) et non-linéaires. En outre, le code a été appliqué à d'importants problèmes liés à la théorie gyrocinétique. Il est démontré pour la première fois qu'un code delta-f global PIC à cinq dimensions est capable d'atteindre un équilibre thermodynamique à condition que le système contienne de la dissipation. Il s'agit d'un résultat fondamental étant donné que le principal reproche émis à l'encontre des codes delta-f PIC est leur incapacité à effectuer de longues simulations. Puis, le rôle de la non-linéarité parallèle a été étudié et il est montré dans ce travail que ce terme n'a pas de réelle influence sur la turbulence à condition que le bruit numérique soit faible. Ce résultat devrait mettre un terme à la controverse qui est née récemment, dans laquelle des simulations gyrocinétiques utilisant diverses approches numériques ont obtenus des résultats contradictoires. Finalement, grâce à l'optimisation du code, le modèle gyrocinétique a été élargi pour inclure la réponse cinétique des électrons piégés à la place de l'approximation adiabatique (Boltzmann) habituelle. Pour la première fois, des simulations non-linéaires globales de la turbulence de type TEM sont présentées, et le rôle des écoulements zonaux sont analysés. Cette étude permet d'acquérir des connaissances supplémentaires sur la turbulence TEM, qui est moins connue que la turbulence ITG. En conclusion, cette thèse est l'une des étapes principales du développement de ORB5 qui est maintenant un des codes à la pointe pour l'étude de la turbulence ITG et TEM dans la limite non-collisionnelle, et elle a apporté plusieurs contributions utiles à la compréhension de ce phénomène.

Mots clés: plasma, tokamak, fusion, gyrocinétique, turbulence

Abstract

The goal of thermonuclear fusion research is to provide power plants, that will be able to produce one gigawatt of electricity. Among the different ways to achieve fusion, the tokamak, based on magnetic confinement, is the most promising one. A gas is heated up to hundreds of millions of degrees and becomes a plasma, which is maintained - or confined - in a toroidal vessel by helical magnetic field lines. Then, deuterium and tritium are injected and fuse to create an α particle and an energetic neutron. In order to have a favorable power balance, the power produced by fusion reactions must exceed the power needed to heat the plasma and the power losses. This can be cast in a very simple expression which stipulates that the product of the density, the temperature and the energy confinement time must exceed some given value. Unfortunately, present-days tokamaks are not able to reach this condition, mostly due to plasma turbulence. The latter phenomenon enhances the heat losses and degrades the energy confinement time, which cannot be predicted by analytical theories such as the so-called neoclassical theory in which the heat losses are caused by Coulomb collisions. Therefore, numerical simulations are being developed to model plasma turbulence, mainly caused by the Ion and Electron Temperature-Gradient and the Trapped-Electron-Mode instabilities. The plasma is described by a distribution function which evolves according to the Vlasov equation. The electromagnetic fields created by the particles are self-consistently obtained through Maxwell's equations. The resulting Vlasov-Maxwell system is greatly simplified by using the gyrokinetic theory, which consists, through an appropriate ordering, of eliminating the fast gyromotion (compared to the typical frequency of instabilities). Nevertheless, it is still extremely difficult to solve this system numerically due to the large range of time and spatial scales to be resolved. In this thesis, the Vlasov-Maxwell system is solved in the electrostatic and collisionless limit with the Particle-In-Cell (PIC) ORB5 code in global tokamak geometry. This Monte-Carlo approach suffers from statistical noise which unavoidably degrades the quality of the simulation. Consequently, the first part of this work has been devoted to the optimization of the code with a view to reduce the numerical noise. The code has been rewritten in a new coordinate system which takes advantage of the anisotropy of turbulence, which is mostly aligned with the magnetic field lines. The overall result of the optimization is that for a given accuracy, the CPU time has been decreased by a factor two thousand, the total memory has been decreased by a factor

ten and the numerical noise has been reduced by a factor two hundred. In addition, the scaling of the code with respect to plasma size is presently optimal, suggesting that ORB5 could compute heat transport for future fusion devices such as ITER. The second part of this thesis presents the validation of the code with numerical convergence tests, linear (including dispersion relations) and nonlinear benchmarks. Furthermore, the code has been applied to important issues in gyrokinetic theory. It is shown for the first time that a 5D global delta-f PIC code can achieve a thermodynamic steady state on the condition that some dissipation is present. This is a fundamental result as the main criticism against delta-f PIC codes is their inability to deal with long time simulations. Next, the role of the parallel nonlinearity is studied and it is demonstrated in this work that this term has no real influence on turbulence, provided the numerical noise is sufficiently low. This result should put an end to the controversy that recently occurred, in which gyrokinetic simulations using different numerical approaches yielded contradictory results. Finally, thanks to the optimization of the code, the gyrokinetic model has been extended to include the kinetic response of trapped-electrons, in place to the usual adiabatic (Boltzmann) approximation. For the first time, global TEM nonlinear simulations are presented, and the role of the zonal flow on heat transport is analyzed. This study will help in acquiring some knowledge on the less-known TEM turbulence (as compared to ITG). In conclusion, this thesis is one of the main steps of the development of ORB5, which is now a state-of-the-art gyrokinetic code for collisionless ITG and TEM turbulence, and has brought several contributions to the understanding of these phenomena.

Keywords: plasma, tokamak, fusion, gyrokinetics, turbulence

Contents

1	Introduction	1
1.1	Anomalous transport	1
1.2	Numerical treatment of microinstabilities	5
1.3	Contribution of this thesis	6
1.4	Outline	8
2	A local linear model for microinstabilities	9
2.1	Basic concepts	9
2.1.1	Particle drifts	9
2.1.2	Particle trapping	11
2.1.3	Fluid drift	12
2.2	The drift wave	13
2.3	A dispersion relation for slab-ITG instability	15
2.4	A dispersion relation for toroidal-ITG instability	20
2.5	A dispersion relation for TEM instabilities	22
2.6	Coupling of the TEM to the ITG instability	27
3	The ORB5 gyrokinetic model	29
3.1	Geometry and magnetic field	29
3.2	Gyrokinetic theory	32
3.3	Hahm's gyrokinetic equations	33
3.4	The gyro-averaged electric field	35
3.5	The δf method	36
3.6	Poisson equation	39
3.6.1	Ion density	39

3.6.2	Electron density	41
3.6.3	Quasineutrality equation	43
3.7	Energy conservation	44
3.8	Noise control and sources	44
4	Numerical implementation	49
4.1	Initial status of the code	49
4.2	Normalization	50
4.3	PIC discretization	50
4.3.1	Equations of motion	52
4.3.2	Loading of phase space volumes	57
4.3.3	Weight evolution	59
4.3.4	Discretization of the noise control and heating operators	60
4.3.5	Loading of initial conditions	61
4.4	Parallelization	63
4.5	Poisson equation	64
4.5.1	The Galerkin method	64
4.5.2	Determination of the grid size	65
4.5.3	Expression for the matrix and the RHS	66
4.5.4	Solving methods	68
4.5.5	The Fourier field-aligned filter	72
4.5.6	Numerical noise	76
4.5.7	The Fourier field-aligned solver	81
4.5.8	Shielding of the potential at the edge	82
4.6	Temperature and density profiles	83
4.6.1	Profile 1	84
4.6.2	Profile 2	84
4.6.3	Profile 3	84
5	Code validation	87
5.1	Description of typical runs	87
5.2	Scalability	93
5.3	The field-aligned filter	96

5.4	Comparison with linear dispersion relation	104
5.5	Convergence with number of markers	107
5.6	The CYCLONE benchmark	109
6	Application of ORB5 for ITG turbulence: evolution of entropy and parallel nonlinearity	113
6.1	Steady state: evolution of entropy	113
6.1.1	The fluctuation entropy equation	113
6.1.2	Simulation results	118
6.2	The influence of the v_{\parallel} nonlinearity	125
6.2.1	General considerations	125
6.2.2	Results for decaying turbulence	126
6.2.3	Results for driven simulations	132
6.2.4	Variability with initial conditions	136
6.2.5	The influence of the VNL on the fluctuation entropy	139
6.3	Conclusions	144
7	The trapped electron model	147
7.1	General considerations	147
7.2	Implementation	149
7.3	Linear convergence with numerical parameters	153
7.4	Comparison with a linear dispersion relation	158
7.5	The CYCLONE linear benchmark	160
7.6	Implementation of noise control and heating operators on electrons	164
7.7	Nonlinear detrapping	166
7.8	The role of zonal flows in TEM simulations	171
7.8.1	Review of nonlinear results	171
7.8.2	Simulation model	171
7.8.3	Parameters and convergence	173
7.8.4	Analysis	175
8	Conclusions and future work	189
8.1	Conclusions	189

8.2	Future work	191
A	Discretization with splines	195
A.1	Splines notations	195
A.2	Discretization of Finite-Element-Matrices	197
A.3	Discretization of the perturbed density and electric field	202
A.4	Boundary conditions	204
A.5	Discretization of the FEM matrix for the field-aligned-solver	206
A.6	Boundary conditions for the field-aligned solver	208

Chapter 1

Introduction

1.1 Anomalous transport

Thermonuclear fusion is undoubtedly one of the most promising energy sources for the future. The cross section of the nuclear reaction, through which two nuclei of Deuterium and Tritium combine into an α -particle and a neutron, becomes important at very high temperatures, typically 10 KeV. At this temperature, the nuclei and the electrons are not bound anymore. This is called the plasma state and it can be viewed as a gas of charged particles. The sun is an example of a plasma confined by gravitational forces. A plasma is also sensitive to electromagnetic fields. This property has led to the concept of tokamak: in a toroidal vessel, twisted magnetic fields are used to confine charged particles. The toroidal magnetic field is obtained with magnetic coils. A toroidal current is produced by induction, resulting in a poloidal magnetic field. It averages out the vertical drifts of ions and electrons due to the curvature and the inhomogeneity of the toroidal magnetic field. A vertical field is applied to stabilize the plasma. Another alternative for magnetic fusion is the stellerator, in which the poloidal magnetic field is produced by external magnetic coils. In a fusion reactor, several mechanisms are used to heat the plasma: the toroidal current (Ohmic heating), external Radio-Frequency (RF) wave heating, Neutral Beam Injection (NBI) and Coulomb collisions of α -particles. A large power input is needed to create the plasma. Part of this power is lost through various mechanisms such as turbulence or radiation, but power will be produced through the fusion reactions. It is naturally required to have a positive power balance. This is summarized in the Lawson

criterion [1]:

$$n_e T \tau_E \geq 10^{21} [\text{keVs/m}^3] \quad (1.1)$$

where n_e is the electron density, T is the temperature and τ_E is the energy confinement time. The left hand side of this formula is also called the triple product. It simply means that the plasma has to be dense and hot enough for a sufficiently long time. Future reactors such as the International Thermonuclear Experimental Reactor (ITER) [2], should satisfy the Lawson criterion. Then, the ultimate goal of fusion would be to reach *ignition*, for which the plasma temperature is maintained with α -particles heating only. In a tokamak, the density is limited by the Greenwald density limit [3]. The temperature and the energy confinement time are limited by radial heat losses. The latter is linked to a diffusion coefficient D , which can be expressed as a random walk coefficient $D = \Delta x^2 / \Delta t$, where Δx (resp. Δt) are the characteristic size (resp. time) of the diffusive process. The neoclassical estimate, which takes collisions and particle trapping into account, gives, in the low collisionality limit:

$$D \cong \rho_{Li} q^2 \nu \left(\frac{R_0}{a} \right)^{3/2} \quad (1.2)$$

Where ρ_{Li} is the ion Larmor radius, q is the safety factor, measuring the helicity of the magnetic field lines, ν is the collision frequency, R_0 and a are the major and minor radius of the tokamak. Unfortunately, the perpendicular diffusion coefficient measured in existing tokamaks exceeds the neoclassical estimate by up to 2 orders of magnitude for the low confinement regime (L-mode) [4]. This phenomenon is called *anomalous transport* and is one of the most active fields of research in magnetic confinement fusion. Even in the high confinement regime (H-mode) where transport is reduced near the plasma edge, anomalous transport still persists in the core. Anomalous transport is attributed to plasma turbulence [5], which is driven by microstabilities [6]. The latter are mainly generated by free sources of energy in the plasma such as density and temperature gradients. There is a large variety of microstabilities, classified in different ways. Ion instabilities are the Ion-Temperature-Gradient (ITG) modes (often called η_i modes), driven by the ion temperature gradient. They can be divided into the slab-ITG mode, the toroidal-ITG mode (interaction between the temperature gradient and the magnetic field curvature) and the Trapped Ion Mode (TIM). The main electron instabilities are the electron drift

waves, the Electron-Temperature-Gradient (ETG) modes, which are also divided into slab and toroidal branches, and the Trapped-Electron-Mode (TEM) (divided into dissipative and collisionless branches), due to the precessional drift of trapped electrons in a tokamak. In addition to electrostatic instabilities, electromagnetic instabilities such as Kinetic Ballooning Modes (KBM) [7], Alfvénic-Ion-Temperature-Gradient Mode (AITG) [8], and Neoclassical Tearing Modes (NTM) [9] play an important role. Finally, fluid-like instabilities such as resistive ballooning modes may have a significant contribution to the anomalous transport. This brief overview already points out the complexity of the problem of turbulence in magnetised plasmas, as many parameters must be taken into account.

A first simplified approach to study turbulence is given by the Hasegawa-Mima equation [10], which further leads to improved models (see for example [11]). The radial transport is then described as a diffusive process with the heat diffusivity χ estimated from a mixing length argument $\chi \cong \gamma/k_{\perp}^2$, where γ is the maximum growth rate and k_{\perp} is the typical perpendicular wave number of the instability. In other words, it means that the transport depends on the eddy size of the instability. The validity of the mixing-length estimate is controversial [5]. This issue is of considerable importance: transport coefficients, and therefore the energy confinement time, depend on many factors. For ITER, τ_E is determined with empirical scaling laws, such as the ITER reference scaling ITERH-98P(y,2) [4]:

$$\tau_E = 0.0562 H_{H98(y,2)} I^{0.93} B^{0.15} \bar{n}_{19}^{0.41} 9P^{-0.69} R_0^{1.97} \kappa_a^{0.78} \epsilon^{0.58} M^{0.19} \quad (1.3)$$

where $H_{H98(y,2)}$ is some constant of order unity, I is the plasma current [MA], B is the toroidal magnetic field [T], \bar{n}_{19} is the electron density (in 10^{19}m^{-3} units), P is the net heating power [MW], R_0 is the major plasma radius [m], κ_a is the plasma elongation, $\epsilon = a/R_0$ is the inverse aspect ratio and M the average hydrogenic atomic mass number. Other scalings exist, depending on the scenario. Microturbulence affects this scaling, establishing the need for a fundamental understanding of its characteristics. However, the exponents of these scalings are constrained. For example, the Kadomtsev constraint [12] leads to:

$$B\tau_E \sim (\rho^*)^{-2.7} \beta^{-0.9} (\nu^*)^{-0.01} q^{-3} \quad (1.4)$$

where $\rho^* = \rho_s/a$, ρ_s is the ion sound gyroradius, β is the normalized plasma pressure, ν^* is the normalized collisionality and q is the safety factor. This shows the importance of the

plasma size in ρ_s units. Scalings are designed from existing tokamaks experiments that are much smaller than ITER. First principles simulations, i.e. simulations whose model is derived from a Lagrangian or a Hamiltonian approach will be in this sense a useful tool to assess the validity of these scalings: if the eddy size is microscopic (comparable to ρ_s), then the transport scaling is gyro-Bohm, in other words inversely proportional to the plasma size. On the contrary, if the eddy size is macroscopic, the scaling is said to be Bohm-like, i.e. $\chi_i \propto T_e/B$ and the heat transport will scale with the plasma size. Although ρ^* scaling determination leads to different results [13, 14, 15, 16], it is now widely believed that self-organization of turbulence plays a crucial role. It refers to a process in which the internal organization of a system increases without being guided or managed by an outside source. In magnetised plasmas, self-organization mainly appears through two different structures: zonal flows and large-scale transport events (avalanches and streamers).

Zonal flows are linearly stable convective cells elongated in the poloidal and toroidal directions. They can be generated through different processes: the radial gradient of the Reynold stress [17], a secondary instability of the Kelvin-Helmholtz type [18] or by pressure asymmetries on a flux surface due to the geodesic curvature [19]. It is known that zonal flows are stabilizing, since they receive energy from the drift wave and shear the eddies. An overview of zonal flows can be found in [20]. Zonal flows can be experimentally observed by density fluctuations, potential or radial electric field measurements. The main difficulty comes from the poor radial and temporal resolution of the different diagnostics. For example, it is very hard to distinguish between the zonal flow and the mean $\vec{E} \times \vec{B}$ flow. Large-scale events appear in the form of avalanches [21] and streamers [22, 23] which enhance anomalous transport.

Despite all the progress made in the experiments and the turbulence modeling, the development of first-principles simulations remains a crucial point to understand anomalous transport. Its effect affects the whole scaling (1.3). Therefore, there is a need to develop models that contain as many relevant effects as possible, such as collisionality, electron dynamics, impurities, α -particles and diverted geometry, and then to understand the physical processes that control plasma turbulence. Because experimental uncertainties are large and because most of the transport models do not take turbulence effects properly into account, first principles based numerical simulations are very much required.

They are able to isolate the influence of a single physical quantity and operate in a wide range of time and length scales, whereas it is a great challenge to vary only one parameter in a series of experiments and to keep the remaining parameters fixed. Moreover, simulation models can be verified by means of analytical studies, but are only valid over a certain spatio-temporal window.

1.2 Numerical treatment of microinstabilities

There is a wide variety of approaches to describe microinstabilities: the fluid approach consists of computing the time evolution of moments of the distribution function (see for example [24, 25]). Fluid equations have then been modified to include kinetic effects. It is called the gyrofluid approach [26], and is able to handle Landau damping [27], FLR [28] and toroidal drift resonances [29]. Note that gyrofluid codes are also able to study edge turbulence [30], [31]. Unfortunately, fluid and gyrofluid simulations with standard closure artificially damp the zonal flows (a component of which, the Rosenbluth-Hinton residual, is undamped in the collisional limit). Since zonal flows are regulating ITG turbulence, the fluid and gyrofluid models generally overestimate ion transport. Various closures have been proposed to solve this problem.

Obviously, a full kinetic treatment of microinstabilities is needed. In this framework, the gyrokinetic model [32] is the most suitable method: the aim is to get rid of the gyrorange dependence in the original equations, thus reducing the phase space from 6D to 5D. Various gyrokinetic equations can be found in [33, 34, 35, 36]. Three different numerical approaches are used to solve the gyrokinetic equations. In the Eulerian scheme [37, 38, 39], the distribution function is discretized on a fixed grid and is solved with spectral or finite difference methods. The main difficulties come from the Courant-Friedrich-Levy (CFL) condition and the convergence with respect to the 5D grid size, which can be difficult to show. The semi-Lagrangian method [40, 41, 42, 43] uses a fixed grid in time whereas the Vlasov equation is integrated along trajectories. This method removes the CFL constraint, but can, as for Eulerian simulations, lead to negative values of the distribution function. Finally, the Particle-In-Cell (PIC) method [32, 44, 45, 46, 47, 48, 49] is one of the most promising schemes to study microinstabilities in the gyrokinetic framework: the distribution function is sampled along trajectories with numerical particles (markers).

This approach is conceptually simple, easily generalized to multi-dimensional simulations, more adapted for complex geometries such as stellarators [50, 51] and computationally less expensive than the Eulerian and the semi-Lagrangian methods. The disadvantage of the PIC method is the unavoidable statistical noise associated with the sampling using markers. However, significant progresses have been made to limit this numerical noise [52, 53]. In addition to the solving methods, another important distinction between the different models is the simulated domain. In local simulations, turbulence is studied on a single magnetic surface. A less restrictive method is to simulate a flux-tube following a given magnetic-field line. This approach reduces the computer resources needed, but imposes inconsistent T and ∇T profiles (i.e. $T = \text{const}$, $\nabla T = \text{const}$). The global approach is certainly the most realistic model, because it contains the whole radial domain and therefore the effects of profile variation.

Independently of the numerical method used, many assumptions are made for global simulations to keep the CPU time reasonable. In the simplest global ITG model, electrons are adiabatic, turbulence is electrostatic, collisions are neglected and the magnetic surfaces are approximated as circular. However, with the rapid increase of large-scale computers, one is progressively able to relax these assumptions and to take more and more effects into account.

1.3 Contribution of this thesis

The aim of the thesis is the development and the application of the ORB5 code, originally written by Parker [45] and further developed by Tran [44]. ORB5 is a nonlinear gyrokinetic global code which solves the Vlasov-Poisson system in the electrostatic and collisionless limit and has the capability of handling true MHD equilibria [54, 55]. When this work was started, the main weakness of the code was that it did not take advantage of the alignment of turbulence with the magnetic field. The consequences were that numerical noise was exceedingly large and the scaling of computing resources with plasma size was bad. Therefore, the code has been rewritten with a new system of coordinates and an improved Fourier filtering technique. There are numerous benefits: for ITG turbulence, the scaling of CPU time required to simulate a whole plasma of minor radius $a = \rho_s(\rho^*)^{-1}$ goes from $(\rho^*)^{-4}$ to $(\rho^*)^{-2}$, resulting in massive CPU savings: it will be shown why the

time step can be increased and why the number of particles needed for a noise-reduced simulation can be reduced. An acceptable energy conservation has been obtained. The memory has been strongly reduced by developing new solvers for the Poisson equation. Furthermore, a very good scaling with the number of processors has been shown.

When this work was started, electrons were approximated as adiabatic. This underestimates transport of ITG modes, which are destabilized by trapped electrons. Adiabatic electrons do not allow the study of TEM modes. Nonlinearly, it is difficult to study these modes because it is required to solve both the fast electron and the slow ion dynamics. In addition, passing electrons are not adiabatic on rational surfaces and a large radial resolution is needed. For these reasons, a kinetic trapped electrons model has been developed, in which passing electrons remain adiabatic. This model has been applied to study nonlinear physics associated to TEM turbulence. While it is well known that zonal flows shearing acts as a saturation mechanism for ITG turbulence, their effect on TEM turbulence remains unclear [56, 57]. However, these simulations were done in flux-tube geometry. For the first time, the effects of zonal flows on TEM heat transport in a global model are investigated. These huge simulations were possible thanks to the numerous optimizations brought to ORB5.

The improved version of the code has also been used to revisit the impact of the parallel nonlinearity, which has been controversial. Results prove that the differences observed with the old version of ORB5 were due to numerical noise. When this issue is properly treated, the parallel nonlinearity does not significantly modify the zonal flow structure. Finally, one of the most original result presented in this work concerns the entropy. Standard δf PIC simulations reach a quasi-steady state for which the entropy (proportional to numerical noise) grows linearly in time in the late nonlinear phase, making them inadequate for quantitative predictions. In ORB5, a noise-control algorithm has been implemented [58] which has been designed in order to make long simulations. In this thesis it is shown, through the numerical study of a fluctuation entropy balance equation, that ORB5 simulations employing this noise-control algorithm reach a steady-state. This result is a key step towards the reliability of gyrokinetic PIC simulations with the view of comparing them with fusion experiments.

1.4 Outline

The thesis is organized as follows. The basic linear physics of microinstabilities is explained in Chapter 2 with the help of dispersion relations. In Chapter 3, the gyrokinetic model of ORB5 is described. The detailed discretization of the model equations is derived in Chapter 4, and in particular the new implementation using magnetic coordinates. The numerical aspects of ORB5 are shown in Chapter 5, such as noise reduction through the new Fourier filtering technique, linear convergence, comparisons with linear dispersion relations, and benchmark with other gyrokinetic codes. In Chapter 6, ORB5 is applied to two important issues in the gyrokinetic theory: the notion of steady state and the role of the parallel nonlinearity. In Chapter 7, the trapped electron model implemented in ORB5 is presented, together with numerical convergence studies, comparisons with linear dispersion relations and other gyrokinetic codes. The final part of Chapter 7 deals with nonlinear studies of TEM turbulence, in particular the role of the zonal flows. Finally, the conclusions and the future perspectives are presented in Chapter 8.

Chapter 2

A local linear model for microinstabilities

Microinstabilities are electromagnetic perturbations driven through free energy channels such as temperature and density gradients. Although these turbulent processes are fundamentally nonlinear, an analytical study of their linear properties is a good starting point to understand the basic physical phenomena leading to these instabilities. In this Chapter, several dispersion relations originally developed in [59] are presented and the influence of the main parameters are discussed. A comparison with ORB5 will be given in Chapter 5 for the case of adiabatic electrons and in Chapter 7 for the case of kinetic trapped electrons. S.I. units will be used.

2.1 Basic concepts

Before discussing properties of microinstabilities, some basic concepts of plasma physics are introduced.

2.1.1 Particle drifts

The projection of the particle motion on a plane perpendicular to a straight and homogeneous magnetic field \vec{B} is called the *cyclotron* motion. Particle have a helix motion around the field lines. The associated radius is called the *Larmor radius*, $\rho_L = mv_{\perp}/(qB)$, where m is the mass, q is the charge, and v_{\perp} is the velocity perpendicular to the mag-

netic field. The associated frequency is the *cyclotron frequency* $\Omega = qB/m$. However, this motion changes when the particle is submitted to an external force or if the magnetic field becomes curved or inhomogeneous. If the particle is submitted to an external force \vec{F} , supposed constant, then the motion is:

$$v_{\parallel}(t) = v_{\parallel}(t_0) + \frac{F_{\parallel}}{m}(t - t_0) \quad (2.1)$$

$$\vec{v}_{\perp} = \vec{v}_D + \vec{v}_{\perp} \quad (2.2)$$

$$\vec{v}_D = \frac{1}{qB^2} \vec{F}_{\perp} \times \vec{B} \quad (2.3)$$

with \vec{v}_{\perp} is the perpendicular velocity of the cyclotron motion. In addition to its cyclotron motion, the particle has a *drift velocity* \vec{v}_D perpendicular to the magnetic field. For example, if the particle is submitted to a constant electric field \vec{E} , the drift velocity will be $\vec{v}_D = (\vec{E}_{\perp} \times \vec{B})/B^2$, independent of the electric charge. The left plot of Fig. 2.1 displays such a trajectory. During one half of its gyration, the particle is slowed down by the electric field, resulting in a smaller Larmor radius. During the other half, the particle is accelerated by the electric field, resulting in a larger Larmor radius. Electrons and ions would drift in the same direction because both their gyromotion and the electric force change directions. A similar effect occurs if the magnetic field has a perpendicular gradient. Suppose $\vec{B} = B_z(y)\vec{e}_z$. The change of the magnetic field during the particle's gyration modifies the Larmor radius and causes particles to drift. The problem is too complex to be solved analytically; if the magnetic field is slightly inhomogeneous, that is if $\rho_L \ll B/|\nabla B|$, one can expand $B_z(y)$ around $y = 0$, $B_z \cong B_0 + y\partial B_z/\partial y + \mathcal{O}(y^2)$, and so at first order:

$$F_y = -qv_x B_z(y) \cong -qB_0 v_{\perp} \cos(\Omega t) \mp q\rho_L v_{\perp} \cos^2(\Omega t) \frac{\partial B}{\partial y} \quad (2.4)$$

This force is not constant; however by averaging it on an orbit gyration, one have $F_y = \mp \frac{1}{2} q\rho_L v_{\perp} \partial B/\partial y$. The choice of the y axis for the gradient was arbitrary and so using (2.3):

$$v_{\nabla B} = \frac{m}{qB^2} \frac{v_{\perp}^2}{2} \left(\frac{\vec{B}}{B} \times \nabla B \right) \quad (2.5)$$

For this kind of drift, ions and electrons drift in opposite directions.

If the magnetic field is curved with a radius of curvature R_c , it is of the form $\vec{B} = B_{\theta}\vec{e}_r$. Particles will experience a centrifugal force $\vec{F} = mv_{\parallel}^2 \vec{R}_c/R_c^2$, giving rise to a drift:

$$v_R = \frac{m}{qB^2} v_{\parallel}^2 \left(\frac{\vec{B}}{B} \times \nabla B \right) \quad (2.6)$$

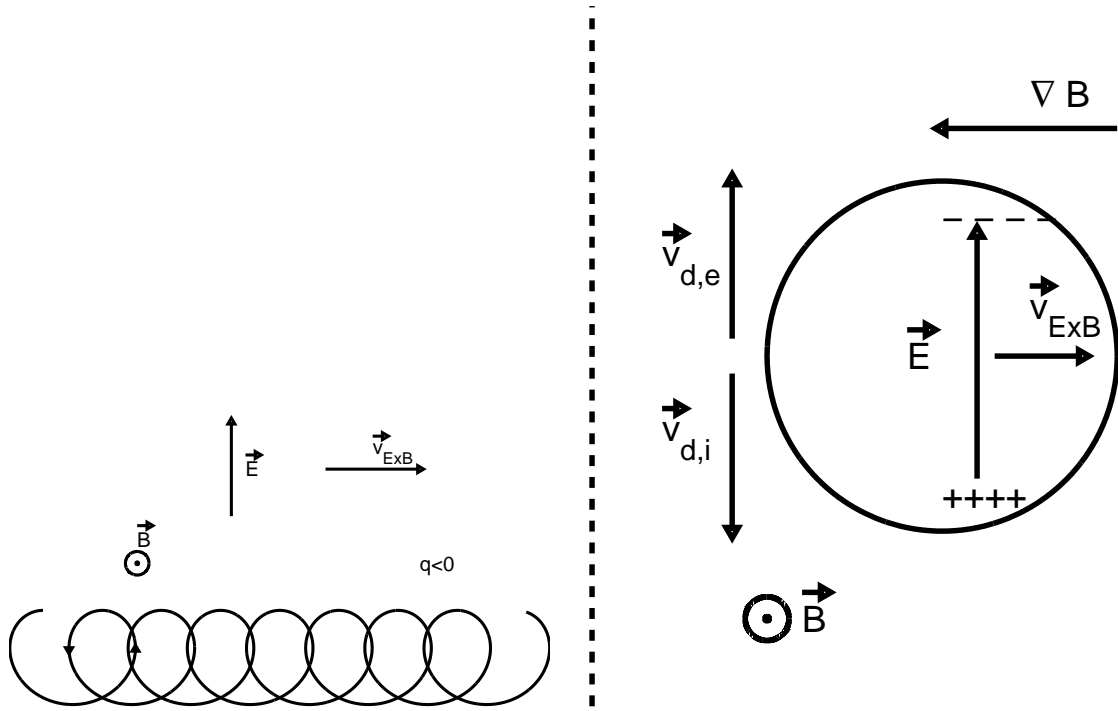


Figure 2.1: The $\vec{E} \times \vec{B}$ drift (left) and the confinement loss in a tokamak (right).

In the vacuum, $\nabla \times \vec{B} = 0$, yielding $\vec{B}_\theta \propto 1/r$: a curved magnetic field must have a gradient, which means that both $v_{\nabla B}$ and v_R contribute to the drift. In particular, it is impossible to confine a plasma with a purely toroidal magnetic field: ions and electrons would rapidly drift in opposite directions, creating a vertical electric field which would give rise to an outward radial $\vec{E} \times \vec{B}$ drift for all charged particles. All particles would hit the edges of the vessel within a few milliseconds. This situation is summarized on the right plot of Fig. 2.1.

2.1.2 Particle trapping

In this Section, the case of a gradient parallel to the magnetic field is examined. Suppose $\vec{B} = B_z(z)\vec{e}_z$, $B_\theta = 0$, $\partial/\partial\theta = 0$. Because of $\nabla \cdot \vec{B} = 0$, the magnetic field must have a radial component:

$$B_r = -\frac{1}{r} \int_0^r r' \frac{\partial B_z}{\partial r'} dr' \quad (2.7)$$

If the gradient does not vary much with r :

$$B_r \cong -\frac{1}{2}r \left. \frac{\partial B_z}{\partial z} \right|_{r=0} \quad (2.8)$$

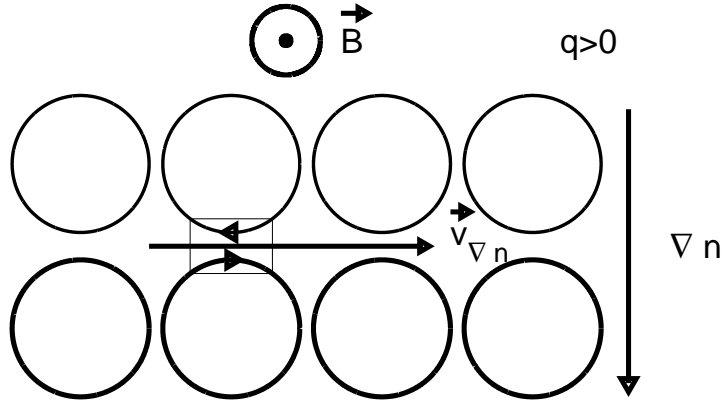


Figure 2.2: Picture of the diamagnetic drift in the case of a density gradient.

This will give a force F_z parallel to the gradient of the magnetic field. Averaging this force on a gyration:

$$F_z = -m\mu \frac{\partial B_z}{\partial z} \quad (2.9)$$

Where $\mu = v_{\perp}^2/(2B)$ is the *magnetic moment* of the particle. The magnetic moment is an *adiabatic invariant*, i.e. it is constant provided the magnetic field does not vary too much in time. This parallel force can cancel the parallel velocity of the particle, which is given by $v_{\parallel} = \sqrt{2E - m\mu B}$ where $E = 1/2mv^2$ is the kinetic energy. When a particle moves up the gradient, v_{\parallel} decreases. If the initial parallel velocity is small enough, one can have $v_{\parallel} = 0$, and then $v_{\parallel} < 0$. The particle will go down the gradient and accelerate. It is then easy to figure out a way to create a magnetic mirror, in which some particles are reflected back and forth. The particle is said to be *trapped* in the magnetic field. The condition for a particle to be trapped is:

$$\sin \lambda > \sqrt{\frac{B_0}{B_{\max}}} \quad (2.10)$$

Where $\lambda = \tan^{-1}(v_{\perp}/v_{\parallel})$ is the *pitch angle* of the particle.

2.1.3 Fluid drift

Many plasma phenomena can be explained by using a *fluid* representation. If this fluid has a density or a temperature gradient, the fluid will drift perpendicularly to \vec{B} and $\nabla n, \nabla T$. This drift is called the *diamagnetic* drift and is explained on Fig. 2.2. Inside a small fluid element, because of the density gradient there will be more particles going to

the right, leading to a net flow. The same phenomenon occurs for a temperature gradient: particles in the high temperature region have a larger velocity and so the fluid will drift.

2.2 The drift wave

In this Section, a simple fluid model is derived to show that the presence of a density gradient leads to a new class of waves called *drift waves*. The equations are:

$$\frac{\partial N_i}{\partial t} + \nabla \cdot (N_i \vec{u}_i) = 0 \quad (2.11)$$

$$m_i \left(\frac{\partial \vec{u}_i}{\partial t} + \vec{u}_i \cdot \nabla \vec{u}_i \right) = e \left(\vec{E} + \vec{u}_i \times \vec{B} \right) \quad (2.12)$$

$$N_e = N_{e0} \exp \left(\frac{e\phi}{T_e} \right) \cong N_{e0} \frac{e\phi}{T_e} \quad (2.13)$$

$$N_{e0} + N_{e0} \frac{e\phi}{T_e} = N_{i0} + \delta N_i \quad (2.14)$$

where ϕ is the electrostatic potential, N_i is the ion density, N_e is the electron density, T_e is the electron temperature and \vec{u}_i is the ion velocity. The first equation is the ion continuity equation, the second equation is the ion momentum equation. Ions are assumed to be cold so there is no pressure gradient term. The third equation expresses the adiabaticity of electrons and the fourth equation is the Poisson equation written in the quasineutrality limit (this approximation will be described in Section 3.6.3). At equilibrium, $N_{e0} = N_{i0} = N_0$. Assuming perturbations of the form $\exp(-i\omega t)$ and linearizing to first order:

$$-i\omega \delta N_i = -N_0 \nabla \cdot \vec{u}_i - \vec{u}_i \cdot \nabla N_0 \quad (2.15)$$

$$-i\omega m_i \vec{u}_i = e \left(-\nabla \phi + \vec{u}_i \times \vec{B} \right) \quad (2.16)$$

$$\delta N_e = \frac{e\phi}{T_e} = \delta N_i \quad (2.17)$$

By taking the cross product of the momentum equation with \vec{B} , the ion velocity becomes:

$$\vec{u} \cong -\frac{\nabla \phi \times \vec{B}}{B^2} + \frac{i\omega}{\Omega_i B} \nabla_{\perp} \phi - \frac{i\Omega_i}{\omega B} \nabla_{\parallel} \phi \vec{e}_{\parallel} \quad (2.18)$$

having assumed low frequencies, i.e. $\omega \ll \Omega_i$ and where $\nabla_{\parallel} = \vec{B}/B \cdot \nabla$ is a scalar operator. The ion velocity is the sum of the $\vec{E} \times \vec{B}$ drift, the polarization drift and the oscillatory parallel motion. Inserting this equation in the continuity equation and replacing δN_i in the quasineutrality equation, one obtains an equation for ϕ :

$$\left(1 - \rho_s^2 \nabla_{\perp}^2 + \frac{c_s^2}{\omega} \nabla_{\parallel}^2 - \frac{1}{i\omega} \vec{v}_{Ne} \cdot \nabla \right) \phi = 0 \quad (2.19)$$

Where $c_s = \sqrt{T_e/m_i}$ is the sound speed, ρ_s is the ion sound radius and the diamagnetic velocity is $\vec{v}_{Ne} = T_e/B^2(\nabla \ln N_0 \times \vec{B})$. The potential is written as $\exp(i\vec{k} \cdot \vec{r})$, with $\vec{k} = k_y \vec{e}_y + k_z \vec{e}_z$. The wave vector must have a small parallel component otherwise the adiabatic assumption is not valid anymore. The dispersion relation finally is:

$$\left[1 + (k_y \rho_s)^2\right] \omega^2 - \omega_{Ne} \omega - c_s^2 k_z^2 = 0 \quad (2.20)$$

with $\omega_{Ne} = \vec{k} \cdot \vec{v}_{Ne}$ is the diamagnetic frequency. If there is no density gradient, the solution is:

$$\omega^2 = \frac{k_z^2 c_s^2}{1 + (k_y \rho_s)^2} \quad (2.21)$$

which is the the dispersion relation of the ion sound wave in homogeneous magnetized plasmas. With a density gradient, the solution is:

$$\omega = \frac{\omega_{Ne} \pm \sqrt{\omega_{Ne}^2 + 4(k_z c_s)^2 [1 + (k_y \rho_s)^2]}}{2[1 + (k_y \rho_s)^2]} \quad (2.22)$$

In the large gradient limit $|\omega_{Ne}| \gg |k_z c_s|$, the solutions become:

$$\omega = \frac{\omega_{Ne}}{1 + (k_y \rho_s)^2} \left\{ 1 + \left(\frac{k_z c_s}{\omega_{Ne}} \right)^2 [1 + (k_y \rho_s)^2] \right\} \quad (2.23)$$

$$\omega = -\frac{\omega_{Ne}}{1 + (k_y \rho_s)^2} \left\{ \left(\frac{k_z c_s}{\omega_{Ne}} \right)^2 [1 + (k_y \rho_s)^2] \right\} \quad (2.24)$$

The physical mechanism for the drift wave is explained on Fig. 2.3. An electrostatic perturbation is propagating in the horizontal direction. This will create local electric fields which will induce $\vec{E} \times \vec{B}$ drifts. Convection cells will rotate clockwise for a potential maximum and counterclockwise for a potential minimum. The adiabatic electrons ensure that the density and the potential are in phase. Due to the density gradient direction, the density will increase on the left of a maximum and will decrease on the right of a maximum: the density will propagate on the left, in the same direction as in the diamagnetic drift. The fluid model exposed in this Section does not show any instability. Although it is possible to develop fluid models that predict unstable waves, the kinetic theory is a more appropriate tool because it accounts for wave-particle interactions. This is the topic of the next Section.

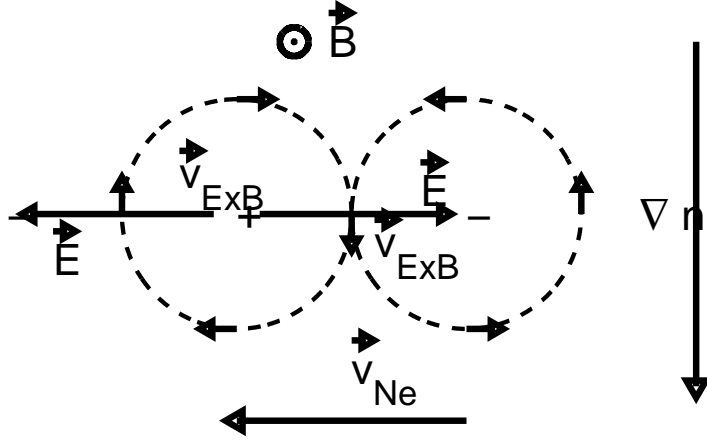


Figure 2.3: Physical mechanism of the drift wave.

2.3 A dispersion relation for slab-ITG instability

In this Section, a simple standard kinetic model, based on [59] is presented to show how density and temperature gradients can lead to instabilities in the plasma. As they degrade the confinement in tokamaks, an understanding of their physical properties is of primary importance. The case of a slab geometry is considered. Let $(\vec{e}_x, \vec{e}_y, \vec{e}_z)$ be a orthonormal coordinate system. The magnetic field is uniform along the z axis, i.e. $\vec{B} = B\vec{e}_z$. The system has temperature and density gradients along the x direction. In addition, this system is submitted to an external force $\vec{F} = F\vec{e}_x$, perpendicular to \vec{B} . The Lagrangian of a particle of charge q and of mass m is:

$$L = \frac{1}{2}m\vec{v}^2 + Fx + qv_yxB \quad (2.25)$$

y is a cyclic coordinate and so $X = x + v_y/\Omega$ is a constant of motion. The plasma state is described with a *distribution function* $f(\vec{x}, \vec{v}, t)$. $f(\vec{x}, \vec{v}, t)d\vec{x}d\vec{v}$ provides the number of particles whose position is between \vec{x} and $\vec{x} + d\vec{x}$ and whose velocity is between \vec{v} and $\vec{v} + d\vec{v}$, at time t . Assuming a collisionless plasma¹, the Vlasov equation that gives the temporal evolution of f is:

$$\frac{df}{dt} = \left[\frac{\partial}{\partial t} + \vec{v} \cdot \frac{\partial}{\partial \vec{r}} + \frac{1}{m}(q\vec{v} \times \vec{B} + \vec{F}) \cdot \frac{\partial}{\partial \vec{v}} \right] f = 0 \quad (2.26)$$

where m is the particle mass and q is the particle charge. A *perturbative* approach is used, i.e. f is separated into an *equilibrium part* f_0 and a *perturbed part* δf with $|\delta f| \ll |f_0|$.

¹The plasma collisionality goes as $T^{-3/2}$. Future fusion devices will create very hot plasmas, which is why the collisionless approximation is often used.

At equilibrium, the plasma is supposed to be Maxwellian, i.e.:

$$f_0(X, H) = \frac{\mathcal{N}(X)}{(2\pi T(X)/m)^{3/2}} \exp\left(-\frac{H}{T(X)}\right) \quad (2.27)$$

Where H is the Hamiltonian given by:

$$H = \vec{v} \cdot \frac{\partial L}{\partial \vec{v}} - L = \frac{1}{2}m\vec{v}^2 - Fx \quad (2.28)$$

$N(X)$ is the density and $T(X)$ is the temperature. In order to have $\frac{d}{dt}f_0 = 0$, f_0 must be function of constants of motion only. The Maxwellian form is, according to the H-theorem, a stationary solution of the collisional Vlasov equation. The gyrokinetic theory assumes that the inhomogeneities related to $\mathcal{N}(X)$ and $T(X)$ are weak compared to the Larmor radii:

$$\epsilon = \frac{\rho_L}{L_A} \ll 1, \rho_L = \frac{v_{\text{th}}}{\Omega}, L_A = \left(\frac{|\nabla A|}{A}\right)^{-1}, A = \mathcal{N}, T \quad (2.29)$$

L_A is the *characteristic length* of the equilibrium quantity A .

Now an electrostatic perturbation is introduced in the system in the form of a small electrostatic potential $\phi \sim \mathcal{O}(\epsilon)$. Writing the Vlasov equation to first order in ϵ :

$$\left. \frac{d}{dt} \right|_{u.t.p.} \delta f = \frac{q}{m} \nabla \phi \cdot \frac{\partial f_0}{\partial \vec{v}} \quad (2.30)$$

where $\left. \frac{d}{dt} \right|_{u.t.p.}$ is the derivative along the unperturbed trajectories of the particles. δf is given by:

$$\delta f(\vec{r}, \vec{v}, t) = \frac{q}{m} \int_{-\infty}^t dt' \nabla \phi \cdot \frac{\partial f_0}{\partial \vec{v}} \Big|_{\vec{r}'(t'), \vec{v}'(t'), t'} \quad (2.31)$$

Local perturbations on the $x = 0$ surface will be considered, and so a plane wave decomposition can be used:

$$\left\{ \phi(x, y, z, t), \delta f(x, y, z, t) \right\} = \left\{ \hat{\phi}(x), \widehat{\delta f}(x) \right\} \exp \left[i(k_y y + k_z z - wt) \right] \quad (2.32)$$

and introducing the unperturbed trajectories:

$$v'_x(t') = (\vec{v} - \vec{v}_F) \cdot \vec{e}_x \cos \left[\Omega(t' - t) \right] + (\vec{v} - \vec{v}_F) \cdot \vec{e}_y \sin \left[\Omega(t' - t) \right] + \vec{v}_F \cdot \vec{e}_x \quad (2.33)$$

$$v'_y(t') = (\vec{v} - \vec{v}_F) \cdot \vec{e}_y \cos \left[\Omega(t' - t) \right] - (\vec{v} - \vec{v}_F) \cdot \vec{e}_x \sin \left[\Omega(t' - t) \right] + \vec{v}_F \cdot \vec{e}_y \quad (2.34)$$

$$v'_z(t') = (\vec{v} - \vec{v}_F) \cdot \vec{e}_z \quad (2.35)$$

$$\begin{aligned}
x'(t') &= x + \frac{1}{\Omega}(\vec{v} - \vec{v}_F) \cdot \vec{e}_x \sin [\Omega(t' - t)] \\
&\quad + \frac{(\vec{v} - \vec{v}_F) \cdot \vec{e}_y}{\Omega} \left\{ 1 - \cos [\Omega(t' - t)] \right\} + \vec{v}_F \cdot \vec{e}_x(t' - t)
\end{aligned} \tag{2.36}$$

$$\begin{aligned}
y'(t') &= y + \frac{1}{\Omega}(\vec{v} - \vec{v}_F) \cdot \vec{e}_y \sin [\Omega(t' - t)] \\
&\quad - \frac{(\vec{v} - \vec{v}_F) \cdot \vec{e}_x}{\Omega} \left\{ 1 - \cos [\Omega(t' - t)] \right\} + \vec{v}_F \cdot \vec{e}_y(t' - t)
\end{aligned} \tag{2.37}$$

$$z'(t') = z + \vec{v} \cdot \vec{e}_z(t' - t) \tag{2.38}$$

$\vec{v}_F = \frac{\vec{F} \times \vec{B}}{qB^2}$ is the drift velocity. One can after some algebra integrate (2.31) to get:

$$\widehat{\delta f} = -\frac{q\hat{\phi}}{T} \left\{ 1 - (\omega'_d - \omega) \sum_{n, n'=-\infty}^{+\infty} \frac{J_n\left(\frac{k_y v_\perp}{\Omega}\right) J_{n'}\left(\frac{k_y v_\perp}{\Omega}\right)}{\omega_F - \omega + n\Omega + k_z v_z} \exp[i\theta(n' - n)] \right\} f_0 \tag{2.39}$$

where:

$$\omega'_d = \omega_N + \omega'_T + \omega_F \tag{2.40}$$

$$\omega_N = \frac{T k_y}{qB} \frac{d \ln \mathcal{N}}{dx}, \quad \omega'_T = \frac{T k_y}{qB} \frac{dT}{dx} \frac{\partial}{\partial T}, \quad \omega_F = -\frac{k_y F}{qB} = \vec{k} \cdot \vec{v}_F \tag{2.41}$$

J_n is the Bessel function of the first kind of order n and θ is the gyroangle. The following property has been used:

$$\exp(ix \sin \theta) = \sum_{n=-\infty}^{+\infty} J_n(x) \exp(-in\theta) \tag{2.42}$$

The Poisson equation in Fourier space reads:

$$-\Delta \hat{\phi} = k^2 \hat{\phi} = \frac{1}{\epsilon_0} \sum_{\alpha} q_{\alpha} \widehat{\delta N}_{\alpha} \tag{2.43}$$

where α represents the different species and $\widehat{\delta N}_{\alpha} = \int d\vec{v} \widehat{\delta f}_{\alpha}$. The dispersion relation solution is obtained by solving the dielectric function:

$$\epsilon(\vec{k}, \omega) = 1 - \sum_{\alpha} \frac{q_{\alpha}}{k^2 \epsilon_0 \hat{\phi}} \widehat{\delta N}_{\alpha} \tag{2.44}$$

Gyrokinetics only considers low frequencies in the sense that $\omega \ll \Omega_{\alpha} \forall \alpha$ and finally the dielectric function is:

$$\epsilon(\vec{k}, \omega) = 1 + \sum_{\alpha} \frac{1}{k^2 \lambda_{D\alpha}^2} \left\{ 1 - (\omega'_{d\alpha} - \omega) \frac{\Lambda_0(k_y^2 \rho_{L\alpha}^2)}{\omega - \omega_{F\alpha}} \left[W\left(\frac{\omega - \omega_{F\alpha}}{|k_z| v_{\text{th}\alpha}}\right) - 1 \right] \right\} \tag{2.45}$$

Where $\lambda_{D\alpha} = \sqrt{\epsilon_0 T_\alpha / (q_\alpha^2 N_\alpha)}$ is the Debye length of the species α , $\Lambda_0(x) = I_0(x) \exp(-x^2)$ is the scaled modified Bessel function of the first kind of order 0, $\rho_{L\alpha} = v_{th\alpha} / \Omega_\alpha$ is the Larmor radius and $W(z)$ is the dispersion function:

$$W(z) = \frac{1}{\sqrt{2\pi}} \int_{-\infty}^{\infty} \frac{x}{x-z} \exp\left(-\frac{1}{2}x^2\right) dx \quad (2.46)$$

To get (2.45), the following property has been used (see [60]):

$$\int_0^{\infty} dx \exp(-\rho^2 x^2) J_p(\alpha x) J_p(\beta x) = \frac{1}{2\rho^2} \exp\left(-\frac{\alpha^2 + \beta^2}{2}\right) I_p\left(\frac{\alpha\beta}{2\rho^2}\right) \quad (2.47)$$

The following expansions will be used:

$$W(z) = 1 + iz\sqrt{\frac{\pi}{2}} \exp\left(-\frac{1}{2}z^2\right) + \sum_{n=0}^{+\infty} \frac{(-1)^{n+1}}{(2n+1)!!} z^{(2n+2)} \quad |z| \ll 1 \quad (2.48)$$

$$W(z) = iz\sqrt{\frac{\pi}{2}} \exp\left(-\frac{1}{2}z^2\right) - \sum_{n=1}^{+\infty} \frac{(2n-1)!!}{z^{2n}} \quad |z| \gg 1 \quad (2.49)$$

Note that causality is expressed by imposing $Im(\omega) > 0$. Although many approximations have been used, Eq. (2.45) contains all the basic physics of the slab-ITG mode. The effects of density and temperature gradients are contained in the operator $\omega'_{d\alpha}$. The FLR effects are contained in $\Lambda_0(k_y^2 \rho_{L\alpha}^2)$, and the wave-particle interaction, in this case the Landau damping, is contained in the dispersion function W . To get a deeper understanding of this instability, further approximations need to be made: suppose a plasma made of ions and electrons, and no force is applied to the system so $\omega_{Fi} = \omega_{Fe} = 0$. The frequencies of interest are in the range $|k_z|v_{thi} \ll |\omega| \ll |k_z|v_{the}$ so that $W[\omega/(|k_z|v_{thi})] \cong k_z^2 v_{thi}^2 / \omega^2$ and $W(\omega/(|k_z|v_{the})) \cong 1$ (the exponentially decreasing imaginary part has been neglected). This last assumption means that electrons are adiabatic. The wavelengths of interest are in the range $k_y \rho_{Li} \sim 1$ such that $k_y \rho_{Le} \ll 1$ and so $\Lambda_0(k_y^2 \rho_{Le}^2) \sim 1$. Finally quasineutrality is assumed, in other words $k^2 \lambda_{D\alpha}^2 \ll 1$, because the Debye length is much smaller than the Larmor radius which is the typical spatial scale of the system, so the plasma is considered to be quasineutral. (2.45) becomes:

$$\epsilon(\vec{k}, \omega) = \frac{1}{k^2 \Lambda_{De}^2} + \frac{1}{k^2 \Lambda_{Di}^2} \left\{ 1 + \left(1 - \frac{\omega_{Ni} + \omega'_{Ti}}{\omega} \right) [W(z_i) - 1] \Lambda_0(\xi_i) \right\} \quad (2.50)$$

where $\xi_i = k_y^2 \rho_{Li}^2$ and $z_i = \omega / (|k_z| v_{thi})$. Using $W'(z) = (1/z - z)W(z) - 1/z$ and $\Lambda'_0(\xi) = \Lambda_1(\xi) - \Lambda_0(\xi)$, one has:

$$\begin{aligned} \epsilon(\vec{k}, \omega) &= \frac{1}{k^2 \Lambda_{De}^2} + \frac{1}{k^2 \Lambda_{Di}^2} \left(1 + \left(1 - \frac{\omega_{Ni} - \omega_{Ti}/2}{\omega} \right) [W(z_i) - 1] \Lambda_0(\xi_i) \right. \\ &\quad \left. - \frac{\omega_{Ti}}{\omega} \left\{ \xi_i [\Lambda_1(\xi_i) - \Lambda_0(\xi_i)] [W(z_i) - 1] + \frac{z_i^2}{2} W(z_i) \Lambda_0(\xi_i) \right\} \right) \end{aligned} \quad (2.51)$$

where $\omega_{Ti} = T k_y / (qB) d \ln T / dx$. To identify the instability boundary, $\epsilon(\vec{k}, \omega_B) = 0$ must be solved separately for the real and imaginary parts: by solving for z_i^2 in the first equation and for ω_B / ω_{Ti} for the second, one gets:

$$z_i^2 = \frac{2(1 + \tau^{-1}) \omega_B}{\Lambda_0(\xi_i) \omega_{Ti}} > 0 \quad (2.52)$$

$$\frac{\omega_B}{\omega_{Ti}} = \frac{\Lambda_0(\xi_i)}{2[\tau^{-1} + 1 - \Lambda_0(\xi_i)]} \left(1 - \frac{2}{\eta_i} - 2\xi_i \frac{\Lambda_1(\xi_i) - \Lambda_0(\xi_i)}{\Lambda_0(\xi_i)} \right) \quad (2.53)$$

From these two equations, one sees that an instability can develop only if:

$$\eta_i > 2 \left(1 - 2\xi_i \frac{\Lambda_1(\xi_i) - \Lambda_0(\xi_i)}{\Lambda_0(\xi_i)} \right)^{-1} \quad (2.54)$$

$$|k_{\parallel}| < \frac{k_y \rho_{Li}}{2L_{Ti}} \frac{\Lambda_0(\xi_i)}{\sqrt{1 + \tau^{-1}} \sqrt{\tau^{-1} + 1 - \Lambda_0(\xi_i)}} \sqrt{1 - \frac{2}{\eta_i} - 2\xi_i \frac{\Lambda_1(\xi_i) - \Lambda_0(\xi_i)}{\Lambda_0(\xi_i)}} \quad (2.55)$$

and therefore the ITG instability has a gradient threshold and a maximum k_{\parallel} beyond which the instability is suppressed by Landau damping. An estimate of the growth rate and real frequencies can be obtained by assuming that FLR effects are weak such that $\xi_i \ll 1 \Rightarrow \Lambda_0(\xi_i) \cong 1$, and that resonant effects are weak such that $z_i \gg 1 \Rightarrow W(z_i) \cong 1 - k_z^2 v_{thi}^2 / \omega^2$ and the dispersion relation finally is:

$$1 - \left(\frac{k_z c_s}{\omega} \right)^2 \left(1 - \frac{\omega_{Ti}}{\omega} \right) \quad (2.56)$$

The slab-ITG instability can be viewed as a deformation of the sound wave branch $\omega = \pm k_z c_s$. In the strong gradient $\omega_{Ti} \gg \omega$, (2.56) gives:

$$\omega = \left(\frac{1}{2} + i \sqrt{\frac{3}{2}} \right) |\omega_{Ti} (k_z c_s)^2|^{1/3} \quad (2.57)$$

which is true if $|k_z c_s| \ll |\omega_{Ti}|$ or if:

$$\frac{|k_z|}{|k_y|} \ll \frac{T_i \rho_{Li}}{T_e L_{Ti}} \quad (2.58)$$

The intuitive picture that a strong gradient leads to a stronger instability is recovered. In addition, one sees that the wave needs a finite parallel wavenumber much smaller than the perpendicular one. If $k_z = 0$, then the electron adiabaticity assumption becomes wrong. Note also that if the perpendicular wavelength becomes of the order of the electron Larmor radius, then $\xi_i = (k_y \rho_{Li})^2 \gg 1$, $\Lambda_0(\xi_i) \rightarrow 0$: ions have an adiabatic-like response. One then speaks of the ETG-instability, which is isomorphic to the ITG instability from the linear point of view.

2.4 A dispersion relation for toroidal-ITG instability

Tokamaks and stellarators have curved magnetic fields, whose main effect is to introduce a drift velocity on the particles. This Section shows how a new branch, namely the toroidal-ITG branch appears. To model the curvature of the magnetic field, an external force is introduced:

$$\vec{F} = -m \left(\frac{v_\perp^2}{2} + v_z^2 \right) \nabla_\perp \ln B \quad (2.59)$$

This force models the curvature and gradient of the magnetic field. It is important to take into account the velocity dependence of this force as resonant effects become important near the marginal points. Defining $R = |\nabla_\perp \ln B|^{-1}$, \vec{F} leads to the characteristic frequency:

$$\omega_F = \vec{k} \cdot \vec{v}_F = -\frac{k_y F}{qB} = \frac{k_y m}{qBR} \left(\frac{v_\perp^2}{2} + v_z^2 \right) \quad (2.60)$$

One goes back to equation (2.39):

$$\widehat{\delta f} = -\frac{q\hat{\phi}}{T} \left\{ 1 - (\omega'_d - \omega) \sum_{n,n'=-\infty}^{+\infty} \frac{J_n \left(\frac{k_y v_\perp}{\Omega} \right) J_{n'} \left(\frac{k_y v_\perp}{\Omega} \right)}{\omega_F - \omega + n\Omega + k_z v_z} \exp \left[i\theta(n' - n) \right] \right\} f_0 \quad (2.61)$$

Because \vec{F} models the effect of a non-uniform magnetic field, it does not modify the energy of the system. The ω_F appearing in the ω'_d in the numerator can be dropped because it is related to the modification of energy by the external force. However the ω_F term appearing in the denominator is related to the particles velocity and must be retained. The dielectric response becomes:

$$\epsilon(\vec{k}, \omega) = 1 + \sum_\alpha \frac{1}{k^2 \Lambda_{D\alpha}^2} [1 + (\omega - \omega_{N\alpha} - \omega'_{T\alpha})] \int d\vec{v} \frac{f_{0\alpha}}{N_\alpha} \frac{J_0^2 \left(\frac{k_y v_\perp}{\Omega_\alpha} \right)}{k_z v_z + \omega_{F\alpha}(v_z, v_\perp) - \omega} \quad (2.62)$$

Having considered again only the $n = 0$ harmonics and $v_z \cong v_{\parallel}$. The temperature derivatives appear in f_0 only. Invoking a plasma made out of ions and electrons, quasineutrality and adiabatic electrons, one gets:

$$0 = \frac{1}{\tau} + \left[1 + (\omega - \omega_{Ni}) \int d\vec{v} \frac{f_{0i}}{N} \frac{J_0^2\left(\frac{k_y v_{\perp}}{\Omega}\right)}{\omega_{Fi}(v_z, v_{\perp}) - \omega + k_z v_z} \right] - \omega_{Ti} \int d\vec{v} \frac{f_{0i}}{N} \left(\frac{E}{T_i} - \frac{3}{2} \right) \frac{J_0^2\left(\frac{k_y v_{\perp}}{\Omega}\right)}{\omega_{Fi}(v_z, v_{\perp}) - \omega + k_z v_z} \quad (2.63)$$

This equation can be solved numerically to obtain the real frequency and the growth rate of the instability. To get a physical picture of the toroidal ITG instability, a fluid limit $|\omega/(k_z v_{\text{thi}})| \gg 1$, $|\omega/\omega_F| \gg 1$ is considered, as well as negligible FLR effects $\xi_i \ll 1$. The Bessel function and the denominator can be expanded and the integral can be performed, yielding the following dispersion relation:

$$\frac{1}{\tau} + \frac{\omega_{Ni}}{\omega} - \left(1 - \frac{\omega_{Ni} + \omega_{Ti}}{\omega} \right) \left[\frac{k_z^2 v_{\text{thi}}^2}{\omega^2} + \frac{\langle \omega_{Fi} \rangle}{\omega} - (k_y \rho_{Li})^2 \right] = 0 \quad (2.64)$$

where $\langle \omega_{Fi} \rangle = 2T_i k_y / (eBR)$. Considering the effect of a temperature gradient and neglecting FLR effects:

$$1 - \left(1 - \frac{\omega_{Ti}}{\omega} \right) \left[\left(\frac{k_z c_s}{\omega} \right)^2 + \tau \frac{\langle \omega_{Fi} \rangle}{\omega} \right] = 0 \quad (2.65)$$

This equation is very similar to equation (2.56): the slab-ITG dispersion relation is further deformed by a non-uniform magnetic field. Taking a perpendicular propagation $k_z = 0$ and a large temperature gradient, the solution is:

$$\omega = \pm \sqrt{-2\tau \left(\frac{k_y T_i}{eB} \right)^2 \nabla \ln T_i \cdot \nabla \ln B} \quad (2.66)$$

This leads to one of the fundamental property of the toroidal-ITG mode: it is unstable only if the gradients of temperature and magnetic field are in the same direction. In tokamaks, this is the case in the Low-Field-Side (LFS) region: one says that the mode has a *ballooning* character. ITG modes can have a slab-like or a toroidal-like character, depending on the ratio between the terms $(k_z c_s / \omega)^2$ and $T_e / T_i \cdot \langle \omega_{Fi} \rangle / \omega$: the pure toroidal ITG mode appears in the limit $k_z \rightarrow 0$. Finally, a stability condition can be derived for $k_z \rightarrow 0$ and $k_y \rho_{Li}$. The dispersion relation (2.65) gives:

$$\frac{\omega}{\omega_{Ni}} = \left(2\epsilon_N - 1 \pm \sqrt{(2\epsilon_N - 1)^2 - \frac{8\epsilon_N}{\tau}(1 + \eta_i)} \right) \frac{\tau}{2} \quad (2.67)$$

where $\epsilon_N = L_N/R$. Thus if $\epsilon_N > 0$ the mode is unstable if:

$$\eta_i > \frac{\tau}{8} \frac{(2\epsilon_N - 1)^2}{\epsilon_N} - 1 \quad (2.68)$$

Like for the slab-ITG instability, the toroidal ITG has a treshhold behaviour.

With this very simple model, many properties of ITG modes have been derived. The main missing effect is the effect of the *magnetic shear* defined by (for circular geometry):

$$\hat{s} = \rho \frac{q'(\rho)}{q(\rho)} \quad (2.69)$$

The shear describes the variation of the safety factor across magnetic surfaces. To include it, the ballooning transform [61, 62] is the most appropriate formalism. It exploits the fact that toroidal ITG modes tend to align with the field lines, i.e. $\vec{e}_{\parallel} \cdot \nabla \phi \cong 0$ and so:

$$\phi = \sum_n \sum_k \hat{\phi}_n(nq, \theta - \theta_0 + 2\pi k) \exp \left\{ [in\varphi - nq(\theta - \theta_0 + 2\pi k)] \right\} \quad (2.70)$$

For circular magnetic surfaces:

$$\vec{k} = i\nabla = i\frac{n}{r}\vec{e}_{\varphi} - \frac{nq}{\rho}\vec{e}_{\theta} - \frac{nq}{\rho}\theta\hat{s}\vec{e}_{\rho} \quad (2.71)$$

where n is the toroidal mode number, q is the safety factor, φ is the toroidal angle, θ is the poloidal angle. This representation contains the effects of the shear but is more complicated to solve as a 1D eigenvalue equation has to be solved for $\hat{\phi}_n(\theta)$.

2.5 A dispersion relation for TEM instabilities

In the tokamak, the magnetic field is mainly toroidal, i.e. $\vec{B} \cong B_0 R_0 / r \vec{e}_{\varphi}$, and is in particular non-uniform, which means that particles can be trapped. A typical trapped orbit is shown on Fig. 2.4. When a particle goes from the LFS to the HFS, the perpendicular velocity increases because of magnetic moment conservation and the parallel velocity decreases due to energy conservation. The parallel velocity can then change sign. In the poloidal plane, the particle will go to the LFS and then to the HFS where it will be reflected again. However, after a banana the particle has moved toroidally. This motion is the *precessional* drift and can enter in resonance with a wave, leading to the so-called Trapped Ion Mode (TIM) or Trapped Electron Mode (TEM) instability. The

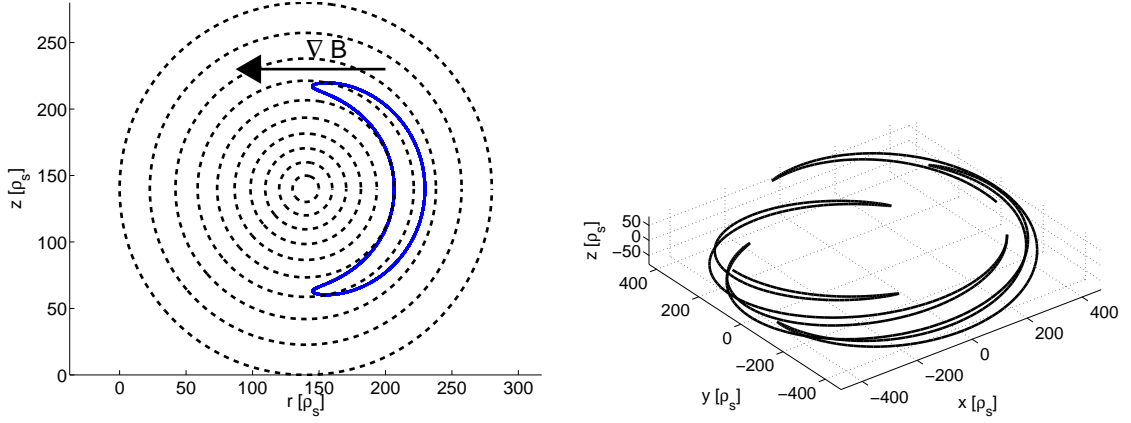


Figure 2.4: Typical banana orbit in the poloidal plane (left) and 3D orbit of a trapped particle (right).

following model, based on a bounce-average method is able to capture the TIM or the TEM instability. The starting point is again the linearized Vlasov equation:

$$\left. \frac{d}{dt} \right|_{u.t.p.} \delta f = \frac{q}{m} \nabla \phi \cdot \frac{\partial f_0}{\partial \vec{v}} \quad (2.72)$$

In a tokamak geometry, the Maxwellian is a function of kinetic energy and toroidal angular momentum $\psi_0 = \psi + \frac{mrv_\varphi}{q}$ where ψ is the poloidal magnetic flux. The ordering is done with respect to the small parameter $\epsilon = \rho_{Li}/a$, assuming $\omega/\Omega_i \sim \mathcal{O}(\epsilon)$, $k_{\parallel}\rho_{Li} \sim \mathcal{O}(1)$, $k_{\perp}\rho_{Li} \sim \mathcal{O}(1)$. Two orthonormal, right-handed systems of coordinates are used, $(\vec{e}_n, \vec{e}_p, \vec{e}_\varphi)$ and $(\vec{e}_n, \vec{e}_b, \vec{e}_{\parallel})$, with $\vec{e}_n = \nabla\psi/|\nabla\psi|$ and $\vec{e}_{\parallel} = \vec{B}/B$. By expanding Vlasov up to $\mathcal{O}(\epsilon)$, one gets:

$$\left. \frac{d}{dt} \right|_{u.t.p.} \delta g = \frac{qf_0}{T} \frac{\partial \phi}{\partial t} - \frac{1}{B} \nabla_b \phi \nabla_n f_0 + \mathcal{O}(\epsilon^2) \quad (2.73)$$

with $\delta g = \delta f + q\phi/T f_0$ the non-adiabatic part of the perturbed distribution function and with the notations $\nabla_n = |\nabla\psi|\partial/\partial\psi = -rB_p\partial/\partial\psi$ and $\nabla_b = \vec{e}_b \cdot \nabla$. To get the previous equality, the property $\vec{e}_\varphi = B_\varphi/B\vec{e}_{\parallel} + B_p/B\vec{e}_b$ has been used. From now on the mass will be set to 1. The next step is to write the operator $\left. \frac{d}{dt} \right|_{u.t.p.}$ in the guiding center variables $(\vec{R}, E, \mu, \alpha, \sigma)$ defined by:

$$\vec{v} = v_{\perp} (\cos \alpha \vec{e}_n + \sin \alpha \vec{e}_b) + v_{\parallel} \vec{e}_{\parallel} \quad (2.74)$$

$$\vec{R} = \vec{r} + \frac{1}{\Omega} (\vec{v} \times \vec{e}_{\parallel}) \quad (2.75)$$

$$\mu = \frac{v_{\perp}^2}{2B}, \quad E = \frac{1}{2}(v_{\parallel}^2 + v_{\perp}^2), \quad \sigma = \text{sign}(v_{\parallel}) \quad (2.76)$$

After some algebra, one gets $\frac{d}{dt}\Big|_{u.t.p.} = L^{(0)} + L^{(1)}$, with $L^{(0)} \sim \mathcal{O}(1)$ and $L^{(1)} \sim \mathcal{O}(\epsilon)$ defined by:

$$L^{(0)} = -\Omega \frac{\partial}{\partial \alpha}, \quad L^{(1)} = \frac{\partial}{\partial t} + [\vec{v}_{\parallel} + \vec{v}_d] \cdot \frac{\partial}{\partial \vec{R}} + \underbrace{\frac{d\mu}{dt} \frac{\partial}{\partial \mu}}_{=0} + \frac{d\alpha}{dt} \frac{\partial}{\partial \alpha} \quad (2.77)$$

and $\vec{v}_d = 1/\Omega \vec{e}_{\parallel} \times \left(v_{\parallel}^2 \vec{e}_{\parallel} \cdot \nabla \vec{e}_{\parallel} + v_{\perp}^2 / 2 \nabla \ln B \right)$. By expanding $\delta g = \delta g^{(0)} + \delta g^{(1)}$, at order 0 one has $L^{(0)} \delta g^{(0)} = 0$ and so $\delta g^{(0)} \neq \delta g^{(0)}(\alpha)$. Finally, gyroaveraging the first order equation yields the gyrokinetic equation:

$$\frac{d}{dt}\Big|_{u.t.g.} \delta g^{(0)} = \frac{q}{T} \frac{\partial \langle \phi \rangle}{\partial T} f_0 - \frac{1}{B} \nabla_b \langle \phi \rangle \nabla_n f_0 \quad (2.78)$$

$$\langle \phi \rangle = \frac{1}{2\pi} \int_0^{2\pi} d\alpha \phi \left(\vec{r} = \vec{R} - \frac{\vec{v} \times \vec{e}_{\parallel}}{\Omega}, t \right) \quad (2.79)$$

Due to their small mass, the electron Larmor radius effects can be ignored, and so $\langle \phi \rangle \cong \phi$. This is the *drift-kinetic* approximation. The subscript 0 will be omitted. For a potential of the form $\phi \exp(-i\omega t + in\varphi)$, this equation becomes:

$$\frac{d}{dt}\Big|_{u.t.g.} \delta g = -i \frac{q f_0}{T} \phi (\omega - \omega_*) \quad (2.80)$$

where:

$$\omega_* = \omega_N \left[1 + \eta \left(\frac{E}{v_{th}^2} - \frac{3}{2} \right) \right], \quad \omega_N = -\frac{T}{qB} \nabla_n \ln N \frac{B}{B_p} k_{\varphi} \quad (2.81)$$

Note that the definition of ω_N in this Section is equivalent to the definition (2.41) to first order in ϵ . To get the bounce-averaged drift kinetic equation, one expands the distribution function with the small parameter $\epsilon_b = \omega/\omega_b \ll 1$ where $\omega_b \sim v_{\parallel}/(q_s r) \sqrt{\epsilon}$. ω_b is the *bounce frequency* and $\epsilon_a = a/R$ is the inverse aspect ratio. Let $\delta g = \delta g^{(0)} + \delta g^{(1)}$. The drift kinetic equation becomes:

$$\frac{\partial}{\partial t} (\delta g^{(0)} + \delta g^{(1)}) + \left(\frac{d\psi}{dt} \frac{\partial}{\partial \psi} + \frac{d\chi}{dt} \frac{\partial}{\partial \chi} + \frac{d\varphi}{dt} \frac{\partial}{\partial \varphi} \right) (\delta g^{(0)} + \delta g^{(1)}) = -i \frac{q f_0}{T} \phi (\omega - \omega_*) \quad (2.82)$$

Let $\langle \dots \rangle_b$ be the bounce-average operator. It is known from guiding center theory that $\langle d\psi/dt \rangle_b = \langle d\chi/dt \rangle_b = 0$ because the orbits are closed in the poloidal plane, due to the conservation of the canonical momentum. Moreover, $\langle d\varphi/dt \rangle_b \cong \langle d\varphi/dt \rangle_{\parallel} \rangle_b \sim \langle B_{\varphi} v_{\parallel} / (Br) \rangle_b \sim \omega_b$. At order 0, assuming $\omega \sim \omega^*$

$$\left(\vec{v}_g \cdot \frac{\partial}{\partial \vec{R}} - \langle \dot{\varphi} \rangle_b \frac{\partial}{\partial \varphi} \right) \delta g^{(0)} = 0 \quad (2.83)$$

At order 1:

$$\left(\vec{v}_g \cdot \frac{\partial}{\partial \vec{R}} - \langle \dot{\phi} \rangle_b \frac{\partial}{\partial \varphi} \right) \delta g^{(1)} - i(\omega - n \langle \dot{\phi} \rangle_b) \delta g^{(0)} = -i \frac{q f_0}{T} \phi(\omega - \omega^*) \quad (2.84)$$

Bounce averaging this equation:

$$\delta g^{(0)} = \frac{q}{T} f_0 \frac{\omega - \omega^*}{\omega - n \langle \dot{\phi} \rangle_b} \langle \phi \rangle_b \quad (2.85)$$

With:

$$\langle \phi \rangle_b = \frac{1}{\tau_b} \int_0^{\tau_b} dt \phi(\vec{R}'), \quad \vec{R}'(t=0) = \vec{R} \quad (2.86)$$

The non-adiabatic density is now:

$$\widehat{N}_b^{n.a.} = \int_{\text{trapped}} d\vec{v} \delta g^{(0)} = 4\pi \alpha_b \int dE \sqrt{2E} \delta g^{(0)} \quad (2.87)$$

where α_b is the fraction of trapped particles. In equation (2.85), both ω^* and $\langle \dot{\phi} \rangle_b$ depend on the energy E . The next step is to compute $\langle \dot{\phi} \rangle$ for a circular, large aspect ratio tokamak. One finds:

$$\langle \dot{\phi} \rangle = -\frac{m}{q} \frac{\frac{\partial I_{\parallel}}{\partial \psi}}{\frac{\partial I_{\parallel}}{\partial E}}, \quad I_{\parallel} = 2 \int_{\theta_1}^{\theta_2} d\theta J B |v_{\parallel}| \quad (2.88)$$

I_{\parallel} is the longitudinal invariant, expressed here for a trapped particle, θ_1 and θ_2 being the turning points. The proof can be found in [59]. The longitudinal invariant is:

$$I_{\parallel} = 16 R q_s \sqrt{E \lambda \epsilon} \left[(X - 1) F(X) + E(X) \right] \quad (2.89)$$

where q_s is the safety factor, $X = (1 - \lambda + \lambda \epsilon)/(2\lambda \epsilon)$, $\lambda = \mu B_0/E$, ϵ is the local aspect ratio and $E(X)$ and $F(X)$ are the complete elliptic integral of the first and second kind.

After some algebra, the toroidal precessional drift is:

$$\langle \dot{\phi} \rangle = -\frac{1}{\Omega} \frac{q_s}{\rho} \frac{E}{R} G \quad (2.90)$$

Where G is:

$$G = 4\lambda \left\{ \hat{s} \left[(X - 1) + \frac{E(X)}{F(X)} \right] + \frac{1}{2} \left[\frac{E(X)}{F(X)} - \frac{1}{2} \right] \right\} \quad (2.91)$$

Eq. (2.90) and (2.91) reveal the effect of the shear. Fig. 2.5 shows that for a strong reverse shear, the averaged value of G on a magnetic surface $\langle G \rangle$ changes sign and so the

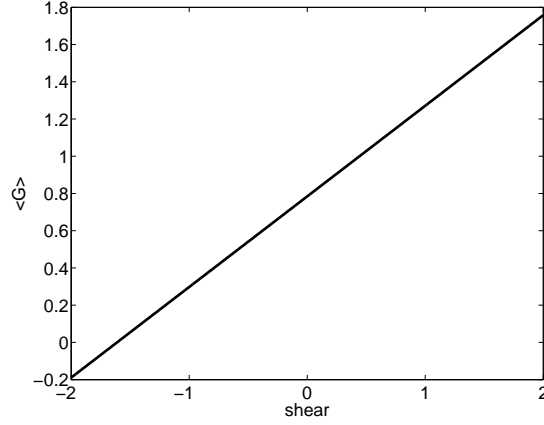


Figure 2.5: $\langle G \rangle$ as a function of \hat{s} for $\epsilon = 0.2$.

toroidal precessional drift is reversed, which has a stabilising effect: a wave can propagate only if it rotates in the same direction as $\langle \dot{\phi} \rangle$. Inserting Eq. (2.90) into Eq. (2.87), the non adiabatic density reads:

$$\widehat{\delta N}_b^{n.a.} = -2\alpha_b N \frac{q\phi}{T} \frac{1}{\omega_\phi} \left\{ \left[\omega - \omega_N \left(1 - \frac{3}{2}\eta\right) \right] W(z_b) - \omega_N \eta \left[\frac{\omega}{\omega_\phi} W(z_b) + \frac{1}{2} \right] \right\} \quad (2.92)$$

Where $\omega_\phi = \omega_N \epsilon_N G$, $z_b = \text{sign}(\omega_\phi) \sqrt{2\omega/\omega_\phi}$. This definition is due to the causality and the fact that $\text{Im}(\omega_\phi) > 0$.

In order to isolate the TEM, the ion-drive is neglected, by assuming slab-like ions, no temperature gradient and $k_z v_z = k_y v_\perp = 0$ so that $n_i = -\frac{N_e \phi}{T_i} \omega_{Ne}/\omega$. The dispersion relation is:

$$-\frac{\omega_{Ne}}{\omega} + 1 + \frac{2\alpha_b}{\omega_{\phi e}} \left\{ \left[\omega - \omega_{Ne} \left(1 - \frac{3}{2}\eta_e\right) \right] W(z_{be}) - \omega_{Ne} \eta_e \left[\frac{\omega}{\omega_{\phi e}} W(z_{be}) + \frac{1}{2} \right] \right\} \quad (2.93)$$

Setting $\tau = 1$ and expanding $W(z)$ according to (2.49), one gets:

$$0 = 1 + \alpha_b \left[-1 + \frac{\omega_{Ne} - 3\omega_{\phi e}/2}{\omega} + \frac{3\omega_{\phi e}\omega_{Ne}(1 + \eta_e)}{2\omega^2} \right] - \frac{\omega_{Ne}}{\omega} \quad (2.94)$$

In case of $\eta_e \gg 1$, the growth rate is:

$$\gamma = \sqrt{\frac{\frac{3}{2}\alpha_b \omega_{\phi e} \omega_{Ne} (1 + \eta_e)}{1 - \alpha_b}} \quad (2.95)$$

From this equation it can be concluded that the growth rate increases with the trapped fraction of electrons. As $\omega_{\phi e} \omega_{Ne} \sim 1/L_N$, the growth rate increases with increasing density and temperature gradients.

2.6 Coupling of the TEM to the ITG instability

Assuming kinetic trapped electrons and including the ion drive, the following dispersion relation is obtained:

$$\begin{aligned}
0 &= \frac{1}{\tau} + \frac{1}{\tau} \frac{2\alpha_b}{\omega_{\varphi,e}} \left\{ \left[\omega - \omega_{Ne} \left(1 - \frac{3}{2} \eta_e \right) \right] W(z_{be}) - \omega_{Ne} \eta_e \left[\frac{\omega}{\omega_{\varphi e}} W(z_{be}) + \frac{1}{2} \right] \right\} \\
&+ \frac{1}{1 + (\omega - \omega_{Ni})} \int d\vec{v} \frac{f_{0i}}{N} \frac{J_0^2 \left(\frac{k_y v_{\perp}}{\Omega} \right)}{\omega_{Fi}(v_z, v_{\perp}) - \omega + k_z v_z} \\
&- \omega_{Ti} \int d\vec{v} \frac{f_{0i}}{N} \left(\frac{E}{T_i} - \frac{3}{2} \right) \frac{J_0^2 \left(\frac{k_y v_{\perp}}{\Omega} \right)}{\omega_{Fi}(v_z, v_{\perp}) - \omega + k_z v_z} \tag{2.96}
\end{aligned}$$

Kinetic trapped electrons reduce the adiabatic response of electrons and can therefore destabilize ITG modes. Fig. 2.6 shows the real frequencies and the growth rates, obtained from Eq. (2.96), as a function of $k_y \rho_{Li}$. The parameters are $\tau = 1, \epsilon_N = 0.2, \eta_i = 2, \eta_e = 2, q_s = 2, \hat{s} = 1, \epsilon = 0.15, \alpha_b = \sqrt{2\epsilon}$. $G \cong \langle G \rangle(\hat{s}, \epsilon)$ has been used. An ITG mode and a TEM coexist. At short wavelength, the ITG mode is stabilized by FLR effects. The TEM is not sensitive to FLR effects and remains unstable. Comparison with the adiabatic case shows a strong destabilization of ITG modes.

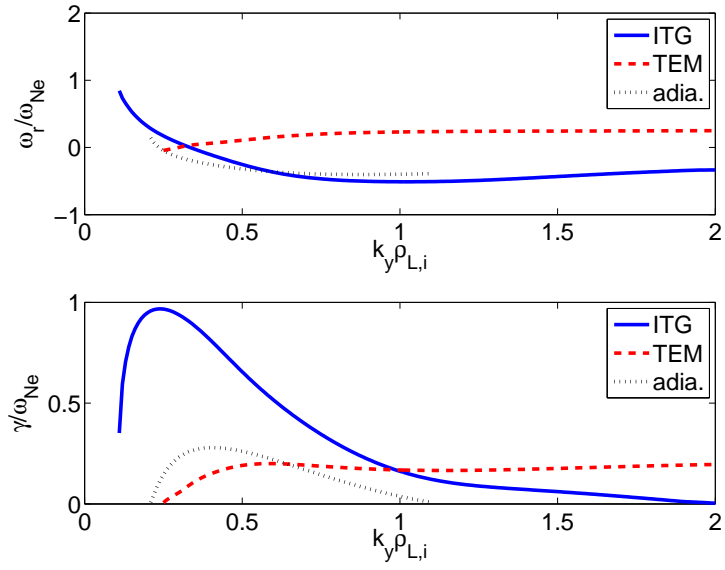


Figure 2.6: Real frequency (top) and growth rate (bottom) of disp. rel. (2.96) as a function of $k_y \rho_{Li}$ for $\tau = 1$, $\epsilon_N = 0.2$, $\eta_i = 2$, $\eta_e = 2$, $q_s = 2$, $\hat{s} = 1$, $\epsilon = 0.15$, $\alpha_b = \sqrt{2\epsilon}$. A TEM mode (red, dashed line) and an ITG mode (blue, solid line) coexist. Positive real frequencies indicate the electron diamagnetic direction. Black dotted curved shows adiabatic results, solution of (2.62).

Chapter 3

The ORB5 gyrokinetic model

In this Chapter, the 5D gyrokinetic model solved by ORB5 is presented.

3.1 Geometry and magnetic field

In this Section, general properties of the magnetic equilibrium are presented. The tokamak is supposed to be axisymmetric. The most general axisymmetric magnetic field satisfying $\nabla \cdot \vec{B} = 0$ is:

$$\vec{B} = F(\psi)\nabla\varphi + \nabla\psi \wedge \nabla\varphi \quad (3.1)$$

Where ψ is the poloidal flux, constant on each magnetic surface, φ is the toroidal angle and $F(\psi)$ is the poloidal current flux function, therefore $\vec{B} \cdot \nabla\psi = 0$. The axisymmetric equilibria is determined by three of the ideal MagnetoHydroDynamic (MHD) equations:

$$\nabla p = \vec{j} \wedge \vec{B}, \quad \nabla \wedge \vec{B} = \mu_0 \vec{j}, \quad \nabla \cdot \vec{B} = 0 \quad (3.2)$$

Where p is the pressure and \vec{j} is the current density. The ideal MHD equations suppose the plasma to be a single fluid with no resistivity. The first equation describes the balance between the magnetic force and the plasma pressure. The second equation is one of the Maxwell's equations where the displacement current has been neglected. From the first MHD equation, $\vec{B} \cdot \nabla p = 0$ and so the pressure is a flux function. Taking the cross product of the second MHD equation with \vec{B} and inserting the third one leads, in the radial direction, to the *Grad-Shafranov* equation:

$$\nabla^2\psi - \frac{2}{r}\frac{\partial\psi}{\partial r} = -F'(\psi)F(\psi) - r^2p'(\psi) = -rj_\varphi \quad (3.3)$$

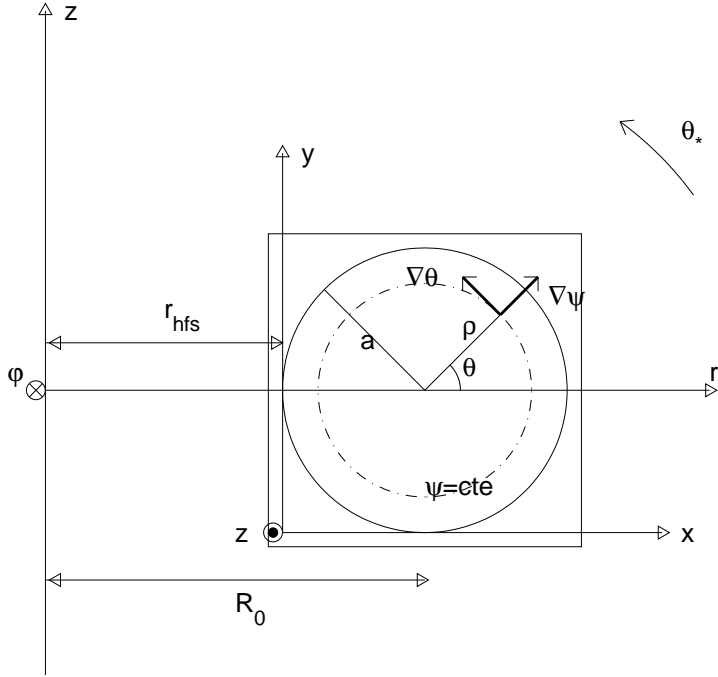


Figure 3.1: System of coordinates used in ORB5

For given $F(\psi)$ and $p'(\psi)$ profiles, the Grad-shafranov equation gives the form of the magnetic field.

ORB5 is coupled to the CHEASE code [63] which solves this equation. Instead of using a real magnetic equilibria, *ad hoc* equilibrium are often used. The magnetic surfaces are approximated as circular and concentric. In this case the magnetic field is given by:

$$\vec{B} = \frac{B_0 R_0}{r} \vec{e}_\varphi - \frac{B_0 \rho}{\bar{q}(\rho) r} \vec{e}_\theta \quad (3.4)$$

Where B_0 is the magnetic field at axis, R_0 is the major radius of the tokamak, r is the cylindrical radial coordinate, ρ is the polar radius coordinate and $\bar{q}(\rho)$ is the pseudo-safety factor. $\psi'(\rho) = B_0 \rho / \bar{q}(\rho)$ for this configuration. The tokamak geometry in the case of *ad hoc* equilibria is summarized on Fig. 3.1. Analytical Grad-Shafranov solutions can be obtained, for example when $F(\psi)$ and $p'(\psi)$ are constant: they are called Solovév equilibria [64] and are defined by:

$$\psi = \frac{\psi_{\text{edge}}}{(R_0 a)^2} \left[(rz)^2 + \frac{1}{4} (r^2 - R_0^2)^2 \right] \quad (3.5)$$

In the large aspect ratio limit, i.e. $R_0/a \gg 1$, the Solovév solution reduces to $\psi = \psi_{\text{edge}} \rho^2 / a^2$, i.e. magnetic surfaces are circular. The *ad hoc* equilibrium can be viewed as

a Solovév solution with a pseudo safety factor profile, but *it is not a true solution of the Grad-Shafranov equation*. The real safety factor profile, measuring the helicity of the field lines, is defined by:

$$q(\psi) = \frac{1}{2\pi} \int_0^{2\pi} \frac{\vec{B} \cdot \nabla \varphi}{\vec{B} \cdot \nabla \theta} d\theta \quad (3.6)$$

Inserting the magnetic field (3.4), one finds:

$$q(\psi) = \frac{\bar{q}(\rho)}{\sqrt{1 - \frac{\rho^2}{R_0^2}}} \quad (3.7)$$

$\bar{q}(\rho)$ is therefore called *pseudo safety factor* because it is very close to the real safety factor. The *straight-field-line* angle is defined by:

$$\theta_* = \frac{1}{q(\psi)} \int_0^\theta \frac{\vec{B} \cdot \nabla \varphi}{\vec{B} \cdot \nabla \theta'} d\theta' \quad (3.8)$$

It is easy to show that $\vec{B} \cdot \nabla \theta_* = q(\psi) \vec{B} \cdot \nabla \varphi$. It means that if one unwraps a magnetic surface in the (θ_*, φ) plane, the field lines are straight: θ_* is better suited than θ to describe microinstabilities because it is constructed to align with the field line. The magnetic surfaces can be labelled with s , defined by:

$$s = \sqrt{\frac{\psi}{\psi_{\text{edge}}}} \quad (3.9)$$

In this work, s and ψ will equivalently label radial surfaces. For circular geometry, magnetic surfaces can also be labelled with ρ . It is convenient to describe physical quantities in Fourier space:

$$\phi(\vec{x}, t) = \sum_{m,n} \hat{\phi}_{m,n}(\psi, t) e^{im\theta_*} e^{in\varphi} \quad (3.10)$$

where m is the *poloidal wave number* and n is the *toroidal wave number*. Due to the gyrokinetic ordering $k_{\parallel} \ll k_{\perp}$, m and n cannot take arbitrary values. By assumption $\vec{B} \cdot \nabla \phi \rightarrow 0$:

$$\vec{B} \cdot \nabla \phi = i(n\vec{B} \cdot \nabla \varphi + m\vec{B} \cdot \nabla \theta_*) = inB_\varphi \left(1 - \frac{m}{nq(\psi)}\right) \cong 0 \Rightarrow m \approx nq(\psi) \quad (3.11)$$

Note that strictly speaking m relates to the poloidal angle and should formally be written m_{θ_*} . The latter relation does not hold with m_θ as $q(\psi) \neq \vec{B} \cdot \nabla \varphi / (\vec{B} \cdot \nabla \theta)$

3.2 Gyrokinetic theory

In this Section, the general framework of gyrokinetic theory is given. The most advanced way to study microinstabilities is to use kinetic theory. Each plasma species is described by a distribution function $f_\alpha(\vec{x}, \vec{v})$, which provides the probability to find a particle at position \vec{x} with velocity \vec{v} . The Vlasov equation is:

$$\frac{df_\alpha}{dt} = \sum_{\beta} C_{\alpha\beta}[f_\alpha, f_\beta] + S(f_\alpha) \quad (3.12)$$

where $C_{\alpha\beta}[f_\alpha, f_\beta]$ is the collision operator between the species α and β and S is a source operator. Electromagnetic fields are external but are also generated by the particles. They must be computed self-consistently with Maxwell's equations, with the charge density and the current given by (in the absence of external contributions):

$$\rho = \sum_{\alpha} q_{\alpha} \int d\vec{v} f_{\alpha}(\vec{x}, \vec{v}, t) \quad (3.13)$$

$$\vec{j} = \sum_{\alpha} q_{\alpha} \int d\vec{v} \vec{v} f_{\alpha}(\vec{x}, \vec{v}, t) \quad (3.14)$$

It is a 6D problem which cannot be solved analytically and which is too large to be solved numerically, due to the wide range of spatial and temporal scales: the typical size of microinstabilities is of the order of the ion Larmor radius $\rho_{Li} \sim 10^{-3}$ m, but the size of a tokamak is of the order of 10^0 m. The typical frequencies of microinstabilities are of the order of the drift frequency, which is around 10^6s^{-1} for fusion-type plasmas, but the cyclotron frequency of ions (resp. electrons) is around 10^8s^{-1} (resp. 10^{11}s^{-1}). In order to be able to study microinstabilities with reasonable computing time, the most efficient way is to go from the kinetic to the gyrokinetic theory. In Section 2.5, an example of a gyrokinetic equation has been given. It relies on the fact that the typical frequency of the wave is much smaller than the cyclotron frequency of ions: the microinstability wave perturbation does not "see" the cyclotron motion of ions and electrons. It can be averaged out and the trajectories of the *guiding centers* of particles are solved instead of the trajectories of the particles. The problem goes from 6D to 5D and the numerical time step can be strongly increased, thus allowing massive CPU savings. This approximation is alone not enough to have a reasonable problem size. In fact, the gyrokinetic theory assumes different small parameters. This is called the *gyrokinetic ordering*. The gyrokinetic ordering used here is taken from [33]:

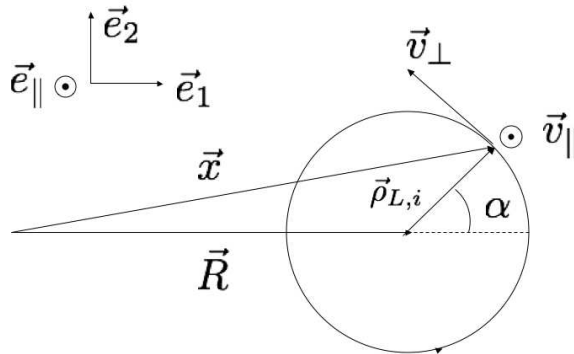


Figure 3.2: Guiding center coordinates.

$$\frac{\omega}{\Omega_i} \sim \frac{k_{\parallel}}{k_{\perp}} \sim \frac{e\phi}{T_e} \sim \frac{\rho_{Li}}{L_n} \sim \frac{\rho_{Li}}{L_{Ti}} \sim \frac{\rho_{Li}}{L_{Te}} \sim \mathcal{O}(\epsilon_g), \quad \frac{\rho_{Li}}{L_B} \sim \mathcal{O}(\epsilon_B), \quad k_{\perp}\rho_{Li} \sim \mathcal{O}(1) \quad (3.15)$$

where ω is the characteristic fluctuation frequency, $\Omega_i = q_i B_0 / m_i$ is the ion cyclotron frequency k_{\parallel} and k_{\perp} are the parallel and perpendicular components of the wave vector with respect to the magnetic field, ϕ is the fluctuating electrostatic potential, ρ_{Li} is the ion gyroradius, and L_n, L_{Ti}, L_{Te}, L_B are the characteristic lengths associated with the density, ion temperature, electron temperature and magnetic field profiles. ϵ_g and ϵ_B are small parameters, $\epsilon_g \sim \rho^*$, $\epsilon_B \sim \epsilon_a \epsilon_g$, with $\rho^* = \rho_s / a \ll 1$ and ϵ_a is the inverse aspect ratio. In addition to the fundamental assumption of the gyrokinetic theory, the gyrokinetic ordering used here states that the turbulence essentially aligns with the field line, its energy is small compared to the plasma thermal energy, the density and temperature profile variations are small on the scale of the Larmor radius, the characteristic length of the magnetic field is much larger than the Larmor radius and the perpendicular wavelength can be comparable to the ion Larmor radius.

3.3 Hahm's gyrokinetic equations

There are several approaches for deriving a gyrokinetic equation. A first intuitive approach is to average the Vlasov equation over the gyroangle. An example is given in [34]. However this formulation does not have an energy conservation property. From a theoretical point of view, it is more appropriate to have a model based on a Lagrangian or a Hamiltonian approach, for which one or several conservation properties are automatically satisfied.

Simulations based on such models are called *first principles* simulations. These models are obtained with the help of the Lie perturbation technique. The latter has been used in slab geometry [65] and then been extended in toroidal geometry [33] in the case of electrostatic perturbations in collisionless plasmas. The idea of Lie transform is to find a new appropriate set of variables, with a right choice of gauge such that the Lagrangian containing an electrostatic perturbation written in these new variables does not depend on the gyroangle. The equations for ions are:

$$\frac{d\vec{R}}{dt} = \frac{1}{B_{\parallel}^*} \left(v_{\parallel} \vec{B}^* + \frac{v_{\perp}^2}{2\Omega_i} \vec{h} \times \nabla \vec{B} + \vec{h} \times \nabla \langle \phi \rangle \right) \quad (3.16)$$

$$\frac{dv_{\parallel}}{dt} = -\frac{\vec{B}^*}{\vec{h} \cdot \vec{B}^*} \cdot \left(\frac{v_{\perp}^2}{2B} \nabla B + \frac{q_i}{m_i} \nabla \langle \phi \rangle \right) \quad (3.17)$$

$$\frac{d\mu}{dt} = 0 \quad (3.18)$$

with:

$$\vec{h} = \frac{\vec{B}}{B}, \quad \vec{B}^* = \vec{B} + \frac{m_i}{q_i} v_{\parallel} \nabla \times \vec{h} \quad (3.19)$$

$$B_{\parallel}^* = B + \frac{m_i}{q_i} v_{\parallel} (\nabla \times \vec{h}) \cdot \vec{h} \quad (3.20)$$

$$\mu = \frac{v_{\perp}^2}{2B} \quad (3.21)$$

μ is the magnetic moment. These equations have been derived by assuming $\Psi \cong \langle \phi \rangle$, where Ψ is the renormalized potential [33]. \vec{B}^* can be written as:

$$\vec{B}^* = B_{\parallel}^* \vec{h} + \frac{m_i v_{\parallel}}{q_i} \left(\vec{h} \times \frac{\nabla B}{B} \right) - \frac{m_i v_{\parallel}}{q_i} \vec{h} \times \left[\vec{h} \times \left(\frac{\nabla \times \vec{B}}{B} \right) \right] \quad (3.22)$$

The final form of the equations of motion are:

$$\begin{aligned} \frac{d\vec{R}}{dt} = & v_{\parallel} \vec{h} + \frac{1}{\Omega_i B_{\parallel}^*} \left(v_{\parallel}^2 + \frac{v_{\perp}^2}{2} \right) (\vec{h} \times \nabla B) - \frac{v_{\parallel}^2}{\Omega_i B_{\parallel}^*} \vec{h} \times [\vec{h} \times (\nabla \times \vec{B})] \\ & + \frac{\langle \vec{E} \rangle \times \vec{B}}{B_{\parallel}^* B} \end{aligned} \quad (3.23)$$

$$\begin{aligned} \frac{dv_{\parallel}}{dt} = & \frac{1}{2} v_{\perp}^2 \nabla \cdot \vec{h} + \frac{v_{\perp}^2 v_{\parallel}}{2B_{\parallel}^* \Omega_i B} \left\{ \vec{h} \times [\vec{h} \times (\nabla \times B)] \right\} \cdot \nabla B \\ & + \langle \vec{E} \rangle \cdot \left\{ \frac{q_i}{m_i} \vec{h} + \frac{v_{\parallel}}{B B_{\parallel}^*} (\vec{h} \times \nabla B) - \frac{v_{\parallel}}{B B_{\parallel}^*} \left\{ \vec{h} \times [\vec{h} \times (\nabla \times B)] \right\} \right\} \end{aligned} \quad (3.24)$$

$$\frac{d\mu}{dt} = 0 \quad (3.25)$$

Eq. (3.23) contains the parallel motion $\sim \mathcal{O}(1)$, the curvature and ∇B drifts $\sim \mathcal{O}(\epsilon_B)$, the diamagnetic drift $\sim \mathcal{O}(\epsilon_B)$ and the $\vec{E} \times \vec{B}$ drift $\sim \mathcal{O}(\epsilon_g)$. Eq. (3.24) contains the mirror term $\sim \mathcal{O}(\epsilon_B)$ and the parallel electric field acceleration term $\sim \mathcal{O}(\epsilon_g^2)$. The last term, of order $\sim \mathcal{O}(\epsilon_g \epsilon_B)$, is an interaction between the electric field and the parallel component of the curvature and diamagnetic drifts. The diamagnetic drift appears more explicitly when using MHD equations (3.2):

$$\vec{h} \times \left[\vec{h} \times \left(\nabla \times \vec{B} \right) \right] = -\frac{\mu_0}{B} \vec{h} \times \nabla p \quad (3.26)$$

Because adhoc equilibria are not true solutions of the Grad-Shafranov equation, one could question the inclusion of the diamagnetic drift (computed with the magnetic field) in the equations of motion. For real equilibria, CHEASE provides the pressure gradient.

Eq. (3.25) is the conservation of the magnetic moment. The equations of motion can be written as:

$$\frac{d\vec{R}}{dt} = \frac{d\vec{R}}{dt} \Big|_0 + \frac{d\vec{R}}{dt} \Big|_1, \quad \frac{dv_{\parallel}}{dt} = \frac{dv_{\parallel}}{dt} \Big|_0 + \frac{dv_{\parallel}}{dt} \Big|_1 \quad (3.27)$$

Where $\dots|_1$ describes the terms with the electric field (the nonlinear terms of the equations of motion) and $\dots|_0$ describes the other terms, i.e. the linear terms of the equations of motion. In addition to the magnetic moment, particles have two other constants of motion at order 0, the kinetic energy $\epsilon_k = 1/2(v_{\parallel}^2 + v_{\perp}^2)$ and the canonical momentum ψ_0 defined by:

$$\psi_0 = \psi + \frac{m_i}{q_i} v_{\parallel} \frac{F(\psi)}{B} \quad (3.28)$$

The conservation of ψ_0 is a consequence of the axisymmetry of the tokamak. It implies that orbits are closed in the poloidal plane.

3.4 The gyro-averaged electric field

The gyro-averaged electric field is computed from the gyro-averaged electric potential:

$$\langle \phi \rangle(\vec{R}, \mu, t) = \frac{1}{2\pi} \int_0^{2\pi} d\alpha \phi \left(\vec{R} + \vec{\rho}_{Li}(\alpha, \vec{R}, \mu), t \right) \quad (3.29)$$

$$\Rightarrow \langle \vec{E} \rangle = -\nabla_{\vec{R}} \langle \phi \rangle(\vec{R}, \mu, t) = -\frac{1}{2\pi} \int_0^{2\pi} d\alpha \nabla_{\vec{R}} \phi \left(\vec{x}(\alpha, \vec{R}, \mu, t) \right) \quad (3.30)$$

The positions of the guiding center and the particle are linked through:

$$\vec{x}(\alpha, \vec{R}, \mu, t) = \vec{R}(t) + \vec{\rho}_{Li}(\alpha, \vec{R}, \mu, t) \quad (3.31)$$

Therefore:

$$\nabla_{\vec{R}} \phi(\vec{x}, t) = \nabla_{\vec{x}} \phi(\vec{x}, t) - \underbrace{(\vec{\rho}_{Li} \cdot \nabla_{\vec{x}} \phi(\vec{x}, t))}_{\mathcal{O}(\epsilon_g)} \underbrace{\nabla_{\vec{R}} \ln B}_{\mathcal{O}(\epsilon_B)} \quad (3.32)$$

-0

It means that the gradient of the gyro-averaged potential is approximated by the gyro-average of the gradient and finally

$$\langle \vec{E} \rangle(\vec{R}, \mu, t) \cong -\langle \nabla_{\vec{x}} \phi(\vec{x}, t) \rangle(\vec{R}, \mu, t) = -\frac{1}{2\pi} \int_0^{2\pi} d\alpha \nabla_{\vec{x}} \phi(\vec{x}, t) \quad (3.33)$$

3.5 The δf method

The δf method [52] consists in separating the full guiding center distribution function into an analytically known, equilibrium part f_0 and a time dependent perturbed function δf . For the species α :

$$f_{\alpha}(\vec{R}, v_{\parallel}, \mu, t) = f_{\alpha 0}(\vec{R}, v_{\parallel}, \mu) + \delta f_{\alpha}(\vec{R}, v_{\parallel}, \mu, t) \quad (3.34)$$

$f_{\alpha 0}$ is the background equilibrium function, and must be solution of the equilibrium gyrokinetic equation. In other words, $f_{\alpha 0}$ is any function which depends only on the constant of motions. It is common to choose a *canonical Maxwellian* for $f_{\alpha 0}$:

$$f_{\alpha 0}(\epsilon_k, \mu, \psi_0) = \frac{n_{\alpha 0}(\psi_0)}{(2\pi)^{3/2} v_{\text{th}\alpha}^3(\psi_0)} \exp\left(-\frac{\epsilon_k}{T_{\alpha}(\psi_0)}\right) \quad (3.35)$$

$v_{\text{th}\alpha}$ is the thermal velocities of the species α

$$v_{\text{th}\alpha}(\psi_0) = \sqrt{\frac{eT_{\alpha}}{m_{\alpha}}} \quad (3.36)$$

$n_{\alpha 0}(\psi_0)$ and $T_{\alpha}(\psi_0)$ are input profiles for the specie α . It is common to prescribe profiles with a radial coordinate such as ψ . In that case, $f_{\alpha 0}(\epsilon_k, \mu, \psi)$ is called *local Maxwellian* and the following equality holds:

$$n_{\alpha} = \int d\vec{v} f_{\alpha 0}[\epsilon_k(\vec{v}), \mu(\vec{v}), \psi] \quad (3.37)$$

But:

$$n_\alpha \neq \int d\vec{v} f_{\alpha 0} \left[\epsilon_k(\vec{v}), \mu(\vec{v}), \psi_0(\vec{v}) \right] \quad (3.38)$$

Where n_α is the equilibrium density profile. This is due to the θ and v_{\parallel} dependence of ψ_0 . This is problematic because the input profiles used in $f_{0\alpha}$ are given as a function of ψ , but $f_{0\alpha}$ needs to be a function of constants of the unperturbed motion. The profiles reconstructed with the canonical Maxwellian are flatter. A way to overcome this is to choose another constant of motion $\hat{\psi}$ defined by:

$$\hat{\psi} = \psi_0 + \psi_{0,\text{corr}}(\epsilon_k, \mu) \quad (3.39)$$

$$\psi_{0,\text{corr}}(\epsilon, \mu) = -\text{sign}[v_{\parallel}(t_0)] \frac{q_\alpha}{m_\alpha} R_0 \sqrt{2(\epsilon_k - \mu B_0)} \mathcal{H}(\epsilon_k - \mu B_0), \quad (3.40)$$

where $\mathcal{H}(x)$ is the Heavyside function, therefore $\psi_{0,\text{corr}}$ is nonzero only for passing particles and trapped particles that have $B > B_0$, i.e. particles trapped with their turning point at the HFS of the magnetic axis. For this class of particles, $\hat{\psi}$ is not a constant of motion because the sign of the parallel velocity changes after a turning point. Other definitions for $\hat{\psi}$ exist, for example by taking B_{max} instead of B_0 [66]. $\hat{\psi}$ can be seen as the closest constant of motion to ψ . For passing particles one has:

$$\begin{aligned} \psi_0 - \psi &= \frac{m_\alpha v_{\parallel}}{q_\alpha} \frac{F(\psi)}{B} = \frac{m_\alpha \text{sign}(v_{\parallel}) \sqrt{2(\epsilon_k - \mu B)}}{q_\alpha} \frac{F(\psi)}{B} \\ &\cong \frac{m_\alpha \text{sign}(v_{\parallel}(t_0)) \sqrt{2(\epsilon_k - \mu B_0)} B_0 R_0}{q_\alpha B} \cong -\psi_{0,\text{corr}}(\epsilon_k, \mu) \end{aligned} \quad (3.41)$$

From now on, the equations will apply on ions and the subscript $\alpha \rightarrow i$ will be neglected. Inserting the δf Ansatz in the Vlasov equation gives:

$$\frac{d\delta f}{dt} = -\frac{df_0}{dt} = \tau(\vec{E}) = \underbrace{\frac{\partial f_0}{\partial t}}_{=0} - \frac{\partial f_0}{\partial \Upsilon} \bigg|_{\epsilon_k, \mu} \frac{d\Upsilon}{dt} - \frac{\partial f_0}{\partial \epsilon_k} \bigg|_{\Upsilon, \mu} \frac{d\epsilon_k}{dt} - \frac{\partial f_0}{\partial \mu} \bigg|_{\Upsilon, \epsilon_k} \underbrace{\frac{d\mu}{dt}}_{=0} \quad (3.42)$$

For the next steps of the derivation, let us assume that the profiles appearing in the Maxwellian are functions of a variable Υ , which is not necessary a constant of motion. The Vlasov equation finally is:

$$\frac{d\delta f}{dt} = \tau(\vec{E}) \quad (3.43)$$

$$\tau(\vec{E}) = -f_0 \kappa(\Upsilon) \frac{d\Upsilon}{dt} \bigg|_1 + \frac{q_i f_0}{T_i(\Upsilon)} \langle \vec{E} \rangle \cdot \frac{d\vec{R}}{dt} \bigg|_0 \quad (3.44)$$

Where

$$\kappa(\Upsilon) = \frac{\partial \ln f_0}{\partial \Upsilon} = \frac{n'_0(\Upsilon)}{n_0(\Upsilon)} - \frac{3T'_i(\Upsilon)}{2T_i(\Upsilon)} + \frac{m_i \epsilon_k}{T_i(\Upsilon)^2} T'_i(\Upsilon) \quad (3.45)$$

and the term $d\Upsilon/dt|_0$ has been dropped out. This is correct when $\Upsilon = \psi_0, \hat{\psi}$ but not for $\Upsilon = \psi$. A local Maxwellian can lead to spurious zonal flow oscillations [49], since it is not a true equilibrium distribution function, as $df_0(\psi)/dt|_0 \propto d\psi/t|_0 \neq 0$. When using a canonical Maxwellian, the quasineutrality equation is no longer satisfied as electron and ion equilibrium densities are different. In order to enforce quasineutrality, a radial electric field quickly develops. To eliminate this spurious field generation, the electron equilibrium density is further integrated from the ion distribution function after the particle loading (see Section 4.3) and averaged over the poloidal angle:

$$n_{e0}(\psi) = \frac{1}{2\pi} \int_0^{2\pi} \left(\int f_{i0}(\psi_0, \epsilon_k, \mu) \delta(\vec{R} + \vec{\rho}_{Li} - \vec{x}) B_{\parallel}^* d\vec{R} dv_{\parallel} d\mu d\alpha \right) d\theta, \quad (3.46)$$

which minimizes the difference between n_{e0} and n_{i0} . Note that for small ρ^* plasmas, there is little difference between ψ and ψ_0 and the local Maxwellian becomes close to the canonical Maxwellian. Issues related to this choice are discussed in details in Ref. [67] and [66]. When $\Upsilon = \hat{\psi}$, the approximation $d\hat{\psi}/dt|_1 \cong d\psi_0/dt|_1$ is done:

$$\frac{d\hat{\psi}}{dt} = \underbrace{\frac{\partial \hat{\psi}}{\partial t}}_{=0} + \underbrace{\frac{\partial \hat{\psi}}{\partial \psi_0}}_{=1} \frac{d\psi_0}{dt} \Big|_1 + \frac{\partial \hat{\psi}}{\partial \epsilon_k} \Big|_{\psi_0, \mu} \frac{d\epsilon_k}{dt} \Big|_1 + \frac{\partial \hat{\psi}}{\partial \mu} \Big|_{\psi_0, \epsilon_k} \underbrace{\frac{d\mu}{dt}}_{=0} \Big|_1 \quad (3.47)$$

The term $\partial \hat{\psi}/\partial \epsilon_k$ is singular for $\epsilon_k = \mu B_0$; this term is nonetheless small for resonating particles. For ITG turbulence they are characterized by $\sqrt{\epsilon_k - \mu B_0} \sim v_{\text{thi}}$. In the Vlasov equation it would introduce an additional term proportional to $d\epsilon_k/dt$ that is small compared to $\partial f_0/\partial \epsilon_k$:

$$\left| \frac{f_0 \kappa(\hat{\psi}) \frac{\partial \hat{\psi}}{\partial \epsilon_k}}{\frac{\partial f_0}{\partial \epsilon_k}} \right| \sim \frac{\kappa(\rho) R_0 T_i m_i}{|\nabla \psi| m_i q_i} \sim \frac{\kappa(\rho) \epsilon_a}{\rho_s} \bar{q}(\rho) \rho_s \sqrt{\tau^{-1}} \sim \mathcal{O}(\epsilon_g \epsilon_a) \quad (3.48)$$

The RHS of Eq. (3.43) describes the growth and/or damping of the instability. The first term is the driving term. One has:

$$\kappa(\Upsilon) \frac{d\Upsilon}{dt} \Big|_1 = \kappa(\Upsilon) \frac{\langle \vec{E} \rangle \times \vec{B}}{B B_{\parallel}^*} \cdot \nabla \psi + \mathcal{O}(\epsilon_g^2 \epsilon_B, \epsilon_g^3) \quad (3.49)$$

The growth of δf is in fact due to the advection of the $\vec{E} \times \vec{B}$ velocity down the gradients, and is proportional to $\kappa(\Upsilon)$, i.e. mainly dependent on the temperature and density gradients as well as the kinetic energy of the particles. The second term of Eq. (3.43) describes the wave-particle interaction, as $f_0 \left. \frac{d\epsilon_k}{dt} \right|_1 = q_i f_0 \langle \vec{E} \rangle \cdot \left. \frac{d\vec{R}}{dt} \right|_0 \sim \vec{j} \cdot \langle \vec{E} \rangle$. This term contains the Landau damping.

δf can be obtained in a different way by using the fact that f is constant along trajectories:

$$\delta f(\vec{R}, v_{\parallel}, \mu, t) = f[\vec{R}(t_0), v_{\parallel}(t_0), \mu(t_0)] - f_0[\Upsilon(t), v_{\parallel}(t), \mu(t_0)]. \quad (3.50)$$

Details of this scheme, called *direct* δf , are given in Refs. [68] and [67]. ORB5 can be used with the standard or the direct δf scheme. In this work, only the standard δf scheme has been used because it allows a larger time step. A final important remark is that the approach used here in ORB5 is not a δf model valid for small perturbations only. No assumption $|\delta f| \ll |f_0|$ is made. Finally, note that from the numerical point of view it is desirable to have $|\delta f|$ as small as possible in order to minimize the discretization errors but formally $|\delta f| \ll |f_0|$ is not required. The δf method is an example of control variates methods which are widely used in the Monte-Carlo approach [69].

3.6 Poisson equation

The Vlasov equation is valid for any species. It must be closed with the Poisson equation. ORB5 assumes that the plasma is composed of an ion species of charge $q_i = Z_i e$ and of mass m_i and electrons, who have a charge $-e$ and a mass m_e . The Poisson equation reads:

$$\nabla^2 \phi(\vec{x}, t) = \frac{e}{\epsilon_0} [n_e(\vec{x}, t) - Z_i n_i(\vec{x}, t)] \quad (3.51)$$

3.6.1 Ion density

According to Hahm's equation [33], the ion density is:

$$\begin{aligned} n_i(\vec{x}, t) &= \int B_{\parallel}^* f_i(\vec{R}, v_{\parallel}, \mu, t) \delta(\vec{R} + \vec{\rho}_{Li} - \vec{x}) d\vec{R} dv_{\parallel} d\mu d\alpha \\ &+ \int B_{\parallel}^* \frac{q_i^2}{m_i^2 \Omega_i} \left\{ \left(\phi(\vec{x}, t) - \langle \phi \rangle(\vec{R}, \mu, t) \right) \frac{\partial f_i(\vec{R}, v_{\parallel}, \mu, t)}{\partial \mu} \right. \\ &\left. + \frac{1}{m_i \Omega_i} \left[\nabla(\phi - \langle \phi \rangle) \times \vec{h} \right] \right\} \cdot \nabla f_i \delta(\vec{R} + \vec{\rho}_{Li} - \vec{x}) d\vec{R} dv_{\parallel} d\mu d\alpha \end{aligned} \quad (3.52)$$

The second integral appears when applying the Lie transform to the density and is a Finite Larmor Radius effect. Both terms of the second integral are of order $\mathcal{O}(\epsilon_g^2)$. However, the Poisson equation will be linearized. So ∇f_i will be replaced by ∇f_{i0} , which is now of order $\mathcal{O}(\epsilon_g)$, because of the gradients of density and temperature. The following approximation is done:

$$\left| \frac{1}{m_i \Omega_i} \left[\nabla(\phi - \langle \phi \rangle) \times \vec{h} \right] \cdot \nabla f_{i0} \right| \ll \left| \frac{q_i}{\Omega_i} (\phi - \langle \phi \rangle) \frac{\partial f_i}{\partial \mu} \right| \quad (3.53)$$

The term on the l.h.s. of this inequality is ϵ_g smaller than the term on the r.h.s. and will be neglected. Finally, the ion density is:

$$n_i(\vec{x}, t) = \langle n_i \rangle(\vec{R}, t) + n_{i,\text{pol}}(\vec{x}, t) \quad (3.54)$$

$$\langle n_i \rangle(\vec{x}, t) = \int d\vec{R} dv_{\parallel} d\mu d\alpha B_{\parallel}^* f_i(\vec{R}, v_{\parallel}, \mu, t) \delta(\vec{R} + \vec{\rho}_{Li} - \vec{x}) \quad (3.55)$$

$$\begin{aligned} n_{i,\text{pol}}(\vec{x}, t) &= \frac{q_i^2}{m_i^2} \int d\vec{R} dv_{\parallel} d\mu d\alpha B_{\parallel}^* \frac{1}{\Omega_i} \left(\phi(\vec{x}, t) - \langle \phi \rangle(\vec{R}, \mu, t) \right) \\ &\quad \frac{\partial f_i}{\partial \mu} \delta(\vec{R} + \vec{\rho}_{Li} - \vec{x}) \end{aligned} \quad (3.56)$$

$n_{i,\text{pol}}$ is called the *polarization density*. Physically, it comes from the fact the guiding center and the particle densities are not equal. Therefore it describes the shielding associated with the finite ion Larmor radius. Its expression is further simplified by assuming that the typical wavelength of the instability is smaller than the ion Larmor radius:

$$k_{\perp} \rho_{Li} \ll 1 \quad (3.57)$$

The gyro-averaged potential can be written:

$$\langle \phi \rangle(\vec{R}, \mu, t) = \frac{1}{(2\pi)^3} \int d\vec{k} \hat{\phi}(k, t) J_0 \left(\frac{k_{\perp} v_{\perp}}{\Omega_i} \right) e^{i\vec{k} \cdot \vec{R}} \quad (3.58)$$

By expanding $J_0(x)$ for $x \ll 1$ up to second order, $J_0(x) = 1 - 1/4x^2 + \mathcal{O}(x^3)$, one has:

$$\langle \phi \rangle(\vec{R}, \mu, t) = \phi(\vec{R}, t) + \frac{\mu m_i^2}{2B^2 q_i^2} \nabla_{\perp}^2 \phi(\vec{R}, t) + \mathcal{O} \left[\left(\frac{k_{\perp} v_{\perp}}{\Omega_i} \right)^4 \right] \quad (3.59)$$

A similar expansion for the Dirac function can be performed

$$\begin{aligned} \int_0^{2\pi} \delta(\vec{R} - \vec{\rho}_{Li} - \vec{x}) d\alpha &= 2\pi \left[\delta(\vec{R} - \vec{x}) + \frac{\mu m_i^2}{2B^2 q_i^2} \nabla_{\perp}^2 \delta(\vec{R} - \vec{x}) \right] \\ &\quad + \mathcal{O} \left[\left(\frac{k_{\perp} v_{\perp}}{\Omega_i} \right)^4 \right] \end{aligned}$$

By integrating $n_{i,\text{pol}}(\vec{x}, t)$ by parts and inserting the last two relations and their μ derivative in the the polarization density:

$$n_{i,\text{pol}}(\vec{x}, t) = \nabla_{\perp} \cdot \left(\frac{\langle n_i \rangle(\vec{R}, t)}{B\Omega_i} \nabla_{\perp} \phi(\vec{x}, t) \right) \quad (3.60)$$

The ion density can be written:

$$n_i(\vec{x}, t) = \langle n_{i0} \rangle(\vec{x}) + n_{i,\text{pol}}(\vec{x}, t) + \delta n_i(\vec{x}, t) \quad (3.61)$$

Where:

$$\langle n_{i0} \rangle(\vec{x}) = \int d\vec{R} dv_{\parallel} d\mu d\alpha B_{\parallel}^* f_{i0}(\vec{R}, v_{\parallel}, \mu) \delta(\vec{R} + \vec{\rho}_{Li} - \vec{x}) \quad (3.62)$$

$$\delta n_i(\vec{x}, t) = \int d\vec{R} dv_{\parallel} d\mu d\alpha B_{\parallel}^* \delta f_i(\vec{R}, v_{\parallel}, \mu, t) \delta(\vec{R} + \vec{\rho}_{Li} - \vec{x}) \quad (3.63)$$

3.6.2 Electron density

The electron density n_e can be evaluated by assuming adiabatic (or Boltzmann) electrons. Using a fluid model for the electrons, the equation of motion reads:

$$m_e n_e \frac{dv_{e\parallel}}{dt} = e n_e \nabla_{\parallel} \phi - T_e \nabla_{\parallel} n_e \quad (3.64)$$

The adiabaticity means that the inertia of electrons is neglected: $m_e \rightarrow 0$. The solution of this first order differential equation is:

$$n_e(\vec{x}, t) = C(\psi) \exp\left(\frac{e\phi(\vec{x}, t)}{T_e(\psi)}\right) \quad (3.65)$$

$C(\psi)$ can be fixed by saying that the number of electrons is conserved on each flux surface:

$$\bar{n}_e(\psi, t) \equiv \frac{\int n_e(\psi, \theta_*, \varphi, t) J_{\theta_*\psi\varphi}(\psi, \theta_*) d\theta_* d\varphi}{\int J_{\theta_*\psi\varphi}(\psi, \theta_*) d\theta_* d\varphi} = n_{e0}(\psi) \quad (3.66)$$

Where $J_{\theta_*\psi\varphi}(\psi, \theta_*)$ is the Jacobian for the coordinates $(\theta_*, \psi, \varphi)$, defined by:

$$J_{\theta_*\psi\varphi}(\psi, \theta_*) = \frac{1}{(\nabla\theta_* \times \nabla\psi) \cdot \nabla\varphi} = \frac{r^2 q(\psi)}{F(\psi)} \quad (3.67)$$

Inserting (3.65) in (3.66):

$$C(\psi) \frac{\int \exp\left(\frac{e\phi}{T_e}\right) J_{\theta_*\psi\varphi}(\psi, \theta_*) d\theta_* d\varphi}{\int J_{\theta_*\psi\varphi}(\psi, \theta_*) d\theta_* d\varphi} = n_{e0}(\psi) \quad (3.68)$$

With the help of the gyrokinetic ordering the exponential in the previous equation can be expanded to find:

$$C(\psi) = n_{e0}(\psi) - \frac{en_{e0}(\psi)}{T_e} \bar{\phi} + \mathcal{O} \left[\left(\frac{e\phi}{T_e} \right)^2 \right] \quad (3.69)$$

$\bar{\phi}(\psi, t)$ is the flux-surface-averaged potential and is given by:

$$\bar{\phi}(\psi, t) = \frac{\int \phi(\psi, \theta_*, \varphi, t) J_{\theta_* \psi \varphi}(\psi, \theta_*) d\theta_* d\varphi}{\int J_{\theta_* \psi \varphi}(\psi, \theta_*) d\theta_* d\varphi} \quad (3.70)$$

Replacing (3.69) in (3.65) gives:

$$n_e(\vec{x}, t) = n_{e0}(\psi) + \frac{en_{e0}(\psi)}{T_e(\psi)} (\phi(\vec{x}, t) - \bar{\phi}(\psi, t)) + \mathcal{O} \left[\left(\frac{e\phi}{T_e} \right)^2 \right] \quad (3.71)$$

Expressing $\bar{\phi}$ in Fourier space with (3.10), yields:

$$\bar{\phi}(\psi, t) = \frac{1}{\int d\theta_* J_{\theta_* \psi \varphi}(\psi, \theta_*)} \sum_m \int d\theta_* \hat{\phi}_{m,0}(\psi, t) J_{\theta_* \psi \varphi}(\psi, \theta_*) e^{im\theta_*} \quad (3.72)$$

$\bar{\phi}(\psi, t)$ only gives a contribution to the $n = 0$ mode. In a cylinder geometry, the Jacobian would be a function of the radial coordinate only and $\bar{\phi}(\psi, t)$ would be a function of the $n = 0, m = 0$ mode only. In tokamak geometry, there is a poloidal coupling between the modes $(m, 0)$ due to the poloidal dependence of the r^2 term in the Jacobian. For adhoc equilibria, it can be written in the form:

$$J_{\theta_* \psi \varphi} = \sum_{m'=0}^{\infty} C_{m'}(\psi) \epsilon^{m'} \cos(m'\theta_*) \quad (3.73)$$

Where ϵ is the local inverse aspect ratio. The main poloidal coupling for the $n = 0, m = 0$ mode is with the $n = 0, m = \pm 1$ modes, which are called the *Geodesic Acoustic Modes* (GAM). For shaped equilibria the coupling between $n = 0, m = 0$ and $n = 0, m = \pm 2$ may also be important. The purely radial mode $n = 0, m = 0$, called the *zonal flow* as well as the GAM play an important role in regulating turbulence, as shown for example in [67, 70].

3.6.3 Quasineutrality equation

Using Eqs. (3.51), (3.61) and (3.71) gives:

$$\begin{aligned} \nabla^2 \phi(\vec{x}, t) &= \frac{e}{\epsilon_0} \left\{ n_{e0}(\psi) + \frac{en_{e0}(\psi)}{T_e(\psi)} \left[\phi(\vec{x}, t) - \bar{\phi}(\psi, t) \right] \right. \\ &\quad \left. - Z_i \langle n_{i0} \rangle(\vec{x}) - Z_i n_{i,\text{pol}}(\vec{x}, t) - Z_i \delta n_i(\vec{x}, t) \right\} \end{aligned} \quad (3.74)$$

First, it is assumed that the gyro-averaged equilibrium density is equal to the guiding center density.

$$\langle n_{i0} \rangle(\vec{x}) \cong n_{i0}(\vec{x}) \quad (3.75)$$

Using a long wavelength approximation, it is easy to show that:

$$\langle n_{i0} \rangle(\vec{x}) \cong n_{i0}(\vec{x}) + \frac{m_i^2}{q_i^2} \nabla_{\perp}^2 \left[\frac{n_{i0}(\psi) v_{\text{th}}^2(\psi)}{B^2} \right] \quad (3.76)$$

The correction is clearly a second order term and can be neglected. The density n_{i0} which comes from the ions is in fact constructed with the Maxwellian $f_0(\Upsilon, \epsilon_k, \mu)$, so in general $n_{e0}(\psi)$ and $Z_i n_{i0}(\vec{x})$ cannot be canceled out, except for the case $\Upsilon = \psi$. But in the latter $df_0(\psi)/dt \neq 0$ and so f_0 would not be an equilibrium function. Therefore it is assumed that:

$$Z_i n_{i0}(\Upsilon) \cong n_{e0}(\psi) \quad (3.77)$$

In this approximation, the Poisson equation becomes:

$$\begin{aligned} \nabla^2 \phi(\vec{x}, t) &+ \frac{T_e(\psi)}{T_i(\psi)} \frac{\rho_{Li}^2}{\lambda_{Di}^2} \nabla_{\perp}^2 \phi(\vec{x}, t) + \frac{q_i}{\epsilon_0} \nabla_{\perp} \cdot \left(\frac{n_i(\vec{x}, t)}{B\Omega_i} \right) \cdot \nabla \phi(\vec{x}, t) \\ &= \frac{e}{\epsilon_0} \frac{en_{e0}(\psi)}{T_e(\psi)} \left(\phi(\vec{x}, t) - \bar{\phi}(\psi, t) \right) - \frac{q_i}{\epsilon_0} \delta n_i(\vec{x}, t) \end{aligned} \quad (3.78)$$

where the ion Debye length is here defined as:

$$\lambda_{Di} = \sqrt{\frac{\epsilon_0 k_B T_e}{q_i^2 n_i}} \quad (3.79)$$

For typical tokamak parameters $\lambda_{Di} \ll \rho_{Li}$ and the term $\nabla^2 \phi(\vec{x}, t)$ can be dropped out. This approximation is called the quasineutrality constraint, and is equivalent to setting $n_e = Z_i n_i$. As just mentioned the final step is to linearize the Poisson equation, i.e. to set $n_i(\vec{x}, t) \cong n_{i0}(\psi)$ in (3.78). The Poisson equation is then:

$$\frac{en_0(\psi)}{T_e(\psi)} \left[\phi(\vec{x}, t) - \bar{\phi}(\psi, t) \right] - \nabla_{\perp} \cdot \left[\frac{n_0(\psi)}{B\Omega_i} \nabla_{\perp} \phi(\vec{x}, t) \right] = \delta n_i(\vec{x}, t) \quad (3.80)$$

with $n_0(\psi) \equiv n_{i0}(\psi)$.

3.7 Energy conservation

Despite all the approximations made in the previous Sections, a particle number and an energy invariant can be derived (see Ref. [53] for the proof). The kinetic energy of the plasma is

$$E_{\text{kin}} = \int m_i \left(\mu B + \frac{v_{\parallel}^2}{2} \right) f B_{\parallel}^* d\vec{R} dv_{\parallel} d\mu d\alpha. \quad (3.81)$$

Its time derivative is

$$\frac{dE_{\text{kin}}}{dt} = q_i \int \frac{d\vec{R}}{dt} \cdot \langle \vec{E} \rangle f B_{\parallel}^* d\vec{R} dv_{\parallel} d\mu d\alpha. \quad (3.82)$$

In this model, the electrostatic energy is defined as

$$E_{\text{f}} = \frac{q_i}{2} \int d\vec{x} [\langle n_i \rangle(\vec{x}, t) - n_0(\vec{x})] \phi(\vec{x}, t). \quad (3.83)$$

The energy and particle number conservation are written:

$$\frac{dE_{\text{kin}}}{dt} = -\frac{dE_{\text{f}}}{dt}, \quad (3.84)$$

$$\frac{dN_{\text{ph}}}{dt} = \frac{d}{dt} \int f B_{\parallel}^* d\vec{R} dv_{\parallel} d\mu d\alpha = 0. \quad (3.85)$$

It is important to mention that the energy conservation written here depends on the approximation used here, i.e. the long wavelength approximation, and on the fact that the quasineutrality equation has been linearized.

3.8 Noise control and sources

ORB5 solves the collisionless Vlasov equation. Profiles are computed self-consistently. Typical runs will be explained in Section 5.1. The simulations experience *profile relaxation*: heat is transported (generally outwards) by the particles, which flattens the temperature gradient and so the turbulence decays. The relaxation rate depends on the plasma size ρ^* : the smaller ρ^* is, the longer the relaxation rate will be, but the final state of the simulation is a quasi-steady state with vanishing turbulence and an equilibrium radial potential. This potential evolves on a long time scale as compared to the turbulent modes. As it will be seen in Section 4.3, the gyrokinetic model presented in this Section

will be solved with a Particle-In-Cell method, which suffers from the accumulation of statistical noise. It is therefore difficult to make quantitative predictions with such a method. Clearly, an algorithm that is able to control the noise on long times is highly needed. A noise-control algorithm has been implemented by B. F. McMillan with a Krook operator (see [58]), based on the idea of a W-stat proposed by Krommes [71]. The Krook operator implementation will be detailed in this work for completeness. In addition, a study on the notion of steady state in PIC simulations will be presented in Section 6.1, which is based on the noise-control algorithm. It is therefore crucial to understand the physics behind the Krook operator. The basic idea behind it is to introduce an artificial damping term γ_K :

$$\frac{d\delta f}{dt} = \tau(\vec{E}) - \underbrace{\gamma_K \delta f(\vec{R}, v_{\parallel}, \mu, t)}_{\equiv S_K(\vec{R}, v_{\parallel}, \mu, t)} \quad (3.86)$$

Evidently, the coefficient γ_K must be small not to affect significantly the turbulence. This mechanism obviously brings back the distribution function to its equilibrium state by slowly damping all the modes of the system. A small damping is acceptable for the non-axisymmetric modes that are Landau damped. However this damping will affect the undamped component of the zonal flow perturbation $m = 0, n = 0$ (as noted in [71]), and will modify the turbulence by attenuating the Dimits shift effect (see Sec. 5.1). This is why the Vlasov equation has then been modified in such a way that the density and the long-time zonal flow structure given in Ref. [72] are conserved:

$$\frac{d\delta f}{dt} = \tau(\vec{E}) + \underbrace{S_K(\vec{R}, v_{\parallel}, \mu, t) + S_{RH}(\vec{R}, v_{\parallel}, \mu, t) + S_n(\vec{R}, v_{\parallel}, \mu, t)}_{\equiv S} \quad (3.87)$$

With the following properties:

$$0 = \overline{\int d\vec{v} S(\vec{R}, v_{\parallel}, \mu, t) \left(\frac{v_{\parallel}}{B} - \overline{\left(\frac{v_{\parallel}}{B} \right)} \right)} \quad (3.88)$$

$$0 = \overline{\int d\vec{v} S(\vec{R}, v_{\parallel}, \mu, t)} \quad (3.89)$$

Where the overbar is the flux-surface-average and the tilde is the bounce-average, defined for a quantity A by:

$$\tilde{A} = \frac{\int_{\text{orbit}} A dt}{\int_{\text{orbit}} dt} = \frac{\int_{\text{orbit}} \frac{A}{v_{\parallel}} dl}{\int_{\text{orbit}} \frac{1}{v_{\parallel}} dl} \quad (3.90)$$

In addition, one would eventually like that the Krook operator conserves any moment of the distribution function on magnetic surfaces. The general form of the Vlasov equation becomes:

$$\frac{d\delta f}{dt} = \tau(\vec{E}) + S_K(\vec{R}, v_{\parallel}, \mu, t) + S_{\text{corr}}(\vec{R}, v_{\parallel}, \mu, t) \quad (3.91)$$

where:

$$S_{\text{corr}}(\vec{R}, v_{\parallel}, \mu, t) = \sum_{i=1}^{N_{\text{mom}}} g_i(s, t) f_0[\vec{R}(t), v_{\parallel}(t), \mu(t_0)] M_i(\vec{R}, v_{\parallel}, \mu) \quad (3.92)$$

Where $s = \sqrt{\psi/\psi_{\text{edge}}}$ is the radial label and $\{M_i(\vec{R}, v_{\parallel}, \mu)\}$ are a set of given moments (for example the density is obtained with $M = 1$). At each time step, the $g_i(s)$ functions are the unknowns. They are obtained through the property:

$$\int d\vec{v} M_j(\vec{R}, v_{\parallel}, \mu) \left(S_{\text{corr}}(\vec{R}, v_{\parallel}, \mu, t) + S_K(\vec{R}, v_{\parallel}, \mu, t) \right) = 0 \quad (3.93)$$

By inserting the definitions of S_{corr} and S_K a linear system is obtained:

$$\sum_{i=1}^{N_{\text{mom}}} S_{ij}(s, t) g_i(s, t) = \delta S_j(s, t) \quad (3.94)$$

With:

$$S_{ij}(s, t) = \int d\vec{v} M_j(\vec{R}, v_{\parallel}, \mu) M_i(\vec{R}, v_{\parallel}, \mu) f_0(\vec{R}(t), v_{\parallel}(t), \mu(t_0)) \quad (3.95)$$

$$\delta S_j(s, t) = \gamma_K \int d\vec{v} \delta f(\vec{R}, v_{\parallel}, \mu, t) M_j(\vec{R}, v_{\parallel}, \mu) \quad (3.96)$$

Physical consequences of this algorithm are reviewed in [58]. In particular, the Krook operator prevents the weights increase and controls the signal to noise ratio which now scales proportionally to γ_K instead of $1/t_{\text{sim}}$ where t_{sim} is the total simulation time. However, by restoring f towards its equilibrium value, the Krook operator acts like a heating operator. By choosing to conserve the kinetic energy on magnetic surfaces, the Krook operator will not add thermal energy into the system and the restoring process of the temperature gradient is blocked: the heating effect disappears. This leads to *transient* simulations, similar to the one without the Krook operator, with the important difference that they are noise-controlled. As a rule of thumb, the value of γ_K is generally set to one tenth of the maximal linear growth rate. It does not modify significantly the linear

phase of the simulation and it allows high signal to noise ratios. One can then introduce a heating operator to control separately the temperature gradient:

$$\frac{d\delta f}{dt} = \tau(\vec{E}) + S_K(\vec{R}, v_{\parallel}, \mu, t) + S_{\text{corr}}(\vec{R}, v_{\parallel}, \mu, t) + S_H(\vec{R}, v_{\parallel}, \mu, t) \quad (3.97)$$

Where the heating operator S_H is defined by:

$$S_H(\vec{R}, v_{\parallel}, \mu, t) = -\gamma_H(s) \left(\delta\check{f}(\epsilon_k, s, t) - \check{f}_0(\epsilon_k, s) \frac{\int d\epsilon_k \delta\check{f}(\epsilon_k, s, t)}{\int d\epsilon_k \check{f}_0(\epsilon_k, s)} \right) \quad (3.98)$$

Where:

$$\check{A}(\epsilon_k, s) = \frac{\sqrt{2\epsilon_k} d\epsilon_k ds \int d\theta_* d\varphi d\lambda \frac{2\pi B_{\parallel}^*}{B} J(s, \theta_*) \sin \lambda A(s, \theta_*, \varphi, \epsilon_k, \lambda, t)}{\sqrt{2\epsilon_k} 4\pi \Sigma(s) d\epsilon_k ds} \quad (3.99)$$

This operator is constructed in such a way as to conserve the density on magnetic surfaces: $\int d\vec{v} S_H(\vec{R}, v_{\parallel}, \mu, t) = 0$. Furthermore, it is built by averaging δf on all dimensions of phase space except the energy and the radial direction. It means that this operator does not influence the noise caused by phase space filamentation in v (or equivalently in ϵ_k): the temperature profile can be controlled with the heating operator independently of the Krook operator. The heating amplitude is characterized by $\gamma_H(s)$. The radial bounds of the heating are controlled with two input parameters $s_{H_{\min}}$ and $s_{H_{\max}}$ which define a radial step function for $\gamma_H(s)$. In conclusion, there are therefore two ways of heating the plasma: the Krook operator and the heating operator. In theory, the heating operator conserves the long time zonal flow structure as the latter is odd in v_{\parallel} . It is a smooth quantity that will not remove the small velocity scales. Its effect is therefore slightly different to the Krook operator where all scales are treated equally.

Chapter 4

Numerical implementation

This Chapter presents a detailed derivation of the discretized equations solved by ORB5. This code contains about 40000 programming lines, and has been developed by several persons. Some algorithms, developed and implemented by other scientists have been used or improved in this work. They will nevertheless be presented in this Chapter for completeness, and the names of the persons who originally wrote them will be mentioned.

4.1 Initial status of the code

This thesis is the result of four years and a half of work. The goal was to implement a kinetic electron response into ORB5. The CPU time needed for such simulations increases by roughly $2\sqrt{m_i/m_e}$ compared to an adiabatic simulation and becomes extremely long. This is why the first part of this work has been devoted to the optimization of ORB5. The first paper on ORB5 has been published by T.M. Tran [44] in 1998. At this time, the code could simulate nonlinear ITG turbulence with adiabatic electrons without the zonal flow response, using a PIC approach, for CHEASE equilibria only. The quasineutrality equation, which reduces to a linear system, was solved with a sparse iterative solver using a SSOR preconditioned conjugated-gradient method. The code was parallelized along the toroidal direction for both the particles and the electrostatic potential. The major problem was the bad conservation of energy, Eq. (3.84), due to the statistical noise inherent to the PIC method. Then, from 1998 to the beginning of this work in June 2004, many improvements have been done. Adhoc equilibria have been implemented by A. Bottino, the zonal flow response and a diagonal Fourier filter have been introduced by P. An-

gelino [73]. The latter needed a direct solver, also introduced by P. Angelino. Numerical improvements have been achieved with noise optimization techniques such as optimized loading and adaptive gyro-average, originally developed in a bumpy pinch geometry [53], and further introduced in ORB5 by A. Bottino and R. Hatzky [74]. Although massive amelioration in the energy conservation was obtained, a high level of numerical noise was still observed, hence the need for further improvements. During this work, the parallelization of the code has been improved with a domain cloning algorithm, introduced in ORB5 by A. Bottino and R. Hatzky [75]. The noise measurement diagnostic has been introduced by A. Bottino and results on ETG turbulence published in [76]. The Krook and heating operators have been implemented by B. F. McMillan and results on ITG turbulence published in [58].

4.2 Normalization

Normalization quantities are summarized in table 4.1. It is assumed that the plasma contains electrons and an ion species with a mass m_i and a charge $q_i = eZ_i$.

4.3 PIC discretization

The Particle-In-Cell (PIC) method [77] is commonly employed in gyrokinetic simulations [32, 78, 49, 53, 47]. The perturbed distribution function is discretized in the 5D phase space along trajectories with N markers (also called *tracers*), carrying a *weight* w . In ORB5, δf is discretized as:

$$\delta f \approx \delta f_s = \frac{N_{\text{ph}}}{N} \sum_{p=1}^N \frac{1}{2\pi B_{\parallel}^*} w_p(t) \delta(\vec{R} - \vec{R}_p(t)) \delta(v_{\parallel} - v_{\parallel p}(t)) \delta(\mu - \mu_p(t_0)) \quad (4.1)$$

where $N_{\text{ph}} = \bar{n}V$ is the number of physical particles, $\bar{n} = 1/V \int ds n(s) \Sigma(s)$ is the volume averaged density. δf_s is in fact the sampled perturbed distribution function and must formally be differentiated from the true perturbed distribution function δf because δf_s is singular but δf is smooth. From now on the subscript "s" will be omitted. Each marker is characterized by its weight $w_p(t)$ and by its location $(\vec{R}_p(t), v_{\parallel p}(t), \mu_p(t_0))$ in phase space. Note that a marker is not a physical particle, but describes a portion of the

charge	q_i
mass	m_i
time	Ω_i^{-1}
length	ρ_s
speed	$c_s = \rho_s \Omega_i$
temperature	$T_e(s_0)$
electric potential	$\frac{T_e(s_0)}{q_i}$
electric field	$\frac{T_e(s_0)}{\rho_s q_i}$
magnetic field	B_0

Table 4.1: Normalisation quantities in ORB5. s_0 labels a given reference magnetic surface.

phase space. This discretization does not give the pure local information for δf because δf_s is singular. Instead, 5D integrals can be computed for arbitrarily small volumes, such as the gyro-averaged density in the quasineutrality equation. The physical information is therefore obtained by doing *binings* with the markers. Integrating Eq. (4.1) over a volume Ω_p :

$$\int_{\Omega_p} \delta f B_{\parallel}^* d\vec{R} dv_{\parallel} d\mu d\alpha = \int_{\Omega_p} B_{\parallel}^* d\vec{R} dv_{\parallel} d\mu d\alpha \frac{N_{\text{ph}}}{N} \sum_{r=1}^N \frac{1}{2\pi B_{\parallel}^*} w_r(t) \delta(\vec{R} - \vec{R}_r(t)) \delta(v_{\parallel} - v_{\parallel r}(t)) \delta(\mu - \mu_r(t_0)) \quad (4.2)$$

In the limit $\Omega_p \rightarrow 0$, δf can be assumed as constant, $\delta f \cong \delta f_p$, where δf_p is the average value of δf over Ω_p :

$$\lim_{\Omega_p \rightarrow 0} \int_{\Omega_p} \delta f B_{\parallel}^* d\vec{R} dv_{\parallel} d\mu d\alpha = \delta f_p \int_{\Omega_p} B_{\parallel}^* d\vec{R} dv_{\parallel} d\mu d\alpha = \delta f_p \Omega_p \quad (4.3)$$

In addition to this, in the limit $\Omega_p \rightarrow 0$ it is always possible to find a small enough Ω_p , centered around a single $(\vec{R}_r, v_{\parallel r}, \mu_r)$ which does not cross any other small volume Ω . Then the property $\int_a^b f(x) \delta(x - x') dx = 0$ when x' is outside $[a : b]$ is used such that:

$$\delta f_p \Omega_p = \frac{N_{\text{ph}}}{N} w_p(t) \Leftrightarrow w_p(t) = \frac{N}{N_{\text{ph}}} \delta f_p \Omega_p \quad (4.4)$$

Ω_p is the *phase space volume* occupied by one marker, in other terms:

$$\Omega_p = \frac{B_{\parallel}^* d\vec{R} dv_{\parallel} d\mu d\alpha}{dN} \quad (4.5)$$

where dN is the number of markers in an infinitesimal volume of the phase space. dN describes the distribution according to which the markers are loaded, and can be freely specified. Eq. (4.4) is the link between the numerical and the physical number of particles. After discretization, the temporal evolution of δf_p is obtained by solving the gyrokinetic equation integrated over Ω_p for each weight:

$$\frac{d\delta f_p \Omega_p}{dt} = \frac{N_{\text{ph}}}{N} \frac{dw_p}{dt} = \tau(\vec{E}_p) \Omega_p \quad (4.6)$$

with $\tau(\vec{E}_p)$ given by (3.44). At the same time the weights are evolved, the equations of motions for \vec{R}_p and $v_{\parallel p}$ are solved.

4.3.1 Equations of motion

Introducing the magnetic field (3.1) in Eqs. (3.23) and (3.24), and projecting along (s, θ_*, φ) according to $dA/dt = d\vec{R}/dt \cdot \nabla A$ gives:

$$\left. \frac{ds}{dt} \right|_0 = \frac{m_i \left(v_{\parallel}^2 + \frac{v_{\perp}^2}{2} \right)}{q_i B_{\parallel}^* B^2 J_{\theta_* s \varphi}} F(\psi) \frac{\partial B}{\partial \theta_*} \quad (4.7)$$

$$\left. \frac{ds}{dt} \right|_1 = \langle E_{\varphi} \rangle \frac{\nabla \psi \cdot \nabla s}{r^2 B B_{\parallel}^*} - \langle E_{\theta_*} \rangle \frac{F(\psi)}{J_{\theta_* s \varphi} B B_{\parallel}^*} \quad (4.8)$$

$$\left. \frac{d\theta_*}{dt} \right|_0 = \frac{v_{\parallel}}{J_{\theta_* \psi \varphi} B} - \frac{m_i \left(v_{\parallel}^2 + \frac{v_{\perp}^2}{2} \right)}{q_i B_{\parallel}^* B^2 J_{\theta_* s \varphi}} F(\psi) \frac{\partial B}{\partial s} - \frac{m_i v_{\parallel}^2 \mu_0 p'(\psi) F(\psi)}{q_i B_{\parallel}^* B^3 J_{\theta_* \psi \varphi}} \quad (4.9)$$

$$\left. \frac{d\theta_*}{dt} \right|_1 = \langle E_{\varphi} \rangle \frac{\nabla \psi \cdot \nabla \theta_*}{r^2 B B_{\parallel}^*} + \langle E_s \rangle \frac{F(\psi)}{J_{\theta_* s \varphi} B B_{\parallel}^*} \quad (4.10)$$

$$\begin{aligned} \left. \frac{d\varphi}{dt} \right|_1 &= \frac{v_{\parallel} F(\psi)}{B r^2} + \frac{m_i \left(v_{\parallel}^2 + \frac{v_{\perp}^2}{2} \right)}{q_i B_{\parallel}^* B^2 r^2} \left(\frac{\partial B}{\partial s} \nabla \psi \cdot \nabla s + \frac{\partial B}{\partial \theta_*} \nabla \psi \cdot \nabla \theta_* \right) \\ &\quad + \frac{m_i v_{\parallel}^2 \mu_0 p'(\psi) |\nabla \psi|^2}{q_i B_{\parallel}^* B^3 r^2} \end{aligned} \quad (4.11)$$

$$\left. \frac{d\varphi}{dt} \right|_1 = -\langle E_s \rangle \frac{\nabla \psi \cdot \nabla s}{r^2 B B_{\parallel}^*} - \langle E_{\theta_*} \rangle \frac{\nabla \psi \cdot \nabla \theta_*}{r^2 B B_{\parallel}^*} \quad (4.12)$$

$$\left. \frac{dv_{\parallel}}{dt} \right|_0 = -\frac{v_{\perp}^2}{2B^2 J_{\theta_* s \varphi}} \frac{\partial B}{\partial \theta_*} + \frac{m_i v_{\perp}^2 v_{\parallel}}{2q_i B_{\parallel}^*} \frac{\mu_0 p'(\psi) F(\psi)}{J_{\psi \theta_* \varphi} B^4} \frac{\partial B}{\partial \theta_*} \quad (4.13)$$

$$\begin{aligned} \left. \frac{dv_{\parallel}}{dt} \right|_1 &= \langle E_s \rangle \frac{v_{\parallel}}{B_{\parallel}^*} \frac{F(\psi)}{B^2 J_{\theta_* s \varphi}} \frac{\partial B}{\partial \theta_*} + \langle E_{\theta_*} \rangle \left(\frac{q_i}{m_i} \frac{1}{J_{\theta_* \psi \varphi} B} - \frac{v_{\parallel}}{B_{\parallel}^*} \frac{F(\psi)}{B^2 J_{\theta_* s \varphi}} \frac{\partial B}{\partial s} \right. \\ &\quad \left. - \frac{v_{\parallel}}{B_{\parallel}^*} \frac{\mu_0 p'(\psi) F(\psi)}{B^3 J_{\theta_* \psi \varphi}} \right) + \langle E_{\varphi} \rangle \left[\frac{q_i}{m_i} \frac{F(\psi)}{r^2 B} + \frac{v_{\parallel}}{B_{\parallel}^*} \left(\frac{\partial B}{\partial s} \nabla s \cdot \nabla \psi + \frac{\partial B}{\partial \theta_*} \nabla \psi \cdot \nabla \theta_* \right) \frac{1}{B^2 r^2} \right. \\ &\quad \left. + \frac{v_{\parallel}}{B_{\parallel}^*} \frac{\mu_0 p'(\psi) |\nabla \psi|^2}{B^3 r^2} \right] \end{aligned} \quad (4.14)$$

At each time step and for each marker, the new phase space coordinates and the weight are obtained. This operation is called the *particle pushing*.

The electric field is expressed as:

$$\langle \vec{E} \rangle = \langle E_s \rangle \nabla s + \langle E_{\theta_*} \rangle \nabla \theta_* + \langle E_{\varphi} \rangle \nabla \varphi \quad (4.15)$$

The Jacobian is:

$$J_{\theta_* s \varphi} = \frac{d\psi}{ds} J_{\theta_* \psi \varphi} = 2s \psi_{\text{edge}} \frac{r^2 q(\psi)}{F(\psi)} \quad (4.16)$$

B_{\parallel}^* is:

$$B_{\parallel}^* = B + \frac{m_i v_{\parallel}}{q_i} \left(F'(\psi) + \frac{F(\psi) \mu_0 p'(\psi)}{B^2} \right) \quad (4.17)$$

The magnetic field derivatives are given by:

$$\left. \frac{\partial B}{\partial s} \right)_{\theta_*} = \frac{\frac{\partial B}{\partial r})_z \frac{\partial \theta_*}{\partial z})_r - \frac{\partial B}{\partial z})_r \frac{\partial \theta_*}{\partial r})_z}{\frac{\partial \psi}{\partial r})_z \frac{\partial \theta_*}{\partial z})_r - \frac{\partial \psi}{\partial z})_r \frac{\partial \theta_*}{\partial r})_z}, \quad \left. \frac{\partial B}{\partial \theta_*} \right)_s = \frac{\frac{\partial B}{\partial z})_r \frac{\partial \psi}{\partial r})_z - \frac{\partial B}{\partial r})_z \frac{\partial \psi}{\partial z})_r}{\frac{\partial \psi}{\partial r})_z \frac{\partial \theta_*}{\partial z})_r - \frac{\partial \psi}{\partial z})_r \frac{\partial \theta_*}{\partial r})_z} \quad (4.18)$$

All the coefficients needed can be computed from the metric and with $p'(\psi)$, $F(\psi)$, $F'(\psi)$.

For adhoc equilibria, $F(\psi) = B_0 R_0$, $F'(\psi) = 0$ and $p'(\psi)$ is:

$$\mu_0 p'(\psi)^{AH} = -\frac{1}{r^2} \left(\nabla^2 \psi - \frac{2}{r} \frac{\partial \psi}{\partial r} + F'(\psi) F(\psi) \right) \quad (4.19)$$

The poloidal flux is given by:

$$\psi(\rho) = \int_0^{\rho} \frac{B_0 \rho'}{\bar{q}(\rho')} d\rho' \quad (4.20)$$

This integral is computed numerically. For a parabolic profile $\bar{q}(\rho) = q_0 + (q_{\text{edge}} - q_0) \rho^2/a^2$ it can be computed analytically:

$$\psi(\rho) = \frac{a^2 B_0}{2(q_{\text{edge}} - q_0)} \ln \left(1 + \frac{q_{\text{edge}} - q_0}{q_0 a^2} \rho^2 \right) \quad (4.21)$$

$$s = \sqrt{\frac{\ln \left(1 + \frac{q_{\text{edge}} - q_0}{q_0 a^2} \rho^2 \right)}{\ln \left(1 + \frac{q_{\text{edge}} - q_0}{q_0} \right)}} \quad (4.22)$$

$$\rho = a \sqrt{\frac{q_0}{q_{\text{edge}} - q_0} \left[\left(1 + \frac{q_{\text{edge}} - q_0}{q_0} \right)^{s^2} - 1 \right]} \quad (4.23)$$

The first derivatives of ψ are given by:

$$\frac{\partial \psi}{\partial r} = \frac{B_0 \rho}{\bar{q}(\rho)} \cos \theta, \quad \frac{\partial \psi}{\partial z} = \frac{B_0 \rho}{\bar{q}(\rho)} \sin \theta \quad (4.24)$$

The second derivatives of ψ are given by:

$$\frac{\partial^2 \psi}{\partial r^2} = \psi''(\rho) \cos^2 \theta + \frac{\psi'(\rho)}{\rho} \sin^2 \theta, \quad \frac{\partial^2 \psi}{\partial z^2} = \psi''(\rho) \sin^2 \theta + \frac{\psi'(\rho)}{\rho} \cos^2 \theta \quad (4.25)$$

$$\frac{\partial^2 \psi}{\partial r \partial z} = \psi''(\rho) \sin \theta \cos \theta - \frac{\psi'(\rho)}{\rho} \sin \theta \cos \theta, \quad \psi''(\rho) = \frac{B_0}{\bar{q}(\rho)} \left(1 - \frac{\rho \bar{q}'(\rho)}{\bar{q}(\rho)} \right) \quad (4.26)$$

θ_* can be computed analytically for adhoc equilibria:

$$\theta_* = 2 \arctan \left(\frac{\sqrt{1-\epsilon}}{\sqrt{1+\epsilon}} \tan(\theta/2) \right) \Leftrightarrow \theta = 2 \arctan \left(\frac{\sqrt{1+\epsilon}}{\sqrt{1-\epsilon}} \tan(\theta_*/2) \right) \quad (4.27)$$

Where $\epsilon = \frac{\rho}{R_0}$ The θ_* derivatives are given by:

$$\frac{\partial \theta_*}{\partial \theta} = \frac{1 - \epsilon \cos \theta_*}{\sqrt{1 - \epsilon^2}}, \quad \frac{\partial \theta_*}{\partial \psi} = -\frac{1}{B_0 R_0^2} \frac{\bar{q}(\rho)}{\epsilon} \frac{\sin \theta}{1 + \epsilon \cos \theta} \frac{1}{\sqrt{1 - \epsilon^2}} \quad (4.28)$$

$$\frac{\partial \theta_*}{\partial r} = \frac{\partial \theta_*}{\partial \psi} \frac{\partial \psi}{\partial r} - \frac{1}{\rho} \sin \theta \frac{\partial \theta_*}{\partial \theta}, \quad \frac{\partial \theta_*}{\partial z} = \frac{\partial \theta_*}{\partial \psi} \frac{\partial \psi}{\partial z} + \frac{1}{\rho} \cos \theta \frac{\partial \theta_*}{\partial \theta} \quad (4.29)$$

Equilibrium coefficients are stored on a (s, θ_*) grid whose dimensions are input parameters. During the marker pushing, coefficients are then obtained by linear interpolation. For adhoc equilibria, equilibrium coefficients could be directly computed at the marker position but it would strongly slow down the simulation. For shaped equilibria, the values of $s, \partial \psi / \partial r, \partial \psi / \partial z, \partial^2 \psi / \partial r^2, \partial^2 \psi / \partial r \partial z, \partial^2 \psi / \partial z^2, F(\psi)$ and $F'(\psi)$ are read from CHEASE and stored on a (s, θ_*) grid. For each point on the equilibrium (s, θ_*) grid, these values are obtained by linear interpolation, and all the remaining coefficients can be computed. The only difference is the coefficient $\partial \theta_* / \partial \psi$, which is obtained with a cubic spline interpolation with tension [79]. This procedure has been adopted due to the original version

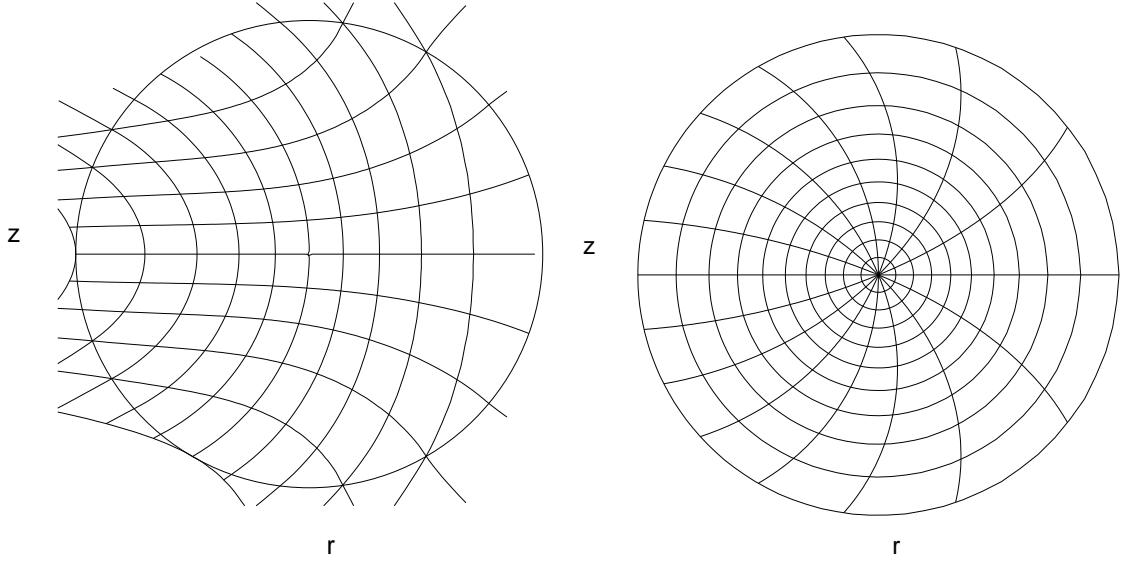


Figure 4.1: Example of (ξ, η) (left) and (s, θ_*) coordinates (right) in the poloidal plane for an aspect ratio of 2.

of ORB5 which pushed the tracers in cartesian coordinates. It would be better to read equilibrium coefficients from CHEASE directly on a (s, θ_*) grid to avoid multiple interpolations. This work will be done in the future.

In the poloidal plane, particles are pushed in (s, θ_*) . At the magnetic axis $s = 0$, it causes a numerical instability because $d\theta_*/dt \propto 1/s$ diverges. This problem is solved by using pseudo-cartesian coordinates (ξ, η) coordinates defined by:

$$\xi = s \cos \theta_* \quad \eta = s \sin \theta_* \quad (4.30)$$

and so:

$$\frac{d\xi}{dt} = \frac{ds}{dt} \cos \theta_* - \frac{d\theta_*}{dt} s \sin \theta_*, \quad \frac{d\eta}{dt} = \frac{ds}{dt} \sin \theta_* + \frac{d\theta_*}{dt} s \cos \theta_* \quad (4.31)$$

The singularity disappears because $sd\theta_*/dt$ is not divergent. An example of (s, θ_*) and (ξ, η) coordinates is given on Fig. 4.1. The lower the aspect ratio, the more the θ_* lines are dense in the HFS region. The effect is the same for a high shear or shaping effects such as positive triangularity and elongation. For negative triangularity, the θ_* lines are more dense in the LFS region. The integration of trajectories with these coordinates has also been implemented in the linear global code LORB5 [80]. Particles are pushed in (ξ, η) if $s < s_{\text{push}}$, where s_{push} is an input parameter, otherwise they are pushed in (s, θ_*) . A reasonable value for s_{push} can be estimated with the condition $ds/d|_0 \Delta t = s_{\text{push}}$ with

defines a circle that a marker can cover in one time step Δt with no electric field. The previous relation, evaluated at magnetic axis in the case of adhoc equilibria, gives an estimation of s_{push} . The following approximations are done: $v_{\parallel}^2 + v_{\perp}^2/2 \sim \kappa_v^2 v_{\text{thi}}(0)^2 = \kappa_v^2 c_s^2 T_i(0)/T_e(s_0)$, $\partial B/\partial \theta_* \sim B_0 \rho/R_0$, $J_{\theta_* s \varphi} \sim R_0 q_0/B_0 2s \psi_{\text{edge}}$. Then, with (4.7):

$$\left. \frac{ds}{dt} \right|_0 \Delta t \cong \frac{1}{2} \frac{\kappa_v^2}{R_0} c_s^2 \frac{m_i}{q_i} \frac{T_i(0)}{T_e(s_0)} \lim_{s \rightarrow 0} \frac{\rho}{s q_0 \psi_{\text{edge}}} \quad (4.32)$$

By furthermore assuming a parabolic safety factor, using Eqs (4.21), (4.22), (4.23), s_{push} is finally approximated by:

$$s_{\text{push}} = (\rho^*)^2 \kappa_v^2 \epsilon_a \frac{T_i(0)}{T_e(s_0)} \sqrt{\frac{q_{\text{edge}} - q_0}{q_0}} \frac{1}{\sqrt{\ln \left(1 + \frac{q_{\text{edge}} - q_0}{q_0} \right)}} \Omega_i \Delta t \quad (4.33)$$

The larger the plasma is, the smaller s_{push} can be. Nonlinear effects should not modify this estimation because the turbulence is weak on axis.

Equations of motions and Vlasov equation are integrated with a Runge-Kutta integrator of order 4. It is possible to run ORB5 with integrators of order 2 or 3 but they have not been used in this work. Finally, a marker can leave the plasma, i.e. it can have $s < s_{\text{f,min}}$ or $s > s_{\text{f,max}}$. Since the gyrokinetic model is collisionless, the number of particles is conserved. So when a marker leaves the plasma, it must be reintroduced somewhere. In ORB5, if a particle is outside the domain, it is reflected: $\theta_* \rightarrow -\theta_*$. This scheme may lead to some problems: if the equilibrium is not up-down symmetric, this reflection does not conserve any of the three constants of motion: $B(s, \theta_*) \neq B(s, -\theta_*)$, the magnetic moment $\mu = v_{\perp}^2/2B$ is changed but is, by default, supposed constant. The perpendicular velocity will change and the energy conservation will be violated. The change in the magnetic field also leads to the violation of the toroidal angular momentum. It would be more realistic to reinject the particle at $(s, -\theta_*, \varphi_{\text{new}})$ where $(-\theta_*, \varphi_{\text{new}})$ is on the same field line, in order not to change the phase of the potential, but this scheme would be too consuming in terms of CPU, because particles are parallelized in the toroidal direction. The particle pushing is speeded up (by up to 40 %) by using a cache sorting algorithm [81]: particles are sorted in the poloidal plane every n_{CS} time steps, where n_{CS} is given on input. Sorting the particle in s and θ_* allows cache reuse as all the equilibrium coefficients are stored on a (s, θ_*) grid. It is also efficient for the charge assignment, described in Section 4.5.3.

4.3.2 Loading of phase space volumes

The number of markers in an infinitesimal phase space volume dN can be freely specified. Markers are loaded independently in space and velocity such that:

$$dN = \frac{N}{N_{\text{ph}}} (f_L(\vec{R}) d^3x) (f_v(v_{\parallel}, v_{\perp}) d^3v) \quad (4.34)$$

$$= \frac{N}{N_{\text{ph}}} f_L(\vec{R}) J_{\theta_* s \varphi}(s, \theta_*) ds d\theta_* d\varphi f_v(v_{\parallel}, v_{\perp}) v_{\perp} dv_{\parallel} dv_{\perp} d\alpha \quad (4.35)$$

Inserting this relation in (4.5), Ω_p becomes:

$$\Omega_p = \frac{N_{\text{ph}} B_{\parallel}^*}{N B} \frac{1}{f_L(\vec{R}) f_v(v_{\parallel}, v_{\perp})} \quad (4.36)$$

In ORB5, f_L is

$$f_L(\vec{R}) = f_L(s) = K \left\{ 1 - f_g + f_g \exp \left[- \left(\frac{s - s_{0L}}{\Delta s_L} \right)^2 \right] \right\} \equiv K p(s) \quad (4.37)$$

This scheme is called the *specified loading*. s_{0L} and Δs_L are input parameters. f_g is a input parameter between 0 and 1. K is the normalisation constant:

$$1 = K \int f_L(\vec{R}) J_{\theta_* s \varphi}(s, \theta_*) ds d\theta_* d\varphi = K \int_{s_{f,\min}}^{s_{f,\max}} ds \Sigma(s) p(s) \quad (4.38)$$

$s_{f,\min}$ and $s_{f,\max}$ are the inner and outer boundaries of the annulus and $\Sigma(s)$ is the flux-surface-averaged Jacobian $\Sigma(s) = \int d\theta_* d\varphi J_{\theta_* s \varphi}$. f_L is then:

$$f_L(\vec{R}) = \frac{1 - f_g + f_g \exp \left\{ - \left(\frac{s - s_{0L}}{\Delta s_L} \right)^2 \right\}}{\int_{s_{f,\min}}^{s_{f,\max}} ds \Sigma_s(s) p(s)} \quad (4.39)$$

In the special case where $f_g = 0$ ($\Rightarrow p(s) = 1$), the scheme is called *uniform loading*: the number of markers in a given cell is proportional to its volume. Note that for linear simulations the specified loading is more appropriate because one can load more markers in the vicinity of the magnetic surface with the highest temperature gradient, i.e. where ITG modes develop. However, f_g should not be too close to 1 as poorly discretized regions of phase space may degrade the convergence of the results. Two options exist for the loading of f_v . In the first option, $f_v(v_{\parallel}, v_{\perp})$ is defined as:

$$f_v(v_{\parallel}, v_{\perp}) = \frac{M}{v_{\perp}} \quad (4.40)$$

M is a normalization constant:

$$1 = \int f_v(v_{\parallel}, v_{\perp}) v_{\perp} dv_{\perp} dv_{\parallel} d\alpha = M \int_0^{+\infty} dv_{\perp} \int_{-\infty}^{+\infty} dv_{\parallel} \quad (4.41)$$

With $f_v \sim 1/v_{\perp}$, the loading is uniform in $(v_{\parallel}, v_{\perp})$. The problem is that the integral in the last equation diverges. Markers obviously cannot be loaded with an infinite velocity. However, the distribution function is close to a Maxwellian, which is proportional to $\exp\{-(v/v_{\text{thi}}(s))^2\}$. Markers with a high velocity will have an extremely small contribution to the distribution function. The following approximation is done:

$$\int_0^{+\infty} dv_{\perp} \int_{-\infty}^{+\infty} dv_{\parallel} \cong \pi \int_0^{\kappa_v v_{\text{thi}}(s)} v dv = \frac{\pi}{2} [\kappa_v v_{\text{thi}}(s)]^2 \quad (4.42)$$

κ_v is a constant defined on input, usually $\kappa_v = 5$. This approximation means that markers are loaded in a half sphere of radius $\kappa_v v_{\text{thi}}(s)$. $f_v(v_{\parallel}, v_{\perp})$ is then:

$$f_v(v_{\parallel}, v_{\perp}) = \frac{1}{v_{\perp} [\pi \kappa_v v_{\text{thi}}(s)]^2} \quad (4.43)$$

Ω_p is finally:

$$\Omega_p = \frac{N_{\text{ph}} B_{\parallel}^*}{N B} \frac{v_{\perp}}{p(s_p)} [\pi \kappa_v v_{\text{thi}}(s_p)]^2 \int_{s_{\text{f,min}}}^{s_{\text{f,max}}} ds \Sigma(s) p(s) \quad (4.44)$$

A disadvantage of this loading is that it is not specifically optimized for δf in velocity space. In the nonlinear phase, the amplitude of the weights may vary significantly. During the charge assignment, noise will be produced where large weights (in absolute value) are present, which, due to its cumulative character, will alter the quality of the simulation. A way to overcome this difficulty is to apply an *optimized loading* scheme [53], based on the statistical method of importance sampling [69] of $|\delta f|$. The basic idea is to load markers with a probability function $f_{OL}(s, v)$ proportional to $|\delta f|$ at a time t_{NL} in the nonlinear phase. A first simulation is done with a uniform loading. $f_{OL}(s, v)$ is obtained by binning the markers at their initial position at a given time t_{NL} in the nonlinear phase. A second simulation is then performed using this new $f_{OL}(s, v)$, which determines initial phase space coordinates $(\vec{R}_p, v_{\parallel p}, \mu_p)$ and phase space volume Ω_p of the markers. In the nonlinear phase of this restarted simulation, the statistical variance of the weights will be smaller, hence the numerical noise will have a lower level (see Eq. (4.134)). The reason is that the optimized loading avoids the appearance of large weights in the nonlinear stage of a simulation. This technique has been successfully applied in cylindrical [53] and

tokamak [74] geometry.

The phase space loading can be checked with the following identity:

$$V_{ps} = \frac{4\pi}{3} \kappa_v^3 \int_{s_{f,\min}}^{s_{f,\max}} \Sigma(s) v_{\text{thi}}^3(s) ds = \sum_{p=1}^N \Omega_p \quad (4.45)$$

$V_{ps} = \int B_{\parallel}^* d\vec{R} dv_{\parallel} d\mu d\alpha$ is the phase space volume. The integral containing the term $B_{\parallel}^* - B$ vanishes because it is odd in v_{\parallel} . The velocity loading can further be checked with the following identity:

$$E_{\text{kin,ps}} = \frac{3}{2} \int_{s_{f,\min}}^{s_{f,\max}} ds \Sigma(s) n_0(s) v_{\text{thi}}^2(s) = \sum_{p=1}^N \frac{1}{2} m_i v_p^2 \Omega_p \quad (4.46)$$

Where $E_{\text{kin,ps}} = \int f_0(\vec{R}, v_{\parallel}, \mu) (v_{\parallel}^2/2 + \mu B) B_{\parallel}^* d\vec{R} dv_{\parallel} d\mu d\alpha$ is the unperturbed kinetic energy of the phase space. The integral containing the term $B_{\parallel}^* - B$ vanishes because it is odd in v_{\parallel} . Eqs. (4.45), (4.46) are true in the limit of an infinite number of markers and for $\kappa_v \rightarrow \infty$. In practice, the relative error is typically of the order of $10^{-2}\%$.

4.3.3 Weight evolution

The time evolution equation for the weights is Eq. (4.4) with $\tau(\vec{E})$ given by:

$$\tau(\vec{E}) = -f_0 \kappa(\Upsilon) \left. \frac{d\Upsilon}{dt} \right|_1 + \frac{q_i f_0}{T_i(\Upsilon)} \langle \vec{E} \rangle \cdot \left. \frac{d\vec{R}}{dt} \right|_0 \quad (4.47)$$

For $\Upsilon = \psi_0$, one has:

$$\begin{aligned} \left. \frac{d\psi_0}{dt} \right|_1 &= \frac{1}{B_{\parallel}^*} \left(1 + \frac{m_i v_{\parallel}}{q_i} \frac{F'(\psi)}{B} \right) (\vec{h} \times \nabla \psi) \cdot \langle \vec{E} \rangle \\ &\quad - \frac{m_i v_{\parallel}}{q_i B_{\parallel}^*} \frac{F(\psi)}{B^3} (\vec{B} \times \nabla B) \cdot \langle \vec{E} \rangle + \frac{m_i}{q_i} \frac{F(\psi)}{B} \left. \frac{dv_{\parallel}}{dt} \right|_1 \end{aligned} \quad (4.48)$$

$$(\vec{h} \times \nabla \psi) \cdot \langle \vec{E} \rangle = -\frac{F(\psi)}{J_{\theta_* \psi \varphi} B B_{\parallel}^*} \langle E_{\theta_*} \rangle + \frac{|\nabla \psi|^2}{r^2 B B_{\parallel}^*} \langle E_{\varphi} \rangle \quad (4.49)$$

$$\begin{aligned} -\frac{F(\psi)}{B^3} (\vec{B} \times \nabla B) \cdot \langle \vec{E} \rangle &= -\frac{F(\psi)^2}{B^3 J_{\theta_* s \varphi}} \frac{\partial B}{\partial \theta_*} \langle E_s \rangle + \frac{F(\psi)^2}{B^3 J_{\theta_* s \varphi}} \frac{\partial B}{\partial s} \langle E_{\theta_*} \rangle \\ &\quad - \frac{F(\psi)}{B^3 r^2} \left(\frac{\partial B}{\partial s} \nabla s \cdot \nabla \psi + \frac{\partial B}{\partial \theta_*} \nabla \psi \cdot \nabla \theta_* \right) \langle E_{\varphi} \rangle \end{aligned} \quad (4.50)$$

$$\left. \frac{d\vec{R}}{dt} \right|_0 \cdot \langle \vec{E} \rangle = \langle E_s \rangle \left. \frac{ds}{dt} \right|_0 + \langle E_{\theta_*} \rangle \left. \frac{d\theta_*}{dt} \right|_0 + \langle E_\varphi \rangle \left. \frac{d\varphi}{dt} \right|_0 \quad (4.51)$$

For $\Upsilon = \psi$, one has:

$$\left. \frac{d\psi}{dt} \right|_1 = \left. \frac{d\vec{R}}{dt} \right|_1 \cdot \nabla\psi = \frac{1}{B_{\parallel}^*} \left(\vec{h} \times \nabla\psi \right) \cdot \langle \vec{E} \rangle \quad (4.52)$$

4.3.4 Discretization of the noise control and heating operators

The linear system that has to be solved for the source operator, Eq. (3.94), is discretized with markers, integrated over a small phase space volume and solved on N_S flux surfaces. The unknown functions $g_i(s)$, once discretized are noted $g_i^k, k = 1, \dots, N_S$ and are obtained through the system:

$$\sum_{i=1}^{N_{\text{mom}}} S_{ij}^k g_i^k = \delta S_j^k \quad \forall k = 1, \dots, N_S \quad (4.53)$$

$$S_{ij}^k = \frac{1}{V_k} \sum_{\substack{1 \leq r \leq N \\ r: sr \in [s_{k-1}: s_k]}} f_0(\vec{R}_r, v_{\parallel r}, \mu_r) \Omega_r M_i(\vec{R}_r, v_{\parallel r}, \mu_r) M_j(\vec{R}_r, v_{\parallel r}, \mu_r) \quad (4.54)$$

$$\delta S_j^k = \frac{1}{V_k} \sum_{\substack{1 \leq r \leq N \\ r: sr \in [s_{k-1}: s_k]}} w_r \Omega_r \gamma_K M_j(\vec{R}_r, v_{\parallel r}, \mu_r) \quad (4.55)$$

And the weights are modified after the usual RK integration using a 1st order approximation. It means that the sources are computed once every time step:

$$w_r \Omega_r = w_r \Omega_r - \gamma_K \Delta t w_r \Omega_r + \Delta t \sum_{i=1}^{N_{\text{mom}}} f_0(\vec{R}_r, v_{\parallel r}, \mu_r) M_i(\vec{R}_r, v_{\parallel r}, \mu_r) g_i^{k_r} \Omega_r \quad (4.56)$$

where k_r is the index of $\{g_i\}$ for the marker r .

The bounce-average of v_{\parallel}/B is pre-computed on a (ψ_0, μ) grid using a 0th order approximation, i.e. assuming that ions follow their magnetic surface such that:

$$\tilde{A} = \frac{\int A \frac{B}{v_{\parallel} \vec{B} \cdot \nabla \theta_*} d\theta_*}{\int \frac{B}{v_{\parallel} \vec{B} \cdot \nabla \theta_*} d\theta_*} \quad (4.57)$$

N_{ϵ_k} intervals in ϵ_k , labelled with v , and N_{sH} intervals in s , labelled with w , are used for the heating operator $S_H(\vec{R}, v_{\parallel}, \mu, t)$. For each marker r it gives a contribution $S_{H,p}^{v,w}$:

$$S_{H,p}^{v,w} = -\frac{\gamma_H(s_p)}{V_{vw}} \sum_{\substack{1 \leq r \leq N \\ r: \epsilon_{kr} \in [\epsilon_{k,v-1}: \epsilon_{k,v}] \\ r: sr \in [s_{w-1}: s_w]}} w_r \Omega_r - f_0^{v,w} \Omega_r \frac{\sum_{\substack{1 \leq p \leq N \\ p: sp \in [s_{w-1}: s_w]}} w_p \Omega_p}{\sum_{v=1}^{N_{\epsilon_k}} f_0^{v,w}} \quad (4.58)$$

$$V_{vw} = \sum_{\substack{1 \leq r \leq N \\ r: \epsilon_{kr} \in [\epsilon_{k,v-1}: \epsilon_{k,v}] \\ r: sr \in [s_{w-1}: s_w]}} \Omega_r, \quad f_0^{v,w} = f_0(s_{w+1/2}, \epsilon_{k,v+1/2}) \quad (4.59)$$

The upper bound of the binning in energy is $1/2\kappa_v^2 T_i(0)$. Like for the noise-control operator, the heating is applied once at each time step using a 1st order approximation:

$$w_p \Omega_p = w_p \Omega_p + S_{H,p}^{v,w} \Delta t \quad (4.60)$$

4.3.5 Loading of initial conditions

At the beginning of a simulation, markers are loaded "randomly" with the help of Hammersley sequences (which is a particular case of the more general Halton sequences, see [82]), defined by:

$$H_r(p) = \sum_{j=0}^{N_p} \frac{a_j}{r^{j+1}} \quad (4.61)$$

Where r is a prime number and p a natural number written in base r :

$$p = \sum_{j=0}^{N_p} a_j r^j, \quad N_p = [\log_r(p)] \quad (4.62)$$

The Hammersley sequence ensures that if r is a prime number, $H_r(p) \neq H_r(j)$ for $p \neq j$. Besides, $0 < H_r(p) < H_{\max}(r, p)$:

$$H_{\max}(r, p) = 1 - \left(\frac{1}{r}\right)^{N_p+1} \quad (4.63)$$

In the limit of an infinite number of particles, $H_{\max}(r, p) = 1$. The Hammersley sequence gives a standard deviation proportional to $1/N$, which is much better than the standard

deviation produced by the Fortran implemented random generator, proportional to $1/\sqrt{N}$.

For the marker p , s_p and θ_{*p} are loaded by solving the following equations:

$$H_{r_1}(p) = \int_0^{s_p} \int_0^{2\pi} f_L(s', \theta_*) J_{\theta_* s \varphi}(s', \theta_*) ds' d\theta_* \quad (4.64)$$

$$H_{r_2}(p) = \int_0^{\theta_{*p}} f_L(s_p, \theta'_*) J_{\theta_* s \varphi}(s_p, \theta'_*) ds' d\theta'_* \quad (4.65)$$

φ can be loaded uniformly or with a Hammersley sequence. The magnetic moment and the parallel velocity are obtained through:

$$\lambda = \pi H_{r_3}(p), \quad |v| = \kappa_v \sqrt{v_{\text{thi}}(s) H_{r_4}(p)} \quad (4.66)$$

ORB5 has two ways of initializing the weights. For the *random noise initialization*:

$$\delta f_p(t_0) = H_{r_5}(p) f_0 \left[\vec{R}_p(t_0), v_{\parallel p}(t_0), v_{\perp p}(t_0) \right] \quad (4.67)$$

$H_{r_5}(p)$ is such that:

$$-A_0 < H_{r_5}(p) < A_0, \quad \frac{1}{N} \sum_{p=1}^N H_{r_5}(p) = 0 \quad (4.68)$$

A_0 is given on input. The initial perturbation is a small number, $A_0 \sim 10^{-5} - 10^{-3}$. This scheme has the disadvantage that the initial perturbation is inversely proportional to the number of markers in the simulation. The simulation takes an increasing time, roughly proportional to the number of markers, until the physical modes emerge of the initial noise. Instead, the idea is to build a physical initialization, called *mode initialization*, independent of the number of markers:

$$\begin{aligned} \delta f_i(t_0) &= \Omega_i \frac{A_0 f_0(\vec{R}_i(t_0), v_{\parallel i}(t_0), \mu_i(t_0))}{(m_2 - m_1 + 1)(n_2 - n_1 + 1)} \left| \frac{T_i(s_0)}{\nabla T_i(s_0)} \right| \left| \frac{\nabla T_i(s_i(t_0))}{T_i(s_i(t_0))} \right| \\ &\times \sum_{m=m_1}^{m_2} \sum_{n=n_1}^{n_2} \cos [m\theta_{*i}(t_0) - n\varphi_i(t_0)]. \end{aligned} \quad (4.69)$$

where m_1, m_2, n_1, n_2 are input parameters. For linear simulations it is convenient to choose $m_0 = m_1 = m_2 = [-n_0 q(s_0)]$ with $n_1 = n_2 = n_0$, where [...] denotes the integer part, which corresponds to a mode with $k_{\parallel} \rightarrow 0$, as ITG modes are aligned with the field lines. This initialization has the advantage that the initial perturbation converges with the number of markers and the initial phase of the simulation, until the physical modes develop, is independent of the number of markers.

4.4 Parallelization

Good convergence requires a high number of particles and therefore large memory and number of processors. Physical simulations also need a high resolution grid for the Poisson equation, which leads to high memory requirements. That is the reason why ORB5 is massively parallelized with MPI [83].

Initially, the code had a 1D toroidal decomposition based on the so-called *general concurrent PIC algorithm* (GCPIC) [84]. A new 2D parallelization algorithm based on the *domain cloning* algorithm [85, 75] has been implemented. The P processors used in a simulation are decomposed as:

$$P = P_C \times P_\varphi \tag{4.70}$$

where P_φ is the number of processors in the φ direction, and P_C is the number of clones. When $P_C = 1$, the domain cloning algorithm is equivalent to the GCPIC algorithm. The density is computed on a 3D grid. The torus grid is divided into toroidal slices and distributed among the different processors. The memory size of all arrays defined on this 3D grid is then divided by P_φ .

The Poisson equation is solved in real or Fourier space. N_φ toroidal slices or toroidal Fourier modes need to be solved. Each processor will have N_φ/P_φ modes to solve. Each of the P_C clone contains P_φ processors. All the clones are equivalent in the sense that they contain the whole toroidal domain for the field quantities. The particles are evenly distributed among all the processors. Each processor will own N/P particles (with some small differences since N modulo P maybe not equal to 0). During the time evolution, particles move in the toroidal direction and must be sent to the corresponding processors. Field quantities such as the perturbed density must be summed over the clones at each time step. The general picture of domain cloning is displayed on Fig. 4.2. This 2D decomposition is obviously better than a 1D toroidal decomposition as the latter is constrained by $P \leq N_\varphi$ (one must have at least one Fourier mode per processor). As the plasma size increases, more and more toroidal modes need to be solved. In order to have a reasonable memory for the field arrays such as electric potential, many toroidal slices must be used. But in that case more and more particles must be sent to other processors as they move toroidally. The same problem appears when kinetic electrons are added to the simulation: because their toroidal motion is much faster than the ion one, more

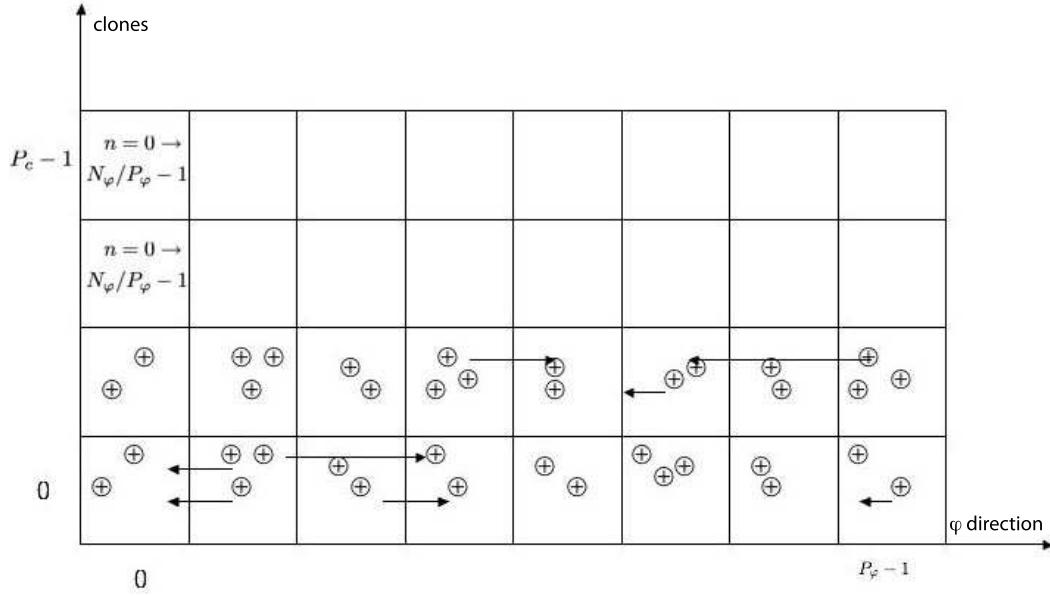


Figure 4.2: The domain cloning scheme for ORB5.

particles must be sent. When using $P_C = 1$, the time needed for parallel communication can strongly dominate the simulation. In conclusion, an optimum decomposition can be found, depending on the memory and the inter-connection of the processors.

4.5 Poisson equation

4.5.1 The Galerkin method

The Poisson equation is solved with a *finite element* method [86]. The fundamental idea is to discretize the potential as follows:

$$\phi(\vec{x}, t) = \sum_{\mu} \phi_{\mu}(t) \Lambda_{\mu}(\vec{x}) \quad (4.71)$$

Where $\phi_{\mu}(t)$ are real numbers, and $\{\Lambda_{\mu}(\vec{x})\}$ are the tensor product of *B-splines* [87] (see annex A.1). B-splines are polynomial functions of order p . In ORB5, $p = 1, 2$ or 3 is implemented. The discretization of ϕ , Eq. (4.71) and the discretization of δf , Eq. (4.1) are inserted in the quasineutrality Eq. (3.80). The Galerkin method consists of two steps. First, the equation is multiplied by a test function $\Lambda_{\nu}(\vec{x})$ which has the same shape as the B-spline used for the potential discretization. Second, the equation is integrated over

the whole plasma. The quasineutrality equation turns into a linear system:

$$\sum_{\mu} (A_{\mu\nu} + A_{\mu\nu}^{ZF}) \phi_{\mu} = b_{\nu}^i \quad (4.72)$$

With:

$$A_{\mu\nu} = \int d\vec{x} \left\{ \frac{en_0(\psi)}{T_e(\psi)} \Lambda_{\nu}(\vec{x}) \Lambda_{\mu}(\vec{x}) + \frac{n_0(\psi)}{B\Omega_i} \nabla_{\perp} \Lambda_{\nu}(\vec{x}) \cdot \nabla_{\perp} \Lambda_{\mu}(\vec{x}) \right\} \quad (4.73)$$

$$A_{\mu\nu}^{ZF} = - \int d\vec{x} \frac{en_0(\psi)}{T_e(\psi)} \Lambda_{\nu}(\vec{x}) \bar{\Lambda}_{\mu}(s) \quad (4.74)$$

$$b_{\nu}^i = \frac{N_{\text{ph}}}{N_i} \sum_{r=1}^{N_i} \frac{1}{2\pi} \int d\alpha \Lambda_{\nu}(\vec{R}_r + \vec{\rho}_{Lir}) w_r(t) \quad (4.75)$$

Both A and A^{ZF} matrices are symmetric and positive definite. To get to this equation, an integration by parts has been done on the polarization density by using the divergence theorem. The surface term is:

$$\sum_{\mu} \phi_{\mu} \int_{\sigma} \Lambda_{\nu} \frac{n_0(\psi)}{B\Omega_i} \nabla_{\perp} \Lambda_{\mu} \cdot \vec{d}\sigma \quad (4.76)$$

At $s = s_{f,\text{max}}$, $\phi = 0$ is imposed so that the surface term is 0. When $s_{f,\text{min}} = 0$, the surface term is 0. For $s_{f,\text{min}} \neq 0$, the surface term is not 0 but has been neglected.

The computation of b_{ν}^i , Eq. (4.75), is called the *charge assignment*: the charge density is obtained by assigning the weights to gyro-rings and projecting them on the splines. The details are presented on annex A.3. The charge assignment is a Monte-Carlo integral and will contain statistical noise. More details on this topic will be given in Section 4.5.6

4.5.2 Determination of the grid size

Depending on the physical case under study, the ORB5 numerical parameters should be set up as follows. The radial mesh resolution depends on the maximum $k_s \rho_{Li}$ that should be resolved, where k_s is the radial component of the wave number. With cubic B-spline finite elements there should be at least 3 points per wavelength. Thus

$$N_s > \frac{3}{2\pi} (k_s \rho_{Li})_{\text{max}} \frac{a}{\rho_{Li}} \quad (4.77)$$

Similarly, for a maximum $k_{\theta_*} \rho_{Li}$ that should be resolved up to the magnetic surface s_{max} , where k_{θ_*} is the poloidal component of the wave number, the poloidal mesh should be set

to

$$N_{\theta_*} > 3s_{\max} (k_{\theta_*} \rho_{Li})_{\max} \frac{a}{\rho_{Li}}. \quad (4.78)$$

Since the perturbations tend to be aligned with magnetic field lines the toroidal mesh should be chosen as

$$N_\varphi \approx N_{\theta_*} / q(s) \quad (4.79)$$

4.5.3 Expression for the matrix and the RHS

Before discretizing in more details the linear system, an additional approximation is done. The ∇_\perp operator can be written:

$$\nabla_\perp = \nabla_s \frac{\partial}{\partial s} + \nabla\theta_* \frac{\partial}{\partial\theta_*} + \nabla\varphi \frac{\partial}{\partial\varphi} - \vec{h} \left[\frac{F(\psi)}{r^2 B} \right] \left[\frac{\partial}{\partial\varphi} + \frac{1}{q(\psi)} \frac{\partial}{\partial\theta_*} \right] \quad (4.80)$$

The operator in the square brackets can be neglected due to the alignment of microinstabilities with the field line:

$$\frac{\partial}{\partial\varphi} \cong -\frac{1}{q(\psi)} \frac{\partial}{\partial\theta_*} \quad (4.81)$$

Finally:

$$\nabla_\perp \cong \nabla_{\text{pol}} = \nabla_s \frac{\partial}{\partial s} + \nabla\theta_* \frac{\partial}{\partial\theta_*} \quad (4.82)$$

Where $|\nabla\varphi \frac{\partial}{\partial\varphi}|$ has been neglected over $|\nabla\theta_* \frac{\partial}{\partial\theta_*}|$. The ratio of these term is equal to $\rho/r \sim \mathcal{O}(\epsilon_a)$. This assumption could be avoided by using (4.81) for ∇_\perp :

$$\nabla_\perp \cong \nabla_s \frac{\partial}{\partial s} + \left(\nabla\theta_* - \frac{1}{q(\psi)} \nabla\varphi \right) \frac{\partial}{\partial\theta_*} \quad (4.83)$$

This option has been implemented in ORB5 but has not been used in this work, as it has been checked that it does not give any significant difference on the results. Note that for a field-aligned-solver (see Section 4.5.7), the true ∇_\perp operator could in principle be implemented.

The quasineutrality equation must be solved on a 3D grid. However, due to the axisymmetry of the tokamak, the linear system can be transformed into a 2D system by writing ϕ_μ and b_μ^i in Fourier space:

$$\phi_\mu = \phi_{j',k',l'} = \sum_{n=0}^{N_\varphi-1} \hat{\phi}_{j',k'}^{(n)} \exp\left(\frac{2\pi i}{N_\varphi} nl'\right) \quad (4.84)$$

$$b_\nu^i = b_{j,k,l} = \sum_{n=0}^{N_\varphi-1} \hat{b}_{j,k}^{(n)} \exp\left(\frac{2\pi i}{N_\varphi} nl\right) \quad (4.85)$$

With this Ansatz, the integral over φ that only involves B-splines can be computed analytically. The quasineutrality equation written in Fourier space is simply:

$$\sum_{\mu} (A_{\mu\nu} + A_{\mu\nu}^{ZF}) \hat{\phi}_{\mu}^{(n)} = \frac{\hat{b}_{\nu}^{(n)}}{M^{(n)}} \quad (4.86)$$

where $(\mu, \nu) = (jk, j'k')$ now stand for 2D indices and:

$$A_{\mu\nu} = \int ds d\theta_* J_{\theta_* s \varphi}(s, \theta_*) \left\{ \frac{en_0(s)}{T_e(s)} \Lambda_{\nu}(s, \theta_*) \Lambda_{\mu}(s, \theta_*) + \frac{n_0(s)}{B\Omega_i} \nabla_{\text{pol}} \Lambda_{\nu}(s, \theta_*) \cdot \nabla_{\text{pol}} \Lambda_{\mu}(s, \theta_*) \right\} \quad (4.87)$$

$$A_{\mu\nu}^{ZF} = - \int ds d\theta_* J_{\theta_* s \varphi}(s, \theta_*) \frac{en_0(s)}{T_e(s)} \bar{\Lambda}_{\mu}(s) \Lambda_{\nu}(s, \theta_*) \quad (4.88)$$

$$\sum_{l'=0}^{N_{\varphi}-1} \int d\varphi \Lambda_{l'}(\varphi) \Lambda_l(\varphi) \exp\left(\frac{2\pi i}{N_{\varphi}} nl'\right) = M^{(n)} \exp\left(\frac{2\pi i}{N_{\varphi}} nl\right) \quad (4.89)$$

A generic formula can be given for $M^{(n)}$ (see Annex A.1). For linear, quadratic and cubic splines $M^{(n)}$ is given by:

$$M^{(n)} = \frac{2\pi}{N_{\varphi}} \begin{cases} \frac{2}{3} + \frac{1}{3} \cos\left(\frac{2\pi}{N_{\varphi}} n\right) & \text{for } p = 1 \\ \frac{11}{20} + \frac{13}{30} \cos\left(\frac{2\pi}{N_{\varphi}} n\right) + \frac{1}{60} \cos\left(\frac{2\pi}{N_{\varphi}} 2n\right) & \text{for } p = 2 \\ \frac{151}{315} + \frac{397}{840} \cos\left(\frac{2\pi}{N_{\varphi}} n\right) + \frac{1}{21} \cos\left(\frac{2\pi}{N_{\varphi}} 2n\right) + \frac{1}{2520} \cos\left(\frac{2\pi}{N_{\varphi}} 3n\right) & \text{for } p = 3 \end{cases} \quad (4.90)$$

When the zonal flow matrix is included, the system is solved in toroidal Fourier space to avoid communication among processors. When it is not included, the system can be solved equivalently in real or Fourier space. The discretized form of the matrices is given in Annex A.2. In order to compute the RHS b_{ν}^i , the integral over α is done through a N_{gr} points sum, where:

$$N_{gr} = \min \left[32, \max(4, 4\rho_{Lir}/\rho_{Li}) \right] \quad (4.91)$$

ρ_{Lir} is the ion Larmor radius at the marker's position. The number of points used for the gyro-average depends on the Larmor radius of the marker's guiding center. This technique is called the *gyro-adaptative* method and reduces noise [53]. It is also assumed that the Larmor ring lies in the poloidal plane:

$$\varphi_r(\alpha) \cong \varphi_{rGC} + \vec{\rho}_{Lir}(\alpha) \cdot \nabla \varphi|_{r_{rGC}, z_{rGC}} \cong \varphi_{rGC} \quad (4.92)$$

where:

$$\vec{\rho}_{Li} = \rho_{Li} \left(\frac{\nabla s}{|\nabla s|} \cos \alpha + \frac{\vec{B} \times \nabla s}{|\vec{B} \times \nabla s|} \sin \alpha \right) \quad (4.93)$$

The neglected term goes like $\rho^* \epsilon_a$ and is therefore ϵ_a smaller than the other terms appearing in the gyro-average. To get the position of the marker on the Larmor ring, one uses a Taylor expansion:

$$\xi_{r\alpha} \cong \xi_{rGC} + \vec{\rho}_{Li} \cdot \nabla \xi|_{GC}, \quad \eta_{r\alpha} \cong \eta_{rGC} + \vec{\rho}_{Li} \cdot \nabla \eta|_{GC} \quad (4.94)$$

And then $s_{r\alpha}, \theta_{*r\alpha}$ are obtained analytically. This is done to avoid $(r, z) \rightarrow (s, \theta_*)$ transformations. $\vec{\rho}_{Li} \cdot \nabla \xi$ and $\vec{\rho}_{Li} \cdot \nabla \eta$ are obtained by linear interpolation and are given by:

$$\begin{aligned} \vec{\rho}_{Li} \cdot \nabla \xi &= \rho_{Li} \left[\left(|\nabla s| \cos \theta_* - \frac{\nabla s \cdot \nabla \theta_*}{|\nabla s|} s \sin \theta_* \right) \cos \alpha \right. \\ &\quad \left. + \frac{F(\psi)}{J_{\theta_* s \varphi} B |\nabla s|} s \sin \theta_* \sin \alpha \right] \end{aligned} \quad (4.95)$$

$$\begin{aligned} \vec{\rho}_{Li} \cdot \nabla \eta &= \rho_{Li} \left[\left(|\nabla s| \sin \theta_* + \frac{\nabla s \cdot \nabla \theta_*}{|\nabla s|} s \cos \theta_* \right) \cos \alpha \right. \\ &\quad \left. - \frac{F(\psi)}{J_{\theta_* s \varphi} B |\nabla s|} s \cos \theta_* \sin \alpha \right] \end{aligned} \quad (4.96)$$

The gyropoints are not located exactly on a circle but the error is small, even at the magnetic axis (see Fig. 4.3). When computing the gyropoints, a random phase, different for each tracer but constant in time can be added. This option has not been used in this work as no noise reduction has been observed. The following boundary conditions are applied. At the plasma edge, $\phi(s_{f,\max}, \theta_*, \varphi) = 0 \forall \theta_*, \varphi$ is imposed. When $s_{f,\min} = 0$, the unicity of the potential is imposed, $\phi(s = 0, \theta_*, \varphi) = \phi_{axis} \forall \theta_*, \varphi$. When $s_{f,\min} \neq 0$, one can either impose nothing or impose $\phi(s_{f,\min}, \theta_*, \varphi) = 0 \forall \theta_*, \varphi$. The details of the boundary conditions implementation are presented in Annex A.4

4.5.4 Solving methods

The initial solver in ORB5 was an iterative sparse solver, using a SSOR preconditioned conjugated-gradient method. The sparse solver is useful for $A_{\mu\nu}$ because most of its

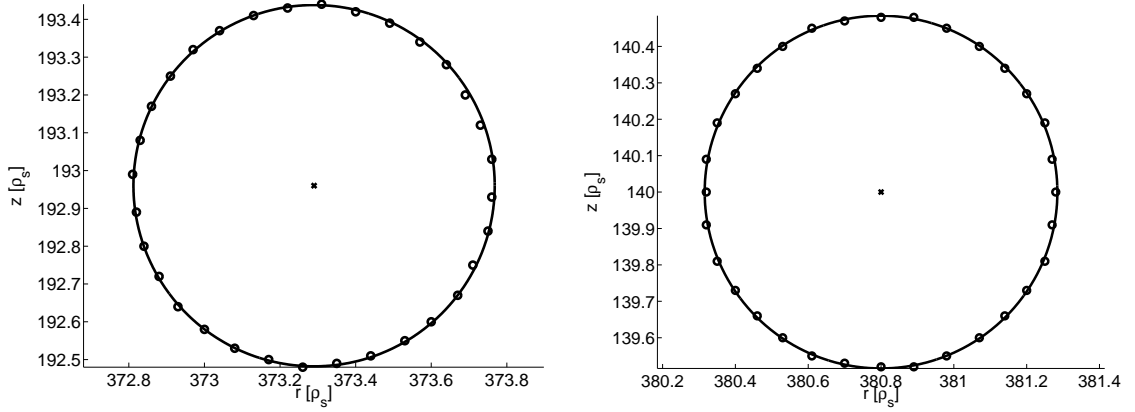


Figure 4.3: Gyropoints for a marker at $s = 0.5, \theta = \pi/2$ (left) and at $s = 0$ (right).

elements are 0. By storing the row pivot, the location, the value and the number of non-zero elements, the total memory size required by the solver for splines of order p is:

$$M_{\text{sparse}} = \frac{5}{512}(N_s + p) \frac{N_{\theta_*}}{512} [\text{Mb}] \quad (4.97)$$

This solver has the advantage to use very few memory, but its iterative character makes it slow. A further disadvantage is that in practice it cannot be used for $A_{\mu\nu}^{ZF}$ because this matrix is not sparse and so the advantage of a low memory is lost.

Another possibility is to use a direct LAPACK [88] solver. In that case the band matrix is stored, whose memory size is:

$$M_{\text{LAPACK}} = 2(p + 1) \left(\frac{N_{\theta_*}}{256} \right)^2 (N_s + p) [\text{Mb}] \quad (4.98)$$

This solver is faster than the iterative solver, but requires one order of magnitude higher memory. The zonal flow matrix requires the same memory. In order to avoid storing two matrices per processors, processors containing the $n = 0, \dots, N_\varphi/P_\varphi - 1$ density Fourier modes send the $n = 1, \dots, N_\varphi/P_\varphi - 1$ modes to other processors. The solutions for these modes are then sent back to the original processors. Although the matrix memory is reduced by a factor 2, the direct solver rapidly becomes inadequate in terms of memory as the plasma size increases. Actual tokamaks have a size of about $\rho_* = 1/200$. Solving up to $(k_\perp \rho_{Li}) = 1$ at mid-radius means solving up to $m = \frac{1}{2\rho_*} = 100$, which means that N_{θ_*} should be around 400. N_s should be of the order of $1/\rho_*$, which gives, according to (4.98), a memory of about $1GB$. The direct solver for tokamaks of the size of ITER would require a memory of several tens of GB. In addition the time needed per time step for the system

solve would be around 10 minutes with present days computers, clearly demonstrating the need for a more efficient solver. With the aim of reducing the memory and the CPU time of the solver, a parallel solver using ScaLAPACK [89] has been developed. The matrix is parallelized in the clone direction, i.e. P_C processors are used for the parallelization. The size of the matrix is:

$$M_{\text{ScaLAPACK}} = 2 \frac{(p+1) \left(\frac{N_{\theta_*}}{256}\right)^2 (N_s + p)}{P_C} [\text{Mb}] \quad (4.99)$$

The number of unknowns $N_u = (N_s + p)N_{\theta_*}$ is also divided by P_C . Each processor will contain part of the solution vector. Unfortunately, ScaLAPACK requires the local number of unknowns to be larger than the total bandwidth of the matrix:

$$\frac{(N_s + p)N_{\theta_*}}{P_C} > 2[(p+1)N_{\theta_*} - 1] \quad (4.100)$$

This gives an upper limit for P_C :

$$P_C < \frac{(N_s + p)N_{\theta_*}}{2[(p+1)N_{\theta_*} - 1]} \lesssim \frac{N_s}{2(p+1)} \quad (4.101)$$

where the limit $N_{\theta_*} \gg 1$, $N_s \gg p$ has been used. ScaLAPACK requires additional arrays of size approximately equal to $M_{\text{ScaLAPACK}}$. For the upper limit of P_C , the total memory is approximatively:

$$M_{\text{ScaLAPACK}}^{\text{tot}} \cong 8(p+1)^2 \left(\frac{N_{\theta_*}}{256}\right)^2 [\text{Mb}] \quad (4.102)$$

The gain of memory when going from the serial to the parallel direct solver is approximatively $N_s/(4p+4)$. For the typical plasma sizes used in this work, N_s is 128 and the gain is 8. However, one sees that this solver will not be sufficient for ITER-size plasmas. A better solver will be presented in Section 4.5.7. The RHS must be distributed in P_C parts among the different processors. After the backsolve, the whole solution must be reassembled, which is done through a `MPI_GATHER` operation. Note that the ScaLAPACK solver imposes a limit on the number of processors for a given simulation:

$$P < \frac{N_s}{2(p+1)} N_\varphi \quad (4.103)$$

A proper detailed scalability study of the ScaLAPACK solver is beyond the scope of this work. Instead, the use of this solver in practical situations is presented. The CPU

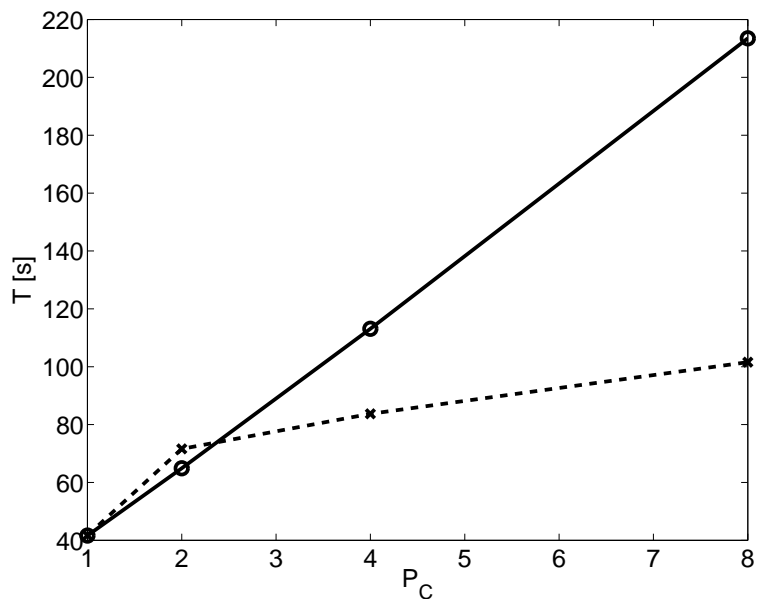


Figure 4.4: Time per iteration for solving the quasineutrality equation vs number of clones P_C for the serial LAPACK solver (solid line) and the parallel ScaLAPACK solver (dashed line).

time per time step devoted to the field equation is due to several parameters: the size of the matrix per processor (depending on N_s and N_{θ^*}), the number of Fourier modes per processor (depending on P_φ) and the parallel communication due to the toroidal Fourier transform: the information for φ being local on each processor, the density has to be transposed such that each processor owns the whole toroidal domain. After this operation the arrays are parallelized in the poloidal direction. If the matrix computed with the LAPACK solver can enter into the memory, then the optimal parallelization will be $P_\varphi = N_\varphi$, because there will be one mode per processor to be solved. The case $P_\varphi > N_\varphi$ is impossible. By increasing P_C more processors can be used, the scalability of the code in the clone direction being almost perfect. If the toroidal communication for particles becomes dominant, then P_φ should be decreased in favour of P_C , but this situation is, in practice, quite unlikely.

Figure 4.4 presents the time per iteration for the "fields" part (system solve+ Fourier transforms) at fixed $P = 128$ versus the number of clones P_C for the LAPACK and ScaLAPACK solvers. The grid size is $N_s = 64$, $N_{\theta^*} = 256$, $N_\varphi = 128$. For the LAPACK solver, the time per iteration increases linearly with P_C because more RHS need to be

solved. The same applies for the ScaLAPACK solver from $P_C = 2$. For $P_C = 1$, both methods are identical but the ScaLAPACK solver becomes faster (up to a factor 2) as soon as $P_C > 2$.

4.5.5 The Fourier field-aligned filter

With the purpose of reducing numerical noise, a Fourier filter is applied to the perturbed density such that the quasineutrality equation reads:

$$\sum_{\mu} (A_{\mu\nu} + A_{\mu\nu}^{ZF}) \phi_{\mu} = \mathcal{F}(b_{\nu}^i) \quad (4.104)$$

where:

$$\mathcal{F}(b_{\nu}^i) = \mathcal{F}(b_{j,k,l}^i) = \sum_{m=0}^{N_{\theta_*}-1} \sum_{n=0}^{N_{\varphi}-1} b_j^{i,m,n} f_j^{m,n} \exp\left(\frac{2\pi i}{N_{\theta_*}} mk\right) \exp\left(\frac{2\pi i}{N_{\varphi}} nl\right) \quad (4.105)$$

$$b_j^{i,m,n} = \sum_{k=0}^{N_{\theta_*}-1} \sum_{l=0}^{N_{\varphi}-1} b_{j,k,l}^i \exp\left(\frac{2\pi i}{N_{\theta_*}} mk\right) \exp\left(\frac{2\pi i}{N_{\varphi}} nl\right) \quad (4.106)$$

The filter acts in toroidal and poloidal Fourier space. A first naive option is to use a *rectangular filter* defined by:

$$f_j^{m,n} = \mathcal{H}(m - m_{\min}) \mathcal{H}(m_{\max} - m) \mathcal{H}(n - n_{\min}) \mathcal{H}(n_{\max} - n) \quad (4.107)$$

where \mathcal{H} is the Heavyside function and m_{\min} , m_{\max} , n_{\min} and n_{\max} are input parameters. It means that a rectangular window of Fourier modes is selected and all the modes outside this window are dropped out of the simulation. This filter is aimed at filtering high harmonics. For example, the maximum poloidal mode in a simulation is $m = N_{\theta_*}/2$. It will not be solved accurately with N_{θ_*} grid points. Although this filter considerably reduces numerical noise, it is not a good choice because it contains modes that are not consistent with the gyrokinetic ordering. The highest k_{\parallel} mode contained in the filter will be:

$$k_{\parallel, \max} = \left(\frac{m + nq(s)}{q(s)r}\right)^{\max} \cong \left(\frac{2m_{\max}}{q(s_0)R_0}\right) \quad (4.108)$$

For this mode $k_{\perp} \cong m_{\max}/\rho_0$ (where ρ_0 is a reference radius) and so:

$$\left(\frac{k_{\parallel}}{k_{\perp}}\right)^{\max} \cong \frac{2\tilde{\rho}_0\epsilon_a}{q(s_0)} \quad (4.109)$$

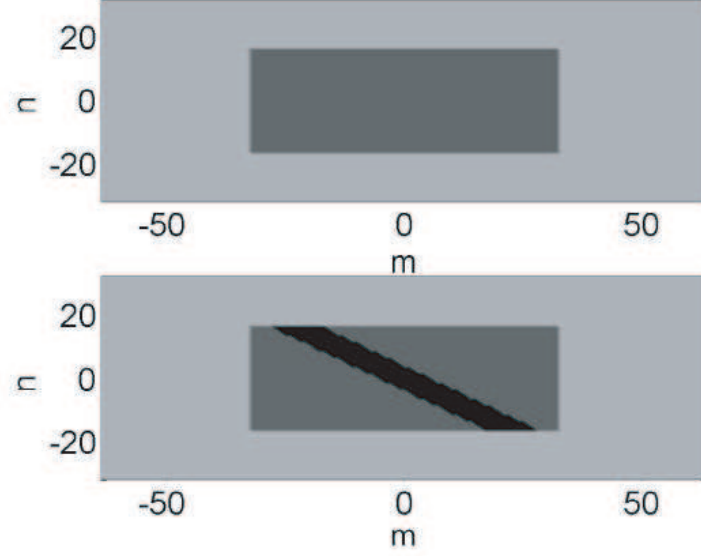


Figure 4.5: Example of rectangular filter (top) and field-aligned filter at a given magnetic surface (bottom).

Where $\tilde{\rho}_0 = \rho_0/a$. Gyrokinetic ordering implies that $(k_{\parallel}/k_{\perp})^{\max} \sim \rho^*$, but the above expression gives a much higher value than typical ρ^* values ($\sim 10^2 - 10^3$): for CYCLONE parameters [90] it is 0.26. A better way to filter the density is to use a *field-aligned filter*, defined by:

$$f_j^{m,n} = \mathcal{H}\left(m - (-nq(s_j) - \Delta m)\right) \mathcal{H}\left((-nq(s_j) + \Delta m) - m\right) \mathcal{H}(n - n_{\min}) \mathcal{H}(n_{\max} - n) \quad (4.110)$$

Where Δm is an input parameter. In this case, the filter is rectangular in the toroidal direction and diagonal in the poloidal direction, with the diagonal width equal to $2\Delta m + 1$. In particular, the filter follows the safety factor profile: it depends on the magnetic surface. Rectangular and field-aligned filters are represented on Fig. 4.5. Filters can be combined. In practice, ORB5 uses a field-aligned filter superposed with a rectangular filter. The width of Δm can be estimated with $k_{\parallel} \cong \Delta m/q(s_0)R_0$ by using the expression for the cut-off in k_{\parallel} in the case of slab-ITG turbulence, Eq. (2.55), which gives, with $\xi_i \ll 1$.

$$\Delta m \cong q(s_0) \frac{k_y \rho_{Li}}{2} \frac{R_0}{L_{Ti}} \frac{1}{\sqrt{1 + \tau^{-1}} \sqrt{\tau^{-1}}} \sqrt{1 - \frac{2}{\eta_i}} \quad (4.111)$$

Note that Δm does not depend on the plasma size as it is independent of ρ^* . With this expression one gets:

$$\left(\frac{k_{\parallel}}{k_{\perp}}\right)^{\max} \cong \frac{\epsilon_a \rho^*}{2} \frac{R_0}{L_{Ti}} \frac{1}{\sqrt{1 + \tau^{-1}}} \sqrt{1 - \frac{2}{\eta_i}} \quad (4.112)$$

which is consistent with the gyrokinetic ordering. Note also that Δm should be large enough so that the filtered perturbed density does not have discontinuities across magnetic surfaces. Mathematically, it is expressed as:

$$\Delta m > \frac{nq'(s)}{N_s} \cong \frac{ak_{\perp}\hat{s}}{N_s} \cong \frac{2\pi}{3} \frac{\hat{s}(k_{\perp}\rho_{Li})_{\max}}{(k_s\rho_{Li})_{\max}} \quad (4.113)$$

Note that these expressions are only valid when using the straight-field-line angle. It is possible to give a quantitative estimation of Δm when the geometrical poloidal angle θ is used. Suppose a single toroidal mode n_0 representing the most unstable linear mode of the system propagating locally in a circular plasma. The $k_{\parallel} = 0$ component is such that:

$$\phi(s_0, \theta_*, \varphi) = \hat{\phi}(s_0)e^{in_0(\varphi - q\theta_*)} \quad (4.114)$$

In the large aspect ratio approximation, θ_* can be written as:

$$\theta_* = \frac{\bar{q}(\rho)}{q(\psi)} \int_0^{\theta} \frac{1}{1 + \epsilon \cos \theta'} d\theta' = \theta - \epsilon \sin \theta + \mathcal{O}(\epsilon^2) \quad (4.115)$$

Inserting this in Eq. (4.114):

$$\phi(s_0, \theta_*, \varphi) = \hat{\phi}(s_0)e^{in_0(\varphi - q\theta)} \sum_{n=-\infty}^{n=+\infty} J_n(-\epsilon n_0 q) e^{in\theta} \quad (4.116)$$

Where J_n are the Bessel functions and Eq. (2.42) has been used. This expression shows that the spectrum is broadened in θ space. Fig. 4.6 shows the coefficients $J_n(\epsilon n_0 q)$ as a function of n for different values of n_0 . $n_0 = 15$ corresponds to the most unstable linear ITG mode for a plasma of size $\rho_* = 140$ (smaller than actual tokamaks), and $n_0 = 120$ could correspond to the most unstable linear ITG mode for a plasma size comparable to ITER. As the argument of the Bessel function increases, the broadening becomes more and more important. The same effect appears when shaping is introduced: for instance, for a large aspect ratio tokamak with elliptic surfaces characterized by an elongation κ , $\theta_* \cong \theta - \epsilon\kappa \sin \theta$. The argument of the Bessel function would be multiplied by κ , thus enhancing the broadening. The broadening becomes formally infinite for an infinite plasma size, i.e. when $\rho_* \rightarrow 0$. Using the asymptotic form of the Bessel function:

$$J_n(x) \rightarrow \sqrt{\frac{2}{\pi x}} \cos\left(x - \frac{n\pi}{2} - \frac{\pi}{4}\right) \quad (4.117)$$

$$\phi(s, \theta_*, \varphi) = \sqrt{\frac{2}{\pi \epsilon n_0 q}} \hat{\phi}(s_0) e^{in_0(\varphi - q\theta)} \sum_{n=-\infty}^{n=+\infty} \cos\left(x - \frac{n\pi}{2} - \frac{\pi}{4}\right) e^{in\theta} \quad (4.118)$$

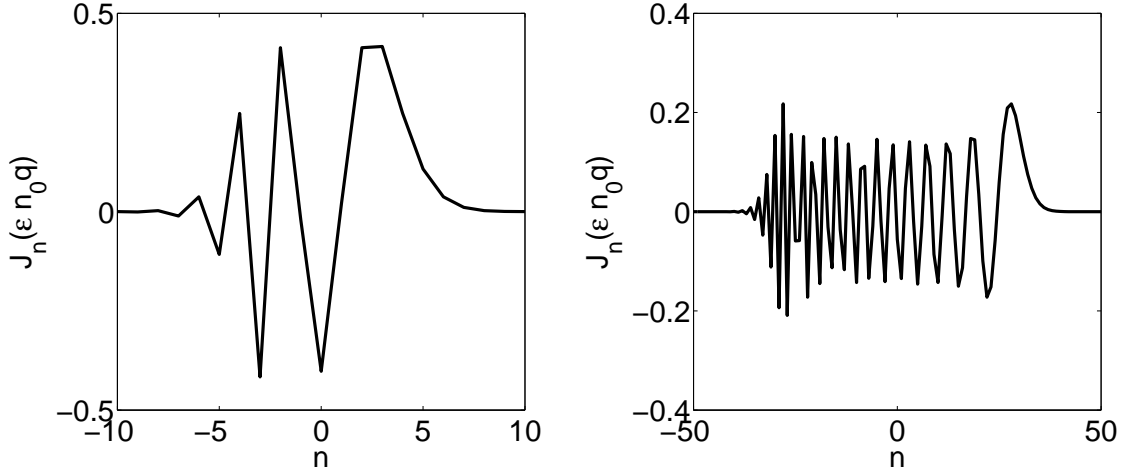


Figure 4.6: $J_n(\epsilon n_0 q)$ as a function of n for $\epsilon = 0.18$, $q = 1.4$, $n_0 = 15$ (left) and $n_0 = 120$ (right).

These expressions clearly show that when the poloidal angle θ is used a very large value of Δm must be used. This has extremely harmful consequences on the numerical noise, which is closely related to the number of markers per Fourier modes included in the simulation (see Section 4.5.6).

The time step of a simulation is closely linked with the Fourier filter. The general time step criterion writes:

$$\omega \Delta t = \delta \ll 1 \quad (4.119)$$

Where ω is the fastest relevant frequency of the system. For ITG turbulence in a tokamak, there are mainly 3 frequencies of interest: the transit frequency $\omega_t = v_{\parallel}/q(s)r$, the frequency related to the $\vec{E} \times \vec{B}$ velocity, $\omega_{\perp} = k_{\perp} v_{\vec{E} \times \vec{B}} \cong M k_{\perp} v_{\text{thi}}$, where M is the Mach number and the frequency related to the parallel velocity, $\omega_{\parallel} = k_{\parallel} v_{\parallel}$. Using previous estimates of $k_{\parallel}^{\text{max}}$ for both kinds of filter, the time step criterion for ω_{\parallel} becomes:

$$\Delta t_{\parallel}^r \Omega_i \cong \frac{\delta}{2} \frac{a}{\rho_0} \frac{1}{q(s_0)} \epsilon_a \quad \text{rectangular filter} \quad (4.120)$$

$$\Delta t_{\parallel}^{fa} \Omega_i \cong \frac{\delta \sqrt{\tau}}{a} \frac{2L_{Ti}}{\sqrt{1 - \frac{2}{\eta_i}}} (\rho^*)^{-1} \quad \text{field - aligned filter} \quad (4.121)$$

The $(\rho^*)^{-1}$ dependence of Eq. (4.121) clearly shows the beneficial influence of the field-aligned filter in the parallel direction. However, quantitative estimates of ω_t and $\omega_{\vec{E} \times \vec{B}}$ are needed to see if the field-aligned filter has an influence on the global time step of

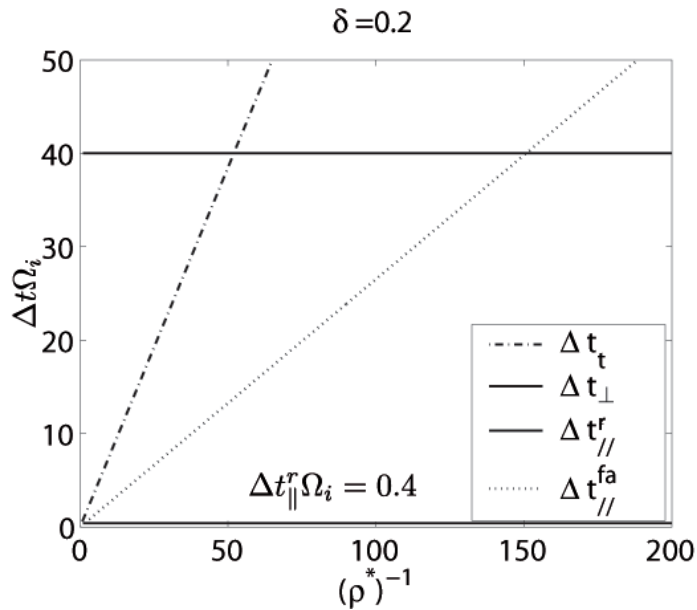


Figure 4.7: Time step criterion as a function of $(\rho^*)^{-1}$ for CYCLONE parameters.

the simulation. Fig. 4.7 shows estimates of the different time steps for modes having the maximum k_{\parallel}/k_{\perp} with the CYCLONE parameters and $M = 5 \cdot 10^{-3}$, which is the typical value observed in these simulations. The value of Δt_{\parallel}^s is extremely small. Since usual time steps are of the order of $5\Omega_i^{-1}$, the evolution of many modes in the rectangular filter will be inaccurate and will impair the quality of the simulation. On the other hand, in the limit of small- ρ^* plasmas, simulation using a field-aligned filter could be run, according to our estimate, with a one order of magnitude higher time step, thus decreasing CPU by the same amount. Note that the Mach number has been taken as independent of ρ^* . Its dependence versus ρ^* should be studied theoretically to provide a more accurate picture of the maximal frequency of the system.

4.5.6 Numerical noise

The PIC method is a Monte-Carlo approach, and introduces numerical statistical noise - roughly proportional to σ/\sqrt{N} where σ is the standard deviation of the markers - in the density. Unfortunately, collisionless δf PIC simulations unavoidably end up noise-dominated: in the nonlinear phase, due to the absence of dissipation, the fluctuation entropy, related to the variance of the weights, increases linearly with time. The reasons will be presented in more details in Section 6.1. In a linear simulation, the electric field

is not included in the trajectories. The noise does not propagate and the noise problem becomes less important. An interesting discussion on Monte-Carlo methods is presented in [69]. In particular, it is shown that the δf method, widely used in the fusion community, is nothing but a control variates method: the idea is to replace as much as possible of the distribution function by an analytical expression.

Estimating the amplitude of the noise and comparing it with the physical signal is a tricky task. An expression has been derived by A. Bottino in [76]. The details of the computation are presented below for the sake of completeness. For simplicity, FLR effects, the profiles variation and the zonal flows will be neglected. The quasi-neutrality equations writes:

$$\frac{en_0}{T_e}\phi(\vec{x}) = \frac{\bar{n}V}{N} \sum_{r=1}^N w_r \delta(\vec{x} - \vec{x}_r) \quad (4.122)$$

The Fourier transform of the potential is:

$$\hat{\phi}(\vec{p}) = \int d\vec{x} \phi(\vec{x}) \exp(-2\pi i \vec{p} \cdot \vec{x}) \quad (4.123)$$

Applying a Fourier transform on the density and squaring this expression:

$$\left| \frac{en_0}{T_e} \hat{\phi}(\vec{p}) \right|^2 = \frac{\bar{n}^2 V^2}{N^2} \sum_{r=1}^N w_r^2 + \sum_{r=1}^N \sum_{\substack{q=1 \\ q \neq r}}^N w_r w_q \exp\left[2\pi i \vec{p} \cdot (\vec{x}_q - \vec{x}_r)\right] \quad (4.124)$$

The second term represents correlations between markers positions and weights, and describes the contribution of waves and turbulence to the spectral density [91], and is therefore neglected in the estimate of an upper bound for the numerical noise. Going to a Discrete Fourier Transform (DFT), $d\vec{x} \cong \Delta x \Delta y \Delta z \cong V/N_m$, where N_m is the number of Fourier modes in the system such that:

$$\left| \frac{en_0}{\bar{n}T_e} \hat{\phi}_k \right|^2 \cong \frac{N_m^2}{N^2} \langle w^2 \rangle, \quad \langle w^2 \rangle = \sum_{r=1}^N w_r^2 \quad (4.125)$$

Note that each radial grid point is considered as a Fourier mode, although it is formally not correct due to non-periodic boundary conditions. The noise estimate must be refined to take into account FLR effects and the numerical schemes employed into account, such as splines and Fourier filtering. The discretized perturbed density from Eq. (4.75) can be written as:

$$\begin{aligned} b_\nu &= \frac{\bar{n}V}{N} \sum_{r=1}^N w_r \frac{1}{2\pi} \int_0^{2\pi} d\alpha d\vec{x} \Lambda_\nu(\vec{x}) \delta(\vec{R}_r + \vec{\rho}_{Lir} - \vec{x}) \\ &= \frac{\bar{n}V}{N} \sum_{r=1}^N w_r \int d\vec{x} \Lambda_\nu(\vec{x}) \int d\vec{p} \exp(2\pi i \vec{p} \cdot \vec{x}) \exp(-2\pi i \vec{p} \cdot \vec{R}_r) J_0(\vec{p} \cdot \vec{\rho}_{Lir}) \end{aligned} \quad (4.126)$$

This expression has a velocity dependence. It can be removed by averaging the contribution of the Bessel function with a Maxwellian distribution:

$$\frac{1}{n_0} \int v_{\perp} dv_{\perp} dv_{\parallel} d\alpha f_0(v_{\parallel}, v_{\perp}) J_0\left(\frac{k_{\perp} v_{\perp}}{\Omega}\right) = \exp\left(-\frac{k_{\perp}^2 \rho_{Li}^2}{2}\right) \quad (4.127)$$

Where this integral has been obtained with Eq. (6.31.1) of [60]:

$$\int_0^{\infty} x^{\mu} e^{-\alpha x^2} J_{\nu}(\beta x) dx = \frac{\beta^{\nu} \Gamma\left(\frac{1}{2}\nu + \frac{1}{2}\mu + \frac{1}{2}\right)}{2^{\nu+1} \alpha^{1/2} (\mu + \nu + 1) \Gamma(\nu + 1)} \Phi\left(\frac{\nu + \mu + 1}{2}, \nu + 1; -\frac{\beta^2}{4\alpha}\right)$$

$$\Phi(\alpha, \gamma; z) = 1 + \frac{\alpha z}{\gamma 1!} + \frac{\alpha(\alpha + 1) z^2}{\gamma(\gamma + 1) 2!} + \frac{\alpha(\alpha + 1)(\alpha + 2) z^3}{\gamma(\gamma + 1)(\gamma + 2) 3!} + \dots$$

Inserting this result in b_{ν} , multiply by the complex conjugate and neglecting again the correlation terms:

$$|b_{\nu}|_{\text{noise}}^2 = \frac{\bar{n}V}{N} \sum_{r=1}^N w_r^2 \int d\vec{p} d\vec{p}' \exp\left[-2\pi i(\vec{p} - \vec{p}') \cdot \vec{R}_r\right] \quad (4.128)$$

$$\exp\left\{-\frac{\left[k_{\perp}^2(p_{\perp}) + k'_{\perp}{}^2(p'_{\perp})\right] \rho_{Li}^2}{2}\right\} \tilde{\Lambda}_{\nu}(-\vec{p}) \tilde{\Lambda}_{\nu}^{\dagger}(-\vec{p}') \quad (4.129)$$

With:

$$\tilde{\Lambda}(-\vec{p}) = \int d\vec{x} \Lambda_{\nu}(\vec{x}) \exp(2\pi i \vec{p} \cdot \vec{x}) \quad (4.130)$$

Due to the randomization of the position of the markers, one can approximate:

$$\exp\left[-2\pi i(\vec{p} - \vec{p}') \cdot \vec{R}_r\right] \cong \frac{1}{V} \int d\vec{R} \exp\left[-2\pi i(\vec{p} - \vec{p}') \cdot \vec{R}\right] \cong \frac{1}{V} \delta(\vec{p} - \vec{p}') \quad (4.131)$$

And so:

$$|b_{\nu}|_{\text{noise}}^2 = \frac{V^2}{N^2} \langle w^2 \rangle S, S = \frac{1}{V} \int d\vec{p} |\tilde{\Lambda}_{\nu}(-\vec{p})|^2 \exp\left(-\frac{k_{\perp}^2 \rho_{Li}^2}{2}\right) \quad (4.132)$$

This formula is similar to (4.125) but contains an extra term S which characterizes the filtering due to FLR and spline representation effects. Another effect is still missing: the splines do not allow for the representation of arbitrary small scale lengths. The finite number of grid points cut the spectrum at a certain wavelength and reduce the noise. To simplify the mathematics one assumes non-overlapping elements and neglect the polarization density and the FLR effects:

$$A_{\mu\nu} \cong \frac{n_0 e}{T_e} \int d\vec{x} \Lambda_{\nu}^2 \delta_{\mu\nu} \Rightarrow \sum_{\mu} A_{\mu\nu} \phi_{\mu} = \frac{n_0 e}{T_e} \int d\vec{x} \Lambda_{\nu}^2(\vec{x}) \phi_{\nu} \quad (4.133)$$

Gathering this result with (4.125), (4.132):

$$\delta n_{i,\text{noise}}^2(t) \cong \frac{N_m}{N} \langle w^2 \rangle(t) G \quad (4.134)$$

$$G = \frac{\int d\vec{p} |\tilde{\Lambda}(-\vec{p})|^2 \exp\left(-\frac{k_{\perp}^2 \rho_{Li}^2}{2}\right)}{\left| \int d\vec{x} \Lambda_{\nu}^2(\vec{x}) \right|^2} \quad (4.135)$$

Eq. (4.134) reveals how the noise can be decreased: by increasing the number of markers, by reducing the number of Fourier modes in the simulation, by using sampling methods such as optimized loading [53] to reduce the statistical variance of the weights or by improving the projection algorithm, for example by increasing the order of the splines.

The value of the noise alone is not representative, but must be compared to a physical signal. Recall that Eq. (4.134) is an upper bound of the numerical noise. In ORB5, the noise is defined as the sum of $|b_i^{(m,n)}|^2$ (components of the perturbed density in toroidal and poloidal Fourier space) for a subset \mathcal{F}_2 of non-resonant modes (outside the field-aligned filter \mathcal{F}) divided by the number of modes inside \mathcal{F}_2 . These modes are Landau damped and their growth is due to numerical noise only. The value of the noise is in fact the noise per mode. It is approximated that each mode in \mathcal{F}_2 contributes equally to the noise.

$$\text{noise} = \frac{\sum_{i=-p_l}^{N_s+p_r-1} \sum_{m,n \in \mathcal{F}_2} |b_i^{(m,n)}|^2}{\sum_{i=-p_l}^{N_s+p_r-1} \sum_{m,n \in \mathcal{F}_2}} \quad (4.136)$$

\mathcal{F}_2 is made of two diagonal bands of width $2\Delta m + 1$, shifted poloidally from the field-aligned filter by $\pm 3\Delta m$. The modes inside this filter have high k_{\parallel} modes which do not belong to the physical modes. The signal is obtained as the sum of $|b_i^{(m,n)}|^2$ (components of the perturbed density in toroidal and poloidal Fourier space) for the resonant modes (inside the field-aligned filter \mathcal{F}) divided by the number of modes inside \mathcal{F} :

$$\text{signal} = \frac{\sum_{i=-p_l}^{N_s+p_r-1} \sum_{m,n \in \mathcal{F}} |b_i^{(m,n)}|^2}{\sum_{i=-p_l}^{N_s+p_r-1} \sum_{m,n \in \mathcal{F}}} \quad (4.137)$$

The definition of \mathcal{F}_2 is not unique and can be questioned. Recall that the noise is normalized by the number of modes inside the filter that defines it: different levels of noise are obtained depending on the definition of \mathcal{F}_2 . Nevertheless, *what matters is to define a threshold for the signal to noise ratio below which the results will be considered as not converged*. Such a rule of thumb is obtained by looking at the physical fluxes, somehow

independently of \mathcal{F}_2 . However, a meaningful requirement is that the modes inside \mathcal{F}_2 must be sufficiently far from the modes belonging to the signal. A better noise estimate could be obtained by looking at the relation between the noise and the wave number.

The link between Eqs. (4.134) and (4.136) has been demonstrated in [76] by choosing \mathcal{F}_2 as two small rectangles containing the modes with the highest k_{\parallel} allowed by the finite element grid. In ORB5, the way to compute the noise is directly related to the field-aligned filter. The same definition could be used with a rectangular filter but in this case $N_m \propto N_s N_{\theta_*} N_{\varphi} \sim (\rho^*)^3$ and for the field-aligned filter $N_m \propto N_s (2\Delta m + 1) N_{\varphi} \sim (\rho^*)^2$. It means that when going from a rectangular to a field-aligned filter, the number of particles can be reduced by approximatively two orders of magnitude and its scaling with ρ^* is one order of magnitude more favorable, provided that the straight-field-line angle is used. If the poloidal angle is used, Δm must be increased (see Section 4.5.5) and the noise reduction will be much lower.

This "signal to noise ratio" procedure can be summarized as follows. It is assumed that the system contains *physical modes* that are inside the field-aligned filter. These modes are physical in the sense that $k_{\parallel}/k_{\perp} \ll 1$ or equivalently $|m - nq(s)| \leq \Delta m$. Here the modes relate to the perturbed density. The signal to noise ratio could also be computed from the potential, but it would not be possible with the Fourier field-aligned solver (see Section 4.5.7). Density modes (computed from the phase space coordinates and the weight of the markers) that are outside the field-aligned filter can have a non-zero contribution. Some of these modes (as defined by \mathcal{F}_2) are interpreted as resulting from discrete particle noise. These definitions of noise are not universally applicable: they neglect the noisy part contained inside the filter \mathcal{F} , therefore they are valid only for signal to noise ratios much larger than one.

A final remark on the numerical noise concerns collisionless full- f PIC simulations. In this case, the weights of the markers describe f and are not evolved on time because f is constant along the orbits. The main advantage is that the noise does not increase with time because $\langle w^2 \rangle(t) = \langle w^2 \rangle(t_0)$, but the main disadvantage is that more markers are required compared to the δf method [69] because $\langle w^2 \rangle_{\text{full-}f} / \langle w^2 \rangle_{\delta f} \sim (f/\delta f)^2 \gg 1$.

4.5.7 The Fourier field-aligned solver

In Section 4.5.4, different solvers have been presented. All of them have inconvenients: they are either too slow or require too much memory. Even if the ScaLAPACK solver is able to reduce the memory, it is still quite large, relatively slow and not very scalable. In the previous Section, it is shown how the density (the r.h.s. of the quasineutrality equation) reduces to very few modes in Fourier space by taking advantage of the alignment of the perturbations with the field lines. A similar method can be applied to the potential (the l.h.s. of the quasineutrality equation). The Fourier field-aligned solver has been initially developed by B. McMillan. Its implementation has been furthermore optimized in this work. The idea is closely related to the field-aligned filter. The linear system describing the quasineutrality equation can be written in toroidal and poloidal Fourier space:

$$Ax = b \Rightarrow \underbrace{(FAF^{-1})}_{\tilde{A}} \underbrace{(Fx)}_{\tilde{x}} = \underbrace{Fb}_{\tilde{b}} \quad (4.138)$$

where F is the discrete Fourier transform (DFT) operator. The discretized form of \tilde{A} is presented in Annex A.5, and the implementation of the boundary conditions is presented in Annex A.6. The idea is then to apply a field-aligned filter of width $2\widetilde{\Delta m} + 1$, where $\widetilde{\Delta m}$ is an input parameter generally equal to Δm , to the Finite-Element-Matrix expressed in poloidal Fourier space \tilde{A} . It means that several poloidal Fourier modes will not be solved, but according to the gyrokinetic ordering their contribution should be negligible provided that $\widetilde{\Delta m}$ is large enough. Note also that this technique neglects the poloidal couplings between the modes inside and outside the matrix filter, but they should be very small if $\widetilde{\Delta m}$ is large enough.

Without any filtering, the matrix can be viewed as $N_s + p$ blocks of size $N_{\theta_*} \times N_{\theta_*}$. With the field-aligned filtering, the matrix can be viewed as $N_s + p$ blocks of size $(2\widetilde{\Delta m} + 1) \times (2\widetilde{\Delta m} + 1)$. The matrix is still a band matrix because the radial couplings are not modified in poloidal Fourier space. The memory required is:

$$M_{FAS} = \frac{N_\varphi}{P_\varphi} (N_s + p)(p + 1) \left(\frac{2\widetilde{\Delta m} + 1}{256} \right)^2 \text{ [Mb]} \quad (4.139)$$

The factor N_φ/P_φ comes from the fact that there must be a different matrix for each toroidal wave number n . If not, then the results will depend on the parallelization because

$\widetilde{\Delta m}$ would have to cover all the toroidal modes in a given processor. In practice, N_φ/P_φ is equal to 1 or sometimes 2 and $\widetilde{\Delta m}$ is usually between 5 and 7. The gain of memory is:

$$G = \frac{M_{\text{ScaLAPACK}}}{M_{\text{FAS}}} = \frac{2(p+1)N_{\theta_*}^2 P_\varphi}{N_\varphi(N_s+p)(2\widetilde{\Delta m}+1)^2} \quad (4.140)$$

Orders of magnitude are gained compared to the ScaLAPACK solver. For a typical CYCLONE test case with $p = 3$, $N_s = 128$, $N_{\theta_*} = 512$, $P_\varphi = N_\varphi$ and $\widetilde{\Delta m} = 5$, the gain of memory is 132. In addition, the matrix becomes so small (typically 1-4 Mb) that the CPU time required to solve the linear system becomes insignificant: it represented 40% for largest cases that could be run with the ScaLAPACK solver but it is now less than 1%. The last advantage is that there is practically no limit on P_c anymore, hence no limit on P .

The matrix is now composed of $N_s + p$ blocks $(2\widetilde{\Delta m} + 1) \times (2\widetilde{\Delta m} + 1)$ that are full. There is no structure difference with the zonal flow matrix. The spline basis transformation and the boundary condition at the edge are similar to the normal direct solver. Unicity on axis is expressed in Fourier space by zeroing all poloidal modes except $m = 0$. It is in fact similar to the unicity condition in real space, Eq. (A.51).

4.5.8 Shielding of the potential at the edge

At the plasma edge, the boundary condition imposed is $\phi = 0$, which is done by imposing δn_i to 0. Markers near the plasma boundary carry some density which is set to 0 just before the Poisson equation is solved, without changing the markers' weight. Moreover, if a marker or a gyro-point lies outside the plasma, it is not taken into account. Therefore, near the edge, the quasineutrality condition is violated and a charge accumulation is observed. In nonlinear simulations, a numerical sheath region is observed near the plasma edge: a spurious radial electric field develops, which can be one order of magnitude higher than the physical electric field. In order to remove this spurious field, the quasineutrality equation is modified as follows:

$$\frac{e\tilde{n}_0(\psi)}{T_e(\psi)} (\phi(\vec{x}, t) - \bar{\phi}(\psi, t)) - \nabla_\perp \cdot \left(\frac{\tilde{n}_0(\psi)}{B\Omega_i} \nabla_\perp \phi(\vec{x}, t) \right) = \delta n_i(\vec{x}, t) \quad (4.141)$$

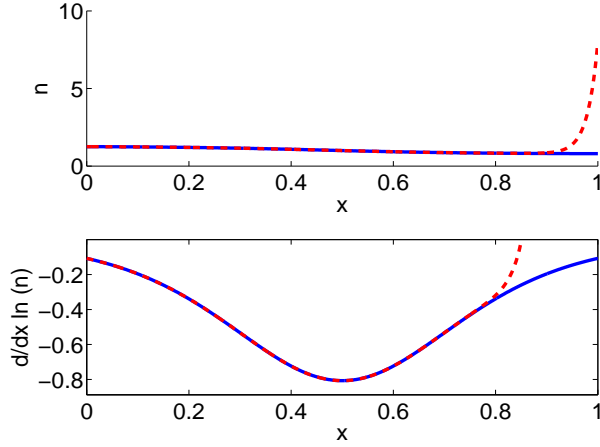


Figure 4.8: Shielding of density near the edge for typical density profiles with $a/L_{nsh} = 9.0$ and $\Delta_{nsh} = 0.02$. x is the radial coordinate.

With:

$$\tilde{n}_0(\psi) = \tilde{n}_0(s) = n_0(s)n_{sh}(s) \quad (4.142)$$

$$n_{sh}(s) = 1 + \frac{a}{L_{nsh}} \frac{\sinh\left(\frac{s-s_{f,\min}}{\Delta_{nsh}(s_{f,\max}-s_{f,\min})}\right)}{\sinh\left(\frac{1}{\Delta_{nsh}}\right)} \quad (4.143)$$

L_{nsh} and Δ_{nsh} are input parameters, and $s_{f,\min}$, $s_{f,\max}$ are the radial boundaries of the plasma. An example of the shielding factor is given in Fig. 4.8. The shielding profile is 1 except near the plasma edge (this is controlled by the input parameter Δ_{nsh}). This model becomes questionable if the turbulence reaches the edge. For a small but finite Δ_{nsh} , the gradient is slightly modified at the axis, and becomes very large at the edge. This modification of the density can be viewed as a change of the dielectric constant near the plasma edge. By artificially increasing the density in this region, the electric potential will have a much weaker response to a numerical increase of the density. This modification still enables the global energy conservation of the system (see Section 3.7).

4.6 Temperature and density profiles

Three different temperature profiles have been used during this work, which will be named profiles 1,2,3. Examples for typical parameters are given in Figs. (4.9), (4.10) and (4.11).

4.6.1 Profile 1

$$\frac{1}{T_i} \frac{dT_i}{d\tilde{\psi}} = K_{T_i} \left\{ \cosh^{-2} \left(\frac{s - s_{0i}}{\Delta_{T_i}} \right) - \cosh^{-2} \left(\frac{s_{0i}}{\Delta_{T_i}} \right) \right\} \quad (4.144)$$

$$K_{T_i} = -\frac{a}{L_{T_i} \left(1 - \cosh^{-2} \left(\frac{s_{0i}}{\Delta_{T_i}} \right) \right)} \quad (4.145)$$

and $\tilde{\psi} = \psi/\psi_{\text{edge}}$. L_{T_i} , Δ_{T_i} and s_{0i} are input parameters. After integration:

$$\begin{aligned} \frac{T_i(s)}{T_i(s_{0i})} = & \left[\cosh \left(\frac{s - s_{0i}}{\Delta_{T_i}} \right) \right]^{-2K_{T_i}\Delta_{T_i}^2} \exp \left[K_{T_i} \cosh^{-2} \left(\frac{s_{0i}}{\Delta_{T_i}} \right) (s^2 - s_{0i}^2) \right. \\ & \left. + 2K_{T_i}\Delta_{T_i}s \tanh \left(\frac{s - s_{0i}}{\Delta_{T_i}} \right) \right] \end{aligned} \quad (4.146)$$

The density profile is defined in a similar way with input parameters L_n , s_{0i} and Δ_n and the electron temperature profile with L_{Te} , Δ_{Te} , s_{0e} . The density profile is normalized with the volume-averaged density. These profiles are such that the gradient is 0 at axis.

4.6.2 Profile 2

$$\frac{d \ln T(\tilde{\rho})}{d\tilde{\rho}} = -\frac{a}{L_{T_i}} \cosh^{-2} \left(\frac{\tilde{\rho} - \tilde{\rho}_{0i}}{\Delta_{T_i}} \right) \quad (4.147)$$

where $\tilde{\rho} = \rho/a$ and $\tilde{\rho}_{0i}$ is an input parameter. After integration:

$$\frac{T(\tilde{\rho})}{T(\tilde{\rho}_{0i})} = \exp \left[-\frac{a\Delta_{T_i}}{L_{T_i}} \tanh \left(\frac{\tilde{\rho} - \tilde{\rho}_{0i}}{\Delta_{T_i}} \right) \right] \quad (4.148)$$

Profiles 2 are useful for benchmarks because many gyrokinetic codes use ρ as radial coordinate. For MHD equilibria, profiles 2 are not defined.

4.6.3 Profile 3

$$\frac{1}{T_i(\tilde{\rho})} \frac{dT_i}{d\tilde{\rho}} = -\frac{a}{2L_{T,i}} \left[\tanh \left(\frac{\tilde{\rho} - \tilde{\rho}_{0i} + \Delta\tilde{\rho}}{\Delta_{T_i}} \right) - \tanh \left(\frac{\tilde{\rho} - \tilde{\rho}_{0i} - \Delta\tilde{\rho}}{\Delta_{T_i}} \right) \right] \quad (4.149)$$

Where $\Delta\tilde{\rho}$ is an input parameter. After integration:

$$\frac{T_i(\tilde{\rho})}{T_i(\tilde{\rho}_{0i})} = \exp \left\{ -\frac{a\Delta_{T_i}}{2L_{T,i}} \ln \left[\frac{\cosh \left(\frac{\tilde{\rho} - \tilde{\rho}_{0i} + \Delta\tilde{\rho}}{\Delta_{T_i}} \right)}{\cosh \left(\frac{\tilde{\rho} - \tilde{\rho}_{0i} - \Delta\tilde{\rho}}{\Delta_{T_i}} \right)} \right] \right\} \quad (4.150)$$

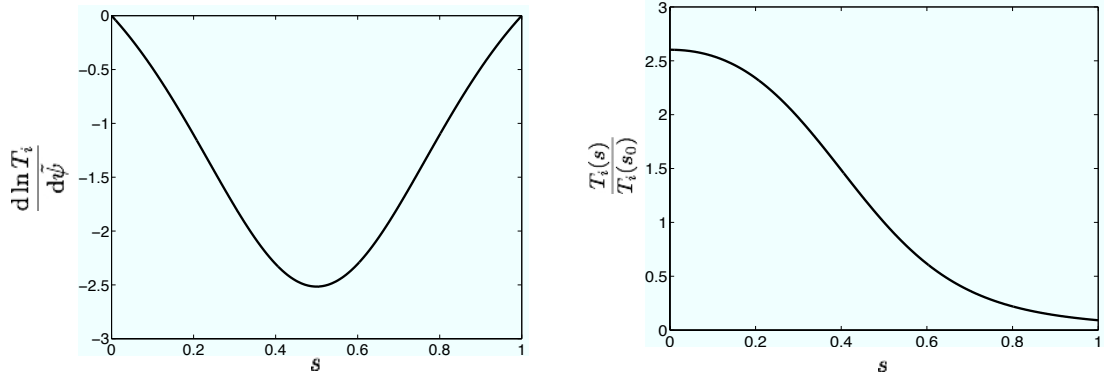


Figure 4.9: Profiles 1, Eqs. (4.144) and (4.146) for $\frac{a}{L_{Ti}} = 2.516$, $\Delta_{Ti} = 0.3$ and $s_0 = 0.5$.

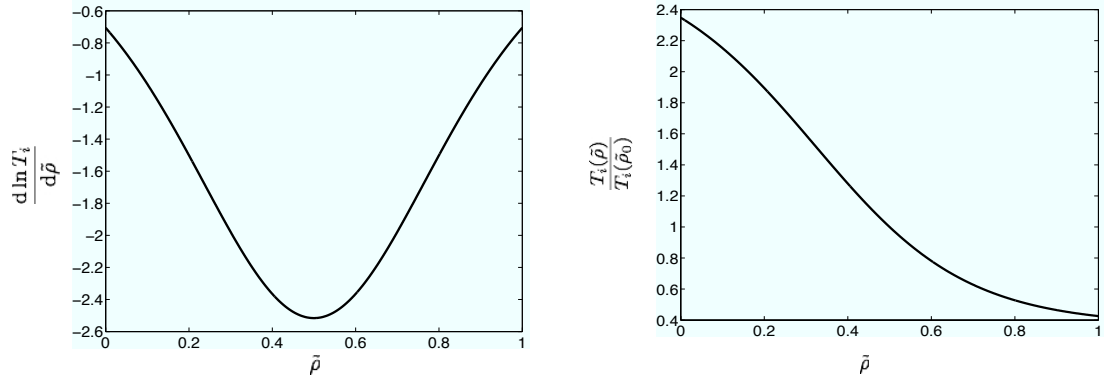


Figure 4.10: Profiles 2, Eqs. (4.147) and (4.148) for $\frac{a}{L_{Ti}} = 2.516$, $\Delta_{Ti} = 0.3$ and $\tilde{\rho}_0 = 0.5$.

Profiles 3 are not very convenient for linear simulations: there can be a wide region where the gradients are high. It is impossible to know in advance where the most unstable linear mode will grow. In fact, beatings are observed with such profiles as many linear modes grow together. Very long simulations might be needed until the most unstable mode emerges from the simulation.

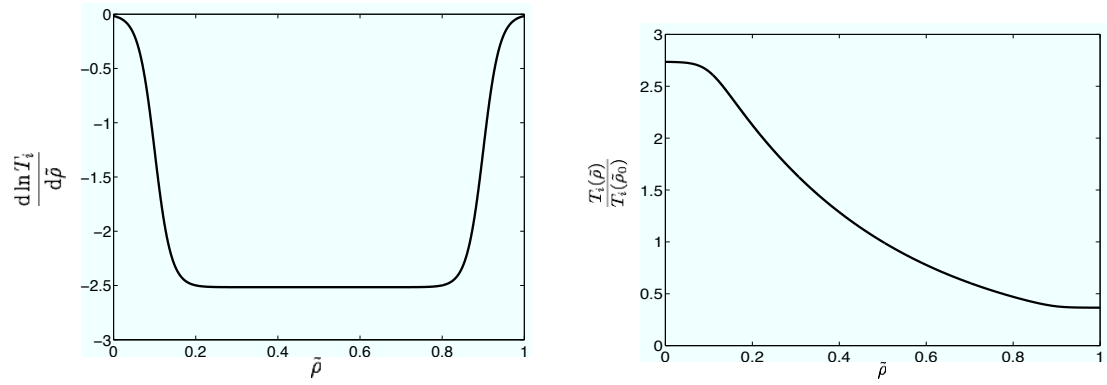


Figure 4.11: Profiles 3, Eqs. (4.149) and (4.150) for $\frac{a}{L_{T_i}} = 2.516$, $\Delta_{T_i} = 0.04$, $\Delta \tilde{\rho} = 0.4$ and $\tilde{\rho}_0 = 0.5$.

Chapter 5

Code validation

5.1 Description of typical runs

In this Section, the basic physics of linear and nonlinear runs is presented. During the initialization phase of a simulation, the code computes the magnetic equilibrium, the finite element matrices, loads the initial attributes of markers and computes the initial electrostatic potential. Then the main temporal loop of the code is the following: the weight and the phase space coordinates of the markers are pushed with the Runge-Kutta integrator. At each sub-step, parallel computations are needed to send the tracers to their corresponding processors due to toroidal motion. Then a charge assignment is performed to obtain the perturbed density and through the quasineutrality equation the corresponding electrostatic potential is obtained. From the latter, the electric field acting on each marker can be computed. It is then used for the phase space attributes and the weights pushing. After each time step, the boundary conditions, the Krook and heating operators are applied. This loop is then repeated until the given number of time steps is reached.

The ORB5 code can be run in *linear mode*. The Vlasov equation then reads:

$$\frac{d\delta f}{dt}\Big|_0 + \underbrace{\frac{d\delta f}{dt}\Big|_1}_{\text{neglected}} = - \underbrace{\frac{df_0}{dt}\Big|_0}_{\equiv 0} - \frac{df_0}{dt}\Big|_1 \quad (5.1)$$

Concretely, it means that the nonlinear terms in the trajectories, i.e. terms containing the electric field are not retained. It implies that the distribution function f is *not* conserved for a linear simulation and there is no energy conservation relation (see Section 3.7).

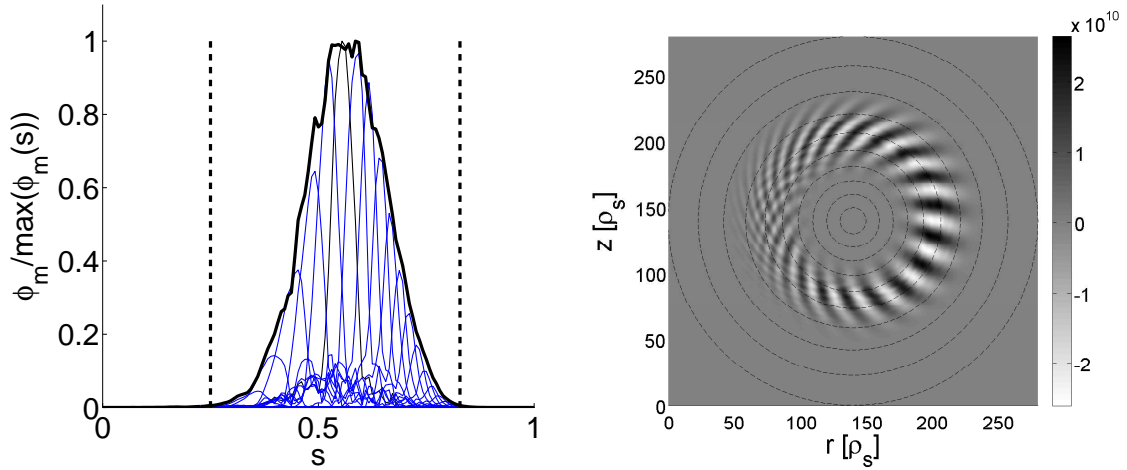


Figure 5.1: Typical $\phi_m(s)$, normalized to the maximum component (left) and poloidal section of the potential (right) for a typical toroidal-ITG simulation.

However, one can compute the power transfer from the particles to the electric field and so Eq. (3.84) can be checked numerically:

$$-\frac{1}{V} \frac{dE_k}{dt} = \frac{1}{V} \int q_i \delta f_i \frac{d\vec{R}}{dt} \cdot \langle \vec{E} \rangle B_{\parallel}^* dv_{\parallel} d\mu d\alpha = \frac{1}{N} \sum_{r=1}^N q_i w_r \Omega_r \left(\frac{d\vec{R}}{dt} \cdot \langle \vec{E} \rangle \right)_{\vec{R}_r, \mu_r, v_{\parallel r}} \quad (5.2)$$

$$\frac{1}{V} \frac{dE_f}{dt} = \frac{1}{V} \frac{d}{dt} \frac{q_i}{2} \int d\vec{x} \delta n_i(\vec{x}, t) \phi(\vec{x}, t) = \frac{1}{V} \frac{d}{dt} \sum_{\mu} \phi_{\mu} b_{\mu} \quad (5.3)$$

where the time derivative of E_f is computed numerically.

Initially, markers a small density perturbation is given to the markers, yielding a small electric field. As the tracers move along their unperturbed trajectory, their weight is modified according to the Vlasov equation, changing the density, the electric potential and the electric field. Depending on the profile gradients, either no instability will develop and the simulation will be stable, or an instability will develop, preferably in the LFS region for toroidal ITG modes. There can be several unstable modes. However, ORB5 is an initial value code so the most unstable mode will inevitably emerge and will dominate. In linear mode, only one toroidal mode is usually evolved, the rest being Fourier filtered. The resulting potential is a superposition of poloidal modes $\phi_m(s)$, giving for e.g. toroidal ITG ballooning-like structure in real space (see Fig. 5.1). The growth rate (local or global) and the real frequency (local) can be extracted. The growth rate can be decomposed in several parts by expliciting the $d\vec{R}/dt$ term in Eq. (5.2) from Eq. (3.23), $\gamma = \gamma_{\parallel} + \gamma_{\nabla B} + \gamma_{\text{curv}} + \gamma_{\nabla p}$ (see Fig. 5.2). On this figure, the ∇B -drift is the higher destabilizing component, showing

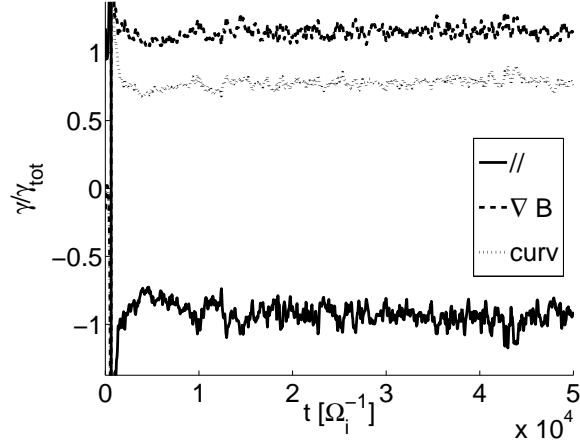


Figure 5.2: Growth rate fraction of different components for a typical toroidal-ITG simulation (usually $\gamma_{\nabla p}$ is very small and has not been inserted in this figure).

the toroidal character of the instability. The parallel component, describing mostly the Landau damping, is stabilizing. Linear simulations generally require less markers because there are less Fourier modes to solve compared to a nonlinear simulation.

Nonlinear physics is much more complex. In this case, the trajectories depend on the electric field and in particular the $\vec{E} \times \vec{B}$ drift. At the beginning of the simulation, the electric field is very small and so nonlinear effects are weak. The simulation starts with a *linear phase*. The exponentially growing instability generates a mainly poloidal and toroidal electric field. The resulting $\vec{E} \times \vec{B}$ drift will mainly be radial, $\nabla s \cdot \vec{v}_{\vec{E} \times \vec{B}} \sim E_{\theta} B_{\varphi}$. A radial electric field, corresponding to the $(0, 0)$ zonal flow is excited nonlinearly by ITG modes. The zonal flows are generated by the turbulence itself and are purely nonlinear effects. Zonal flows are linearly stable because the driving term $\propto \langle \vec{E} \rangle \times \vec{B} \cdot \nabla \Upsilon$ in the Vlasov equation is extremely small for a radial perturbation: it does not causes any radial $\vec{E} \times \vec{B}$ motion and, because the gradients are radial, there is no energy channel for the particles. After the linear phase, the simulation will *saturate*. This can be seen in the field energy of the toroidal modes, left plot of Fig. 5.3. For ITG turbulence, the main saturation mechanism is the $\vec{E} \times \vec{B}$ shearing of the eddies (see Fig. 5.3). The radial electric field generates a poloidal drift velocity via $\nabla \theta_* \cdot \vec{v}_{\vec{E} \times \vec{B}} \sim E_s B_{\varphi}$ which depends on the radial position of the plasma. If the electric field has a sufficiently high radial derivative, the eddies will be sheared by the zonal-flow induced poloidal rotation and the ITG turbulence will be suppressed. Mathematically, the turbulence suppression through $\vec{E} \times \vec{B}$ shearing

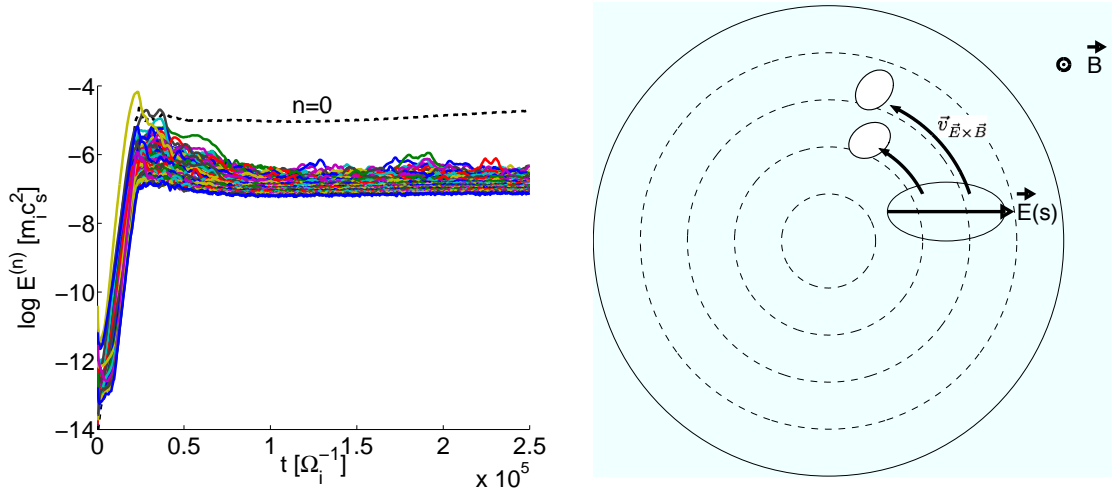


Figure 5.3: Left: temporal evolution of the field energy of toroidal modes in logarithmic scale for a typical ITG simulation. The dashed line is the $n = 0$ mode. Right: basic mechanism of $E \times B$ shearing.

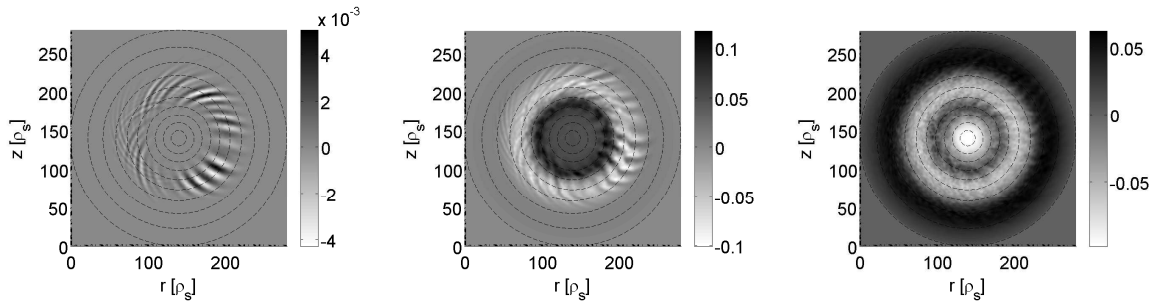


Figure 5.4: Poloidal section of the potential in the linear phase (left), at the beginning of the nonlinear phase (middle) and in the end of the nonlinear phase (right) for a typical ITG simulation.

is expressed via the *shearing rate criterion* [92, 93]:

$$\gamma \gtrsim \omega_s = \left| \frac{\Delta\psi}{\Delta\varphi} \frac{\partial^2 \phi_0(\psi)}{\partial \psi^2} \right| \quad (5.4)$$

Where $\Delta\psi/(R_0 B_\theta)$ and $R_0 \Delta\varphi$ are the correlation length of the ambient turbulence in the radial and toroidal directions. This criterion has been further extended to time dependent $\vec{E} \times \vec{B}$ flows [94].

Typical poloidal sections of the potential are displayed on Fig. 5.4. During the whole simulation, the numerical particles transport heat, measured by the volume-averaged *heat*

flux:

$$Q = \frac{1}{V} \int \delta f_i \frac{1}{2} m_i v^2 \frac{\langle \vec{E} \rangle \times \vec{B}}{B B_{\parallel}^*} \cdot \frac{\nabla \psi}{|\nabla \psi|} B_{\parallel}^* d\vec{R} dv_{\parallel} d\mu d\alpha \quad (5.5)$$

Other fluxes can be measured such as the particle and the momentum fluxes, but this work will focus on heat transport only. After the saturation, the system undergoes a transient phase, consisting of local bursts. These bursts locally decrease the temperature gradient: the heat transport leads to *profile relaxation*. A measure of the transport is given by the *heat diffusivity*:

$$\chi_i = \frac{Q}{n_i |\nabla T_i|} \quad (5.6)$$

As it is defined, the heat flux and so the heat diffusivity could be in principle negative, meaning that the heat flows inward. The χ_i is often normalized to the gyro-Bohm transport coefficient [95]:

$$\chi_{GB} = \frac{\rho_s^2 c_s}{a} \quad (5.7)$$

Because there is no mechanism to restore the distribution function towards the initial Maxwellian, the temperature gradient relaxes towards a critical value for which ITG modes are stable. There is a linear *critical gradient* value, $R_0/L_{Ti} \sim 4 - 5$ and a non-linear critical gradient value which is generally higher. In a famous paper by Rosenbluth and Hinton [72], it is shown that linear collisionless processes do not completely damp the radial zonal flow component of the potential. This residual zonal flow suppresses turbulence which implies that the critical gradient is nonlinearly shifted to a higher value, $R_0/L_{Ti} \sim 6$. This phenomena is called the *Dimits shift* [90]. Typical time evolutions of R_0/L_{Ti} and χ_i/χ_{GB} are shown on Fig. 5.5.

In toroidal geometry, the poloidal coupling induced by the Jacobian transfers energy from the $n = 0, m = 0$ zonal flow mode to the $n = 0, m = \pm 1$ modes, called the *Geodesic Acoustic Modes* (GAMs) [96]. These modes have $k_{\parallel} \neq 0$ and are therefore Landau damped. The GAMs have a finite real frequency and their oscillating nature makes the zonal flow shear less efficient to suppress turbulence [92]. The decaying rate of these modes is proportional to $\exp -q^2$; in general they are present in the edge of the plasma where the safety factor is large. Typical GAMs are shown as vertical quasi-periodic strips on the top part ($s > 0.7$) of Fig. 5.6.

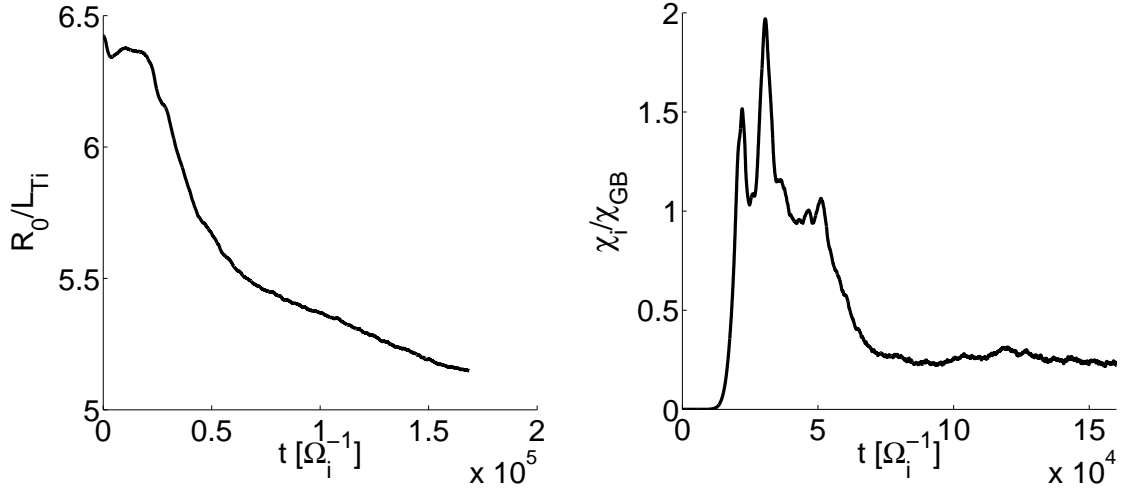


Figure 5.5: Typical time evolution of R_0/L_{Ti} (left) and χ_i/χ_{GB} (right), radially averaged between $\rho = 0.3a$ and $\rho = 0.7a$, in the case of a decaying simulation.

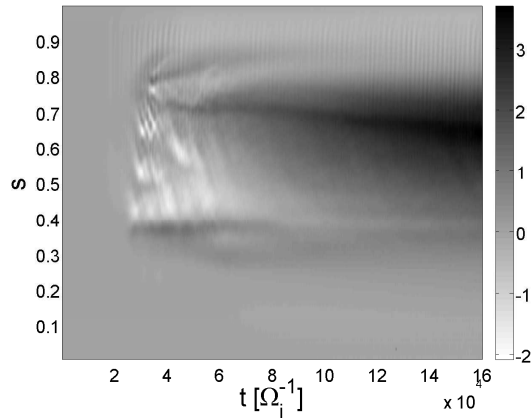


Figure 5.6: $\nabla \bar{\phi}$ as a function of (s, t) for a typical ITG simulation.

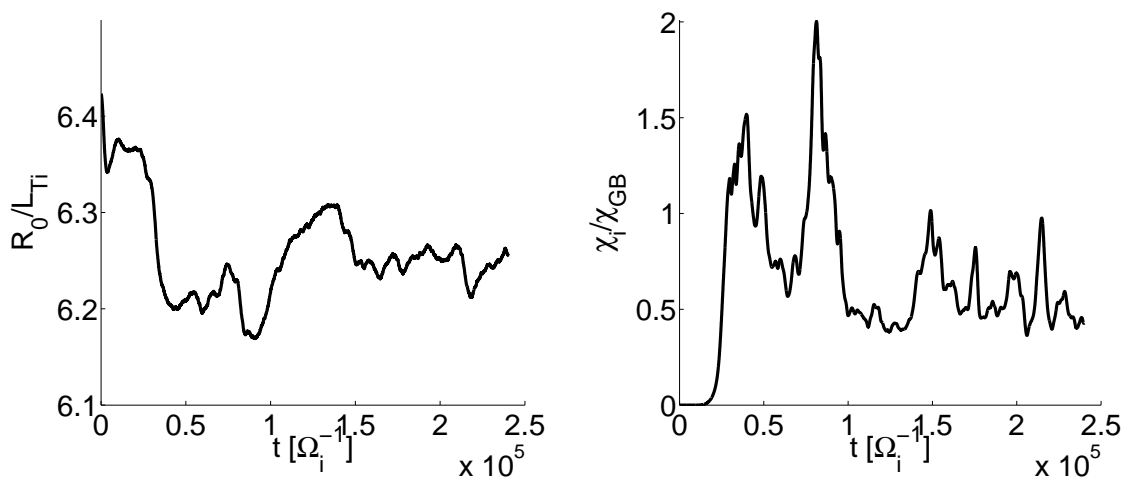


Figure 5.7: Typical time evolution of R_0/L_{Ti} (left) and χ_i/χ_{GB} (right), radially averaged between $\rho = 0.25a$ and $\rho = 0.75a$, for the case of a heated simulation.

The main problem associated with nonlinear PIC simulations is the generation of numerical noise. If the noise is not carefully diagnosed, the transport levels can be purely numerical. In ORB5, the signal to noise ratio is greatly improved by using the noise control operator (see Section 3.8). The use of the noise control and/or the heating operator heats the plasma and therefore maintains the temperature gradient above its nonlinear critical value. In this situation the turbulence does not fade away, but exhibits an endless series of bursts. This is represented on Fig. 5.7.

5.2 Scalability

This Section presents the performance of the code parallelization described in Section 4.4. To measure the scalability, short CYCLONE simulations were performed on the BG/L cluster of the Ecole Polytechnique Fédérale de Lausanne. This cluster contains 4096 nodes that can be used with one processor and 512 Mb of memory (CO mode) or 2 processors with 256 Mb of memory each (VN mode). The grid size is fixed ($N_s = 128, N_{\theta_*} = 256, N_\varphi = 512$ for the VN mode and $N_s = 128, N_{\theta_*} = 256, N_\phi = 256$ for the CO mode). The ScaLAPACK parallel solver with 16 clones is employed. Simulations with 512, 1024, 2048 and 4096 processors have been made by varying the number of processors in the φ direction P_φ . In the VN mode, simulations with 8K, 16K, 32K, 64K, 128K and 256K markers per processor have been done. In the CO mode, because more memory

is available, simulations have been done with $64K$, $128K$, $256K$, $512K$, $1M$ and $1.5M$ markers per processor. Thus, for the VN mode, the total number of markers goes from $2^{22} \cong 4M$ up to $2^{31} \cong 2G$, whereas in the CO mode it goes from $2^{25} \cong 32M$ up to $1.5 \cdot 2^{32} \cong 6.4G$.

Since the size of the matrix is fixed, the time dedicated to the solver (backsolve and Fourier transforms) should be proportional to the number of toroidal slices per processor. The time dedicated for the particles (pushing + charge assignment) is assumed to scale linearly with the number of markers per processor. Finally, the communication time is mainly due to the φ -partition of the markers. It is hard to give a simple estimate for the communication time, since it depends on the time step, the cluster architecture and the ion temperature. For the largest simulation done ($1.5M$ markers/processor), the communication time represents 10% of the total simulation time. Therefore, the time per iteration is modeled as:

$$t_{\text{it}}^f = \underbrace{K_s \frac{N_\varphi P_c}{P}}_{\text{solver}} + \underbrace{K_m \frac{N}{P}}_{\text{markers}} + \underbrace{t_{\text{comm}}}_{\text{communication}} \quad (5.8)$$

where K_s and K_m are constant to be determined. Fig. 5.8 displays the time per iteration t_{it} as a function of the number of markers per processor N/P . The dependence is linear, as expected. However, the slope of these fits, namely K_m seems to slowly increase with P , which illustrates a slight deviation from a non ideal scaling. In fact, a super-scaling can be observed from Fig. 5.8: for a fixed number of markers per processor, the time per iteration decreases when the number of processors increases. This is because P is increased by keeping P_C fixed, and so according to Eq. (5.8) the time per iteration dedicated to the solver decreases. Constants K_s and K_m have been obtained by a linear fit of t_{it} as a function of N/P at fixed $P = 512$. Therefore, the measured time per iteration can further be compared to the fitted time t_{it}^f . Fig. 5.9 shows the ratio $t_{\text{it}}/t_{\text{it}}^f$ as a function of P . The maximum value of the relative degradation due to the increase of the number of processors is only 12%. Effects of t_{comm} can be included by fitting $t_{\text{it}} - t_{\text{comm}}$ instead of t_{it} . In that case, the maximum relative degradation falls down to 10%.

Globally, these results show the excellent scaling properties of ORB5 up to 4096 processors, summarized on Fig. 5.10. The speedup at $P = 4096$ is 3.8, i.e. the degradation of the speedup is only 5%.

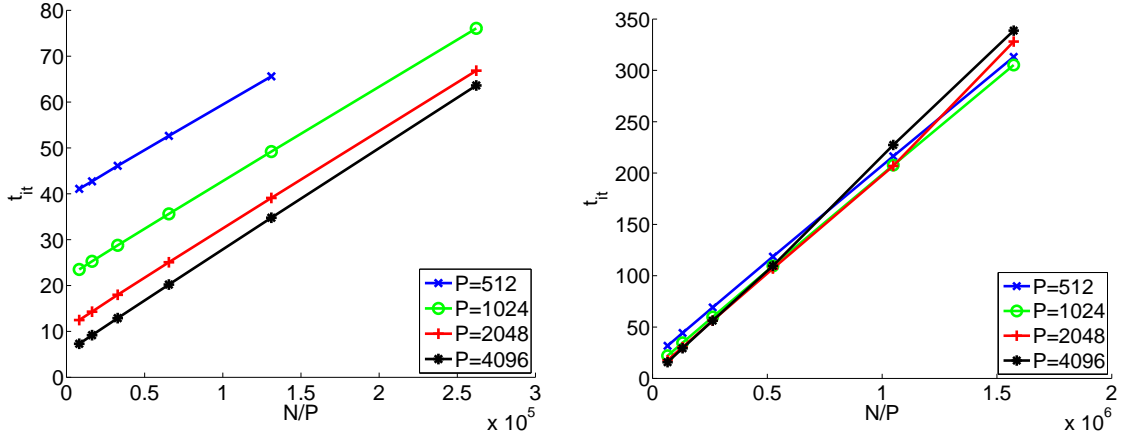


Figure 5.8: Time per iteration as a function of N/P for the VN mode (left) and the CO mode (right).

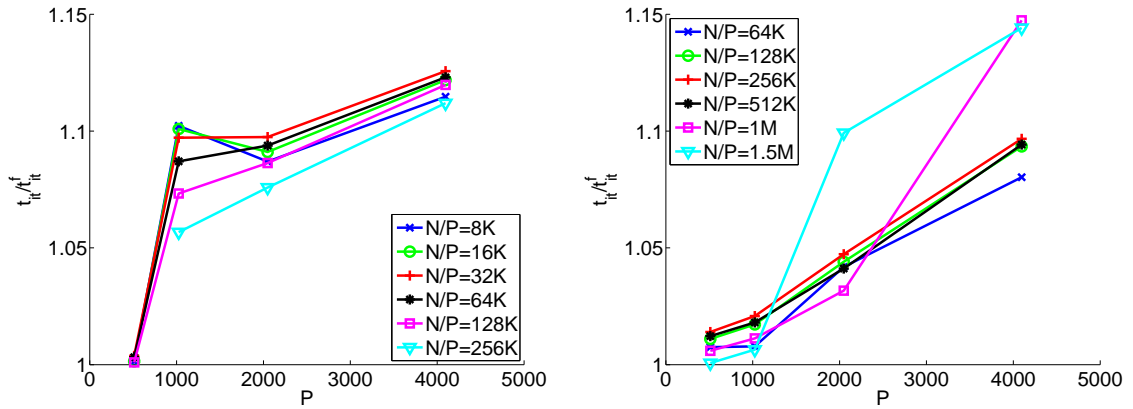


Figure 5.9: t_{it}/t_{it}^f as a function of P for the VN mode (left) and the CO mode (right).

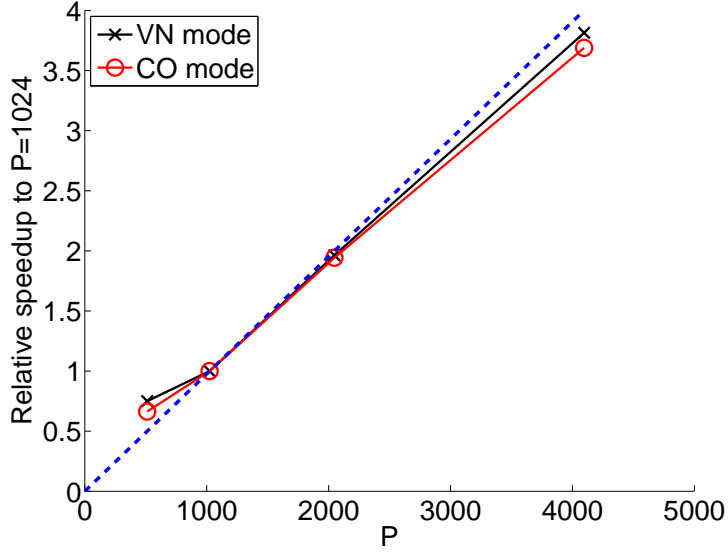


Figure 5.10: Speedup (relative to $P=1024$) as a function of P for a fixed number of markers for the VN mode (black, crosses) and the CO mode (red, circles) compared to an ideal scaling (blue, dashed line).

5.3 The field-aligned filter

The field-aligned filter has been tested with the following input parameters: $m_i = m_p$, $a = 40\rho^*$, $B_0 = 1$ [T], $R_0 = 1$ [m], $R_0/a = 5$. The density profile is flat, profiles 1 (Eqs. (4.144) and (4.146)) have been used with $T_i = T_e$, $R_0/L_{Ti} = 12$, $\Delta_{Ti} = 0.208$, $s_0 = 0.5$ and $\Delta t = 40 \Omega_i^{-1}$. $N = 2^{24} \cong 16$ M markers unless specified otherwise. The initial distribution f_0 is a canonical maxwellian with correction. δf is obtained through the conventional δf scheme and is initialized with white noise. The quasineutrality equation is solved with cubic B-splines on a $N_s = 128$, $N_{\theta_*} = 128$, $N_\varphi = 64$ grid with the parallel direct solver. Fig. 5.11 displays the volume-averaged radial heat flux Q for field-aligned and rectangular simulations. The simulation starts with the linear phase, in which the perturbation grows exponentially. Then nonlinear effects become important and saturation occurs. A transient phase consisting of avalanches and bursts occurs, while the turbulence further decays and the system finally evolves towards a quasi-steady state in which the gradients are relaxed and there is a vanishing perpendicular transport. In Fig. 5.11, for the simulation with the rectangular filter, a numerical heat flux develops in the late nonlinear phase. This kind of phenomenon is typical when too few markers are used. A good indicator of the

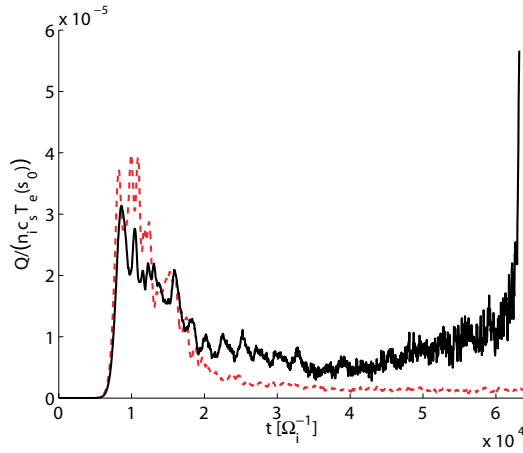


Figure 5.11: Volume-averaged radial heat flux for a rectangular filter simulation (black, solid) and a field-aligned simulation (red, dashed) with $\Delta m = 7$, keeping all other physical and numerical parameters fixed.

quality of a simulation is the energy conservation described by Eq. (3.84). Fig. 5.12 shows the relative energy conservation $\Delta E/E(t_0)$, where $\Delta E = E_{\text{kin}}(t) + E_f(t) - E_{\text{kin}}(t_0) - E_f(t_0)$ for simulations with rectangular and field-aligned filters. In a noise-free simulation, or equivalently in the limit of an infinite numerical accuracy, $\Delta E/E_f$ should be zero. By looking simultaneously at Figs. 5.11 and 5.12, one sees that the energy conservation for the rectangular filter simulation starts to degrade after the top of the overshoot, when nonlinear effects become important. During the burst phase (from $t = 0.8 \cdot 10^4 \Omega_i^{-1}$ to $t = 3 \cdot 10^4 \Omega_i^{-1}$), the energy deviation increases and reaches 1% of the total plasma energy, which is an unacceptable value. From $t = 3 \cdot 10^4 \Omega_i^{-1}$ to the end of the simulation, the system should reach a quasi-steady state but both the heat flux and the energy deviation continue to grow: at the next time step, the simulation explodes due to an unphysical electric field pushing some particles completely out of the simulation domain. On the other hand, a gain of two orders of magnitude in the relative energy conservation is obtained as the filter goes from rectangular to field-aligned: in this case, the relative energy conservation does not exceed 10^{-4} . However, the energy deviation is of the order of the field energy of the system so a good simulation in terms of energy conservation should have $|\Delta E(t)| < \epsilon_E E_f(t)$ in the nonlinear phase, with $\epsilon_E \ll 1$. Simulations presented in this Section have a large ρ^* which implies a very fast relaxation. It is indeed difficult to obtain good energy conservation for these parameters. The origin of the unphysical

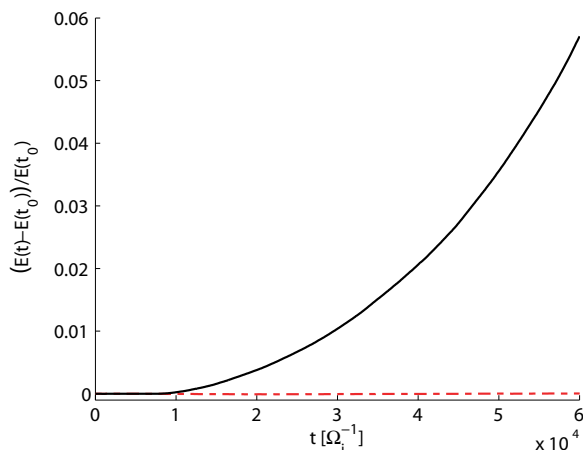


Figure 5.12: Relative energy conservation for a rectangular filter simulation (black, solid) and a field-aligned simulation (red, dashed) with $\Delta m = 7$, keeping all other physical and numerical parameters fixed.

behaviour observed on Fig. 5.11 can be observed on the left plot of Fig. 5.13: the energy of all toroidal modes is growing in time. However, for the field-aligned filter, the energy of $n \neq 0$ modes is constant for late times (see right plot of Fig. 5.13). On Fig. 5.14, the radially averaged energy spectrum of the $n = 6$ mode in the poloidal space, normalized to its maximum m component, is shown at different times for a rectangular filter simulation. In the linear phase, the mode is peaked near $m = -12 = -nq(s_0)$ as $n = 6$ and $q(s_0) = 2$. After the saturation, the peak energy becomes smaller but the spectrum broadens: it is no longer peaked and m components which are far away from $nq(s_0)$ contain a very significant part of the total toroidal mode energy. This causes the field energy of all $n \neq 0$ modes to grow in time: it is a clear evidence that numerical noise is created because of high k_{\parallel} modes. The bad quality of the rectangular filter can also be observed in Fig. 5.15 (left), which shows the electrostatic potential on a magnetic surface. The resulting structure is clearly a superposition of high k_{\parallel} modes, whereas the field-aligned (right) filter naturally preserves the field-aligned structure of ITG modes.

These results show that a field-aligned filter instead of a rectangular one must be employed in ORB5, but it is still crucial to show how to fix the width Δm , and more important to show that this filter will contain all the relevant modes of the system. As the field-aligned filter acts locally on a magnetic surface, a look on the local poloidal energy spectrum is necessary. It must be checked that no physically relevant poloidal

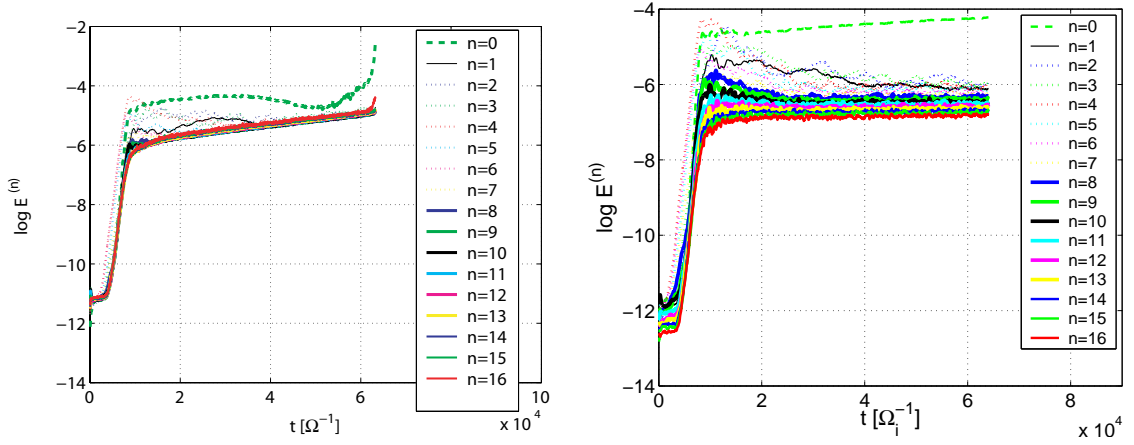


Figure 5.13: Energy of toroidal modes for a rectangular filter simulation (left) and a field-aligned filter with $\Delta m = 7$ (right). Dashed line is the $n = 0$ mode.

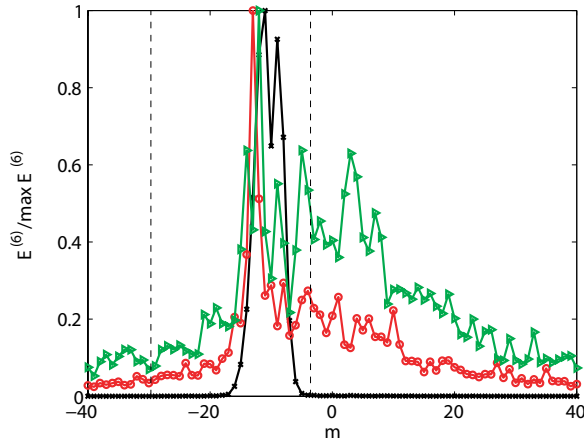


Figure 5.14: Radially averaged poloidal spectrum of energy for toroidal mode $n = 6$, normalized to the largest component, at time $t = 0.8 \cdot 10^4 \Omega_i^{-1}$ (linear phase, black, crosses), $t = 2.4 \cdot 10^4 \Omega_i^{-1}$ (red, circles) and $t = 4.8 \cdot 10^4 \Omega_i^{-1}$ (green, triangles) for a rectangular filter simulation. Dashed lines show $-nq_{\text{axis}} + \Delta m$ and $-nq_{\text{edge}} - \Delta m$.

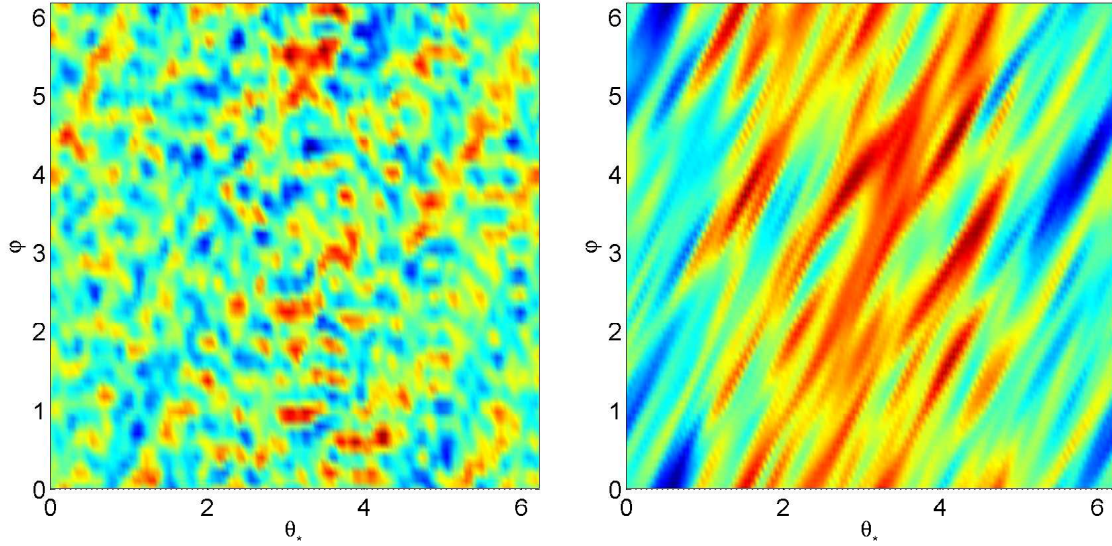


Figure 5.15: Perturbed electric potential along $s_0 = 0.5$ at $t = 5 \cdot 10^4 \Omega_i^{-1}$ in the (θ_*, φ) plane for a rectangular filter (left) and a diagonal filter with $\Delta m = 4$ (right). All other physical and numerical parameters are fixed.

harmonics are locally removed from the simulation. A too small value of Δm will obviously cut some relevant physics, whereas a too large Δm quickly introduces additional numerical noise. A necessary but not sufficient condition to fix Δm is to converge the growth rate of toroidal modes in the linear phase. Fig. 5.16 shows the evolution of the field energy of the mode $n = 6$ for a field-aligned filter with different values of Δm and a rectangular filter. Small Δm cases yield lower growth rates and linear convergence is reached with $\Delta m = 5$. A careful look at the local energy spectrum during the nonlinear phase is still needed, in order to account for a possible broadening of the spectrum. The problem is that for late times, numerical noise also grows inside the field-aligned filter and it becomes hard to separate the physical signal from the noise. The idea to overcome this difficulty is to identify the noisy components of the local energy spectrum by choosing a larger Δm and by varying the number of markers. Fig. 5.17 shows the local energy spectrum, averaged between $t = 1.5 \cdot 10^4 \Omega_i^{-1}$ and $t = 2.4 \cdot 10^4 \Omega_i^{-1}$, of the mode $n = 6$ for two simulations with $\Delta m = 15$ but with 16 M and 67 M markers. In both cases, two noise plateaus are visible near the edges of the filter, where high k_{\parallel} modes are present. The plateau corresponding to the 67 M markers case is lower but the central parts of both spectrums are very similar. Therefore, from Fig. 5.17 one can conclude that $\Delta m = 9$

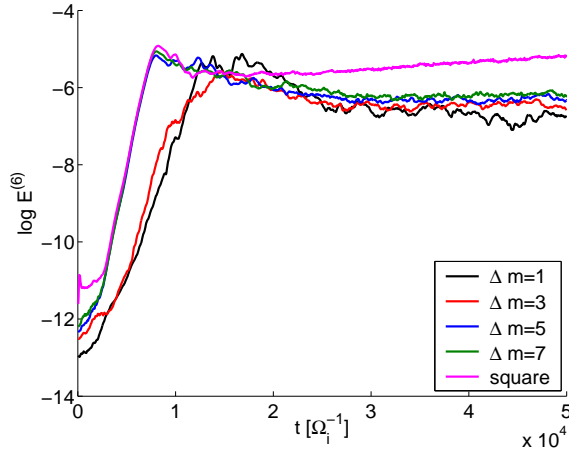


Figure 5.16: Field energy of the $n = 6$ mode for a field-aligned filter with different values of Δm and a rectangular filter.

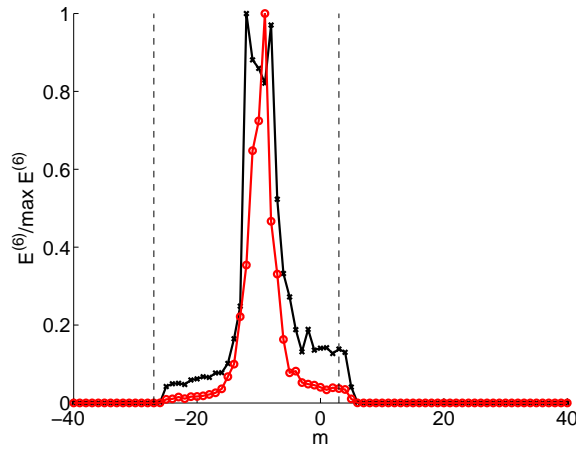


Figure 5.17: Local poloidal spectrum of energy for toroidal mode $n = 6$ at $s = s_0 = 0.5$, normalized to the largest component, for a simulation with 16 M markers (black, crosses) and 67 M markers (red, circles). Both simulations have a field-aligned filter with $\Delta m = 15$. The spectrum is averaged between $t = 1.5 \cdot 10^4 \Omega_i^{-1}$ and $t = 2.4 \cdot 10^4 \Omega_i^{-1}$. The vertical dashed lines show $-nq(s_0) \pm 15$.

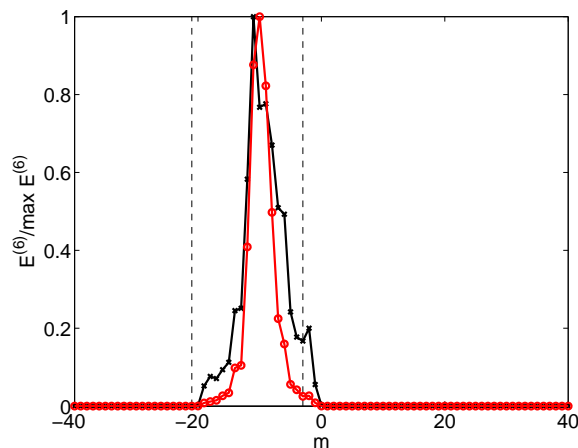


Figure 5.18: Local poloidal spectrum of energy for toroidal mode $n = 6$ at $s = s_0 = 0.5$, normalized to the largest component, for a simulation with 16 M markers (left, crosses) and 67 M markers (red, circles). Both simulations have a field-aligned filter with $\Delta m = 9$. The spectrum is averaged between $t = 1.5 \cdot 10^4 \Omega_i^{-1}$ and $t = 2.4 \cdot 10^4 \Omega_i^{-1}$. The vertical dashed lines show $-nq(s_0) \pm 9$.

is a reasonable value. Fig. 5.18 shows that for a sufficiently high number of markers a field-aligned filter with $\Delta m = 9$ will contain all the locally relevant poloidal modes. The same conclusion can be drawn from Fig. 5.19 for the global energy spectrum. Note that it has also been checked that changing the averaging times of the spectrum does not modify this conclusion. Finally, Fig. 5.20 shows the radial heat flux as a function of Δm for simulations with constant noise, in the sense that the number of markers per Fourier mode is kept constant [76]. One sees that $\Delta m = 9$ is a reasonable value and that using a large Δm does not modify the final state of the system but requires a higher number of markers.

The value of Δm fixes the maximal k_{\parallel} wave number in the simulation. This value can be compared to the maximal k_{\parallel} wave number allowed in an Eulerian gyrokinetic simulation with field-aligned coordinates. The field-aligned coordinate $\alpha = \varphi - \theta_*/q(s)$ usually describes one connection length $L_{\alpha} = 2\pi q(s)R_0$. N_{α} grid points are employed. Four points per wavelength is a reasonable accuracy, thus wavelengths up to $4L_{\alpha}/N_{\alpha}$ will be correctly resolved. Usual resolution in the parallel direction is $N_{\alpha} = 16 \sim 32$, which means that the maximal parallel wave number that is accurately solved is $4/qR_0 \sim 8/qR_0$, corresponding

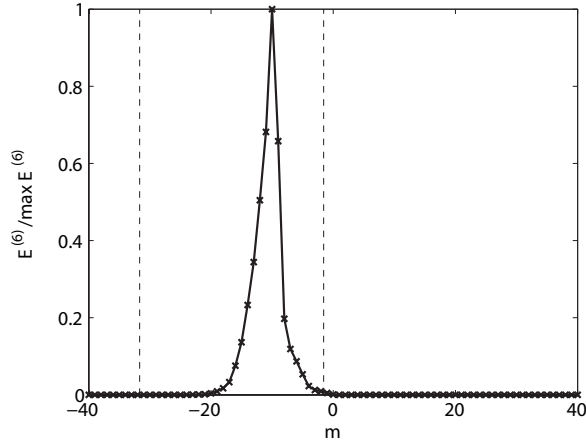


Figure 5.19: Global poloidal spectrum of energy for toroidal mode $n = 6$, normalized to the largest component, for a simulation with 67 M markers. and a field-aligned filter with $\Delta m = 9$. The spectrum is averaged between $t = 1.5 \cdot 10^4 \Omega_i^{-1}$ and $t = 2.4 \cdot 10^4 \Omega_i^{-1}$. The vertical dashed lines show $-nq_{\text{axis}} + \Delta m$ and $-nq_{\text{edge}} - \Delta m$.

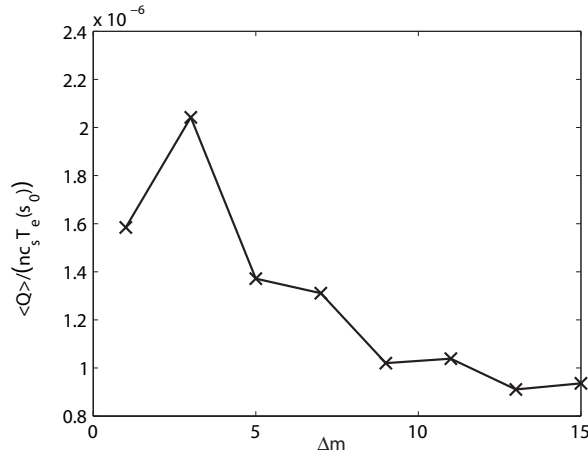


Figure 5.20: Volume-averaged radial heat flux, time-averaged between $t = 4 \cdot 10^4$ and $t = 5 \cdot 10^4 \Omega_i^{-1}$ as a function of Δm . The number of markers has been varied to keep the number of markers per Fourier mode constant.

to $\Delta m = 4 \sim 8$. In the example presented above, $\Delta m = 9$ was the converged value, but usual nonlinear simulations at lower ρ^* are converged by using $\Delta m = 5$. Therefore the value of Δm is consistent with the parallel resolution of Eulerian gyrokinetic codes.

To summarize, smart Fourier filtering is a powerful numerical scheme to improve the quality of a PIC simulation: by relaxing the time step criterion and by decreasing the number of Fourier modes in the simulations, CPU time is reduced by 2 orders of magnitude. In addition, the field-aligned filter should even be more efficient in the limit of small ρ^* plasmas relative to the rectangular filter. Its width Δm is set through the procedure applicable to any set of physical parameters described above.

5.4 Comparison with linear dispersion relation

In an effort to validate the code, ORB5 has been compared to the dispersion relation for toroidal ITG modes (2.63) that depends on the dimensionless parameters $k_y \rho_{Li}$, η_i , τ , R/L_N and $q(s_0)$ through $k_z \cong 1/q(s_0)R$. The plasma parameters are $\rho_* = \frac{2}{113}$, $B_0 = 1T$, $\bar{q}(\rho) = 1.25 + 0.67\tilde{\rho}^2 + 2.38\tilde{\rho}^3 - 0.06\tilde{\rho}^4$, $\tilde{\rho}_0 = 0.6$ such that $q(\tilde{\rho}_0) = 2$, $R_0 = 2[m]$ (R_0 in ORB5 is equivalent to R used in the dispersion relations), $a = 0.5[m]$ such that the aspect ratio is 4. The numerical parameters are $N_s = 32$, $N_{\theta_*} = 128$, $N_\varphi = 64$, $p = 3$. A diagonal filter with $\Delta m = 5$ is used, $N = 2^{17} \cong 131K$ and $\Delta t = 20\Omega_i^{-1}$. Temperature profiles 2 are used with $\Delta_{Ti} = 0.2$.

Fig. 5.21 shows the growth rate and the real frequency for a η_i scan (by varying L_{Ti}) with $k_y \rho_{Li} = 0.354$, $\tau = 1$, $R/L_N = 5.0$, $q(s_0) = 2$. The global tendency is similar, i.e. increasing growth rates and increasing real frequency (in absolute value) when η_i increases. This is expected as an increase of η_i means a higher temperature gradient and so a higher ω_{Ti} . Quantitative differences are due to the numerous approximations employed to derive the dispersion relation. In particular, it does not contain the effect of the shear.

Fig. 5.22 presents the growth rate and the real frequency for a $k_y \rho_{Li}$ scan with $\eta_i = 2.0$, $\tau = 1$, $R/L_N = 5.0$, $q(s_0) = 2$. The global shapes of both curves are similar: at high $k_y \rho_{Li}$, FLR effects attenuates the growth rate. ORB5 finds a stabilization of the modes at $k_y \rho_{Li} \cong 0.8$. For this value, the long wavelength approximation might not give accurate results. Instead, a Padé approximation (see [97]) or a Monte-Carlo solver (see [98]), valid for arbitrary $k_y \rho_{Li}$ should be used. The curves also differ at low $k_y \rho_{Li}$: the dispersion

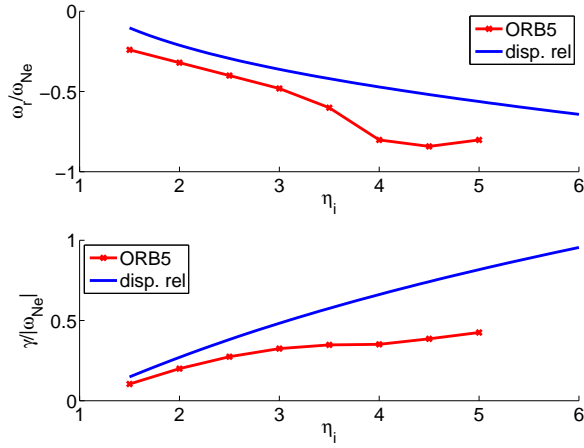


Figure 5.21: Growth rate and real frequency as a function of η_i given by dispersion relation Eq. (2.63) (solid line) and ORB5 (solid line, crosses) for $k_y \rho_{Li} = 0.354$, $\tau = 1$, $R/L_N = 5.0$, $q(s_0) = 2$.

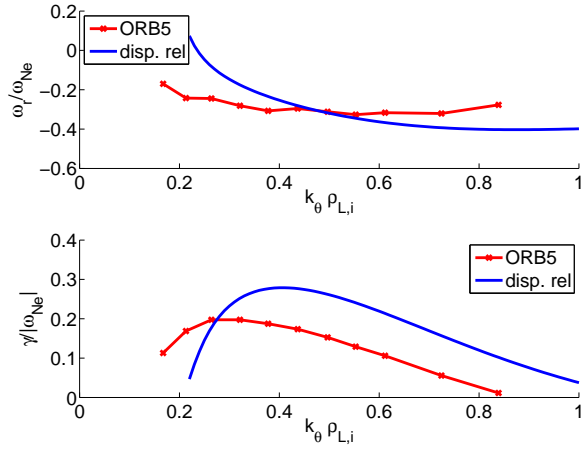


Figure 5.22: Growth rate and real frequency as a function of $k_y \rho_{Li}$ given by dispersion relation Eq. (2.63) (solid line) and ORB5 (solid line, crosses) for $\eta_i = 2.0$, $\tau = 1$, $R/L_N = 5.0$, $q(s_0) = 2$.

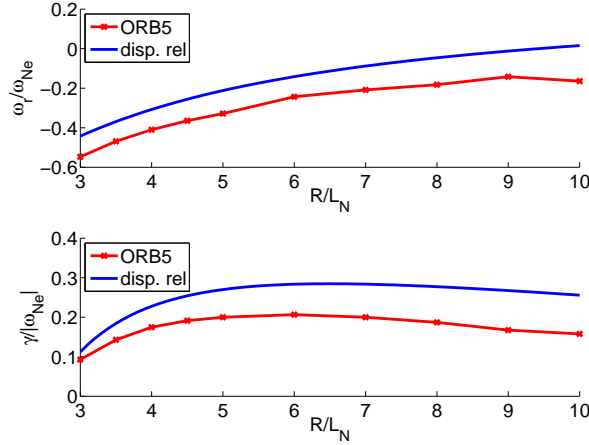


Figure 5.23: Growth rate and real frequency as a function of R/L_N given by dispersion relation Eq. (2.63) (solid line) and ORB5 (solid line, crosses) for $k_y \rho_{Li} = 0.354$, $\tau = 1$, $\eta_i = 2.0$, $q(s_0) = 2$.

relation does not take trapped ions into account.

Fig. 5.23 shows the growth rate and the real frequency for a R/L_N scan with $k_y \rho_{Li} = 0.354$, $\tau = 1$, $\eta_i = 2.0$, $q(s_0) = 2$. Like for the η_i scan, both curves have a similar behaviour: for $R/L_N \gtrsim 6$, the growth rate slowly decreases with R/L_N . Fig. 5.24 shows the growth rate and the real frequency for a τ scan with $k_y \rho_{Li} = 0.354$, $R/L_N = 5$, $\eta_i = 2.0$, $q(s_0) = 2$. In ORB5, one can vary τ by changing T_i or T_e . In the second case, varying τ means varying ρ^* . The real frequency and the growth rate are not affected by the way τ is varied except for the growth rate at $\tau = 0.5$. When T_e is increased it means that ρ^* is decreased: global effects become less important and the growth rate tends to the flux-tube value which is larger. When τ is decreased, the adiabatic response of electrons is enhanced and the growth rate is lowered. When τ is increased, there is less adiabatic response but it lowers the normalized η_i , ω_F and $k_z v_z$. The overall result is a smaller growth rate. The dispersion relation predicts a faster stabilization of the instability for an increasing τ than ORB5. The relatively large discrepancy between both methods is in line with the fact that global effects are important when the plasma size is small, i.e. at large ρ_* (high τ). In summary, although the dispersion relation involves many simplifications, the overall qualitative comparison with ORB5 is good. All the global trends are in agreement. Benchmarks with other gyrokinetic codes are needed to prove that the growth rates and real frequencies of ORB5 are correct. This will be presented in Section 5.6.

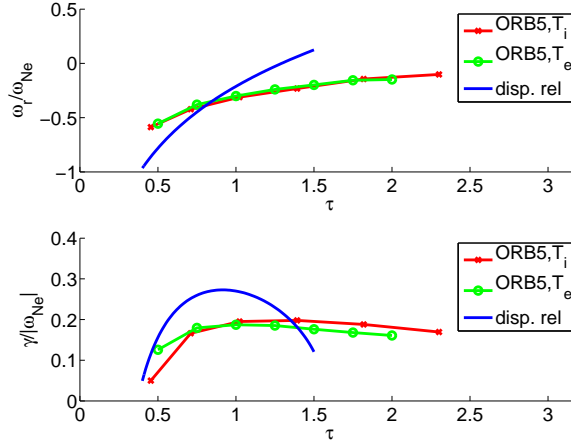


Figure 5.24: Growth rate and real frequency as a function of $\tau = \frac{T_e}{T_i}$ given by dispersion relation Eq. (2.63) (solid line) and by varying T_i (solid line, crosses) and by varying T_e (solid line, circles) in ORB5 for $k_y \rho_{Li} = 0.354$, $R/L_N = 5$, $\eta_i = 2.0$, $q(s_0) = 2$.

5.5 Convergence with number of markers

In collisionless gyrokinetic simulations, nonlinear convergence is a subtle notion. For PIC simulations, not only the time step and the grid resolution need to be carefully chosen, but the number of markers plays a crucial role as well. Indeed, numerical noise inherent to the PIC method may determine the level of transport in ETG simulations [91]. In ITG PIC simulations, due to the strong influence of the zonal flow the situation is different (see Section 7.1 for a more detailed discussion); however, the question of the required number of markers for convergence still remains. By measuring the level of numerical noise in ETG simulations, it has been established that the number of markers required is linked to the number of Fourier modes in the simulation [99]. Here, the question of convergence is approached by means of physics diagnostics. The left plot of Fig. 5.25 shows the evolution of the volume-averaged heat flux for different numbers of markers and the white noise initialization. The overshoot is shifted in time, as the initial level of the perturbation is inversely proportional to \sqrt{N} . This plot alone is not sufficient to say if a reasonable convergence is reached or not. This difficulty can be overcome by using the mode initialization with a single mode (m_0, n_0) . The right plot of Fig. 5.25 shows again Q for a marker number scan performed with the mode initialization. As the number of tracers is increased, the different curves look more and more alike during the whole simulation and the top of the overshoot occurs always at the same time and converges to

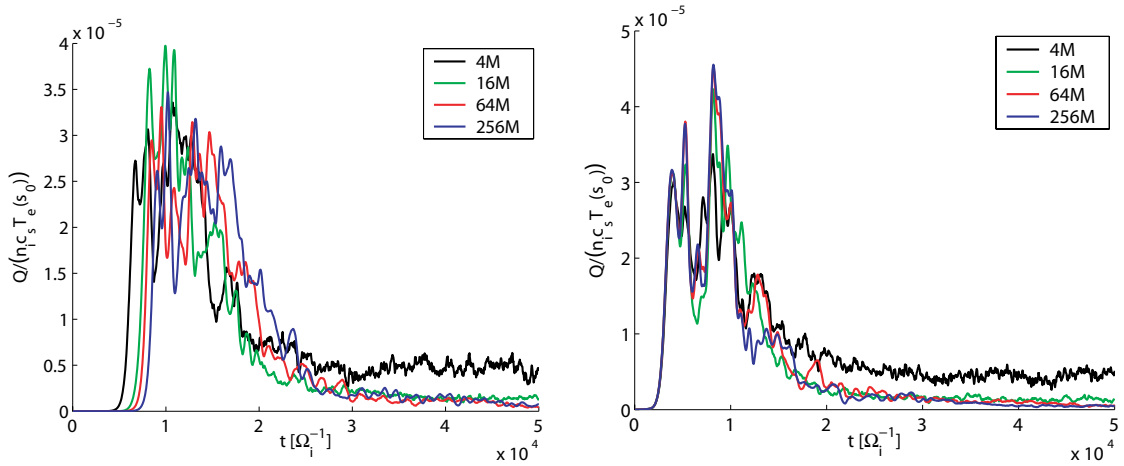


Figure 5.25: Time evolution of radial heat flux for different markers number with a field-aligned filter, a white noise initialization (left) and a single mode initialization (right).

the same level. Fig. 5.26 shows the volume-averaged heat flux Q , time-averaged between $t = 4 \cdot 10^4$ and $t = 5 \cdot 10^4 \Omega_i^{-1}$, i.e. when the system has reached a quasi steady-state, for the two different initializations. For the white noise initialization, it is harder to say for which number of markers the simulation is converged. This is because the system relaxes differently when N is increased, which implies different series of bursts. When the mode initialization is used, the convergence curve is smoother because the different simulations have in this case a more similar nature, and the error bars representing the standard deviation over the averaging times tend to decrease as N is increased, which is not the case for the white noise initialization.

In addition, note that these two initializations give quite different overshoots and therefore quite different profile relaxations: for the mode initialization, a single toroidal mode strongly dominates since the beginning of the simulation, whereas all toroidal modes have approximately the same initial energy when the white noise initialization is employed. In this context, a multiple mode initialization would be more appropriate, but in principle the quasi-stationary state of a simulation should not depend on the initialization (i.e. it must lie within the intrinsic variation of the system due to the chaotic nature of turbulence). The important point is that by initializing the system independently of the number of markers, the notion of convergence with respect to the number of markers becomes easier to handle.

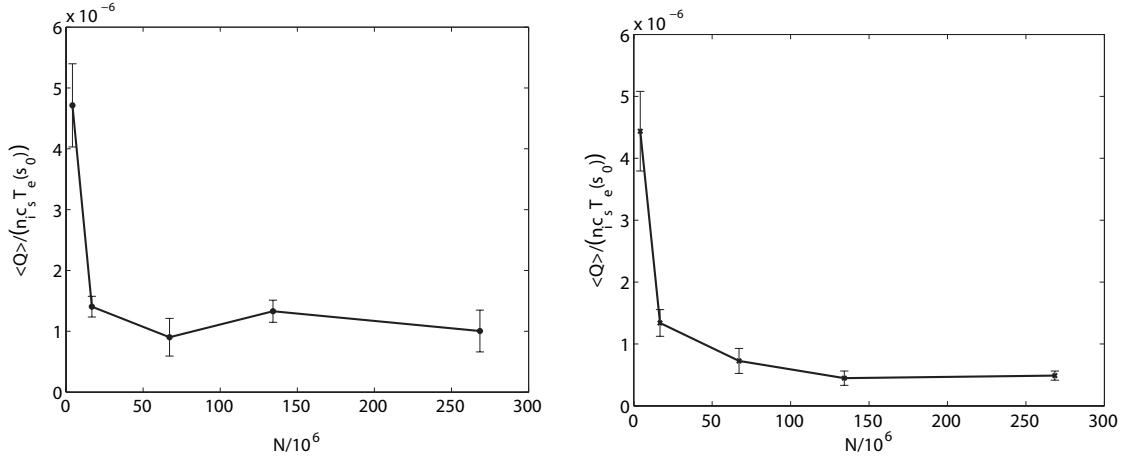


Figure 5.26: Radial heat flux as a function of the number of markers for the white initialization (left) and for the mode initialization (right). The heat flux is averaged between $t = 4 \cdot 10^4$ and $t = 5 \cdot 10^4 \Omega_i^{-1}$. Error bars represent the standard deviation.

5.6 The CYCLONE benchmark

In Ref. [90], several fluid, gyrofluid and gyrokinetic codes are compared for the so called CYCLONE test case, which represents local parameters from an ITER-relevant DIII-D H-mode shot [100]. The physical parameters used here are $\rho^* = 1/175$, $a = 0.48$ [m], $B_0 = 1.91$ [T], $R_0 = 1.32$ [m], $s_0 = 0.624$ (corresponds to $\rho_0 = 0.5a$), $q(s_0) = 1.4$, $T_i = T_e$, $R_0/L_{Ti} = 6.9$, $\eta_i = L_n/L_{Ti} = 3.12$, $\hat{s} = 0.78$, $\Delta_{Ti} = 0.3$. The value of ρ^* has been decreased by increasing the electron and ion temperatures to 2.52 keV to avoid a too fast relaxation and to approach the flux-tube limit $\rho^* \rightarrow 0$ without going beyond the available computational resources. The numerical parameters are the following: $N = 2^{26} \cong 83$ M markers, $\Delta t = 40 \Omega_i^{-1}$. The quasineutrality equation is solved with cubic B-splines on a $N_s = 128$, $N_{\theta_*} = 448$, $N_\varphi = 320$ grid and a field-aligned filter with $\Delta m = 5$ is applied. Benchmarking ORB5 for these parameters is crucial in order to have confidence in the code.

A first simple test is presented on Fig. 5.27, where the growth rates obtained with the ORB5 code run in linear mode are compared with GT3D [49]. ρ^* has been changed to $1/140$, a local maxwellian and the exact same equilibrium profiles have been employed in an effort to have similar parameters between the two codes, which show excellent agreement.

The numerical quality of CYCLONE nonlinear simulation is shown on Fig. 5.28 through

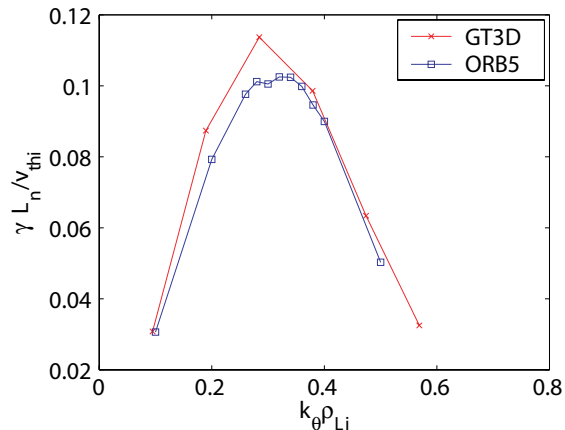


Figure 5.27: Linear growth rates for GT3D and ORB5.

$\epsilon_E(t) = \Delta E(t)/E_f(t)$ which has a meaning only in the end of the linear phase and in the nonlinear phase, where $E_f(t)$ is not too small. For this CYCLONE simulation, energy is conserved up to very long times as $|\epsilon_E| < 0.3$ up to $t = 5 \cdot 10^4 \Omega_i^{-1}$, a time at which the temperature profile is relaxed (see Fig. 5.29). This is a remarkable value for a global PIC code. This energy deviation represents 10^{-5} of the total initial energy of the system. As the quasi-equilibrium state establishes, numerical noise grows and slowly leads to the loss of energy conservation. However, for late times the system is close to marginal stability because of profile relaxation so the state of the system will not provide any new physical information. Hence it is useless to continue a PIC simulation up to very long times without sources and sinks. The situation could be different if collisional sources were added to the simulation.

Nonlinear benchmark is usually performed by plotting the ion diffusivity versus R_0/L_{Ti} . Note that no assumption is done on Q , n_i and ∇T_i : these profiles are reconstructed with appropriate moments of the Vlasov equation and then smoothed using splines with tension interpolation [79]. In [90], Dimits proposed a fit to express χ_i as a function of R_0/L_{Ti} when the system has reached (quasi-)steady state:

$$\frac{\chi_i}{\chi_{\text{Dimits}}} \cong 15.4 \left(1 - 6 \frac{L_{Ti}}{R_0} \right), \quad (5.9)$$

with $\chi_{\text{Dimits}} = \chi_{GB} a/L_n$ and χ_{GB} is defined by (5.7). There are two difficulties in benchmarking ORB5 against the Dimits fit, which has been obtained with a flux-tube code. First, spatial averaging must be applied since ORB5 is a global code. Second, the temperature profile and consequently R_0/L_{Ti} are not frozen as in flux-tube codes and relax

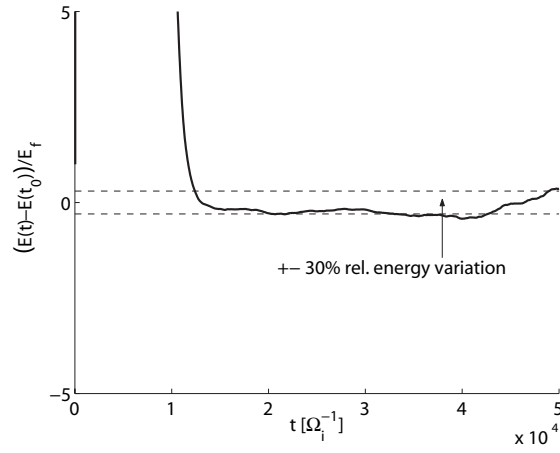


Figure 5.28: Relative energy conservation for a typical CYCLONE simulation.

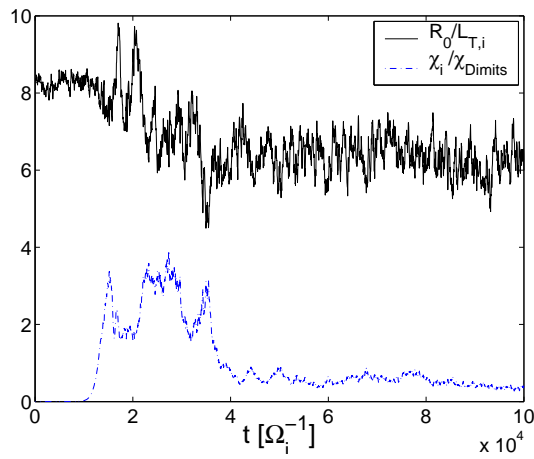


Figure 5.29: Time evolution of $R_0/L_{T,i}$ (blue) and $\chi_i/\chi_{\text{Dimits}}$ at $s = s_0$.

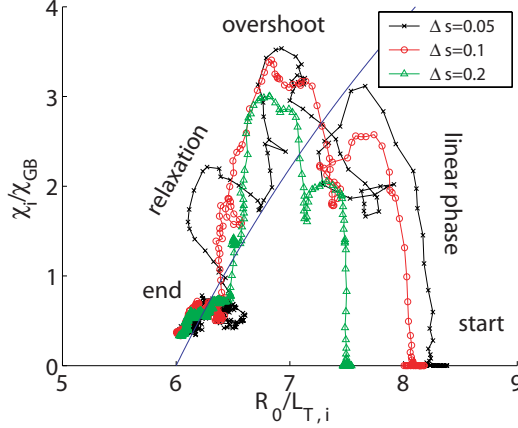


Figure 5.30: Evolution of χ_i vs $R_0/L_{T,i}$. Each point is averaged between $s_0 \pm \Delta s$. A point is computed every $320 \Omega_i^{-1}$. The simulation goes from $t = 0$ up to $t = 10 \cdot 10^4 \Omega_i^{-1}$. The solid blue curve is the Dimits fit (5.9).

during the simulation. It is therefore better to characterize the radial transport by a cloud of points $(\chi_i, R_0/L_{T,i})$ representing the time evolution of space-averaged values rather than with a single point. Such a procedure has been applied in Ref. [31]. ORB5 results are displayed in Fig. 5.30. At the beginning of the simulation, the radial transport is null and the logarithmic gradient variation is very weak. Then the turbulence establishes, leading to profile relaxation. Finally, the system is in quasi-equilibrium state. The cloud of points taken from the relaxation phase is well located near the Dimits fit. The dispersion is more important for small averaging widths Δs . This quantity should be large enough to average bursts, but a too large value would move the temperature gradient too far away from the local value. Remark on Fig. 5.29 how fast the profile relaxes to a quasi-equilibrium state. A way to prevent this phenomenon would be to decrease ρ^* , thus reducing global effects. Unfortunately simulations at lower ρ^* were not possible because of the limited computational power.

Note at the time this benchmark has been performed, the code did not have the noise-control algorithm. Based on the number of markers, the final state of this simulation is quite noisy and that the location of the cloud of points characterizing the final quasi-steady state might be incorrect. Another ORB5 benchmark using the noise-control algorithm, performed in the frame of the EFDA Task Force on Integrated Tokamak Modelling, has been published in [101].

Chapter 6

Application of ORB5 for ITG turbulence: evolution of entropy and parallel nonlinearity

6.1 Steady state: evolution of entropy

6.1.1 The fluctuation entropy equation

In a gyrokinetic simulation, one of the key points to make quantitative predictions is the establishment of a steady state. In δf PIC simulations, a steady state is reached if the fluctuation entropy is constant. In 1999, Krommes [71] showed that in order to get a steady state some dissipation must be present in the system. Whereas in Eulerian codes dissipation is present [102] due to numerical discretization, this effect is absent in collisionless δf PIC simulations. In particular, it means that *collisionless δf PIC simulations cannot achieve a steady state*. The weights, and consequently the fluctuation entropy, proportional to the sum of the weights squared $\langle w^2 \rangle$ grow together with the turbulence and one observes that low order moments saturate but the fluctuation entropy continually increases in time. Therefore, on top of the physical nonzero value of the fluctuation entropy there is a numerical growth of this quantity. This is known as the *entropy paradox* and is due to the Monte-Carlo approach used in PIC codes. This situation is problematic as the noise is proportional to $\langle w^2 \rangle$, see Eq. 4.134. One solution to resolve this entropy paradox is to introduce physical dissipation by implementing a collision operator. A brief

review of collisional methods is presented.

The most general form of a collision operator is usually described with the Landau operator which contains second order velocity derivatives. Its implementation in PIC code is particularly complex as the distribution function is not known on a velocity grid. Instead, some approximations are made. For electron-ion collisions, it is common to use a Lorentz operator, i.e. ions remain fixed due to their large inertia while the effect on electrons is modeled by a pitch-angle scattering [103]. For like-species, two different approaches exist: the weight and velocity of markers are modified in such a way to conserve density, momentum and energy [104], or a binary scheme can be employed, where the random accelerations and displacements of spatially nearby pairs of markers are correlated so as to exactly conserve the energy and momentum of each pair. Unfortunately these methods are noisy, hence inaccurate: the randomization of weights and/or velocities introduces noise in the simulation. The weights must be interpreted statistically; in particular two markers can have different weights at the same location in phase space, which breaks the direct link between the local value of δf and the weight. In this respect, collisional δf methods have been improved by considering the weight as an additional dimension [105], but it induces *weight spreading* and ultimately leads to the breakdown of the δf method. A possible solution to limit this phenomena has been proposed in [106]. A general collisional scheme has also been proposed by Krommes in [71], recovering the scheme proposed by Chen [105]. Note that a deterministic algorithm has been proposed by Lewandowski [107], although this scheme has not been implemented in a 5D gyrokinetic code.

This brief review reveals that implementing collisions in a PIC code is a difficult task. Alternatively, one can remain collisionless and introduce *numerical dissipation*. In ORB5, this is done with the Krook operator exposed in Sec. 3.8, following the idea of the thermostat W -stat proposed by Krommes [71], with the difference that no restriction is imposed to fix the entropy. The idea of a W -stat has been tested on a simple 2D gyrokinetic slab code in Ref. [71], but it has not been tested on a more realistic 5D global PIC code. One of the main criticism addressed to δf PIC codes is their inability to perform long time simulations due to the increase of the sum of squared weights: this phenomenon equivalently relates to numerical noise and a quasi-steady state. Considering this, it is consequently obvious that the demonstration of a global steady state in a 5D gyrokinetic δf PIC code represents a big step in the gyrokinetic community. Note that other types of numerical

dissipation are possible: in the particle-continuum method [108], [109], the weights and the phase space coordinates are periodically reseted on a phase space grid. In the coarse-graining method [110], the weights are binned on a 5D grid and the distribution function is coarse-grained by replacing the Dirac function appearing in the Klimontovitch distribution by shaping functions. This scheme is more complicated to implement compared to the W -stat: it requires large additional memory and computing time, but it preferentially removes small velocity scales of the distribution function, whereas the W -stat does not distinguish them.

The *fluctuation entropy* is defined according to Ref. [111]:

$$\begin{aligned}\delta S &= \int f(\vec{R}, v_{\parallel}, \mu, t) \ln \left[f(\vec{R}, v_{\parallel}, \mu, t) \right] - f_0(\vec{R}, v_{\parallel}, \mu) \ln \left[f_0(\vec{R}, v_{\parallel}, \mu) \right] B_{\parallel}^* d\vec{R} dv_{\parallel} d\mu d\alpha \\ &\cong \frac{1}{2} \int \frac{\delta f^2(\vec{R}, v_{\parallel}, \mu, t)}{f_0(\vec{R}, v_{\parallel}, \mu)} B_{\parallel}^* d\vec{R} dv_{\parallel} d\mu d\alpha\end{aligned}\quad (6.1)$$

where the assumption $|\delta f| \ll |f_0|$ has been made. The fluctuation entropy means a difference between microscopic and macroscopic entropy. The entropy balance has been studied with an Eulerian code in the case of collisionless [111] and collisional [112] plasmas with non-dissipative methods, meaning that the dissipation has a purely physical origin. The general form of the entropy balance equation reads:

$$\frac{d}{dt} (\delta S + W) = \eta_i Q_i + C \quad (6.2)$$

where W is the potential energy, Q_i is the ion heat flux and C is the collisional dissipation. In the collisionless limit $C = 0$, the system can reach a *steady-state* by two different ways. First, the trivial case is when $\frac{d\delta S}{dt}$, $\frac{dW}{dt}$ and Q_i are 0 (no transport). This scenario is impossible to reach with PIC simulations due to the noise increase which always produces a finite numerical transport. The second case is when $\frac{dW}{dt} = 0$ and $\frac{d\delta S}{dt}$ is balancing Q_i . This is the scenario happening in collisionless δf PIC simulations. The low moments of δf saturate but the growth of fine-scale velocity structures contributes to the monotonical increase of δS . This is the general picture of entropy production produced by turbulent transport. An analytical study of the entropy production rate due to turbulence can be found in [113]. Note that entropy production can also be studied in the frame of classical and neoclassical transport. This topic is studied in Ref. [114].

The study of entropy balance has been performed with the Eulerian codes G4D [115] in cylindrical geometry and GYRO [102] in toroidal geometry, but no study has been

done with a global PIC code (in [110], the entropy balance equation is derived but it is not checked numerically). For the first time, the demonstration of a steady state with artificial dissipation in a 5D global gyrokinetic PIC code is presented. The entropy balance equation is obtained by multiplying the Vlasov equation (Eq. 3.91) by $\delta f/f_0$, integrating over phase space and normalizing the result over the plasma volume.

The discretized fluctuation entropy balance equation can be written as:

$$\frac{d\delta S}{dt} = D_{\text{flux}} + D_{\text{field}} + D_{\text{nc}} + D_{\text{heat}} \quad (6.3)$$

with

$$\delta S = \frac{1}{N} \sum_{p=1}^N \left(\frac{1}{2} \frac{w_p^2}{f_{0p}} \right) \quad (6.4)$$

$$D_{\text{flux}} = -\frac{1}{N} \sum_{p=1}^N \left[w_p + \frac{w_p^2}{2f_{0p}} \right] \kappa(\Upsilon_p) \frac{d\Upsilon}{dt} \Big|_{1, \vec{z}_p} \quad (6.5)$$

$$D_{\text{field}} = \frac{1}{N} \sum_{p=1}^N \left[w_p + \frac{w_p^2}{2f_{0p}} \right] \frac{q_i}{T_i(\Upsilon_p)} \langle \vec{E} \rangle \cdot \frac{d\vec{R}}{dt} \Big|_{\vec{z}_p} \quad (6.6)$$

$$D_{\text{nc}} = -\frac{1}{N} \sum_{p=1}^N \gamma_K \frac{w_p^2}{f_{0p}} + w_p \sum_{i=1}^{N_{\text{mom}}} g_i^{k_p}(\vec{z}_p) M_i(\vec{z}_p) \quad (6.7)$$

$$D_{\text{heat}} = \sum_{p=1}^N \frac{w_p}{f_{0p}} S_{H,p}^{m,k} \quad (6.8)$$

where the property $\frac{d}{dt} \left(\frac{1}{2} \frac{w_p^2}{f_{0p}} \right) = \frac{w_p}{f_{0p}} \frac{dw_p}{dt} - \frac{1}{2} \frac{w_p^2}{f_{0p}^2} \frac{df_{0p}}{dt}$ has been used. D_{flux} describes the fluctuation entropy production by the profile gradients. It is instructive to see how D_{flux} relates to the heat diffusivity in the flux tube limit $\rho^* \rightarrow 0$ with constant profiles and gradients:

$$D_{\text{flux}} = \frac{1}{V} \int B_{\parallel}^* d\vec{R} dv_{\parallel} d\mu d\alpha \delta f \left(\frac{n_0'(\Upsilon)}{n_0(\Upsilon)} + \frac{T_i'(\Upsilon)}{T_i(\Upsilon)} + \frac{m_i v^2}{2T_i(\Upsilon)} \right) \frac{\langle \vec{E} \rangle \times \vec{B}}{BB_{\parallel}^*} \cdot \nabla \Upsilon \quad (6.9)$$

Note that the second term entering in definition 6.5 has been neglected because it is $\delta f/f_0$ smaller than the first one. In the local limit, $\Upsilon \rightarrow \psi$ and $B_{\parallel}^* \sim B$ will be assumed for the phase space Jacobian. The first two terms of the integral are proportional to the particle flux which is assumed to be 0 for adiabatic ITG turbulence, the potential being in phase with the density. In practice, there is a finite particle diffusivity of numerical origin which is $10^2 - 10^3$ times smaller than the heat diffusivity peak. The third term gives:

$$D_{\text{flux}} = \frac{1}{V} \int d\psi \frac{T_i'(\psi)}{T_i^2(\psi)} \int |\nabla \psi| \vec{Q} \cdot d\vec{\sigma} \quad (6.10)$$

where:

$$\vec{Q} = \int d\vec{v} \frac{1}{2} m_i v^2 \frac{\langle \vec{E} \rangle \times \vec{B}}{BB_{\parallel}^*} \delta f, \quad \vec{d}\sigma = J_{\theta_* \psi \varphi} d\theta_* d\varphi \frac{\nabla \psi}{|\nabla \psi|} \quad (6.11)$$

For circular surfaces D_{flux} can be further simplified:

$$D_{\text{flux}} = \frac{1}{V} \int d\rho \left[\frac{T'_i(\rho)}{T_i(\rho)} \right]^2 \frac{1}{|\nabla T_i(\rho)|} \int \vec{Q} \cdot \vec{d}\sigma \quad (6.12)$$

If all profiles are approximated as radially constant, then one finally has:

$$D_{\text{flux}} = \frac{a}{V} \left(\frac{a}{L_T} \right)^2 n_0 \chi_i \quad (6.13)$$

This equation is similar to the equation (52) of Ref. [102] and shows that D_{flux} (positive in case of an outward flux) is the driving term, somehow proportional to the heat diffusivity and responsible for the entropy increase.

The second term of Eq. (6.3) describes the rate of entropy created by the transfer of energy from the particles to the field perturbation. From the power balance equation in the case of constant profiles one simply has:

$$D_{\text{field}} \cong - \frac{1}{T_i(\psi)} \frac{dE_f}{dt} \quad (6.14)$$

where the second term entering in definition (6.6) has also been neglected and E_f is the total field energy defined in Eq. (3.83). It means that when the electrostatic potential acquires energy, the entropy is reduced. This term should therefore be negative during the linear phase, and then oscillate around 0 during the nonlinear phase for both the quasi-steady and the steady states. The third term of Eq. 6.3 is the dissipative noise control term which is always negative, thus reducing the entropy:

$$D_{\text{nc}} = \sum_{p=1}^N -\gamma_K \frac{w_p^2}{f_{0p}} + \sum_{k=1}^{N_S} \sum_{\substack{1 \leq p \leq N \\ p: s_p \in [s_{k-1}: s_k]}} w_p \sum_{i=1}^{N_{\text{mom}}} M_i(\vec{R}_p, v_{\parallel p}, \mu_p) g_i(s_p, t) \quad (6.15)$$

By using 4.53, one has:

$$D_{\text{nc}} = \sum_{k=1}^{N_S} \sum_{\substack{1 \leq p \leq N \\ p: s_p \in [s_{k-1}: s_k]}} \frac{1}{\gamma_K f_{0p}} \left[-\gamma_K^2 w_p^2 + \left(\sum_{i=1}^{N_{\text{mom}}} M_i(\vec{R}_p, v_{\parallel p}, \mu_p) f_{0p} g_i(s_p, t) \right)^2 \right] \quad (6.16)$$

Therefore D_{nc} can be negative if for at least one marker the following identity is satisfied:

$$|\gamma_K w_p| < \left| \sum_{i=1}^{N_{\text{mom}}} M_i(\vec{R}_p, v_{\parallel p}, \mu_p) f_{0p} g_i(s_p, t) \right| \quad (6.17)$$

It means that for this marker the contribution of the Krook operator is smaller than the contribution of the correction to the Krook operator. This is of course not possible as S_{corr} is a projection of S_K over a finite number of velocity moments. In extreme cases where the number of markers per bin is of the order unity D_{nc} could be positive, but in practice this never happens as N_S is typically equal to $1/\rho^*$ which is obviously much smaller than the total number of markers.

The fourth term of the fluctuation entropy balance equation describes the contribution of the heating operator to the entropy. The same argument can be used to show that $D_{\text{heat}} < 0$, but contrary to the noise control operator, this term should not contribute significantly to the reduction of the fluctuation entropy. The heating operator is built with different binnings of markers in energy and radius that are smooth in velocity space: it does not affect the filamentation (in the $|v|$ dimension) of the velocity phase space and thus the heating operator should not help reducing the noise. This should be reflected in the evolution of the fluctuation entropy.

6.1.2 Simulation results

The equality 6.3 should be perfect in the limit of infinite numerical accuracy. In order to test it, CYCLONE simulations have been performed with the following parameters: $\rho^* = 1/184.7$, $m_i = 2m_p$, $a = 0.625$ [m], $B_0 = 1.91$ [T], $R_0 = 1.70$ [m], $s_0 = 0.624$ (corresponding to $\tilde{\rho}_0 = 0.5$), $q(s_0) = 1.4$, $T_i = T_e$, $R_0/L_{Ti} = 6.9$, $\eta_i = L_n/L_{Ti} = 3.12$, $\hat{s} = 0.78$. Profiles 3, Eqs. (4.149), (4.150) have been used with $\Delta_{Ti} = 0.04$ and $\Delta\tilde{\rho} = 0.25$ (see Fig. 6.1). The numerical parameters are the following: $N = 80M$ markers, $\Delta t = 40 \Omega_i^{-1}$. The quasineutrality equation is solved with cubic B-splines on a $N_s = 128$, $N_{\theta_*} = 512$, $N_\varphi = 256$ grid and a field aligned solver with $\widetilde{\Delta m} = 5$. A field-aligned filter with $\Delta m = 5$ is applied combined with a rectangular filter $n_1 = 0 < |n| < n_2 = 57$, $m_1 = -128 < m < m_2 = 128$. Poloidal modes above $k_\theta \rho_{Li} = 1.0$ are filtered out. Five simulations have been performed. The first one has no Krook and no heating operators. The second one has no heating operator but a Krook operator with $\gamma_{Ki} = 9 \cdot 10^{-5} \Omega_i$ with conserved density, zonal flow structure and energy, i.e. the Krook operator allows the relaxation of the temperature gradient. The third simulation is similar to the second one except for the conservation of energy which is turned off: the Krook operator acts as a heating. The fourth simulation has no Krook operator but the heating operator is turned

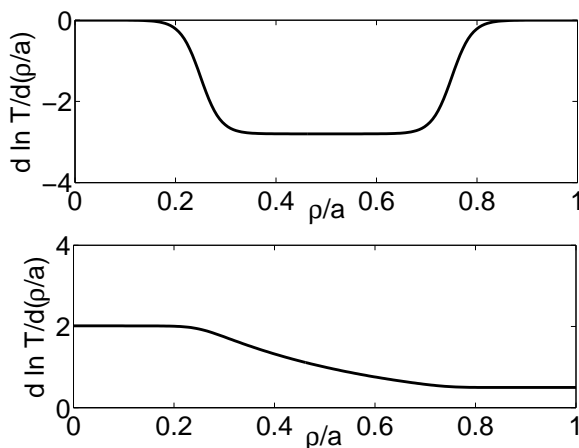


Figure 6.1: Logarithmic temperature gradient and temperature profiles used in Sections 6.1 and 6.2.

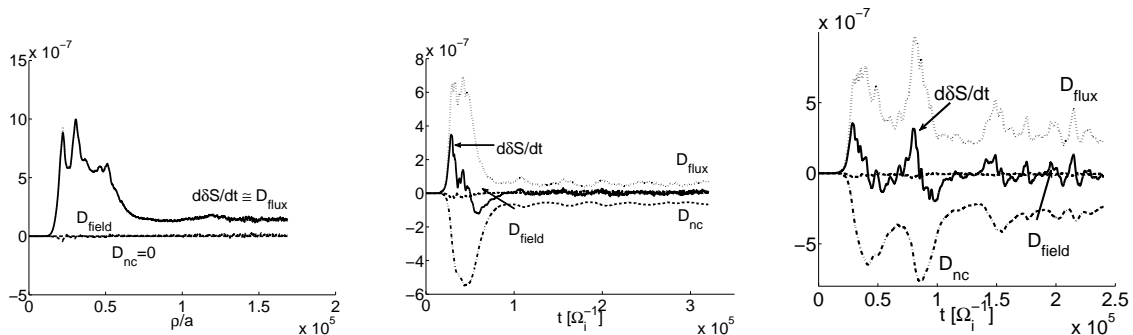


Figure 6.2: Temporal evolution of $\frac{d\delta S}{dt}$ (solid line), D_{flux} (dotted line), D_{field} (dashed line) and D_{nc} (dash-dotted line) for the *transient* (left), *noise-controlled* (middle) and *fixed-gradient-noise-controlled* (right) simulations with 80M markers. For these three simulations the heating contribution D_{heat} is zero.

on with $\gamma_H = 9 \cdot 10^{-5} \Omega_i$. Finally the fifth simulation have both operators turned on with $\gamma_{Ki} = \gamma_H = 9 \cdot 10^{-5} \Omega_i$ and the Krook operator conserves the energy. These simulations will be called *transient*, *noise-controlled*, *fixed-gradient-noise-controlled*, *heated* and *noise-controlled-heated*.

Fig. 6.2 shows the different components of the entropy balance equation for the first three simulations. The *transient* simulation exhibits a quasi steady-state: in the end of the simulation, the entropy production rate is constant and almost equal to D_{flux} , while D_{field} is close to 0. This is the situation with saturated low-order moments and a growing entropy $\delta S \propto \chi_i \cdot t$. This simulation rapidly becomes dominated by numerical noise (the

signal to noise ratio is almost equal to 1 in the end of the simulation).

The *noise-controlled* simulation shows the beneficial effect of D_{nc} on the entropy balance. This term is always negative, balances D_{flux} (although the bursts of D_{nc} are slightly shifted in time with those of D_{flux}). Like for the *transient* case, D_{field} is again extremely close to 0. Consequently, the *noise-controlled* simulation exhibits a steady-state character: in the end of the simulation, the fluctuation entropy is constant while there is a finite heat flux (see left plot of Fig. 6.3). This proves that a W -stat allows for a true steady state. Note that the signal to noise level drops below 10 near $t = 7 \cdot 10^4 \Omega_i^{-1}$ and ends up at around 4, but the simulation seems to remain in a steady state. However, by looking more carefully at the *noise-controlled* fluctuation entropy evolution (Right plot of Fig. 6.3), one sees that it slowly increases with time (from $\delta S = 1.5 \cdot 10^{-3}$ at $t = 1 \cdot 10^5 \Omega_i^{-1}$ to $\delta S = 2.15 \cdot 10^{-3}$ at $t = 3.2 \cdot 10^5 \Omega_i^{-1}$). In this decaying simulation, the heat diffusivity goes to 0 as the temperature profile relaxes. It becomes more and more difficult to accurately represent this low signal with markers and the noise increases. The entropy production due to noise cannot be compensated by the dissipative Krook term anymore and so the fluctuation entropy increases: the system undergoes a transition from steady to quasi-steady. This is better seen on the right plot of Fig. 6.3: for 20M markers, the growth of the noise is more important and the Krook damping rate is clearly not large enough to counteract this effect, while the growth of the fluctuation entropy is smaller for the 80M and the 320M cases. Increasing the dissipation will delay this phenomena but one must then be careful about physical convergence. The important conclusion is that decaying PIC simulations cannot be run for infinitely long times, even when dissipation is introduced in the system. However one hopes to run them for the longest possible time in order to approach the critical gradient. In practice, the signal to noise ratio and the fluctuation entropy diagnostic provides a meaningful way to determine when the simulation becomes flawed and must be stopped. One can then look at the desired physical quantities such as heat diffusivity and temperature gradients. The number of markers and the dissipation are then modified depending on how close is the final state of the system to the marginal point.

Fig. 6.4 shows the time evolution of D_{flux} and χ_i/χ_{GB} (averaged between $\tilde{\rho} = 0.3$ and $\tilde{\rho} = 0.7$). The latter quantity has been rescaled by a constant factor to match the maximum value of D_{flux} . It is remarkable how these curves overlap despite the approximations

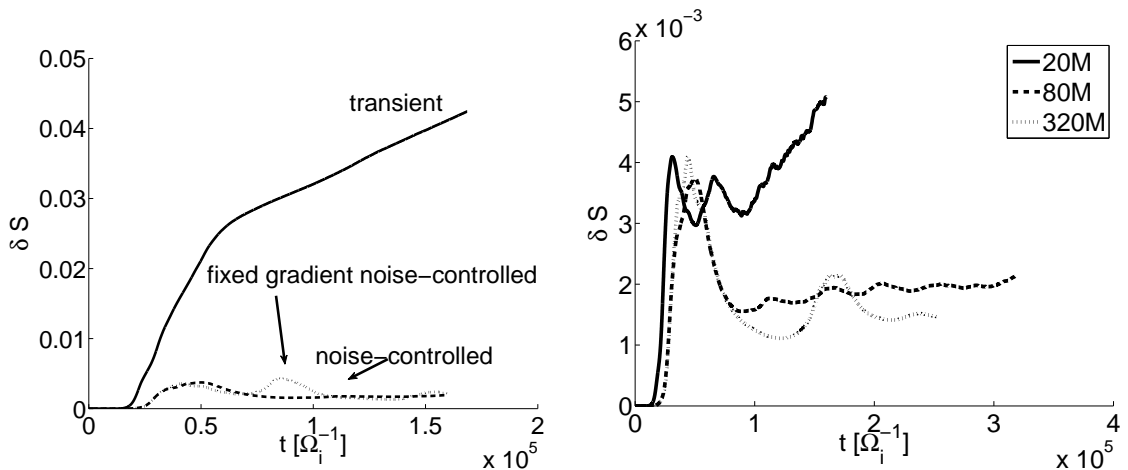


Figure 6.3: Left: time evolution of δS for the *transient* (solid line), *noise-controlled* (dashed line) and *fixed-gradient-noise-controlled* (dotted line) simulations. Right: time evolution of entropy for *noise-controlled* simulations with 20M (solid line), 80M (dashed line), and 320M (dotted line) markers.

made to obtain Eq. (6.13) and the fact that the heat diffusivity is radially averaged (one cannot average over the whole plasma because χ_i goes to infinity when ∇T goes to zero at the magnetic axis and at the plasma edge).

In the *fixed-gradient-noise-controlled* simulation, because the gradient is kept almost fixed, the heat diffusivity and consequently the three components D_{flux} , D_{field} and D_{nc} have a burstier character. Nevertheless, the entropy production rate approaches to 0 on time-average and a true steady state is reached. The state of these simulations is better seen on Fig. 6.3. The *transient* simulation shows a linearly growing entropy, while the *noise-controlled* and the *fixed-gradient-noise-controlled* simulations have, in the end, a constant entropy on average. Note that the fluctuation entropy also provides an additional way to check the numerical convergence of the simulation. This is uniquely defined, in opposite to the signal to noise diagnostic: the latter is obtained by manually defining which modes belong to the noise and which modes belong to the signal, and depends on the field-aligned filter. The criterion of a signal to noise ratio higher than 10 is of course empirical only, because it depends itself on the definition of noise and is based on experience. The fluctuation entropy diagnostic has the advantage that it does not rely on any assumption. It is in fact strongly connected to the sum of the weights squared and has, in addition, a physical interpretation (as seen above, D_{flux} connects to the heat diffusivity,

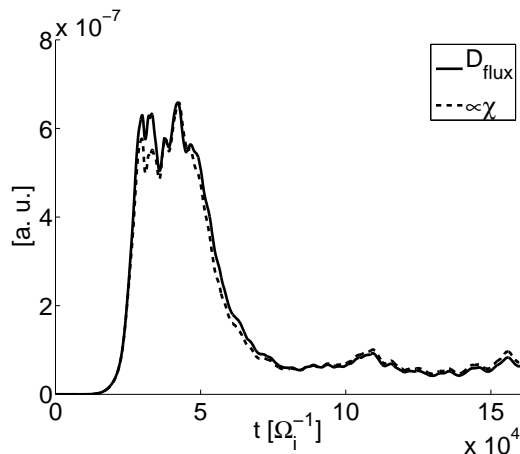


Figure 6.4: Time evolution of D_{flux} (solid line) and χ_i/χ_{GB} (dashed line, radially averaged between $\tilde{\rho} = 0.3$ and $\tilde{\rho} = 0.7$) for a *noise-controlled* simulation with $80M$ markers. χ_i/χ_{GB} has been rescaled by a constant factor to match the maximum of D_{flux} .

D_{field} connects to the energy transfer between the field and particles and D_{nc} connects to the dissipation artificially introduced in the system). Moreover, the fluctuation entropy is defined in a universal way and helps to determine the correctness of the dissipative damping coefficient without any arbitrary choice. It is therefore an extremely useful tool for gyrokinetic PIC simulations.

Finally, the influence of the heating operator on the fluctuation entropy is examined. On Fig. 6.5, the different components of the fluctuation entropy balance equation are represented for the *heated* and the *noise-controlled-heated* simulation. By looking at D_{heat} , one sees that this term, although slightly negative, is small and as expected does not significantly reduce the fluctuation entropy. Like the *transient* case, the *heated* case also exhibits a quasi-steady state, where $\delta S \propto \chi_i \cdot t$. χ_i is much higher than its counterpart in the *transient* simulation, reflecting the effect of the heating, but the noise accumulates: the signal to noise ratios of the *transient* and *heated* case are very similar and are around 2 which clearly demonstrates that these two simulations are noise-dominated. This is why D_{flux} (and equivalently the heat transport) has some fast frequency oscillations and no burst activity. It must be emphasized that the average value of D_{flux} which is proportional to the average value of the heat diffusivity is, in that case, probably not converged. The situation is fortunately much better in the *noise-controlled-heated-case*. D_{heat} is again very small and slightly negative, but here the noise-control component prevents

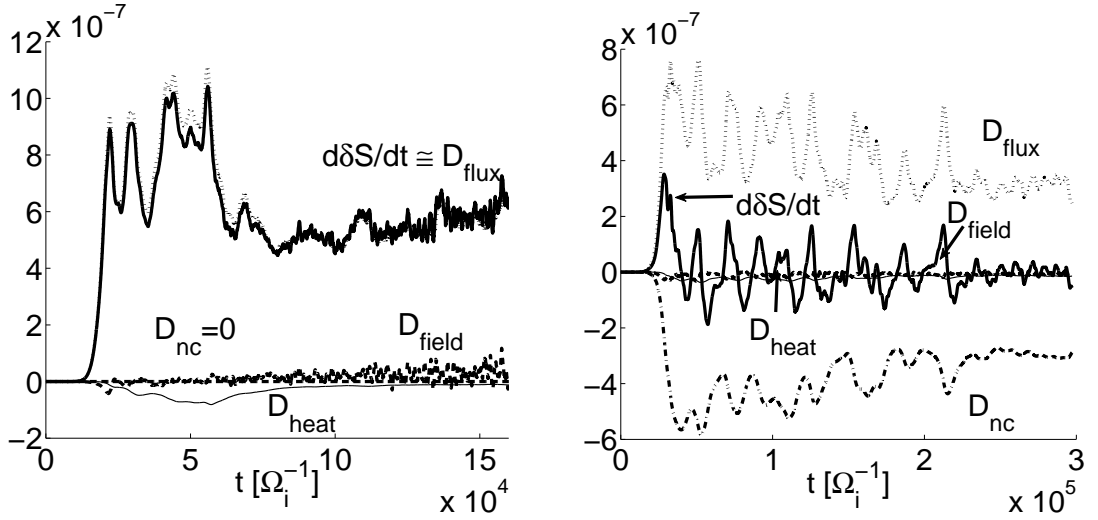


Figure 6.5: Temporal evolution of $\frac{d\delta S}{dt}$ (thick solid line), D_{flux} (dotted line), D_{field} (dashed line), D_{nc} (dash-dotted line) and D_{heat} (thin solid line) for the *heated* (left) and *noise-controlled-heated* (right) simulations with 80M markers.

the entropy from growing. On average, $d\delta S/dt$ is zero which demonstrated that the *noise-controlled-heated* has reached a steady state. The striking difference between both simulations with heating can be observed on D_{flux} . In the *noise-controlled-heated* case, the system undergoes an endless series of heat bursts while in the *heated* case the bursts phenomenon stops and is replaced by fast noise-oscillations. This shows that quasi-steady states obtained with PIC codes not only predict incorrect transport (in the average sense) but lack also at predicting the correct physics. On the contrary, steady states do allow for quantitative predictions. This statement is confirmed by the results depicted on Fig. 6.6, where the radial and temporal evolution of R_0/L_{T_i} is represented. In the *noise-controlled-heated* case, inward propagating avalanches of temperature bursts are clearly visible. When the noise control algorithm is turned off, these bursts disappear and the amplitude of the temperature gradient fluctuations become smaller. This is the manifestation of the filamentation of the velocity phase space.

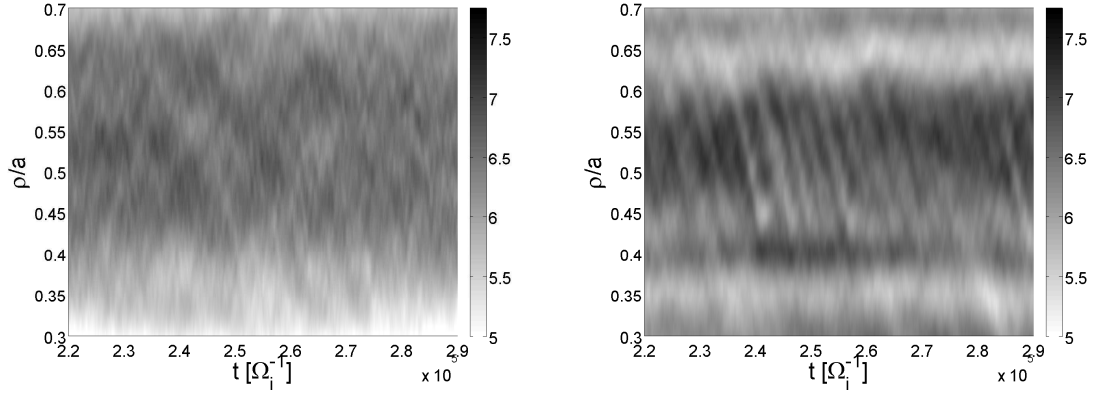


Figure 6.6: Radial and temporal profile of R_0/L_{Ti} for a *heated* (left) and *noise-controlled-heated* (right) simulation at the end of the simulations.

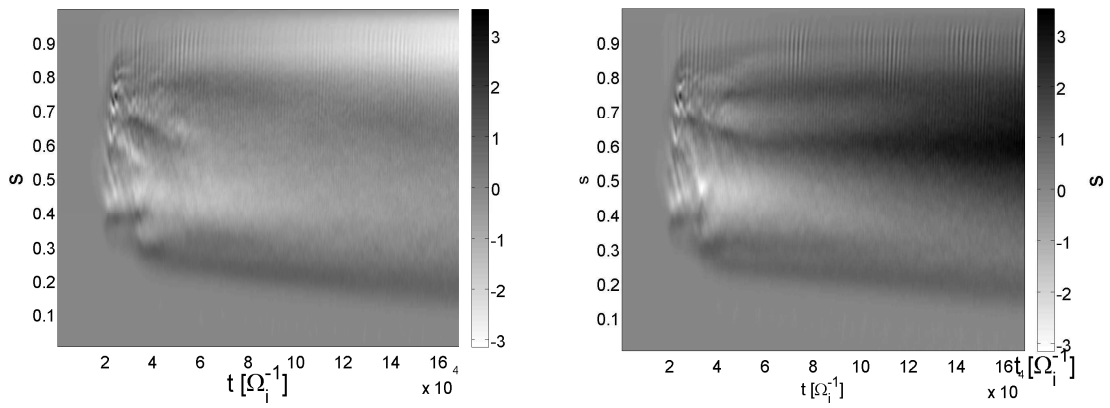


Figure 6.7: Radial and temporal evolution of $\nabla \bar{\phi}$ for a 80M *transient* simulation with (left) and without (right) the VNL.

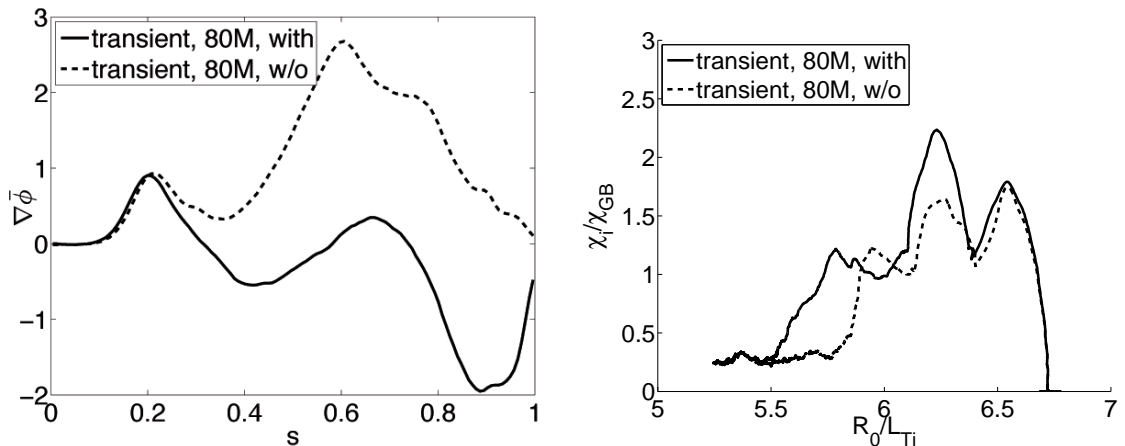


Figure 6.8: Radial structure of $\nabla\bar{\phi}$ averaged between $t = 10^5$ and $t = 1.5 \cdot 10^5 \Omega_i^{-1}$ (left) and χ_i/χ_{GB} as a function of R_0/L_{Ti} (both profiles are radially averaged between $\tilde{\rho} = 0.4$ and $\tilde{\rho} = 0.6$) for a 80M *transient* simulation with (solid line) and without (dashed line) the VNL.

6.2 The influence of the v_{\parallel} nonlinearity

6.2.1 General considerations

In this Section, the role of the v_{\parallel} nonlinearity is examined. Including the v_{\parallel} nonlinearity (VNL) means retaining the term $\left. \frac{dv_{\parallel}}{dt} \right|_1$ in the equations of motion. Historically, this term did not appear when the gyrokinetic equation was obtained by averaging over the gyro-angle [34], but appeared in the Hamiltonian and Lagrangian approach [65]. From the physical point of view, this term produces nonlinear Landau damping. The role of this term is still controversial. It is of order $\mathcal{O}(\epsilon_g^2)$: from the gyrokinetic ordering, its contribution should be small. Significant differences have been observed on the zonal flow structure by the ORB5 code in toroidal geometry [116] at $\rho_* = 1/96$. The same effects were found by the global PIC code UCAN [117] at $\rho_* = 1/90$, where the saturation level was found to be reduced with the v_{\parallel} nonlinearity. However this effect was "strongly diminished" at $\rho_* = 1/180$. In [118], two CYCLONE simulations with and without the VNL with the global PIC code GTC are presented. It is found that the field energy of the zonal flow is two times larger when the VNL is included (in agreement with the UCAN results) and that the relaxation is much faster. The authors invoke possible influence of the VNL, although the study is not very detailed. Unfortunately, all these PIC simulations

used relatively few markers per cell: the UCAN simulations used 4 particles/cell, GTC simulations used 10 and ORB5 simulations used 32. These are quite low numbers for collisionless simulations and no convergence studies have been performed for these cases. In addition, ORB5 simulations did not have the field-aligned Fourier filter technique but had a rectangular filter, thus increasing the number of Fourier modes by 25, but used an optimized loading technique. Later on, ORB5 simulations without optimized loading but with a field-aligned filter revealed few differences when retaining or dropping the VNL [119]. Unfortunately these simulations did not have the noise diagnostic; it is likely that they became noisy during the late nonlinear phase, where differences are observed in the zonal flow structure with and without the VNL (see Fig. 7 of [119]). In Ref. [115], 4D and 5D simulations in slab geometry with the global PIC code G3D and the global Eulerian code G5D revealed an insignificant contribution of the VNL. Finally, local Eulerian simulations using the Eulerian code GYRO and the flux-tube PIC code GEM [120] showed no measurable effects of the VNL.

Now that the numerical properties of ORB5 have been drastically improved with the field-aligned filter, the fluctuation entropy and the noise-control algorithms, the influence of the VNL can be revisited with more confidence in the results. Standard CYCLONE simulations (*transient*, *noise-controlled* and *fixed-gradient-noise-controlled*) presented in the previous Section have been run by dropping the VNL term $\left. \frac{dv_{||}}{dt} \right|_1$ in the equations of motion. The value of ρ^* has been set to $1/184.7$ which is a moderate value. For large ρ^* the VNL may play an important role but no simulations have been performed as such small plasmas are unrealistic.

6.2.2 Results for decaying turbulence

Fig. 6.7 shows the radial and temporal evolution of the gradient of zonal flows $\nabla \bar{\phi}$ for 80M *transient* simulations with and without zonal flows. It can be seen that these structures start to differ after the first burst. In the end of the simulation, the zonal flow profiles are quite different. This is better seen on the left plot of Fig. 6.8 where they are averaged between $t = 10^5$ and $t = 1.5 \cdot 10^5 \Omega_i^{-1}$. The values at the edge are of different sign and $\nabla \bar{\phi}$ is peaked at mid-radius for the case without VNL. From these plots, it could be concluded that the VNL has a strong influence on the zonal flow structures. However, a look at the heat diffusivity as a function of the normalized temperature gradient (right plot of

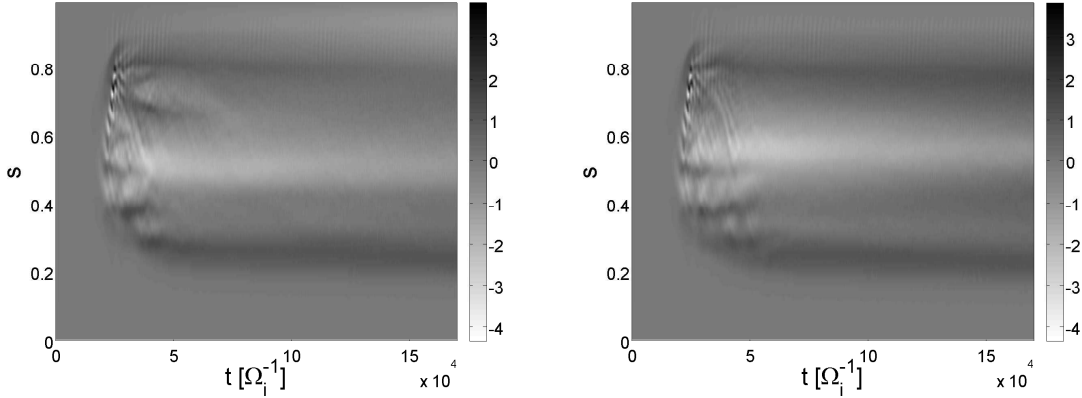


Figure 6.9: Radial and temporal evolution of $\nabla\bar{\phi}$ for a 320M *transient* simulation with(left) and without(right) the VNL.

Fig. 6.8) indicates that the simulations end up completely dominated by noise: R_0/L_{Ti} decreases while χ_i/χ_{GB} stays at a relatively constant value. The signal to noise ratio of these simulations falls below 10 at $t = 4 \cdot 10^4 \Omega_i^{-1}$ and is only around 2 at the end of the simulation (see Fig. 6.11). These simulations have 250 particles per Fourier mode. In the following, the possibility that the differences observed with and without the VNL are due to noise is investigated.

First, *transient* simulations with 320M markers have been performed. The 2D zonal flow gradient structure is plotted on Fig. 6.9 and its time-averaged profile is represented on Fig. 6.10. From these figures, the VNL seems to have very little influence on the zonal flow profile. The comparison between 320M and 80M *transient* simulations tend to confirm that the differences in the zonal flow structure previously attributed to the absence of VNL are due to numerical noise. Note that for all *transient* simulations, the signal to noise ratio for the averaging times of Figs. 6.8 and 6.10 is below 3, indicating that the quality of these simulations for late times is extremely poor. This is also seen in the χ_i/χ_{GB} vs R_0/L_{Ti} plot of the 320M *transient* simulation (see right plot of Fig. 6.10). In the end of the simulation the temperature profile flattens while the heat diffusivity stays constant. Therefore it is desirable to have noise-controlled simulations to further look at the effects of the VNL.

Unsurprisingly, the noise-controlled simulations show a much better signal to noise ratio (see Fig. 6.11) compared to the *transient* simulations. However it continually decreases: the noise control algorithm allows to run a simulation much longer before it gets domi-

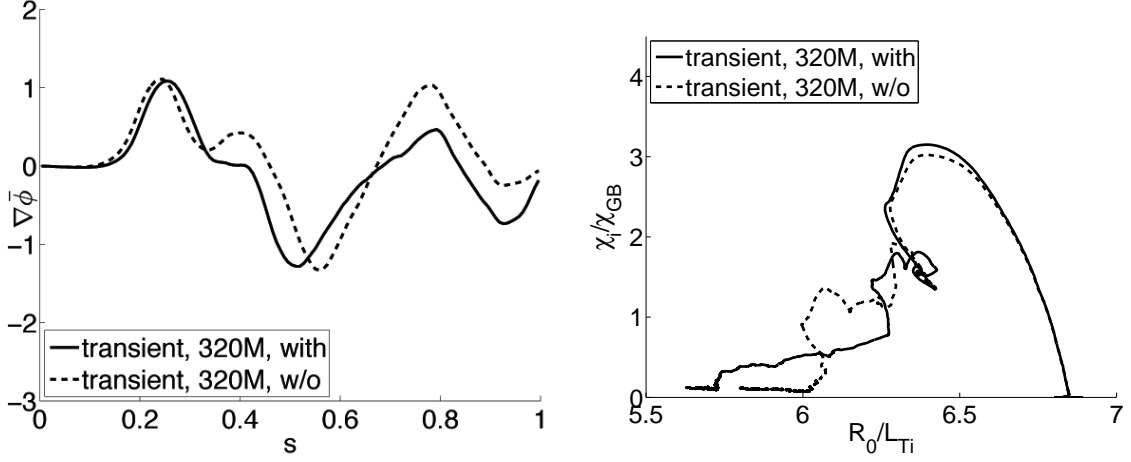


Figure 6.10: Radial structure of $\nabla\bar{\phi}$ averaged between $t = 10^5$ and $t = 1.5 \cdot 10^5 \Omega_i^{-1}$ (left) and χ_i/χ_{GB} as a function of R_0/L_{Ti} (both profiles are radially averaged between $\tilde{\rho} = 0.4$ and $\tilde{\rho} = 0.6$) for a 320M *transient* simulation with (solid line) and without (dashed line) the VNL.

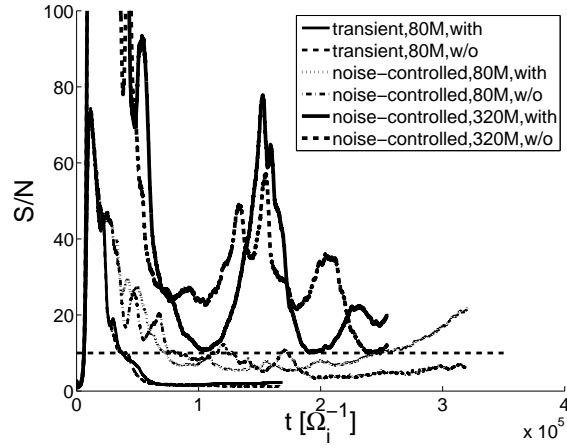


Figure 6.11: Signal to noise ratio vs time for a *transient* simulation with (solid line) and without (dashed line) the VNL, for a 80M markers noise-controlled simulation with (dotted line) and without (dashed-dotted line) the VNL, and for a 320M markers noise-controlled simulation with (thick solid line) and without (thick dashed line) the VNL. The horizontal line shows a signal to noise ratio of 10.

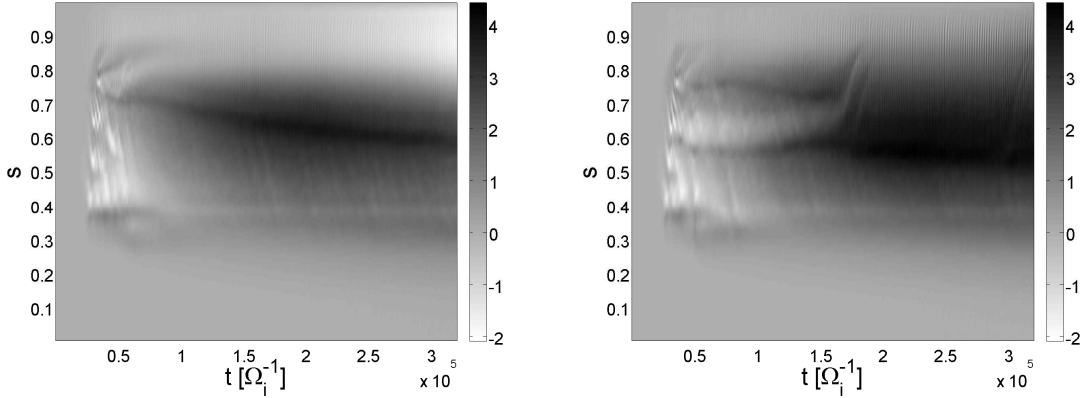


Figure 6.12: Radial and temporal evolution of $\nabla\bar{\phi}$ for a 80M *noise-controlled* simulation with (left) and without (right) the VNL.

nated by statistical noise. At the end of the simulation, the signal to noise ratio increases: when it becomes too small, there is a spurious growth of the zonal flow which in turn affects the signal to noise ratio. This is of course purely numerical and gives the indication that it is useless to pursue the simulation. Like for the *transient* simulation, including the VNL or not does not significantly modify the signal to noise ratio.

Fig. 6.12 presents the radial and temporal evolution of $\nabla\bar{\phi}$ for 80M noise-controlled simulations, and Fig. 6.13 shows the radial structure of $\nabla\bar{\phi}$ averaged between different times of the simulation. Between $t = 10^5$ and $t = 1.5 \cdot 10^5 \Omega_i^{-1}$, the time-averaged structures with and without the VNL are different: the simulation without the VNL has two peaks while the simulation with the VNL has one. Later in time, these two peaks merge to form only one and there are much less differences in the zonal flow structure compared to the *transient* case. The main difference can be observed near the edge where a negative radial potential appear for the case with the VNL, which could explain the late time increase of the signal to noise ratio. According to the empiric rule that this quantity should be higher than 10, the conclusion is that the results are still questionable. Therefore, noise-controlled simulations with $4 \times 80\text{M} = 320\text{M}$ markers have been performed.

Fig. 6.15 shows the radial and temporal evolution of $\nabla\bar{\phi}$ for noise-controlled simulations with 320M markers, with and without the VNL. These structures are very similar even at the end of the simulations. Fig. 6.16 shows the same time-averages of $\nabla\bar{\phi}$ than for the 80M case. There is no numerical growth of the zonal flow near the edge and the VNL seems to play a very little role. This shows that noisy PIC simulations may predict a

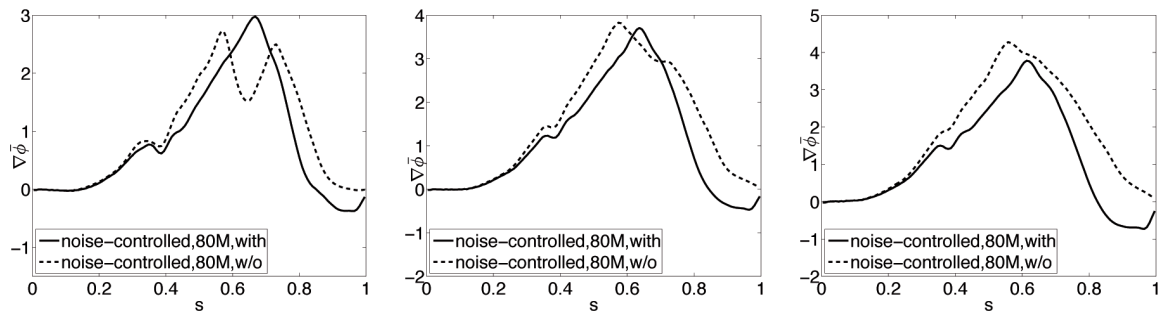


Figure 6.13: Radial structure of $\nabla\bar{\phi}$ with (solid line) and without (dashed line) the VNL, averaged between $t = 10^5$ and $t = 1.5 \cdot 10^5 \Omega_i^{-1}$ (left), between $t = 1.5 \cdot 10^5$ and $t = 2 \cdot 10^5 \Omega_i^{-1}$ (middle) and between $t = 2 \cdot 10^5$ and $t = 2.5 \cdot 10^5 \Omega_i^{-1}$ (right) for a 80M markers noise-controlled simulation.

completely wrong structure of the zonal flow. In this respect, it is extremely likely that the influence of the VNL previously reported has no physical origin but is the consequence of statistical noise. The χ_i/χ_{GB} vs R_0/L_{Ti} plots (Fig. 6.14) reveal that the VNL does not affect the transport much with 320M markers. With 80M markers, these curves are similar to those observed in the *transient* case (Fig. 6.8): the heat diffusivity is constant but the temperature gradient is flattening below the critical value of $R_0/L_{Ti} = 6$, indicating that noise is dominating the simulation.

The most striking result of these simulations is the different zonal flow structures between the 80M and the 320M cases. Even if the VNL does not affect the zonal flow structure it does not imply that the latter is correct. Therefore, one can argue that the irrelevance of the VNL on the zonal flow structure is a necessary, but not sufficient condition for convergence.

Finally, previous works on the VNL are discussed. In the publications dealing with the influence of the VNL with PIC codes in tokamak geometry [117], [118], the noise problem was not mentioned. For PIC simulations in slab geometry [115], the entropy balance equation is derived and the influence of the VNL is thoroughly studied. The simulations used 67M markers, did not have dissipation but were run in slab geometry. In the absence of toroidal effects the VNL is proportional to \vec{E}_{\parallel} which is insensitive to zonal flows. Because the latter are dominant in ITG collisionless simulations, this may explain why the VNL should have little effect. This is not what has been found in Ref. [121] with the TORB code. The simulations done in Ref. [121] have been revisited and new con-

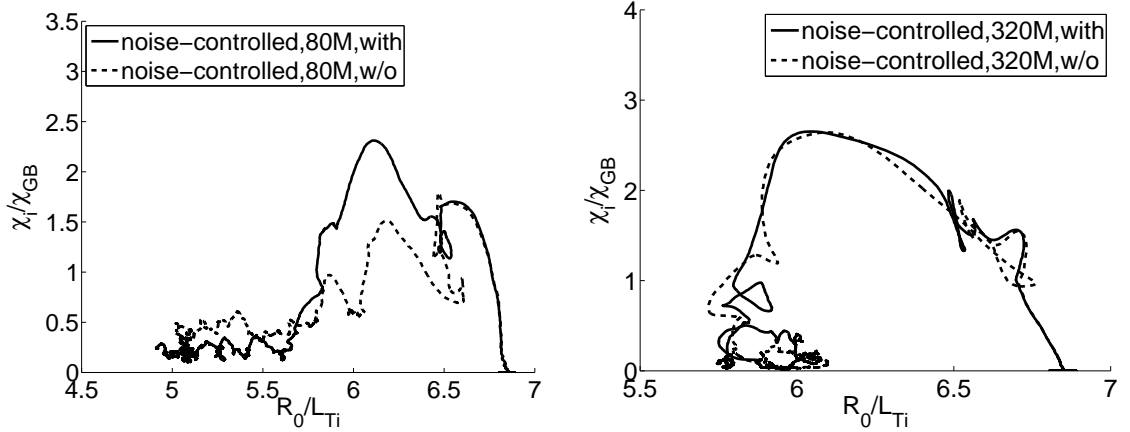


Figure 6.14: χ_i/χ_{GB} as a function of R_0/L_{Ti} (both profiles are radially averaged between $\tilde{\rho} = 0.4$ and $\tilde{\rho} = 0.6$) for a 80M markers (left) and a 320M markers (right) noise-controlled simulation with (solid line) and without (dashed line) the VNL.

clusions have been found. This is due to the different choice of optimized loading. The one used in [121] originates from the markers distribution at a given time in the nonlinear phase and is consequently highly structured in the radial direction due to the zonal flow structure. This was unfortunately an inappropriate choice as this radial structure is indeed time evolving. On the contrary, the optimized loading used in this work has been constructed based on the results of several ITG simulations, is a smoother one and does not degrade the quality of the simulation. Therefore if it is not properly applied, the optimized loading can lead to erroneous conclusions. For ORB5 simulations in tokamak geometry [116], an optimized loading is applied but the numerical properties have only been checked with the energy conservation theorem which is a second order moment: it does not capture the filamentation of phase space in velocity, but it is not sufficient to correctly diagnose a simulation. Although the optimized loading tries to solve this problem by putting more markers in regions where the distribution function has a strong velocity dependence, it is likely that the optimized loading was not sufficient to remove the numerical noise. When using the optimized loading, the sum of the weights squared and consequently the noise, (4.134), is usually decreased by a factor 10. This reduction is much less than the one obtained by going from a rectangular to a field-aligned filter which is approximatively ρ^* . It means that roughly, old ORB5 simulations in Ref. [116] would have needed at least $1/10(\rho^*)^{-1} \sim 10$ times more particles to reach convergence. In addition, the relatively large value of ρ^* for these simulations may have enhanced the

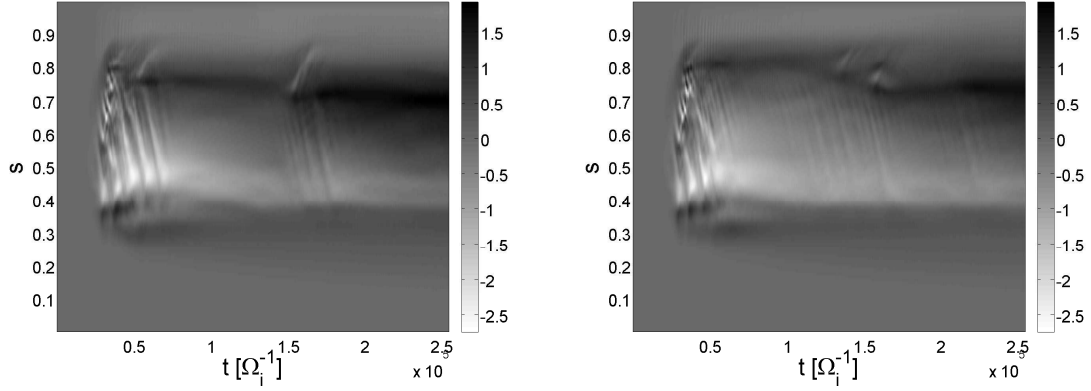


Figure 6.15: Radial and temporal evolution of $\nabla\bar{\phi}$ for a 320M markers noise control simulation with(left) and without(right) the VNL.

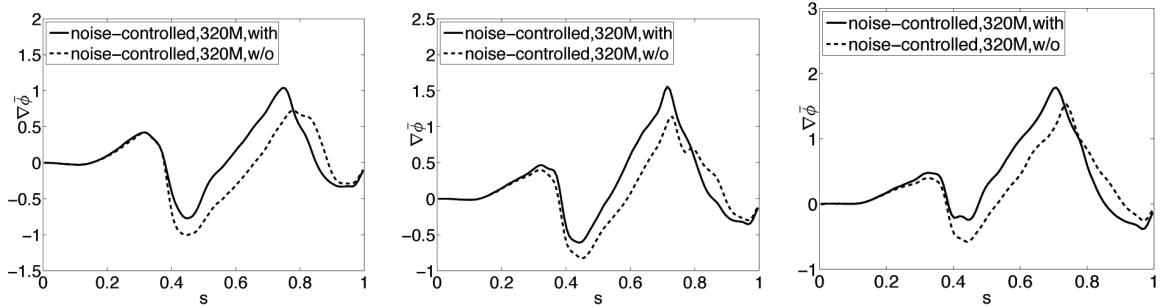


Figure 6.16: Radial structure of $\nabla\bar{\phi}$ with (solid line) and without (dashed line) averaged between $t = 10^5$ and $t = 1.5 \cdot 10^5 \Omega_i^{-1}$ (left), between $t = 1.5 \cdot 10^5$ and $t = 2 \cdot 10^5 \Omega_i^{-1}$ (middle) and between $t = 2 \cdot 10^5$ and $t = 2.5 \cdot 10^5 \Omega_i^{-1}$ (right) for a 320M markers noise-controlled simulation.

role of the VNL. Fortunately, it is now proved with the help of the numerous numerical improvements in ORB5 that the VNL has very little influence on decaying turbulence simulations provided the numerical noise is sufficiently small.

6.2.3 Results for driven simulations

The final case studied is the *fixed-gradient-noise-controlled* case, where the noise-control operator allows the system to maintain an average temperature gradient above the non-linear critical value. The stronger turbulence is reflected in higher electric fields, which means that the influence of the VNL could be bigger. It contains two terms: the first one is proportional to E_{\parallel} and is therefore insensitive to zonal flows as discussed above. The

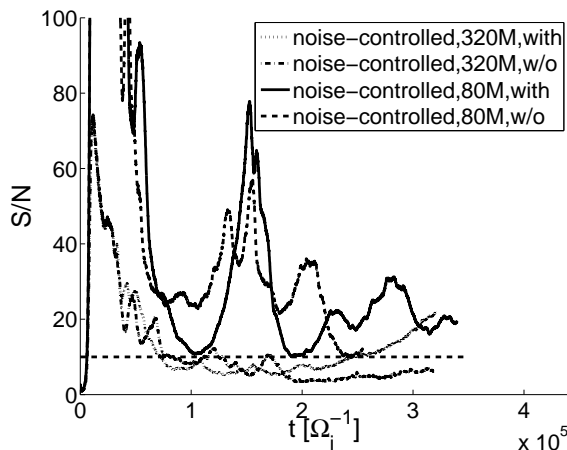


Figure 6.17: Signal to noise ratio vs time for a 320M markers noise-controlled simulation with (solid line) and without (dashed line) the VNL and for a 80M noise-controlled simulation with (dotted line) and without (dash-dot line) the VNL.

second term is a toroidal effect of order $\epsilon_g \epsilon_B$ (which is ϵ_a smaller than the first term) that is sensitive to zonal flows.

Noise-controlled-fixed gradient simulations have high and constant signal to noise ratios, as can be seen from Fig. 6.18. With 80M markers, the signal to noise ratios oscillate around 20. The radial electric field structure is displayed on Fig. 6.19. From these plots the VNL does not seem to play an important role. Although local bursts happen at different times, the global structure of the zonal flow looks the same: on the left plot of Fig. 6.20, the peaks in the radial electric field are radially slightly shifted and have different amplitudes. Such differences are reasonable considering the chaotic character of turbulence. The main discrepancy is located at the edge of the plasma. The only notable difference observed in these simulations is in the zonal density. Fig. 6.21 shows a time average of the radial profile of the zonal density $\delta n_i^{(0,0)}$. These profiles are similar except in the edge region the charge builds up with a different sign depending on whether the VNL is included or not. This phenomenon has also been observed in decaying turbulence. When the VNL is turned on, a positive charge accumulates at the plasma edge but when the VNL is turned off a negative charge builds up. On the other hand, the zonal flow does not follow this behavior as it is shielded near the plasma edge (see Section 4.5.8). The important point is that this unphysical behavior does not affect regions where turbulence is present.

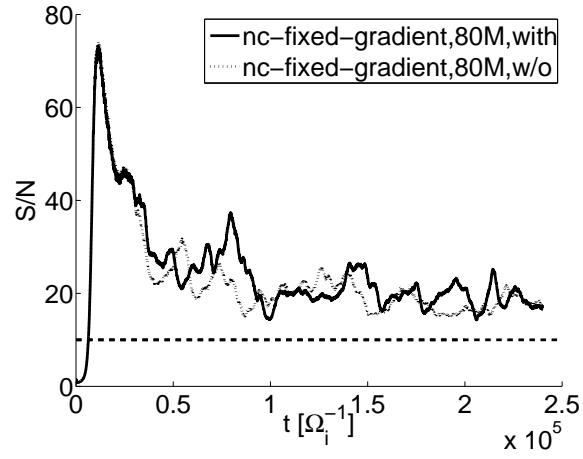


Figure 6.18: Signal to noise ratio vs time for a 80M *fixed-gradient-noise-controlled simulation* with (solid line) and without (dotted line) the VNL. The horizontal line indicates a signal to noise ratio of 10.

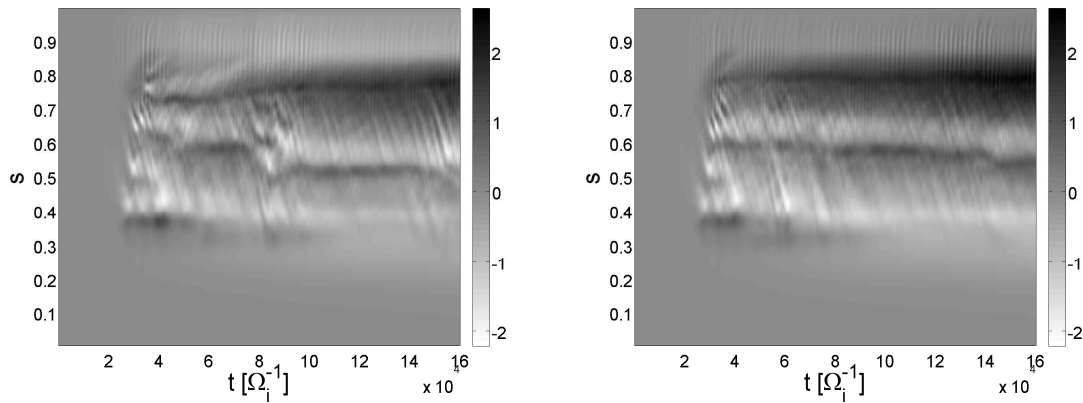


Figure 6.19: Radial and temporal evolution of $\nabla \bar{\phi}$ for a 80M markers *noise-controlled-fixed-gradient* simulation with (left) and without (right) the VNL.

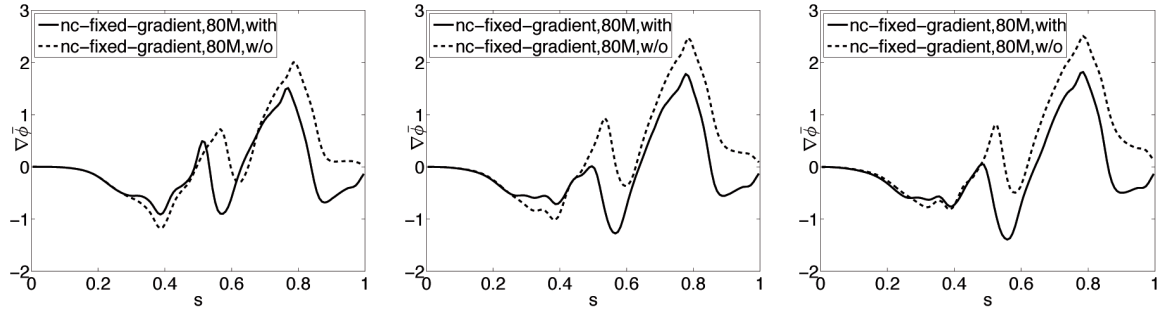


Figure 6.20: Radial structure of $\nabla \bar{\phi}$ with (solid line) and without (dashed line) averaged between $t = 10^5$ and $t = 1.5 \cdot 10^5 \Omega_i^{-1}$ (left), between $t = 1.5 \cdot 10^5$ and $t = 2 \cdot 10^5 \Omega_i^{-1}$ (middle) and between $t = 2 \cdot 10^5$ and $t = 2.5 \cdot 10^5 \Omega_i^{-1}$ (right) for a 80M markers fixed-gradient-noise-controlled simulation.

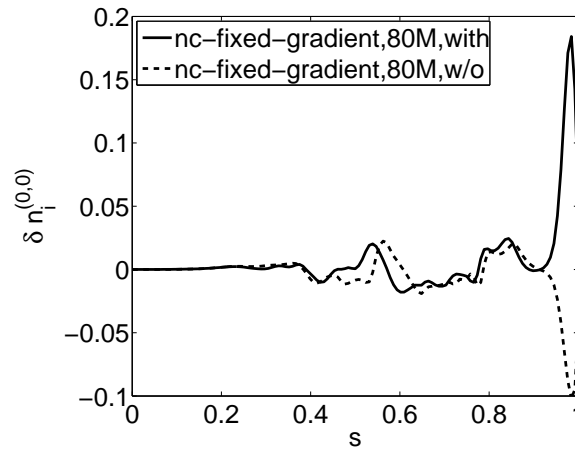


Figure 6.21: Radial profile of the zonal density for 80M *fixed-gradient-noise-controlled* simulations with (solid line) and without (dashed line) the VNL, averaged between $t = 1.5 \cdot 10^5$ and $t = 2 \cdot 10^5 \Omega_i^{-1}$.

6.2.4 Variability with initial conditions

Up to now, the impact of the VNL on the zonal flow structures has been studied for both decaying and fixed-gradient simulations. The influence on the heat diffusivity has been checked for decaying simulations, which are not suited for quantitative predictions. On the other hand, driven simulations reach a steady state and are therefore able to quantify the heat transport. It is of course desirable to provide an error bar on the measured heat fluxes or heat diffusivities. This is closely related to the intrinsic variability of the turbulence, which will be defined as the statistical variation of a physical quantity due to a change of initial conditions. Preferentially, a large number of simulations with different initial states but same physical and numerical parameters must be run to be able to make an ensemble average. This becomes especially important as the critical gradient is approached: the measured transport can have large relative variations. Consequently the variability of these simulations must be estimated as accurately as possible for both cases with and without the VNL. This is done as follows. For a given set of numerical and physical parameters, n_{sim} simulations are run with different initial states. The aim of these simulations is to measure a given physical quantity such as the ion diffusivity χ_i . For each individual simulation, a moving time-average of χ_i , starting at time t_i and of width Δt_{ma} is performed and will be written $\tilde{\chi}_i$. The width Δt_{ma} must be large enough to include a typical life time of a burst. In this work, $\Delta t_{ma} = 400a/c_s$ has been used, based on Ref. [16]. Then, for each time, the average (resp. the sample standard deviation) of $\tilde{\chi}_i$ over the different simulations can be calculated, which will be written $\langle \tilde{\chi}_i \rangle_n(t)$ (resp. $s_n(\tilde{\chi}_i)(t)$). One distinguishes the sample standard deviation with the standard deviation (the difference is a factor $\sqrt{n_{\text{sim}}}/\sqrt{n_{\text{sim}} - 1}$) as in practice $n_{\text{sim}} \gtrsim 3$. The intrinsic variability of the heat diffusivity, noted V_{χ_i} , is then the average over time of $s_n(\tilde{\chi}_i)(t)$:

$$V_{\chi_i} = \langle s_n(\tilde{\chi}_i) \rangle_t \quad (6.18)$$

The error bar of χ_i for a given set of physical parameters is chosen to be twice standard error of the mean, i.e. $2I_{\chi_i} = 2V_{\chi_i}/\sqrt{n_{\text{sim}}}$ in order to have a 95.45% confidence interval. The procedure to fix the error bars on the heat diffusivity assumes that the simulations are numerically converged. Here, the convergence is based on Ref. [58]. The number of markers is sufficient as the signal to noise ratio is around 20. The Krook damping coefficient is one tenth of the maximum linear growth rate and is small enough. Simulations

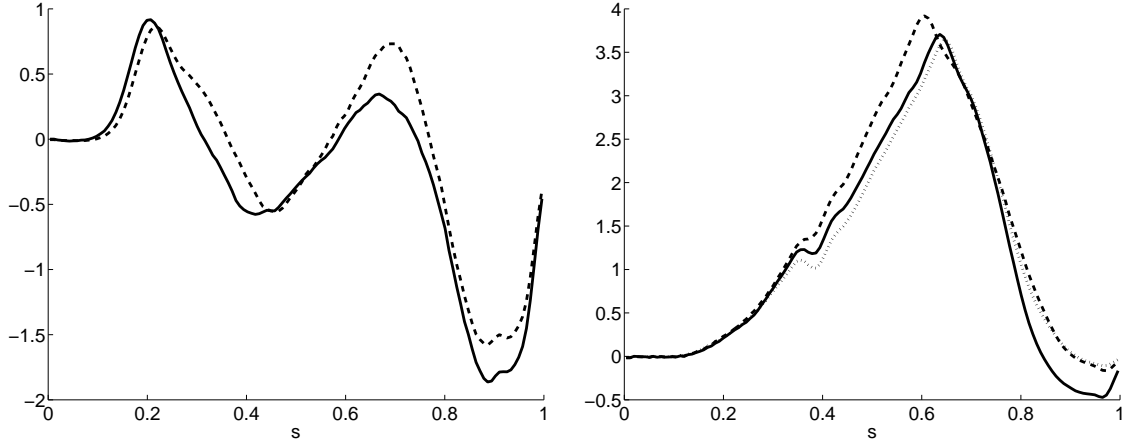


Figure 6.22: Left: radial structure of $\nabla\bar{\phi}$ with white noise (solid line) and mode (dashed line) initialization, averaged between $t = 10^5$ and $t = 1.5 \cdot 10^5 \Omega_i^{-1}$ for a 80M markers *transient* simulation. Right: radial structure of $\nabla\bar{\phi}$ with and (dashed line) and without (dotted line) the VNL and with a mode initialization, averaged between $t = 1.5 \cdot 10^5$ and $t = 2 \cdot 10^5 \Omega_i^{-1}$ for a 80M markers *noise-controlled* simulation. The solid line is the same quantity for a white noise initialization with the VNL.

presented in Section 6.2.1 have been run with three different initializations: a white noise initialization, a mode initialization (see Eq. (4.69)) with $n_1 = 10, n_2 = 30, m_1 = 14$ and $m_2 = 42$ and a mode initialization with $n_1 = 15, n_2 = 25, m_1 = 21$ and $m_2 = 35$. They will be called initialization 1,2 and 3.

The left plot of Fig. 6.22 shows the radial structure of $\nabla\bar{\phi}$, averaged in the end of the nonlinear phase between $t = 10^5$ and $1.5 \cdot 10^5 \Omega_i^{-1}$ for 80M *transient* simulations with white noise and mode initializations (both with the VNL). These profiles are very similar, demonstrating that the results for *transient* simulations presented in Sec. 6.2.2 do not depend on the type of initialization. The right plot of Fig. 6.22 shows again the radial electric field profile for a 80M markers *noise-controlled* simulation with mode initialization, with and without the VNL. The differences are very small and the other initialization used here does not modify the conclusions exposed in Section 6.2.2.

Finally, the role of the initial state is examined for *fixed-gradient-noise-controlled simulations*. Six simulations (three different initializations, with and without the VNL) at an initial $R_0/L_{Ti} = 6.9$ have been performed. The global moving time averages

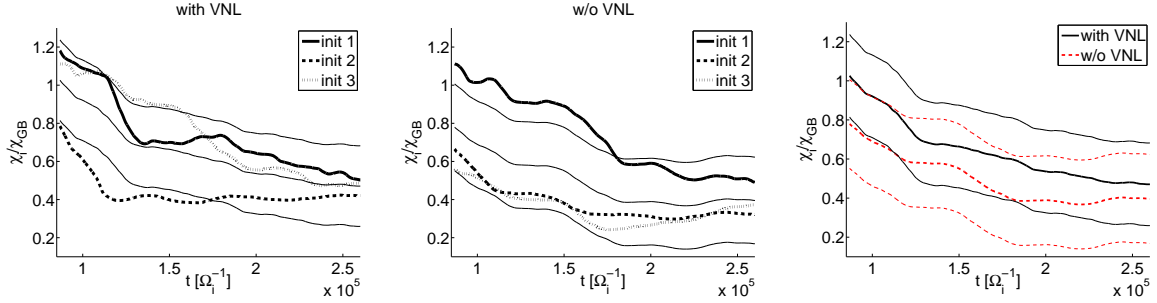


Figure 6.23: Moving time averages $\tilde{\chi}_i$ for a 80M noise-controlled-fixed-gradient simulation with initial $R_0/L_{Ti} = 6.9$ with (left) and without (middle) the VNL for the three different initializations. The thin lines are $\langle \tilde{\chi}_i \rangle_n(t) \pm 2I_{\chi_i}$. The right plot displays $\langle \tilde{\chi}_i \rangle_n(t) \pm 2I_{\chi_i}$ for a 80M noise-controlled-fixed-gradient simulation with (black, solid line) and without (red, dashed line) the VNL.

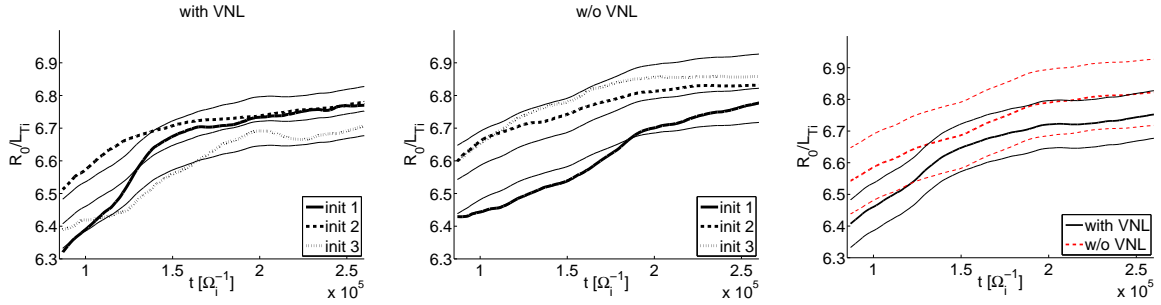


Figure 6.24: Moving time averages $\widetilde{\frac{R_0}{L_{Ti}}}$ for a 80M noise-controlled-fixed-gradient simulation with initial $R_0/L_{Ti} = 6.9$ with (left) and without (middle) the VNL for the three different initializations. The thin lines are $\langle \widetilde{\frac{R_0}{L_{Ti}}} \rangle_n(t) \pm 2I_{R_0/L_{Ti}}$. The right plot displays $\langle \widetilde{\frac{R_0}{L_{Ti}}} \rangle_n(t) \pm 2I_{R_0/L_{Ti}}$ for a 80M noise-controlled-fixed-gradient simulation with (black, solid line) and without (red, dashed line) the VNL.

$\langle \tilde{\chi}_i \rangle_n(t), \langle \frac{R_0}{L_{Ti}} \rangle_n(t)$ with the corresponding error bars $2I_{\chi_i}, 2I_{R_0/L_{Ti}}$ are represented on Figs. 6.23 and 6.24. When the VNL is included, the χ_i/χ_{GB} curves corresponding to the three different initializations are very close. The intrinsic variability is slightly higher when the VNL is removed. However, by looking at the right plot of Fig. 6.23, one sees that the VNL has no significant influence on the heat transport, as the two regions enclosed by $\langle \tilde{\chi}_i \rangle_n(t) \pm 2I_{\chi_i}$ with and without the VNL overlap. The same conclusions hold for R_0/L_{Ti} . The same exercise has been done with an initial gradient of $R_0/L_{Ti} = 7.6$. Here, the intrinsic variability is slightly higher when the VNL is included, however the comparison between the two cases (right plots of Figs. 6.25 and 6.26) indicates a small influence of the VNL, as the two regions spanned with the error measure are almost overlapping. Note that the simulation without the VNL predicts a smaller heat diffusivity with a higher gradient, but one cannot conclude that the VNL has a significant effect on the transport. Therefore, the same set of simulations has been rerun with an initial normalized temperature gradient of $R_0/L_{Ti} = 8.4$. In this case the VNL impact is almost negligible. Note that due to the high turbulent activity it is more difficult to reach a steady state.

In conclusion, with the help of the procedure originally used in [58] for quantifying the intrinsic variability of physical quantities, it has been shown that the effect of the VNL for collisionless ITG *fixed-gradient-noise-controlled* simulations, if any, is small. The major difference between decaying and driven simulations is that the latter exhibit a constant burst activity that has to be measured in an average sense, hence the need for an estimation of the intrinsic variability. In the future, it will be interesting to see if these conclusions still hold for parallel momentum transport.

6.2.5 The influence of the VNL on the fluctuation entropy

Next, the influence of the VNL on the numerical properties of the model is studied. First, as previously observed, the VNL has no influence on the noise to signal ratio for all the cases considered. For *transient* simulations, the energy conservation theorem, Eq. 3.84, is not valid anymore when the VNL term is dropped out. This can be seen on the left plot of Fig. 6.29. The case with the VNL has a relative conservation of energy of about 30% up to $t = 4.6 \cdot 10^4 \Omega_i^{-1}$ which is a good value for a *transient* PIC simulation. After this time, the relative energy conservation degrades linearly. It is interesting to note that this curve

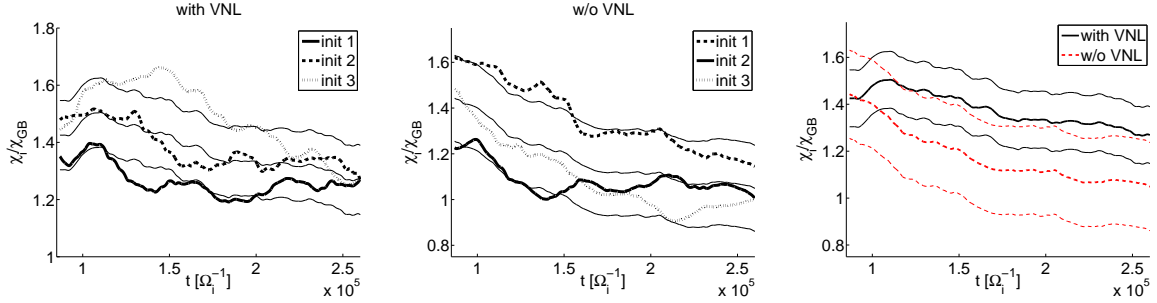


Figure 6.25: Moving time averages $\tilde{\chi}_i$ for a 80M noise-controlled-fixed-gradient simulation with initial $R_0/L_{Ti} = 7.6$ with (left) and without (middle) the VNL for the three different initializations. The thin lines are $\langle \tilde{\chi}_i \rangle_n(t) \pm 2I_{\chi_i}$. The right plot displays $\langle \tilde{\chi}_i \rangle_n(t) \pm 2I_{\chi_i}$ for a 80M noise-controlled-fixed-gradient simulation with (black, solid line) and without (red, dashed line) the VNL.

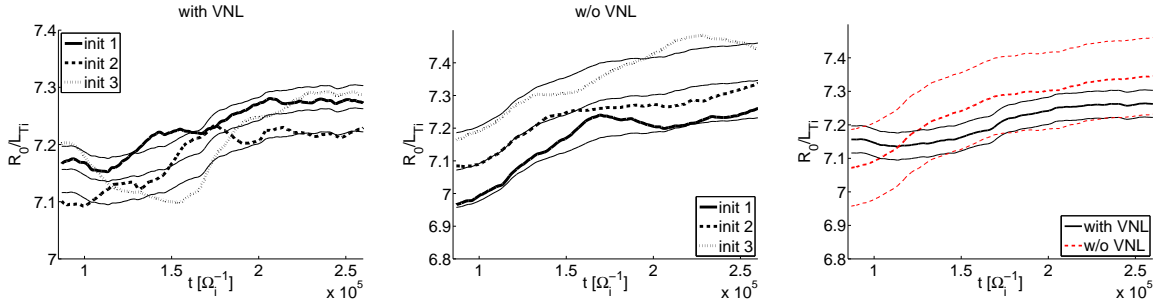


Figure 6.26: Moving time averages $\widetilde{\frac{R_0}{L_{Ti}}}$ for a 80M noise-controlled-fixed-gradient simulation with initial $R_0/L_{Ti} = 7.6$ with (left) and without (middle) the VNL for the three different initializations. The thin lines are $\langle \widetilde{\frac{R_0}{L_{Ti}}} \rangle_n(t) \pm 2I_{R_0/L_{Ti}}$. The right plot displays $\langle \widetilde{\frac{R_0}{L_{Ti}}} \rangle_n(t) \pm 2I_{R_0/L_{Ti}}$ for a 80M noise-controlled-fixed-gradient simulation with (black, solid line) and without (red, dashed line) the VNL.

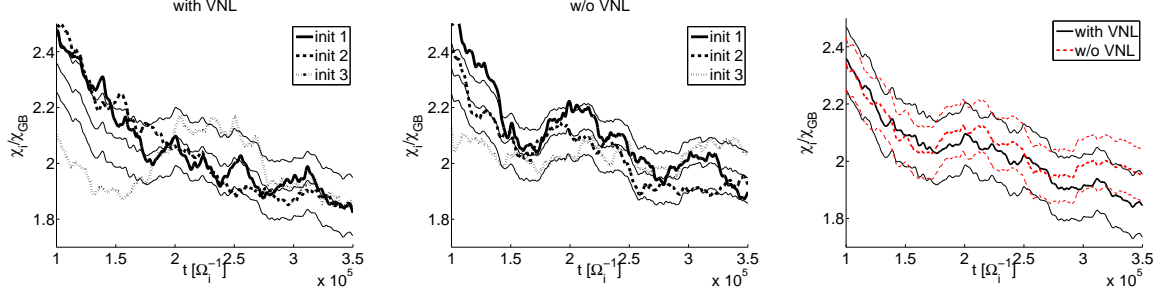


Figure 6.27: Moving time averages $\tilde{\chi}_i$ for a 80M noise-controlled-fixed-gradient simulation with initial $R_0/L_{T_i} = 8.4$ with (left) and without (middle) the VNL for the three different initializations. The thin lines are $\langle \tilde{\chi}_i \rangle_n(t) \pm 2I_{\tilde{\chi}_i}$. The right plot displays $\langle \tilde{\chi}_i \rangle_n(t) \pm 2I_{\tilde{\chi}_i}$ for a 80M noise-controlled-fixed-gradient simulation with (black, solid line) and without (red, dashed line) the VNL.

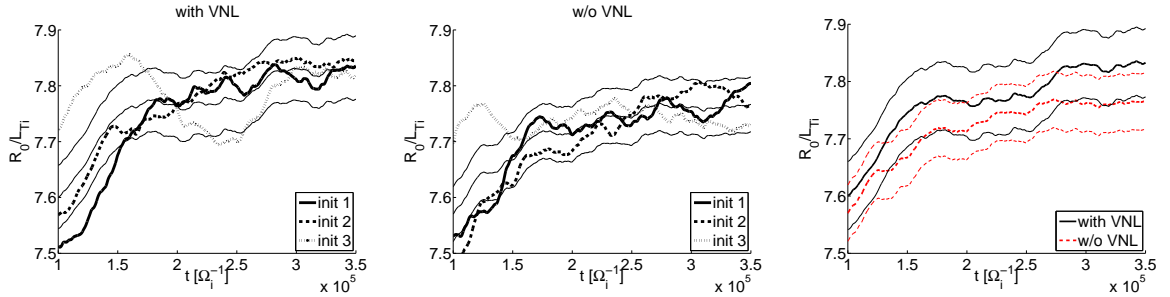


Figure 6.28: Moving time averages $\widetilde{\frac{R_0}{L_{T_i}}}$ for a 80M noise-controlled-fixed-gradient simulation with initial $R_0/L_{T_i} = 8.4$ with (left) and without (middle) the VNL for the three different initializations. The thin lines are $\langle \widetilde{\frac{R_0}{L_{T_i}}} \rangle_n(t) \pm 2I_{R_0/L_{T_i}}$. The right plot displays $\langle \widetilde{\frac{R_0}{L_{T_i}}} \rangle_n(t) \pm 2I_{R_0/L_{T_i}}$ for a 80M noise-controlled-fixed-gradient simulation with (black, solid line) and without (red, dashed line) the VNL.

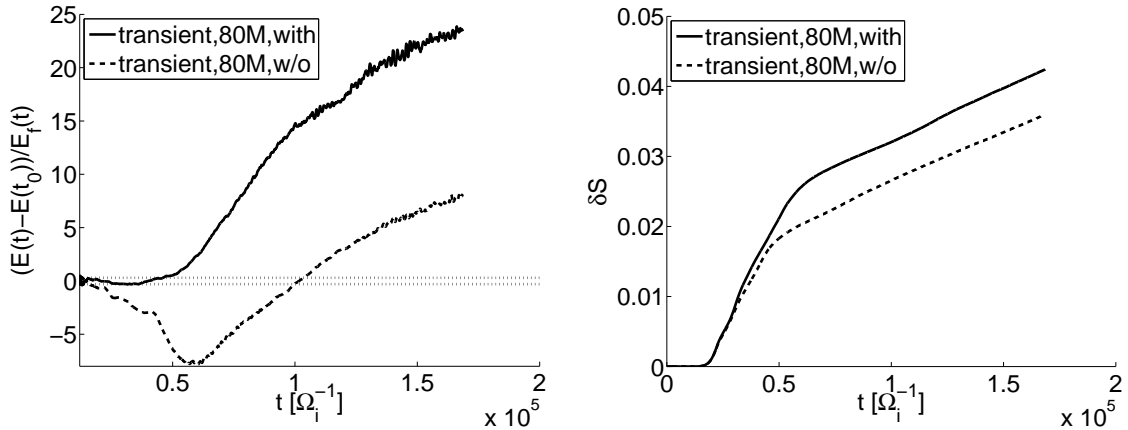


Figure 6.29: Time evolution of relative energy conservation (left) and fluctuation entropy (right) for a 80M markers *transient* simulation with (solid line) and without (dashed line) the VNL. The dotted lines mean a relative conservation of energy of 30%.

starts to rise at the time where the signal to noise ratio falls below 10 (Fig. 6.11). Fig. 6.29 also reveals that the relative energy conservation is completely lost when the VNL is not included, even if this term is of order ρ_* smaller than the others. First, this shows the importance of deriving analytically a conservation theorem without any approximation in order to check the correct implementation of the model and the quality of a simulation. Second, it means that although it has a negligible effect on transport, the VNL should be preferentially kept in *transient* simulations for numerical reasons.

The right plot of Fig. 6.29 shows the time evolution of the fluctuation entropy δS for *transient* simulations. These quantities start to differ at around $t = 5 \cdot 10^4 \Omega_i^{-1}$, when the signal to noise ratio falls below 10. Then the noise becomes dominant and δS linearly grows. The VNL does not seem to have any effect on the growth of entropy. It reflects the fact that the VNL has no influence on numerical noise.

When the Krook operator is turned on, the energy conservation theorem is not valid anymore but the fluctuation entropy balance equation still holds. This equation becomes no longer valid when the VNL is removed. More specifically, the term $\left. \frac{\partial \delta f}{\partial v_{\parallel}} \frac{dv_{\parallel}}{dt} \right|_1$ is neglected in the LHS of Eq. (6.3). This situation is equivalent to a gyrokinetic equation with a spurious source term [115]. In the notations presented above, neglecting the VNL means dropping the curvature and the diamagnetic drift term that appear in D_{field} . This term reaches his maximum around the first peak of the nonlinear phase but is one order of magnitude smaller than D_{flux} ; in the late nonlinear phase, this term goes to zero. It

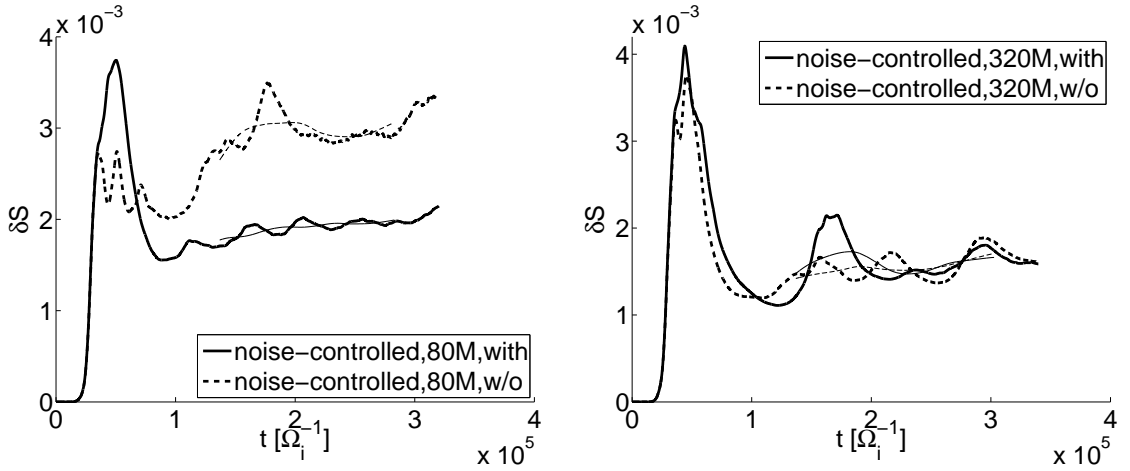


Figure 6.30: Time evolution of fluctuation entropy for a 80M (left) and 320M (right) markers *noise-controlled* simulation with (solid line) and without (dashed line) the VNL. The moving time-averages of width $400a/c_s$ (which corresponds to $7.4 \cdot 10^4 \Omega_i^{-1}$) and starting at $t = 1 \cdot 10^5 \Omega_i^{-1}$ are represented.

is therefore expected that the VNL should not significantly affect the fluctuation entropy balance equation. Fig. 6.30 shows the fluctuation entropy for 80M and 320M markers *noise-controlled* simulations, with and without the VNL. For the 80M case, δS is different depending on whether the VNL is retained or not, but these differences are much less pronounced for the 320M case. Again, the noise is the candidate to explain these discrepancies. In the case of *fixed-gradient-noise-controlled* simulation, due to the bursty character of the fluctuation entropy the moving time average is represented. Differences are relatively small. The non-conservation of the fluctuation entropy can be measured with the following quantity:

$$\delta S_{\text{bal}}(t) = \frac{\delta S(t) - \delta S(0) - \int_0^t \frac{d\delta S}{dt'} dt'}{\delta S(t)} \quad (6.19)$$

It is represented on the right plot of Fig. 6.31. This quantity is much higher for the case without the VNL. This feature has been observed in all the driven simulations. The non-conservation of fluctuation entropy increases due to the violation of the quasi-neutrality condition which leads to a systematic error between δS and $\int (dS/dt') dt'$. When the VNL is dropped off of the equations of motion, it acts like a source term in the Vlasov equation and the systematic error increases.

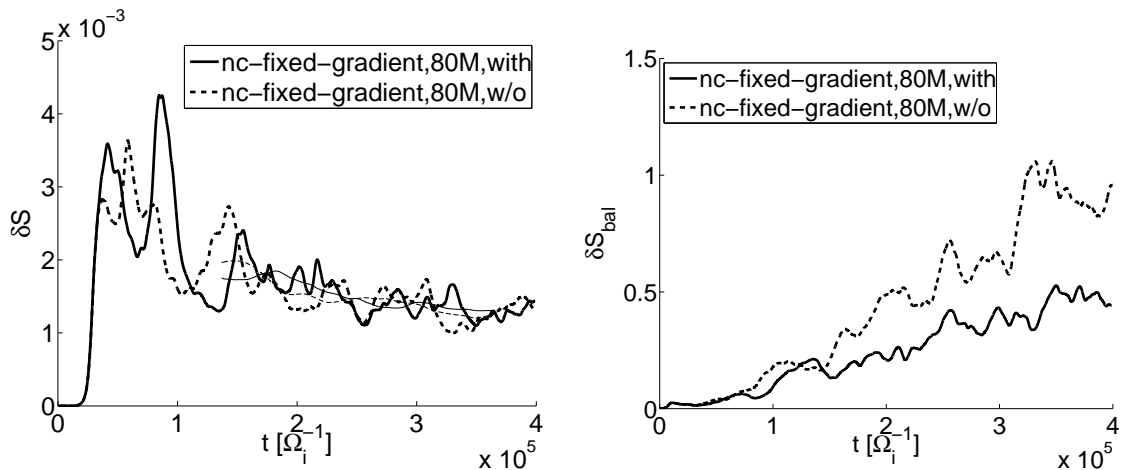


Figure 6.31: Time evolution of the fluctuation entropy (left) and the relative entropy conservation (right) for a $80M$ markers *fixed-gradient-noise-controlled* simulation with (solid thick line) and without (dashed thick line) the VNL. On the left plot, the moving time-averages of width $400a/c_s$ (which corresponds to $7.4 \cdot 10^4 \Omega_i^{-1}$) and starting at $t = 7.5 \cdot 10^4 \Omega_i^{-1}$ are represented.

6.3 Conclusions

In Section 6.1, it has been shown through the noise to signal ratio and the entropy diagnostics that decaying PIC simulations cannot be run for infinitely long times because they become unavoidably noise-dominated. Consequently, it is of primary importance for PIC codes to develop ways for estimating numerical noise to avoid erroneous conclusions. The example of the v_{\parallel} nonlinearity is in this sense representative. Its influence in previous reported works was, in fact, certainly the manifestation of numerical noise. Results presented here show that in reality this term does not play a significant role when the noise problem is correctly treated. It confirms the analytical picture that the VNL is orders of magnitude smaller than the leading terms in the gyrokinetic equation. This work is also in adequacy with Ref. [120]. In this paper, the Eulerian simulations obviously do not suffer from noise issues and no numerical noise study for the flux-tube PIC simulations (which used 32 markers per cell) has been presented. This is the same number used in ORB5 old results [116]. There are three arguments to explain those differences. First, flux-tube simulations do not experience profile relaxation, which could mean that the noise does not accumulate as rapidly as in global simulations where the fluxes go to zero. Second, the

key parameter that determines the noise in ORB5 is the number of markers per Fourier mode [76]: when going from a rectangular to a field-aligned Fourier filter without changing the number of markers the results are strongly improved. It is unclear how this translates in a flux-tube PIC code, but since they use field-aligned coordinates it could be that using a field-aligned filter in a global code is equivalent to using field-aligned coordinates in a flux-tube code. Reversely, one could imagine a flux-tube code in cartesian coordinates: more cells, hence more particles would be needed. Finally, GYRO simulations in Ref. [120] have a small ion-ion collisionality, which tends to isotropize the distribution function in the velocity space and could diminish the effect of the VNL. Unfortunately it is not mentioned whether GEM simulations had some collisions.

Chapter 7

The trapped electron model

7.1 General considerations

All the results presented up to here assumed adiabatic electrons, i.e. a fluid like character neglecting their inertia. From a physical point of view, this assumption is of course wrong at rational surfaces, wrong for trapped electrons and incompatible with electromagnetic perturbations. Another specificity of the Boltzman hypothesis is that the electron density perturbation is in phase with the electric potential. Due to the quasineutrality equation $n_e = n_i$, assuming adiabatic electrons implies that there is no particle transport. Experimentally, both electron anomalous heat and particle transport in tokamaks have been observed [122], [123]. An unexplained phenomenon is the *profile stiffness*: above a given threshold, the electron temperature gradient reacts very weakly to further increase in electron heating power [124]. Microinstabilities are one of the proposed candidates to explain this. The presence of a threshold for the trapped electron mode has been found in experiments [125], as well as well as a stabilization by collisions. The treatment of collisions with PIC code is beyond the scope of this work. However, as a first step towards comparison between experiments and gyrokinetic codes, a kinetic model in ORB5 for electrons is highly desirable.

As already pointed out, electron microinstabilities are composed of the Electron Temperature Gradient mode and the Trapped Electron Mode. The first case can be in general treated with ITG codes. ETG turbulence is unstable at $k_y \rho_{Le} \sim 0.3 \Leftrightarrow k_y \rho_{Le} \sim 13$. At these wavelengths, ions are modeled as adiabatic due to their large Larmor radius, so

in principle there is no modification to do to the code when going to ETG simulation if one switches to electron units. In practice, there are only two modifications: the zonal flow term must be dropped out because the adiabaticity of ions is valid everywhere in the plasma and not only on magnetic surfaces, and the value of ρ_* in ions units must be strongly decreased to be significant in electrons units. Consequently ETG simulations are often run in annular geometry. ETG have often been thought to have negligible contribution: from a mixing length argument, $\chi_e \sim \sqrt{m_e/m_i}\chi_i$. However, due to the different nature of the adiabaticity between ions (resp. electrons) for the ETG (resp. ITG) case, the saturation mechanism of ETG turbulence is different, and the nonlinear behavior, not predictable with a mixing-length argument, can lead to anomalous transport comparable to the ion one. Numerically, this has been proven for the first time in [23] (see also [126]) using the Eulerian codes GENE and GS2 [37]. However, Lin *et al.* showed, in [127], negligible ETG transport using the GTC code [48]. Later, numerical noise has been proposed to explain this discrepancy [91] and a benchmark involving several gyrokinetic Eulerian and PIC codes has been performed [128]. GEM [129] and ORB5 simulations [76] support this hypothesis.

The situation for TEM turbulence is more difficult because TEMs are usually unstable at ion scale, $k_y \rho_{Li} \sim 1$: even if the frequencies of interest are comparable to those of ITG turbulence, the fast electron dynamics must be solved on an ion timescale. The parallel motion of electrons is $\sqrt{m_i/m_e}$ times faster than that of ions and becomes the dominant constraint on the applicable time step: a Courant-like condition $k_{\parallel} v_{\parallel} \Delta t \ll 1$ must be satisfied. In fact, the situation is even worse because when considering the kinetic motion of passing electrons the electrostatic limit of the shear Alfvén modes [130] appears, whose frequency $\omega_H = k_{\parallel}/k_{\perp} \cdot \sqrt{m_i/m_e} \Omega_i$ is even larger. The condition $\Omega_H \Delta t \ll 1$ has been checked in linear gyrokinetic simulations in a bumpy pinch [131]. The time step criterion can be estimated with $k_{\parallel} = \Delta m / (q(s_0) R_0)$:

$$\Delta t \Omega_i = \delta \omega_H \Delta t = \delta \sqrt{\frac{m_e}{m_i}} \frac{k_{\perp} \rho_{Li}}{q(s_0) \Delta m \epsilon_a} \frac{a}{\rho_*} \quad (7.1)$$

with $\delta \ll 1$. A typical value is obtained by setting $k_{\perp} \rho_{Li} = 0.3$, $q(s_0) = 1.4$, $\Delta m = 5$, $\epsilon_a = 0.36$, $a/\rho_* = 140$, $m_i/m_e = 100$ and $\delta = 0.2$ (see Fig. 4.7). It yields $\Delta t \Omega_i = 0.33$ which is 120 times smaller than the usual time step for an ITG simulation. Various algorithms or simplifications have been made to circumvent these high frequencies. The global PIC

code GTC uses a fluid-kinetic hybrid model based on the small electron-to-ion mass ratio parameter. The flux-tube PIC code GEM [45] uses a split-weight scheme [103], [132]. Note that similar algorithms can be developed in the more general frame work of Monte-Carlo techniques via the adjustable control variates method [133], which is also extremely useful in electromagnetic simulations in order to resolve the cancellation problem in Ampere's law [134]. Kinetic electrons can also be implemented with a bounce-average model [135]. This has been done for the GT3D code [136]. A bounce-average model uses the bounce-kinetic ordering $\omega/\omega_{be} \ll 1$, and the time step can be relaxed to values comparable to ITG turbulence.

7.2 Implementation

In the previous Section, the general problematic of kinetic electrons has been introduced and various models have been briefly described. In this Section, another model is presented. This model assumes an adiabatic response for the passing electrons and a drift kinetic (neglecting FLR effects) response for trapped electrons. It has been used for linear simulations in GT3D [137] and in LORB5 [138], and for nonlinear simulations in the UCAN code [47], but very few results are presented. Technically, it consists of adding a kinetic species. The equations are similar to those of ions; the only changes to make are to replace q_i by $-e$ and $\langle \vec{E} \rangle$ by \vec{E} . The equations of motion are given by:

$$\begin{aligned} \frac{d\vec{R}}{dt} &= v_{\parallel} \vec{h} - \frac{1}{\Omega_e B_{\parallel}^*} \left(v_{\parallel}^2 + \frac{v_{\perp}^2}{2} \right) (\vec{h} \times \nabla B) + \frac{v_{\parallel}^2}{\Omega_e B_{\parallel}^*} \vec{h} \times [\vec{h} \times (\nabla \times \vec{B})] \\ &\quad + \frac{\vec{E} \times \vec{B}}{B_{\parallel}^* B} \end{aligned} \quad (7.2)$$

$$\begin{aligned} \frac{dv_{\parallel}}{dt} &= \frac{1}{2} v_{\perp}^2 \nabla \cdot \vec{h} - \frac{v_{\perp}^2 v_{\parallel}}{2 B_{\parallel}^* \Omega_e B} \left\{ \vec{h} \times [\vec{h} \times (\nabla \times B)] \right\} \cdot \nabla B \\ &\quad + \vec{E} \cdot \left\{ -\frac{e}{m_e} \vec{h} + \frac{v_{\parallel}}{B B_{\parallel}^*} (\vec{h} \times \nabla B) - \frac{v_{\parallel}}{B B_{\parallel}^*} \left\{ \vec{h} \times [\vec{h} \times (\nabla \times B)] \right\} \right\} \end{aligned} \quad (7.3)$$

With: $\Omega_e = \frac{eB}{m_e}$. The Vlasov equation is:

$$\frac{d\delta f_e}{dt} = \tau_e(\vec{E}) \quad (7.4)$$

$$\tau_e(\vec{E}) = -f_{e0} \kappa(\Upsilon) \frac{d\vec{R}}{dt} \cdot \nabla \Upsilon - \frac{e f_{e0}}{T_e(\Upsilon)} \vec{E} \cdot \frac{d\vec{R}}{dt} \Big|_0 \quad (7.5)$$

For electrons it is assumed that $\psi_0 \rightarrow \psi$ as $m_e/m_i \ll 1$. The Poisson equation is now:

$$[1 - \bar{\alpha}_b(\psi)] \frac{en_0(\psi)}{T_e(\psi)} [\phi(\vec{x}, t) - \bar{\phi}(\psi, t)] - \nabla_{\perp} \cdot \left[\frac{n_0(\psi)}{B\Omega_i} \nabla_{\perp} \phi(\vec{x}, t) \right] = \delta n_i(\vec{x}, t) - \frac{1}{Z_i} \delta n_e(\vec{x}, t) \quad (7.6)$$

$\bar{\alpha}_b(\psi)$ is the flux-surface-average of the local trapped fraction of electrons:

$$\bar{\alpha}_b(\psi) = \frac{\int \alpha_b(\psi, \theta_*) J_{\theta_* \psi \varphi} d\theta_* d\varphi}{\int J_{\theta_* \psi \varphi} d\theta_* d\varphi} \quad (7.7)$$

and $\alpha_b(\psi, \theta_*)$ is defined by:

$$\alpha_b(s, \theta_*) = \sqrt{1 - \frac{B(\psi, \theta_*)}{B_{\max}(\psi, \theta_*)}} \cong \sqrt{1 - \frac{B(\psi, \theta_*)}{B[\psi, \theta_*(\theta = \pi)]}} \quad (7.8)$$

This last approximation means that electrons follow their magnetic surface and that they feel their maximum magnetic field at $\theta = \pi$. The latter assumption is only valid for up-down symmetric equilibria. A analytical expression can indeed be obtained for adhoc equilibria:

$$\bar{\alpha}_b(\psi) = \frac{\epsilon + 1}{4} - \frac{\epsilon + 1}{2\pi} \arcsin \left(\frac{1 - 3\epsilon}{1 + \epsilon} \right) + \frac{1}{\pi} \sqrt{2\epsilon(1 - \epsilon)} \quad (7.9)$$

An interesting result is to find the angle θ_0 such that $\bar{\alpha}_b(\psi) = \alpha_b(\psi, \theta_0)$:

$$\cos \theta_0 = \frac{\bar{\alpha}_b^2(\psi) - \epsilon}{\epsilon[1 - \bar{\alpha}_b^2(\psi)]} \Rightarrow \theta_0 = \arccos \left(\frac{\bar{\alpha}_b^2(\psi) - \epsilon}{\epsilon[1 - \bar{\alpha}_b^2(\psi)]} \right) \quad (7.10)$$

The left plot of Fig. 7.1 shows that the flux-surface-averaged fraction of trapped electrons is approximatively equal to the local fraction at $\theta = \pi/2$.

One can also derive the flux-surface-averaged fraction of trapped electrons in the limit of a small ϵ to find:

$$\bar{\alpha}(\psi) = \frac{2\sqrt{2}}{\pi} \sqrt{\epsilon} \cong 0.9\sqrt{\epsilon} \quad (7.11)$$

$\bar{\alpha}(\psi)$ and $\bar{\alpha}_b(\psi)$ are indeed very similar as can be seen from the right plot of Fig. (7.1) For MHD equilibria, the maximum magnetic field on a given magnetic surfaces should be computed numerically. Finally note that the model is slightly different from the LORB5 one: in LORB5, $\alpha_b(s, \theta_*)$ instead of $\bar{\alpha}_b(\psi)$ is used in the quasineutrality equation. This is somehow inconsistent with how the electron density is derived: the coefficient in front of

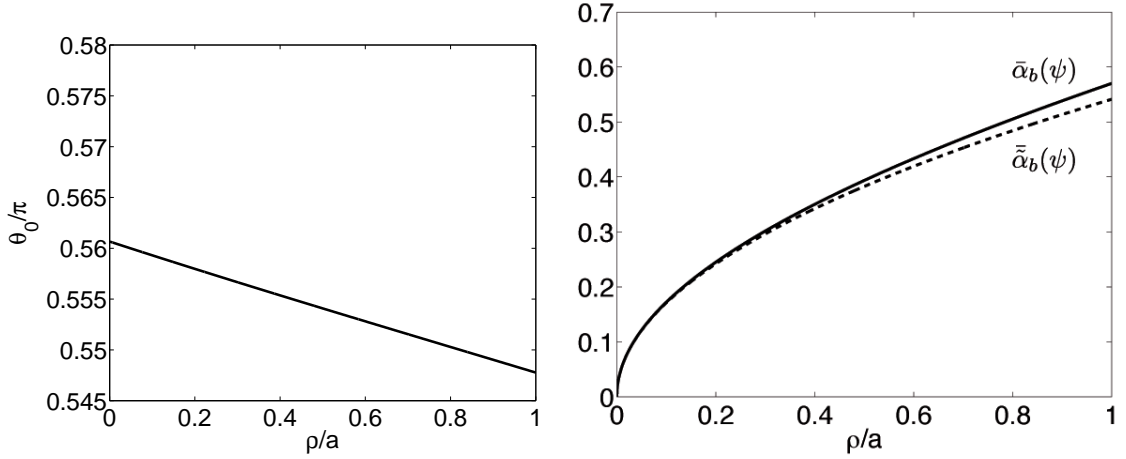


Figure 7.1: θ_0 as a function of ρ/a (left). $\bar{\alpha}_b(\psi)$ (blue) and $\tilde{\alpha}_b(\psi)$ as a function of ρ/a (right) for an aspect ratio of 2.75.

$e\phi/T_e$ must be a flux function according to Eq. (3.65). In addition, the zonal flow matrix is not symmetric anymore when using $\alpha_b(s, \theta_*)$. Note that linear calculations can yield up to 30% higher growth rates when $\alpha_b(s, \theta_*)$ is used, because the TEM instability is caused by deeply trapped electrons located around $\theta_* = 0$. Because $\alpha_b(s, \theta_* = 0) > \alpha_b[s, \theta_*(\theta = \pi)]$, the adiabatic response is decreased and the growth rate increases.

The electron perturbed density is given by:

$$\delta n_e(\vec{x}, t) = \int_{\text{trapped}} \delta f_e(\vec{R}, v_{\parallel}, \mu, t) \delta(\vec{R} - \vec{x}) B^* d\vec{R} dv_{\parallel} d\mu d\alpha \quad (7.12)$$

In practice, it means that the charge assignment must be done for all ions and trapped electrons only. Linearly, a trapped electron will stay trapped during its whole life. Non-linearly, an electron can be *detrapped*, i.e. it can go from the trapped region of phase space to the passing region of phase space, or it can go the other way and it will be *retrapped*. Another difficulty comes from the fact that the trapping condition changes in the presence of an electric field: it is derived from momentum conservation and kinetic energy, which is modified in the presence of an electric potential:

$$\frac{1}{2} m_e [v_{\parallel}^2(t) + v_{\perp}^2(t)] - e\phi[\vec{R}(t)] = \frac{1}{2} m_e [v_{\parallel}^2(t_0) + v_{\perp}^2(t_0)] - e\phi[\vec{R}(t_0)] \quad (7.13)$$

$$\frac{v_{\perp}^2(t)}{2B(t)} = \frac{v_{\perp}^2(t_0)}{2B(t_0)} \quad (7.14)$$

The particle will be trapped when $v_{\parallel}(t) = 0$, happening when:

$$\lambda(t_0) = \sin^{-1} \left[\sqrt{\frac{B(t_0)}{B(t)} \left\{ 1 - \frac{e\phi[\vec{R}(t_0)] - e\phi[\vec{R}(t)]}{\frac{1}{2} m_e v^2(t_0)} \right\}} \right] \quad (7.15)$$

Because the electric potential is computed self-consistently, it is impossible to determine if a particle will be trapped or passing from its initial conditions. However, Eq. (7.15) reveals that the nonlinear trapping condition is almost equivalent to the linear one. Assuming $|\phi[\vec{R}(t_0)]| \ll |e\phi[\vec{R}(t)]|$, the difference comes from a factor which is the ratio of the field energy to the thermal energy. According to the gyrokinetic ordering, this factor is of order $\mathcal{O}(\epsilon_g)$ and should be small. Therefore, ORB5 always uses the linear trapping condition to determine whether a particle is trapped or not. This is also supported by the fact that TEM turbulence mainly comes from the deeply trapped electrons, less subject to nonlinear detrapping. The maximum electrostatic potential is reached at the nonlinear saturation. At this time it might be unclear whether a particle is trapped or passing.

The trapped electron model is implemented in two different ways. In the first one, only trapped electrons are loaded. In the second one, trapped and passing electrons are loaded but the charge assignment is done only with the trapped population. Passing electrons are *passive*: they do not contribute to the perturbed density but they are pushed with the electric field of the ions and the trapped electrons. In nonlinear simulations, if a passing electron becomes trapped, it will become active. If a trapped electron becomes passing, it will become passive. Both models are equivalent for linear simulations, but the first model is faster because it is not necessary to push the passive passing electrons. For nonlinear simulations, the first model is somehow inconsistent because only detrapping is allowed. It is clear that this model would not be suited if electrons-electrons collisions were to be added in the model; in this respect the second one is more realistic. The same conclusion applies for electrons-ions collisions.

Special care must be put on the phase space volumes when loading trapped electrons only. The following identity must hold in the limit of an infinite number of markers:

$$V_{\text{ps,trapped}} = \sum_{\substack{p=1 \\ \text{p trapped}}}^N \Omega_p = \frac{4\pi}{3} \kappa_v^3 \int_{s_{f,\min}}^{s_{f,\max}} \alpha_b(s, \theta_*) J_{\theta_* s \varphi}(s, \theta_*) v_{\text{the}}^3(s) ds d\theta_* \quad (7.16)$$

Where $V_{\text{ps,trapped}} = \int_{\text{trapped}} B_{\parallel}^* d\vec{R} dv_{\parallel} d\mu d\alpha$ is the phase space volume of trapped particles. The integral containing the term $B_{\parallel}^* - B$ vanishes because it is odd in v_{\parallel} . To check the velocity loading, the following identity must hold:

$$E_{\text{kin,ps,trapped}} = \sum_{\substack{p=1 \\ \text{p trapped}}}^N \frac{1}{2} m_i v_p^2 \Omega_p = \frac{3}{2} \int_{s_{f,\min}}^{s_{f,\max}} \alpha_b(s, \theta_*) J_{\theta_* s \varphi}(s, \theta_*) n_0(s) v_{\text{the}}^2(s) ds d\theta_* \quad (7.17)$$

Where $E_{\text{kin,ps,trapped}} = \int_{\text{trapped}} f_0(\vec{R}, v_{\parallel}, \mu) v^2 / 2B_{\parallel}^* d\vec{R} dv_{\parallel} d\mu d\alpha$ is the kinetic energy of the trapped phase space. The integral containing the term $B_{\parallel}^* - B$ vanishes because it is odd in v_{\parallel} . Because there are no or very few trapped electrons at $\theta_* \sim \pi$, the loading of electrons in the poloidal plane will be more adequate if another loading distribution function is used:

$$f_L^t(\vec{R}) = Kp(s)\alpha_b(s, \theta_*) \quad (7.18)$$

The phase space volumes are then:

$$\Omega_p = \frac{N_{\text{ph}} B_{\parallel}^* v_{\perp} [\kappa_v v_{\text{th}}(s_p)]^2 \pi (\pi - 2\lambda_p)}{N B p(s_p) \alpha_b(s_p, \theta_{*p})} \int_{s_{f,\text{min}}}^{s_{f,\text{max}}} \int_0^{2\pi} ds d\theta_* J_{\theta_* s \varphi}(s, \theta_*) p(s) \alpha_b(s, \theta_*) \quad (7.19)$$

For the sake of completeness, the discretized form of the Poisson equation is given:

$$\sum_{\mu} (A_{\mu\nu}^{TEM} + A_{\mu\nu}^{ZF,TEM}) \hat{\phi}_{\mu}^{(n)} = \frac{\hat{b}_{\nu}^{i,(n)} - \hat{b}_{\nu}^{e,(n)}}{M^{(n)}} \quad (7.20)$$

where $(\mu, \nu) = (jk, j'k')$ stand for 2D indices and:

$$A_{\mu\nu}^{TEM} = \int ds d\theta_* J_{\theta_* s \varphi}(s, \theta_*) \left\{ \left[1 - \bar{\alpha}_b(s) \right] \frac{en_0(s)}{T_e(s)} \Lambda_{\nu}(s, \theta_*) \Lambda_{\mu}(s, \theta_*) + \frac{n_0(s)}{B\Omega_i} \nabla_{\text{pol}} \Lambda_{\nu}(s, \theta_*) \cdot \nabla_{\text{pol}} \Lambda_{\mu}(s, \theta_*) \right\} \quad (7.21)$$

$$A_{\mu\nu}^{ZF,TEM} = - \int ds d\theta_* J_{\theta_* s \varphi}(s, \theta_*) \left[1 - \bar{\alpha}_b(s) \right] \frac{en_0(s)}{T_e(s)} \bar{\Lambda}_{\mu}(s) \Lambda_{\nu}(s, \theta_*) \quad (7.22)$$

$\hat{b}^{e,(n)}$ is the toroidal Fourier transform of b_{ν}^e :

$$b_{\nu}^e = \frac{N_{\text{ph}}}{N_e Z_i} \sum_{\substack{r=1 \\ r \text{ trapped}}}^{N_e} \Lambda_{\nu}(\vec{R}_r) w_r(t) \quad (7.23)$$

7.3 Linear convergence with numerical parameters

With the aim of checking the correct implementation of the trapped electron response, the convergence with respect to the main numerical parameters has been thoroughly checked for linear simulations. The test case is inspired by the CYCLONE benchmark [90]. The physical parameters are $\rho^* = 1/140$, $m_i = 2m_p$, $a = 0.47$ [m], $B_0 = 1.91$ [T], $R_0 = 1.30$ [m], $s_0 = 0.624$ (corresponds to $\rho_0 = 0.5a$), $q(s_0) = 1.4$, $T_i(s_0) = T_e(s_0)$,

$R_0/L_{Ti} = 2.23$, $R_0/L_{Te} = 6.9$, $\eta_i = L_n/L_{Ti} = 1$, $\eta_e = L_n/L_{Te} = 3.12$, $\hat{s} = 0.78$, $\Delta_{Ti} = 0.3$. The only difference with the CYCLONE test case is the ion temperature gradient which has been lowered such that the most unstable mode is a TEM. If not mentioned otherwise, the numerical parameters are $N_s = 128$, $N_{\theta_*} = 512$, $N_\varphi = 256$, $\Delta m = \widetilde{\Delta m} = 5$, $N_i = N_e = 2^{19} \cong 500K$, $k_\theta \rho_{Li} = 0.3$, $\kappa_{vi} = \kappa_{ve} = 5$, $m_e = 0.01m_i$ and $\Delta t = 8\Omega_i^{-1}$.

Growth rates are computed by looking at the exponentially growing field energy. The measured growth rate is the time-average of the instantaneous (measured between two successive time steps) growth rate $\gamma_i = 1/2\Delta t \cdot \log [E_f(t + \Delta t)/E_f(t)]$. The first important convergence is the electron mass. This parameter can be set artificially to any value. Obviously, a higher electron mass allows a higher time step. A large amount of CPU time can be saved when heavier electrons are considered, but it must be checked that linear growth rates are converged with respect to the mass ratio. This is shown in Fig. 7.2. The growth rate is converged for $m_i/m_e = 100$. Note that the time step has been scaled proportionally to $\sqrt{m_e/m_i}$. The lower growth rates observed at higher electron mass can be explained by the energy transferred from the particles to the perturbation. When kinetic trapped electrons are added to the simulation, the transfer of energy can be written, by analogy with (5.2):

$$\begin{aligned} -\frac{1}{V} \frac{dE_k}{dt} &= \frac{1}{V} \int q_i \delta f_i \frac{d\vec{R}}{dt} \cdot \langle \vec{E} \rangle B_{\parallel}^* d\vec{R} dv_{\parallel} d\mu d\alpha - \frac{1}{V} \int_{\text{trapped}} e \delta f_e \frac{d\vec{R}}{dt} \cdot \vec{E} B_{\parallel}^* d\vec{R} dv_{\parallel} d\mu d\alpha \\ &= \frac{1}{N_i} \sum_{r_i=1}^N q_i w_{r_i} \Omega_{r_i} \left(\frac{d\vec{R}}{dt} \cdot \langle \vec{E} \rangle \right)_{\vec{z}_i} - \frac{1}{N_e} \sum_{\substack{r_e=1 \\ \text{trapped}}}^N e w_{r_e} \Omega_{r_e} \left(\frac{d\vec{R}}{dt} \cdot \vec{E} \right)_{\vec{z}_e} \end{aligned} \quad (7.24)$$

At low electron mass, the parallel electron contribution $-\int_{\text{trapped}} e \delta f_e v_{\parallel} \vec{h} \cdot \vec{E} B_{\parallel}^* d\vec{R} dv_{\parallel} d\mu d\alpha$ vanishes, because trapped electrons oscillate between their turning points $\pm\theta_0$, roughly on the same magnetic surface, with half of the orbit at positive v_{\parallel} and the other half at negative v_{\parallel} . When the electron mass is increased, the radial drift of electrons become non-negligible: half of the electrons will drift inward and the other half will drift outward. The overall contribution is not zero anymore but gives a stabilizing contribution, hence a lower growth rate. At constant number of markers N_e , the energy transfer signals are noisier for low electron mass, but it has been checked that the growth rates are nevertheless converged for each value of the mass ratio considered in the scan.

The growth rate as a function of electron marker number N_e is represented on the left

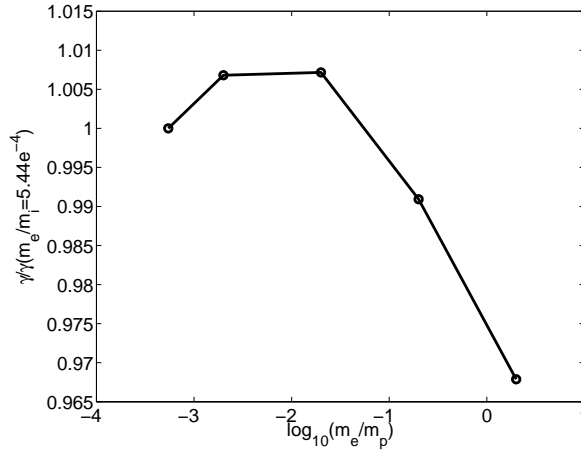


Figure 7.2: Growth rate vs electron mass. Growth rates are normalized to the growth rate at real mass ratio.

plot of Fig. 7.3. The variation of the growth rate is very small such that $N_e = 2^{19} \cong 500K$ is sufficient. The right plot of Fig. 7.3 shows the relative power balance defined by:

$$P_{\text{bal}} = \left| \frac{\frac{dE_k}{dt} - \frac{dE_f}{dt}}{\frac{dE_f}{dt}} \right| \quad (7.25)$$

as a function of $1/N_e$. The dependence is linear as expected. In the limit of an infinite number of markers, P_{bal} does not go to zero: this would only be true if all the numerical parameters simultaneously tend to their optimal value. The convergence with respect to the time step Δt is displayed on Fig. 7.4. In the poloidal plane, two different sets of coordinates, (s, θ_*) or (ξ, η) have been used. A much better convergence is obtained with (s, θ_*) . This is because electrons have a very small radial drift: the s coordinate is more suited for the trajectory integration. When using (ξ, η) , the fast parallel motion has a non-zero component for both coordinates and a smaller time step must be used. This is clearly visible in the middle plot of Fig. 7.4: the number of particle leaving the outer plasma boundary is increasing in time, indicating inaccurate trajectory integrations. This also leads to numerical particle detrapping (see right plot of Fig. 7.4). For the (s, θ_*) integration, the convergence is of order 4, which is the order of the Runge-Kutta integrator. For the (ξ, η) integration, the order of convergence is of order lower than 4. Note that both methods give same growth rates (relative difference of 10^{-4}) for a sufficiently small time step $\Delta t = 4\Omega_i^{-1}$. Another important convergence is the convergence with the field-aligned filter width Δm . The runs were done by simultaneously varying Δm and $\widetilde{\Delta m}$.

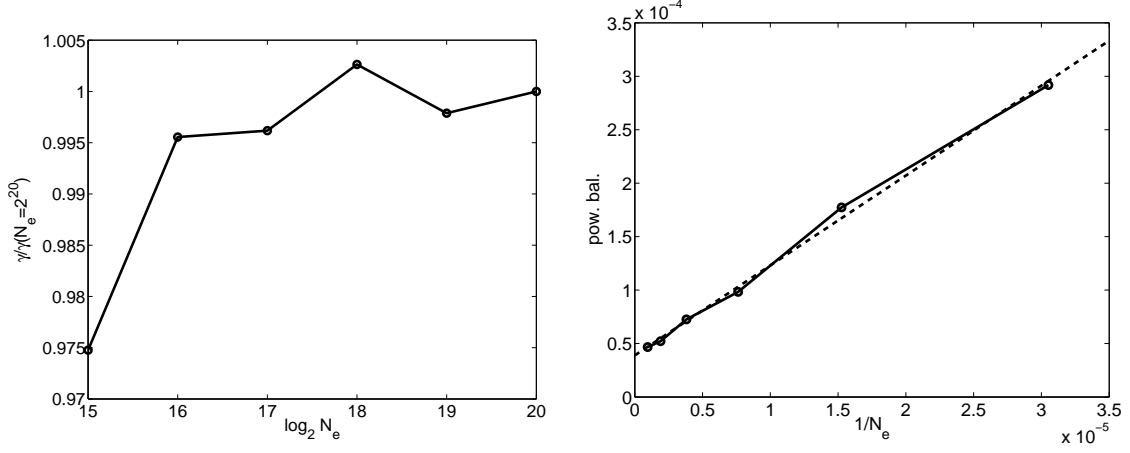


Figure 7.3: Growth rate vs $\log_2(N_e)$. Growth rates are normalized to the growth rate for $N_e = 2^{20} \cong 1M$ markers (left). Power balance P_{bal} vs $1/N_e$ (right). Dashed line is the linear fit.

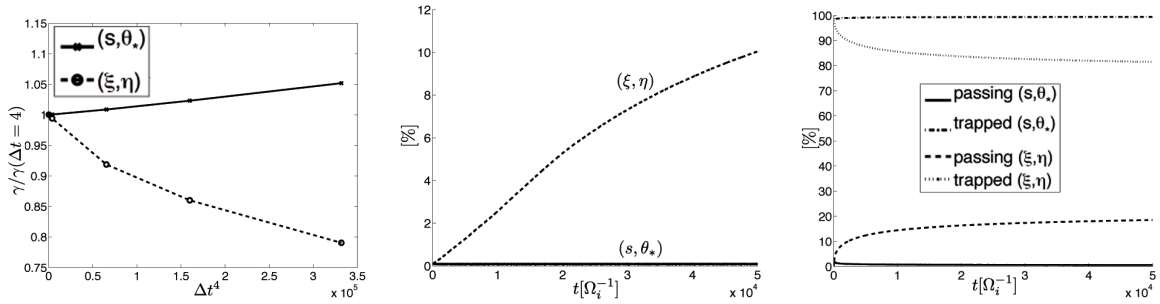


Figure 7.4: Left: growth rate vs Δt^4 for (s, θ_*) (solid line) and (ξ, η) (dashed line) integration. Growth rates are normalized to the growth rate at $\Delta t = 4$. Middle: percentage of electrons leaving the outer plasma boundary. Right: fraction of trapped and passing electrons for (s, θ_*) and (ξ, η) integration.

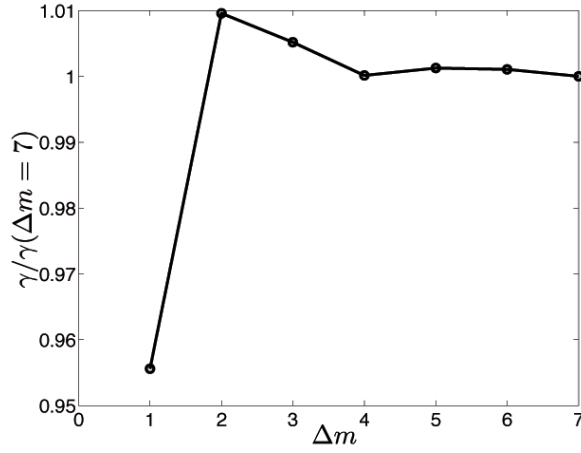


Figure 7.5: Growth rate vs Δm . Growth rates are normalized to the growth rate at $\Delta m = 7$.

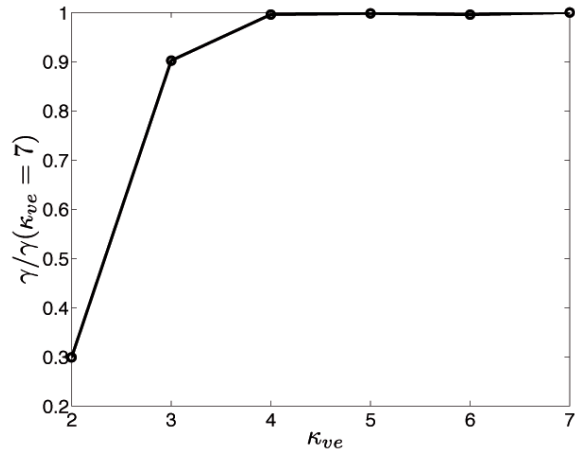


Figure 7.6: Growth rate vs κ_{ve} . Growth rates are normalized to the growth rate at $\kappa_{ve} = 7$.

Like for the ITG case presented in Sec. 5.3, a very small number of k_{\parallel} components are needed, typically $\Delta m = 5$.

Finally, the last important parameter is the velocity cut-off κ_{ve} . In the r.h.s. of the Vlasov equation, Eq. (7.4), the driving term proportional $\kappa(\Upsilon)$ depends on v^2 . It means that electrons with different velocities will have a different influence on the instability. Fig. 7.6 reveals that $\kappa_{ve} = 5$ is sufficient, a value similar for ITG turbulence.

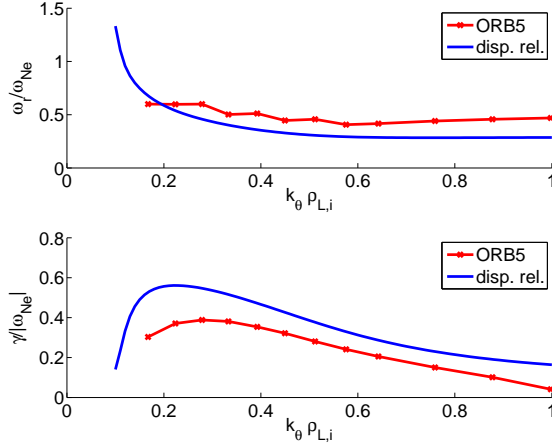


Figure 7.7: Growth rate and real frequency as a function of $k_y \rho_{Li}$ given by dispersion relation Eq. (2.96) (solid line) and ORB5 (solid line, crosses) for $\eta_i = 1.0, \eta_e = 2.0, \tau = 1, R/L_N = 5.0, q(s_0) = 2, \epsilon_a = 0.15$ and $\hat{s} = 1$.

7.4 Comparison with a linear dispersion relation

Like for the ITG case, ORB5 can be compared to a linear dispersion relation for coupled TEM-ITG instability, Eq.(2.96), that depends on the dimensionless parameters $k_y \rho_{Li}, \eta_i, \eta_e, \tau, R/L_N, \epsilon_a, \hat{s}$ and $q(s_0)$. The plasma parameters are $\rho_* = 2/113, B_0 = 1T, \bar{q}(\rho) = 1.25 + 0.67\tilde{\rho}^2 + 2.38\tilde{\rho}^3 - 0.06\tilde{\rho}^4, \tilde{\rho}_0 = 0.6$ such that $q(\tilde{\rho}_0) = 2, R_0 = 2[m], a = 0.5[m]$ such that the aspect ratio is 4 and the local aspect ratio is 6.66. The numerical parameters are $N_s = 32, N_{\theta_*} = 128, N_\varphi = 64$, cubic splines. A diagonal filter with $\Delta m = 5$ is used, $N = 2^{17} \cong 131K, m_e/m_i = 0.01$ and $\Delta t \Omega_i = 8$. Temperature profiles 2 are used with $\Delta T_i = 0.2$. The solution of the dispersion relation has been obtained by setting $G \cong \langle G \rangle(\hat{s}, \epsilon_a)$. The trapped fraction of electrons is $\alpha_b = 0.9\sqrt{\epsilon}$ (instead of the usual $\alpha_b = \sqrt{2\epsilon}$) to match ORB5 definition (7.11). Focus has been put on TEM modes, i.e. the value of η_i has been adjusted to get a TEM mode. Fig. 7.7 shows the comparison between ORB5 and (2.96) for a $k_y \rho_{Li}$ scan with $\eta_i = 1.0, \eta_e = 2.0, \tau = 1, R/L_N = 5.0, q(s_0) = 2, \epsilon_a = 0.15$ and $\hat{s} = 1$. There is a good qualitative agreement except for low $k_y \rho_{Li}$. ORB5 shows a faster stabilization when going to high $k_y \rho_{Li}$, but in this region a solver without the long wavelength approximation should be used. However, the persistence of the growth rate up to $k_y \rho_{Li} \sim 1$ because TEMs are not sensitive to FLR effects is still captured by ORB5.

Fig. 7.8 shows the comparison between ORB5 and (2.96) for a R_0/L_N scan with $\eta_i = 1.0, \eta_e = 2.0, \tau = 1, k_y \rho_{Li} = 0.354, q(s_0) = 2, \epsilon_a = 0.15$ and $\hat{s} = 1$. There is an

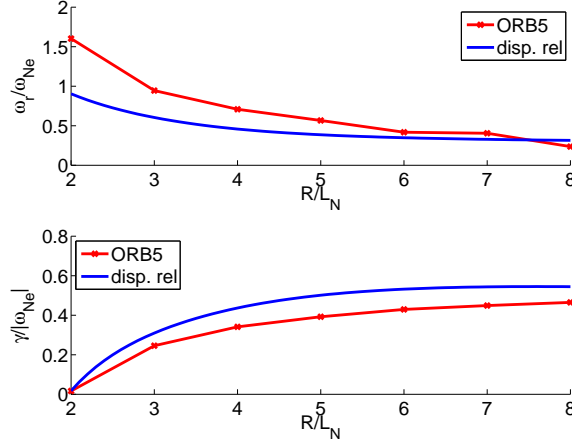


Figure 7.8: Growth rate and real frequency as a function of R/L_N given by dispersion relation Eq. (2.96) (solid line) and ORB5 (solid line, crosses) for $\eta_i = 1.0, \eta_e = 2.0, \tau = 1, k_y \rho_{Li} = 0.354, q(s_0) = 2, \epsilon_a = 0.15$ and $\hat{s} = 1$.

excellent qualitative agreement over the whole range considered. In particular, there is a constant behavior of the growth rate for large R/L_N . Like for the ITG case, the quantitative differences are of course due to the numerous approximations done to obtain the dispersion relation.

Fig. 7.9 compares ORB5 and the dispersion relation for the interesting case of a η_i scan at fixed R/L_N . As η_i is increased, one observes a transition from TEM to ITG mode, clearly visible from the real frequency plot. The transition η_i value of the dispersion relation is slightly higher but the agreement is good. In the TEM region, a decrease of η_i interestingly leads to a destabilization of the TEM: the energy transfer diagnostic reveals that the grad-B drift component of electrons $-\int_{\text{trapped}} e \delta f_e v_{\perp}^2 / 2 (\Omega_i B_{\parallel}^*) (\vec{h} \times \nabla B) \cdot \vec{E} B_{\parallel}^* d\vec{R} dv_{\parallel} d\mu d\alpha$ increases and the stabilizing effect of ion Landau damping decreases as $\eta_i \rightarrow 0$.

The inclusion of trapped electrons includes two additional parameters: the aspect ratio and the magnetic shear. When normalized to ω_{Ne} , the dispersion relation for toroidal ITG mode, Eq. (2.63) does not contain an explicit dependence on the aspect ratio. Toroidal-ITG modes are stabilized when the aspect ratio is increased because the toroidicity becomes smaller. At large aspect ratio the ITG modes have a slab character. The shear also has an important effect on ITG modes: locally, the shear modifies the guiding center frequency and acts somehow like the toroidicity. Globally, a shear variation can increase or decrease the number of rational surfaces inside the unstable region and twists the ed-

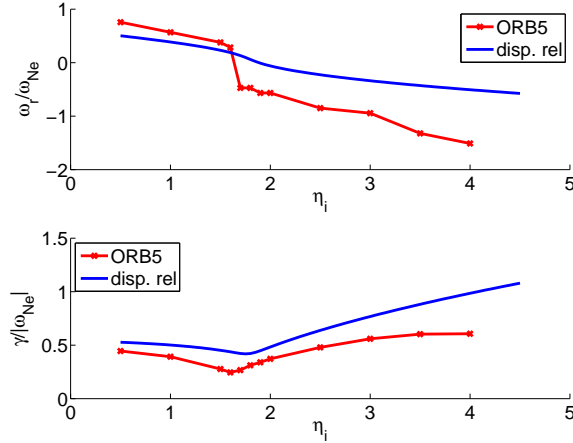


Figure 7.9: Growth rate and real frequency as a function of η_i given by dispersion relation Eq. (2.96) (solid line) and ORB5 (solid line, crosses) for $R/L_N = 5$, $\eta_e = 2.0$, $\tau = 1$, $k_y \rho_{Li} = 0.354$, $q(s_0) = 2$, $\epsilon_a = 0.15$ and $\hat{s} = 1$.

dies. All these effects were not retained in the dispersion relation (2.63). Instead, the ballooning formalism [61], [62] should be used. TEMs are sensitive to ϵ_a through the trapped fraction of electrons α_b , and through the G factor, Eq. (2.91) (see Fig. 7.10). The scan is done with parameters for which ITG modes are stable. When the aspect ratio increases, the trapped fraction decreases which should lead to a stabilization of the TEM. This is confirmed on Fig. 7.11, with a good qualitative agreement.

The comparison between the ITG-TEM dispersion relation and ORB5, shown in Fig. 7.12, is not very concluding: both models predict a stabilizing effect when going to negative shear, but it is quantitatively very different. The magnetic shear introduces many effects: it bends the eddies, it changes the drift frequencies¹, and modifies the distance between rational surfaces (the latter effect will be absent in any local model).

7.5 The CYCLONE linear benchmark

Like for ITG turbulence, the ORB5 code needs to be benchmarked against other gyrokinetic codes. This has been done with the global PIC code GT3D [49] and the Eulerian flux-tube code GENE [38] for the CYCLONE base case parameters. The benchmark has been based on Ref. [137]. The numerical parameters are inspired by the convergence study

¹It can be seen in the framework of the ballooning formalism, in which $\vec{k}_\perp \propto m/\rho(\vec{e}_\theta + \hat{s}\theta\vec{e}_\rho)$

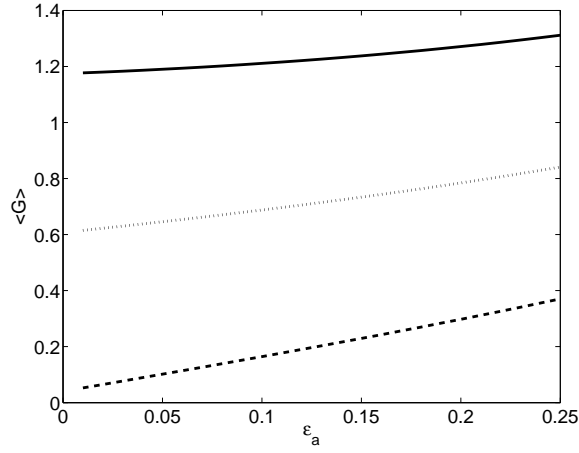


Figure 7.10: $\langle G \rangle$ as a function of ϵ_a for $\hat{s} = 1$ (solid line), $\hat{s} = 0$ (dotted line) and $\hat{s} = -1$ (dashed line).

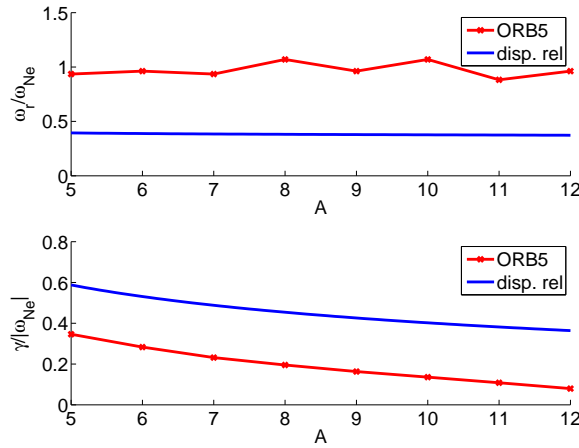


Figure 7.11: Growth rate and real frequency as a function of ϵ_a given by the dispersion relation Eq. (2.96) (solid line) and ORB5 (solid line, crosses) for $R/L_N = 5$, $\eta_i = 1.0$, $\eta_e = 2.0$, $\tau = 1$, $k_y \rho_{Li} = 0.354$, $q(s_0) = 2$ and $\hat{s} = 1$.

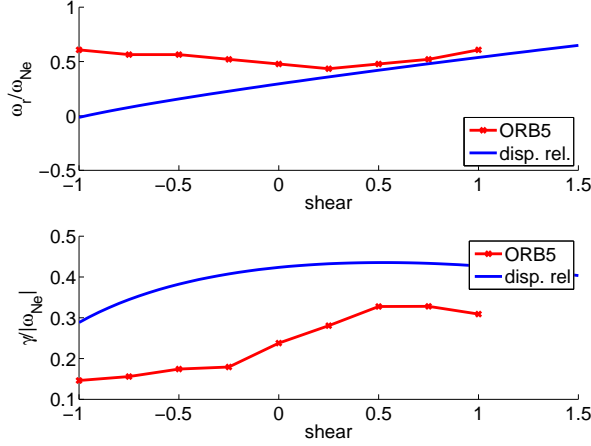


Figure 7.12: Growth rate and real frequency as a function of \hat{s} given by dispersion relation Eq. (2.96) (solid line) and ORB5 (solid line, crosses) for $R/L_N = 5$, $\eta_i = 1.0$, $\eta_e = 2.0$, $\tau = 1$, $k_y \rho_{Li} = 0.354$, $q(s_0) = 2$ and $\epsilon_a = 0.15$.

in Section 7.3: $N_s = 128$, $N_{\theta_*} = 512$, $N_\varphi = 256$, $\Delta m = \widetilde{\Delta m} = 5$, $N_i = N_e = 2^{19} \cong 500K$, $k_\theta \rho_{Li} = 0.3$, $\kappa_{vi} = \kappa_{ve} = 5$, $m_e = 0.01m_i$ and $\Delta t = 8\Omega_i^{-1}$.

First, a $k_\theta \rho_{Li}$ scan has been performed for the nominal CYCLONE value of $\eta_i = 3.12$ (see Fig. 7.13). The unstable mode is an ITG mode. Comparing with the results of the adiabatic electrons case, Fig. 5.27, one can observe a strong destabilization of the ITG mode by trapped electrons. The agreement between ORB5 and GT3D is excellent up to $k_\theta \rho_{Li} = 0.8$. Note, however, that GT3D uses a Padé approximation for the quasineutrality equation, valid up to $k_\perp \rho_{Li} \sim 2$ whereas ORB5 results use a long wavelength approximation that becomes incorrect at large $k_\perp \rho_{Li}$. When FLR effects become important, the mode undergoes a transition from ITG to TEM at $k_\theta \rho_{Li} \sim 0.6 - 0.7$. The GENE code gives a transition at $k_\perp \rho_{Li} \approx 0.5$ and the agreement is reasonable. The difference can be explained by the global effects that are absent in GENE and by the difference between $s - \alpha$ and adhoc equilibria [139]. In fact, GENE results agree well with the radially-local linear continuum eigenvalue FULL code [140], [141] published in [137], whereas ORB5 results agree better with the results from the global PIC code GTC [48] published in [137]. Fig. 7.14 presents a $k_\theta \rho_{Li}$ scan for CYCLONE parameters with $\eta_i = 1.0$. For these parameters, the most unstable mode is a TEM. The agreement between ORB5 and GT3D is excellent up to $k_\theta \rho_{Li} \approx 0.7$. The comments made above on the solver are also valid in these cases. Again, global effects and/or equilibrium approximations made in GENE

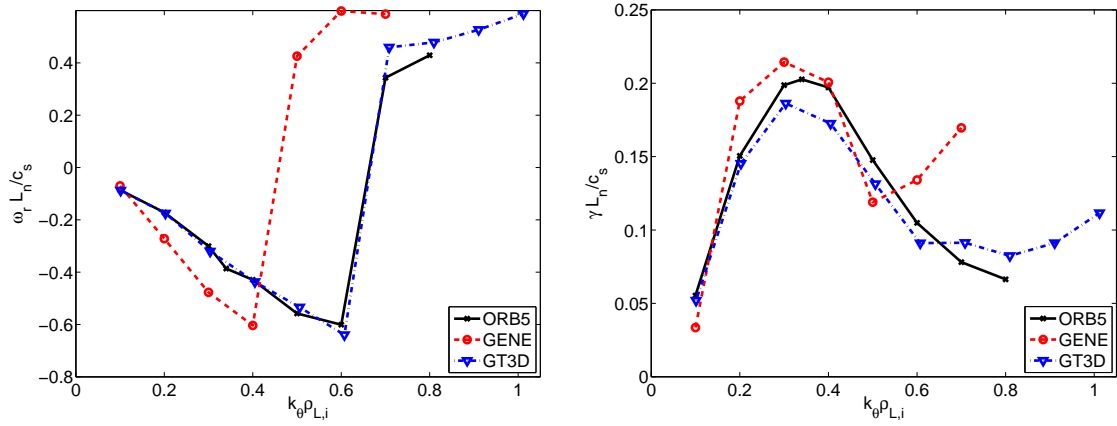


Figure 7.13: Real frequency (left) and growth rates (right) vs $k_\theta \rho_{L,i}$ for CYCLONE parameters.

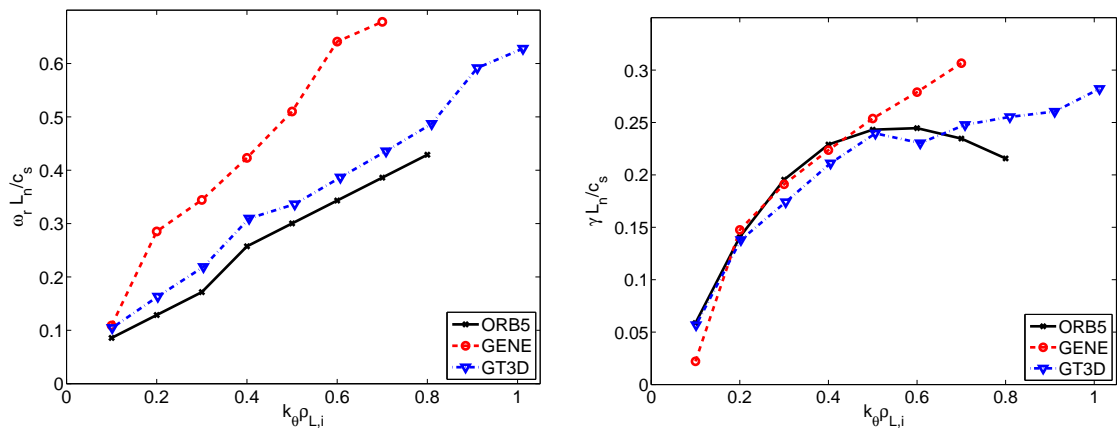


Figure 7.14: Real frequency (left) and growth rates (right) vs $k_\theta \rho_{L,i}$ for CYCLONE parameters with $\eta_i = 1.0$.

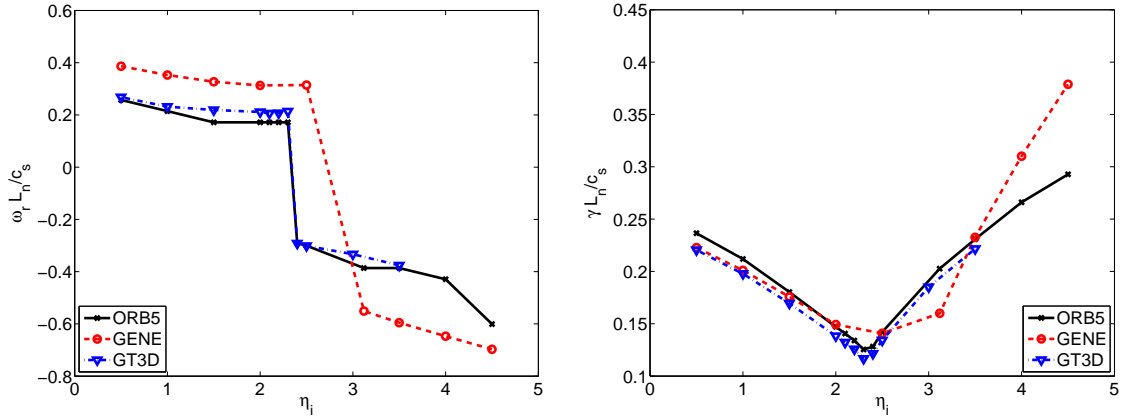


Figure 7.15: Real frequency (left) and growth rates (right) vs η_i for CYCLONE parameters with $k_\theta \rho_{Li} = 0.33$.

yield a difference between ORB5 and GENE, mostly for the real frequency.

The final step of the benchmark is a η_i scan at fixed $k_\theta \rho_{Li} = 0.33$. As η_i is increased, one observes a transition from TEM to ITG. ORB5 and GT3D predict the transition at the same η_i value and the agreement is quasi perfect, while GENE predicts a transition at a slightly higher value of η_i .

7.6 Implementation of noise control and heating operators on electrons

In Section 3.8, a source model has been introduced. It contains a Krook and a heating operator in order to control the noise and the temperature gradient. This model has been implemented in a similar way for electrons. The only difference is the absence of the zonal flow conservation term: it is in fact a radial orbit width expansion term [72], which can be neglected for electrons. A first simple test consists in looking at the effects of the Krook operator on linear simulations. The parameters are those described in Section 7.5. Intuitively, the growth rate should be γ_K smaller when the naive Krook operator is introduced. This is true for adiabatic ITG simulations. When trapped electrons are taken into account, the picture may be a little more complex, as two Krook damping rates γ_{Ki} and γ_{Ke} can be varied separately. The left plot of Fig. 7.16 shows a CYCLONE simulation with $\eta_i = 1.0$, dominated by a TEM mode. ITG modes are completely stable. Introduc-

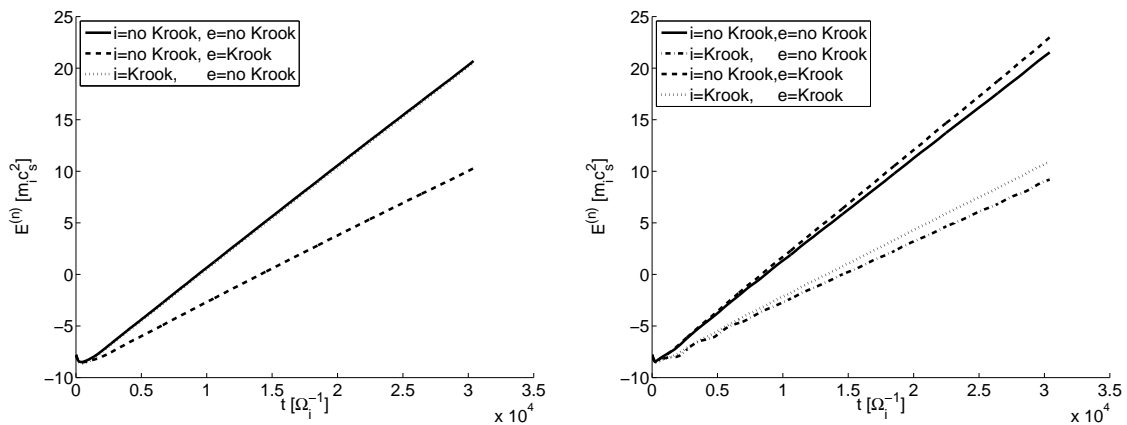


Figure 7.16: Field energy of the toroidal mode as a function of time for a TEM dominated simulation (left) and an ITG dominated simulation (right), with various applications of the naive Krook operator

ing a Krook operator on ions does not modify the growth rate, and applying a Krook operator on electrons reduces the growth rate by γ_{Ke} . The right plot of Fig. 7.16 shows a CYCLONE simulation with $\eta_i = 3.12$ dominated by ITG modes. Electrons contributes to 14% of the growth rate. When the Krook operator is applied to both ions and electrons with $\gamma_{Ki} = \gamma_{Ke}$, the growth rate is reduced by γ_{Ki} . But in the situation $\gamma_{Ki} = 0, \gamma_{Ke} \neq 0$, one sees that the growth rate is slightly amplified (by 5% of its original value for the case considered here, i.e. $\gamma_{Ke} = 4 \cdot 10^{-4} \Omega_i$). The same phenomenon appears when going from $\gamma_{Ki} \neq 0, \gamma_{Ke} = 0$ to $\gamma_{Ki} \neq 0, \gamma_{Ke} \neq 0$. This can be explained by the destabilization mechanism of ITG modes by trapped electrons: the adiabatic response is decreased by a factor $[1 - \bar{\alpha}_b(\psi)]$, and is not influenced by the electron Krook damping rate. The slight difference of the growth rate can be observed by looking at the grad-B drift contribution of electrons $\int v_{\perp}^2 / (2\Omega_i B_{\parallel}^*) (\vec{h} \times \nabla B) \cdot \vec{E} B_{\parallel}^* d\vec{R} dv_{\parallel} d\mu d\alpha$ of the power balance diagnostic.

Another way to check the correct implementation of the noise control algorithm is to perform a so-called Rosenbluth-Hinton test (see [72] for tokamak geometry and [142] for helical geometry), which consists in computing the time evolution of a plasma with constant profiles and initialized with an axisymmetric and poloidally symmetric density perturbation ($m = 0, n = 0$). It is shown in [72] that there is an undamped residual of the $m = 0, n = 0$ component of the associated $\vec{E} \times \vec{B}$ flow. An analytical formula is given for large aspect ratio tokamaks, circular geometry and adiabatic electrons. The standard ORB5 Rosenbluth-Hinton test and the comparison with the analytical formula

can be found in [73]. In this Section, the effects of kinetic trapped electrons on the Rosenbluth Hinton test are analyzed. Because the profiles are constant, the driving term of the Vlasov equation is 0 (first term of the RHS of Eq. (3.44)) and only the term proportional to $\vec{E} \cdot d\vec{R}/dt$ remains. For electrons, this term should be small because the electric field is mostly radial and the radial drift of electrons is extremely small. The parameters are $m_i = 2m_p, a = 63.84\rho^*, B_0 = 1.91$ [T], $R_0 = 1.3$ [m], $R_0/a = 5.88$. The density and temperature profiles are flat, $T_i = T_e$. $\bar{q}(\rho) = 1.24 - 0.22\tilde{\rho} + 2.36\tilde{\rho}^2 - 2.83\tilde{\rho}^3 + 2.56\tilde{\rho}^4$. The grid is $N_s = 64, N_{\theta^*} = 16, N_{\varphi} = 16$, the number of markers is $N_i = 4 \cdot 10^5$. Passing electrons are passive and $N_e = 2 \cdot 10^6$ markers are loaded in order to have $4 \cdot 10^5$ trapped electrons. The mass ratio $m_e/m_D = 5.446 \cdot 10^{-4}$ is used. The time step is $\Delta t = 1\Omega_i^{-1}$ and the amplitude of the initial ($m = 0, n = 0$) density perturbation is $A_0 = 1 \cdot 10^{-2}$. An example of such test is presented in Fig. 7.17. Initially an axisymmetric perturbation is applied to the density. Due to the toroidal geometry and the poloidal dependence of the $\vec{E} \times \vec{B}$ velocity, the $m = 0, n = 0$ zonal flow perturbation will transfer part of its energy to the GAMs $m = \pm 1, n = 0$ that will be subsequently Landau damped. This gives rise to the oscillations in Fig. 7.17. In the end, a residual zonal flow is found to persist in the system. As anticipated, the inclusion of kinetic trapped electrons is almost not distinguishable on the damping and the real frequency of the GAMs. On the right plot of Fig. 7.17, the test is performed with a Krook operator on ions. The residual zonal flow level damps to zero. The inclusion of electrons and a Krook operator does not modify this conclusion. When the zonal flow correction is turned on, the zonal flow residual does not go to zero, as can be seen from the left plot of Fig. 7.18. The right plot of Fig. 7.18 summarizes the test: when the Krook operator is turned on on ions, the zonal flow correction is needed to have a finite residual level. The zonal flow correction does not recover the residual obtained without the Krook operator: this is due to the bounce-average operator which is approximated as a flux-surface-average operator, and finite orbit width effects [143]. Simulation at smaller ρ^* would be required to reduce them.

7.7 Nonlinear detrapping

The electron model presented in this chapter is completely relevant for linear simulations, because trajectories are such that a trapped electron will stay so during its lifetime.

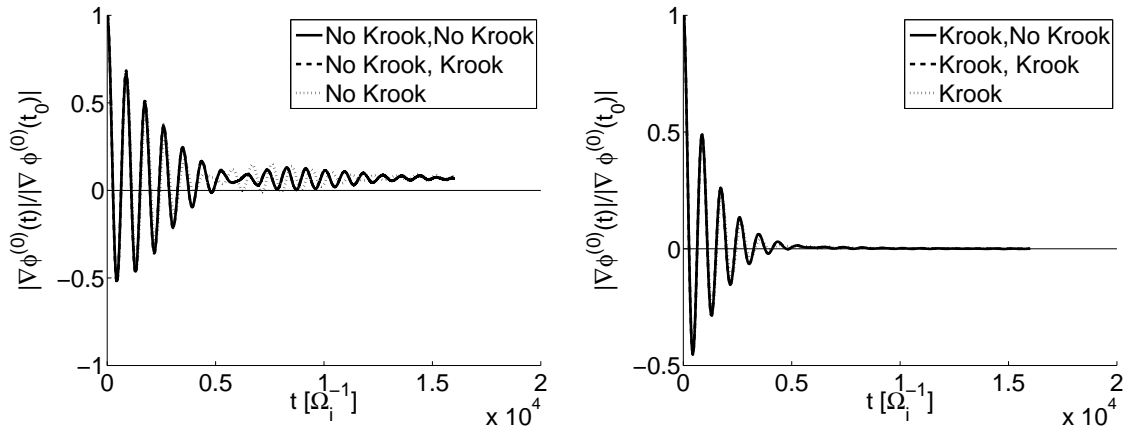


Figure 7.17: Rosenbluth-Hinton test with trapped kinetic electrons without (left) and with (right) ion Krook operator, without electron Krook operator (solid line) and with electron Krook operator (dashed line). The adiabatic electrons case is shown in dotted line.

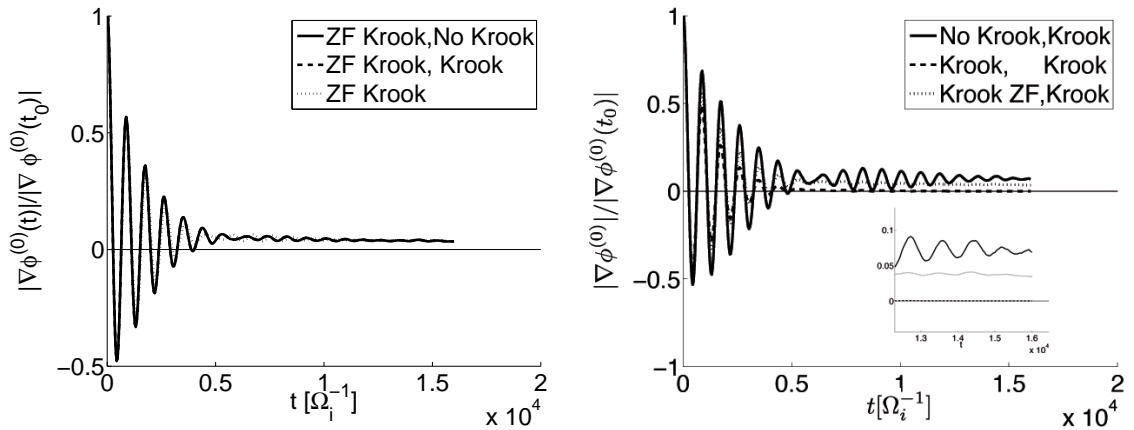


Figure 7.18: Left: Rosenbluth-Hinton test with trapped kinetic electrons with zonal flow preserving ion Krook operator, without electron Krook operator (solid line) and with electron Krook operator (dashed line). The adiabatic case is shown in dotted line. Right: Rosenbluth-Hinton test with electron Krook operator without (solid line), with standard (dashed line) and with zonal flow preserving (dotted line) ion Krook operator.

However, when moving to nonlinear simulations a problem occurs: turbulence induces detrapping and a treatment for detrapped electrons must be found. Intuitively, detrapped electrons should not contribute to the instability, which is driven by deeply trapped electrons, but this statement must be checked to assess the validity of the model. Nonlinear CYCLONE simulations have been performed with a loading of trapped electrons only. The physical parameters are $\rho^* = 1/184.7$, $m_i = 2m_p$, $a = 0.625$ [m], $B_0 = 1.91$ [T], $R_0 = 1.70$ [m], $s_0 = 0.624$ (corresponds to $\rho_0 = 0.5a$), $q(s_0) = 1.4$, $T_i(s_0) = T_e(s_0)$, $R_0/L_{Ti} = 2.23$, $R_0/L_{Te} = 6.9$, $\eta_i = L_n/L_{Ti} = 1$, $\eta_e = L_n/L_{Te} = 3.12$, $\hat{s} = 0.78$. Profiles of type 3, Eqs. (4.149) and (4.150) have been used with $\Delta_{Ti} = \Delta_{Te} = 0.04$, $\tilde{\rho} = 0.5$ and $\Delta\tilde{\rho} = 0.25$. The numerical parameters are $N_i = 1 \cdot 10^7$, $N_e = 32.5 \cdot 10^6$, $\Delta t = 8\Omega_i^{-1}$, $N_s = 128$, $N_{\theta_*} = 512$, $N_\varphi = 256$, $\Delta m = \widetilde{\Delta m} = 5$. The filter boundaries are $n_{\min} = 0$, $n_{\max} = 57$ (corresponding to $k_\theta \rho_{Li} = 0.86$ at $\tilde{\rho} = 0.5$ and $k_\theta \rho_{Li} = 0.88$ at $\tilde{\rho} = 0.75$, from which the profile gradients decrease). Poloidal modes having $k_\theta \rho_{Li} > 1$ (mostly near magnetic axis) are filtered out. The simulations use a Toroidal Mode Filter (TMF) of order 4, meaning that modes $n = \pm 4k$, $k \in \mathbb{N}$ have been retained. It can be viewed as running in a quarter-torus wedge. Less particles are needed because the number of Fourier modes is reduced. Solving only part of the toroidal modes should not affect the results qualitatively. A Krook operator is applied to ions and electrons with $\gamma_{Ki} = \gamma_{Ke} = 1 \cdot 10^{-4}\Omega_i$. A correction to the Krook operator is applied to conserve the density, temperature and late time structure of the zonal flow such that profiles decay. Two models for detrapped electrons are considered. In the first model, referred to as *model 1*, electrons that are detrapped are still pushed and are taken into account in the charge assignment. In the second model, referred to as *model 2*, electrons that are detrapped are normally pushed but do not contribute to the charge assignment. These electrons are taken again into account if they become retrapped by the turbulence.

Nonlinear detrapping is caused by two mechanisms. First, electrons drift radially because of the $\vec{E} \times \vec{B}$ velocity. If they drift inward, the local aspect ratio will be larger and detrapping will occur. Second, the v_{\parallel} nonlinearity can accelerate trapped electrons and detrap them. The detrapping mechanisms are of course more efficient for barely trapped electrons. Fig. 7.19 shows how electrons are detrapped. A binning in (λ, θ) of the phase space volume at $s = 0.61$ is presented for different simulations times. In the linear phase, the electric field is weak and most electrons remain trapped. In the late nonlinear phase,

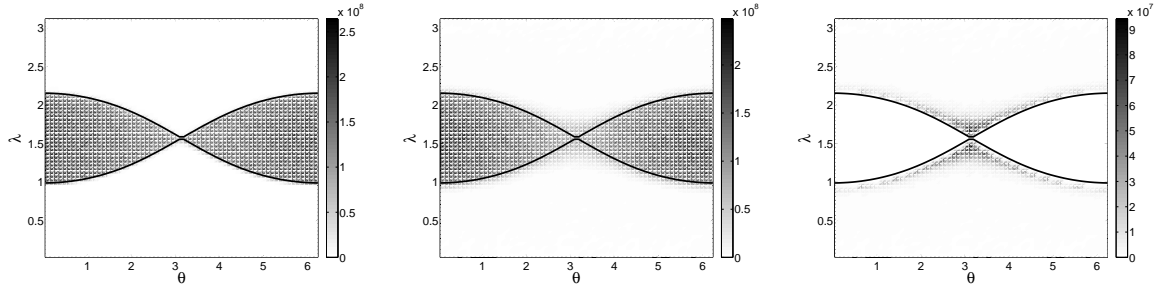


Figure 7.19: Binning of phase space volume at $s = 0.61$ in the linear phase of the simulation (left) and in the late nonlinear phase (middle). Binning of passing region of phase space in the late nonlinear phase (right). Black line shows trapped-passing boundary.

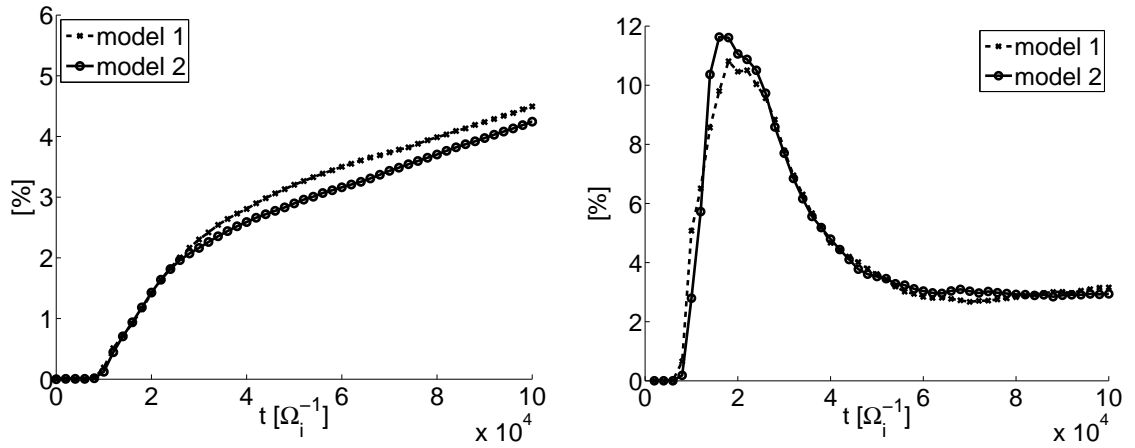


Figure 7.20: Fraction of electrons (left) and δf^2 (right) in passing region of phase space as function of time for model 1 (crosses) and model 2 (circles).

many electrons have moved to the passing region. The right plot of Fig. 7.19 shows the repartition of the phase space volume of detrapped electrons: most of them are located near $\theta = \pi$, where barely trapped electrons are present.

The left plot of Fig. 7.20 shows the fraction of detrapped electrons. In the linear phase, these fractions are zero but as nonlinear effects become important they increase. They reach a maximum at the saturation, where the electric field is the largest. At the end of the simulation, they remain small. This is also valid for the fraction of δf^2 in the passing region of the phase space. It means that detrapped electrons do not carry a significant part of the perturbation. In addition both models yield roughly the same values, which is the sign that detrapped electrons have a very light contribution to the instability independently of how they are treated. A look at the profiles is nonetheless needed. This model

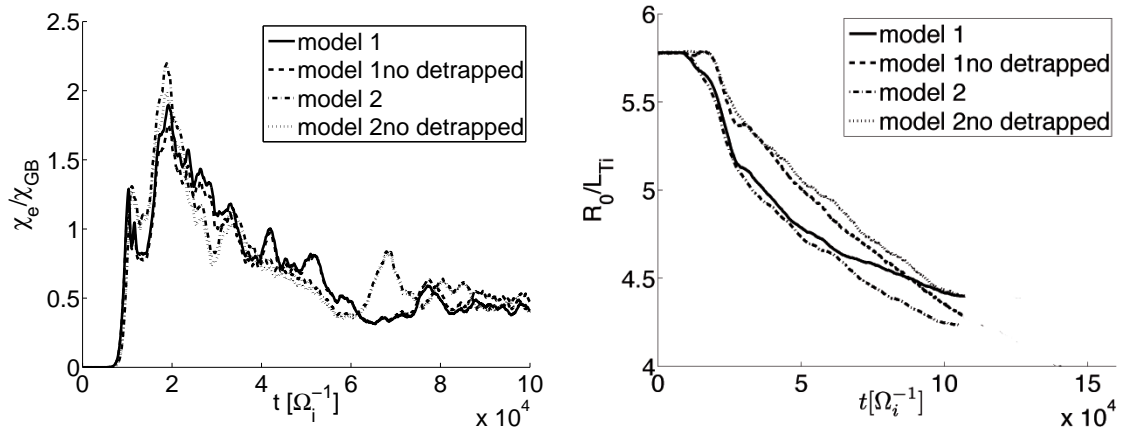


Figure 7.21: Time evolution of the electron heat diffusivity (left) and normalized temperature gradient (right) for models 1 and 2, with or without including detrapped electrons. Profiles are radially averaged between $\tilde{\rho} = 0.2$ and $\tilde{\rho} = 0.8$.

is hybrid in the sense that the contribution of passing electrons is analytic. Due to the nonlinear detrapping, moments of δf can be reconstructed with or without the detrapped kinetic electrons. The left plot of Fig. 7.21 shows the time evolution of the heat diffusivity in gyro-Bohm units, averaged between $\tilde{\rho} = 0.2$ and $\tilde{\rho} = 0.8$. For both models, detrapped electrons have a negligible contribution. There are no significant differences between the two models. The chaotic nature of turbulence implies that the burst phases of the two models are different, however the heat diffusivities are on average the same. The right plot of Fig. 7.21 shows the time evolution of the normalized temperature gradient, averaged between $\tilde{\rho} = 0.2$ and $\tilde{\rho} = 0.8$, where it can be seen that both models are equivalent. However, the inclusion of detrapped electrons tends to increase the temperature gradient. This reveals the conceptual problems when loading only trapped electrons. Another lack of this model is the absence of trapping: passing electrons may become trapped. The aim of these simulations was to see if the trapped-passing boundary in phase space is difficult to handle. From the results presented it seems not to be the case. Having only kinetic trapped electrons seems to be a reasonable model, because barely trapped electrons do not contribute to the instability. However, it is more adequate to load and push both trapped and passing electrons and to retain only the trapped electrons in the charge assignment. First, this model allows the detrapping and the trapping of particles. Second, it is conceptually simpler to reconstruct the profiles. This model will be presented in the next Section.

7.8 The role of zonal flows in TEM simulations

7.8.1 Review of nonlinear results

In Section 7.1, the need for a kinetic electron model as well as the numerical difficulties have been presented. Here, gyrokinetic nonlinear results from the literature are briefly summarized. There are obviously many features that could be studied. The first pioneer works included kinetic electrons for experimental comparisons [144], [15], benchmarks with other gyrokinetic codes [39] and electromagnetic simulations [145], but these works did not specifically deal with the effects of kinetic electrons. The first observations were done by Sydora [47] with the global PIC code UCAN with a model similar to the one used in ORB5. The ion heat flux increased by a factor of 2-3 when drift kinetic trapped electrons were turned on. A more detailed study was done by Dannert *et al.* [56] with the flux-tube continuum code GENE, where basic features of CTEM turbulence were studied. The parameters were similar to the CYCLONE parameters except for τ that was set to 3 to stabilize ETG modes and $R/L_{Ti} = 0$ to stabilize ITG modes, and the density ($R/L_n = 3$) and temperature gradients ($R/L_{Te} = 6$) were slightly different. For these parameters, the influence of the zonal flow was found to be small and it was observed that the linear mode structure persisted in the nonlinear regime. A larger parameter scan was performed by Lang *et al.* [57] with the flux tube PIC code GEM which revealed that the influence of the zonal flows depends on physical parameters such as τ , R/L_n and R/L_{Te} . Recently, it was shown that the zonal density seems to be the physical saturation mechanism leading to saturation when zonal flows are unimportant [146], while flux-tube continuum GENE simulations found that the saturation mechanism was due to particle diffusion [147]. Finally, a study of TEM turbulence inside an internal particle transport barrier with the continuum flux-tube code GS2 revealed a nonlinear upshift of the density gradient [148]. As a consequence of this review, it is noted that there has been no detailed study of TEM turbulence with a global model, mostly due to the huge computational time required. In what follows, global TEM nonlinear simulations with ORB5 are presented.

7.8.2 Simulation model

The electron model presented in Section 7.2 divides the electron phase space into two regions, the trapped and the passing one. The boundary is set by the linear criterion.

In the trapped region, markers are active, i.e. they contribute to the perturbed density, while there are no markers in the passive region: the latter is treated analytically. This separation has been introduced for computational reasons and poses a problem for markers that cross the trapped-passing boundary. This model has shown that the treatment of detrapped electrons does not really matter, but one must be careful about how moments are computed. Results in Section 7.7 were aimed at showing the effects of nonlinear detrapping. However, this model does not describe the trapping of the markers (except the retrapping, i.e. initially trapped markers that have become passing and then trapped again). In particular, it would be impossible to model electron-ion or electron-electron collisions due to the analytical passing region. Therefore, another model is needed.

The new model presented here still divides the electron phase space into trapped and passing regions. In the trapped region, markers are active whereas the passing region is described with passive markers, i.e. not contributing to the electron perturbed density. The phase space coordinates and the weight of these passing markers are evolved with the usual equations of motion and the Vlasov equation. The idea behind is to conserve the distribution function of all markers, active or passive, but it has the drawback of producing a passive, possibly non-adiabatic perturbed distribution function δf_e^p for passing electrons. Non-adiabaticity of δf_e^p could be further enhanced by trapped markers entering the passing region. δf_e^p can be written as:

$$\delta f_e^p(\vec{R}, v_{\parallel}, \mu, t) = \delta f_e^{p,\text{adiab}}(\vec{R}, v_{\parallel}, \mu, t) + \tilde{\delta} f_e^{p,\text{non-adiab}}(\vec{R}, v_{\parallel}, \mu, t) \quad (7.26)$$

$$\delta f_e^{p,\text{adiab}} \equiv [1 - \alpha_b(\psi)] f_0(\vec{R}, v_{\parallel}, \mu) \frac{e\phi(\vec{R}) - \bar{\phi}(\psi)}{T_e(\psi)} \quad (7.27)$$

One expects that the non-adiabaticity of passing electrons is small. In practice, this is checked by looking at different moments of $\delta f_e^{p,\text{adiab}}$ and $\tilde{\delta} f_e^{p,\text{non-adiab}}$. The model is also validated if, for a given moment of interest, the passing contribution is small compared to the trapped one.

For all the simulations performed with this model, it has been observed that the fraction of passing electrons slowly increases by 1% during the total simulation time, which means that the trapping is almost compensated by the detrapping, at least in terms of number of markers. However, it has been observed that some passing electrons are continuously accelerated by the electric field and reach intolerable parallel velocities for the time integrator. Therefore a cut-off in velocity has been introduced. If an electron reaches 1.2

times the maximum initial velocity it will not be pushed anymore. The fraction of electron markers for which the cut-off is applied is of the order of 1%. These highly passing electrons do not contribute to the instability and so removing them from the simulation should not modify significantly the results.

7.8.3 Parameters and convergence

The physical parameters of the simulations presented here mostly follow the CYCLONE parameters [90], $\rho^* = 1/184.7$, $m_i = 2m_p$, $a = 0.625$ [m], $B_0 = 1.91$ [T], $R_0 = 1.70$ [m], $s_0 = 0.624$ (corresponds to $\rho_0 = 0.5a$), $q(s_0) = 1.4$, $T_i(s_0) = T_e(s_0)$, $R_0/L_{Ti} = 2.23$, $R_0/L_{Te} = 6.9$, $\eta_i = L_n/L_{Ti} = 1$, $\eta_e = L_n/L_{Te} = 3.12$, $\hat{s} = 0.78$. Profiles of type 3, Eqs. (4.149) and (4.150) have been used with $\Delta_{Ti} = \Delta_{Te} = 0.04$, $\tilde{\rho}_0 = 0.5$ and $\Delta\tilde{\rho} = 0.25$. Linearly, this situation corresponds to stable ITG modes and unstable TEM modes. In order to limit CPU time consumption, many limitations have been introduced and will be briefly discussed. The electron mass ratio has been set to $m_e/m_D = 0.01$. It corresponds to the value for which linear growth rates are converged. The field-aligned solver uses the long wavelength approximation, i.e. $k_\perp\rho_{Li} \ll 1$. For ITG turbulence this choice is appropriate because the short wavelength modes are stabilized by FLR effects. For TEM turbulence, the short wavelengths are linearly more unstable than the long ones. Therefore a cut-off at a low k -value may seem inappropriate. For ITG turbulence, there is a downward cascade of the modes field energy, meaning that the long wavelength modes dominate in the nonlinear regime. This phenomenon has also been observed in CTEM turbulence [57]. Therefore, it is *a priori* expected that the short wavelength tail of the spectrum should not play a big role in the final state of the simulation. Of course this assumption will have to be relaxed in the future. Theoretically, the different microinstabilities regimes have been studied separately for numerical convenience. The ITG spectrum lies in the long wavelengths ($k_\perp\rho_{Li} \sim 0.3$), the ETG spectrum lies in the short wavelengths ($k_\perp\rho_{Le} \sim 0.3$) and the TEM spectrum lies in between. The issue of which part of the spectrum is actually relevant is of course crucial. Recently, the advances in computational power made it possible to study global ITG and ETG turbulence at electron scale resolution [149], [150], where it is found that most of the electron energy transport arises from ion scales in cases for which ion-scale instabilities are not suppressed. Flux-tube simulations have also started to study ion and electron scale [151], for which it seems that high- k modes

may have a significant contribution when ETG modes are linearly unstable. In what follows, due to computational limitations the question of the spectrum cut-off is left out for future studies. Note also that for very high density gradient ($R/L_n = 10$) and zero ion temperature gradient, it has been observed with the flux-tube code GEM [57] that modes with $k_y \rho_{Li} > 0.8$ do not seem to play any significant role in electron heat transport.

The Krook damping rates have been set to $\gamma_{Ki} = \gamma_{Ke} = 1 \cdot 10^{-4} \Omega_i$ which corresponds to one tenth of the maximum linear growth rate. Finally, the code has been run in an annular region $0.1 < s < 1.0$, with a Toroidal Mode Filter (TMF) of order 4. The number of particles is reduced by a factor 4 while the same signal to noise ratio is kept, without affecting the heat transport too much. The other numerical parameters are $\Delta t = 4\Omega_i^{-1}$, $N_s = 128$, $N_{\theta^*} = 512$, $N_\varphi = 256$, $\Delta m = \widetilde{\Delta m} = 5$. The filter boundaries are $n_{\min} = 0$, $n_{\max} = 57$ (corresponding to $k_\theta \rho_{Li} = 0.86$ at $\tilde{\rho} = 0.5$ and $k_\theta \rho_{Li} = 0.88$ at $\tilde{\rho} = 0.75$, beyond which the profile gradients decrease). Poloidal modes having $k_\theta \rho_{Li} > 1$ are filtered out. All simulations are such that $N_i = N_e^t$, where N_e^t is the number of initially trapped electron markers.

Figure. 7.22 shows the signal (without the zonal component²) to noise ratio vs time for different particle numbers. One can see that this quantity is proportional to $N = N_i + N_e$. The simulation of a full torus at 40M markers and the simulation of a 1/4-torus and 10M markers have the same signal to noise ratio. This plot shows that when a TMF of 4 is used, 20M trapped electrons and ions are needed to get a satisfactory signal to noise ratio (i.e. above 10). Fig. 7.23 shows the time evolution of the electron heat flux and normalized temperature gradient. The 10M simulation exhibits a 15% smaller diffusivity compared to the 40M one, and the 20M is extremely close to the 40M. The temperature gradients behave in the same way: after the first heat burst, the temperature gradient sharply decreases. Note that the slow increase of the temperature gradient is yet unexplained. It might be an indication that the simulations have not yet reached full steady state due to the presence of very long time scales in the response of the system. From these results,

²Removing the zonal component of the signal defines a more stringent criterion for the noise level. First, the zonal flow generally dominates in the nonlinear phase: its field energy is generally two orders of magnitude higher than each of the non-axisymmetric modes. Second, the zonal flow does not cause any heat and particle transport: it is seemingly appropriate not taking it into account in the signal as the fluxes are one of the most important physical quantities to determine the physical convergence of a simulation.

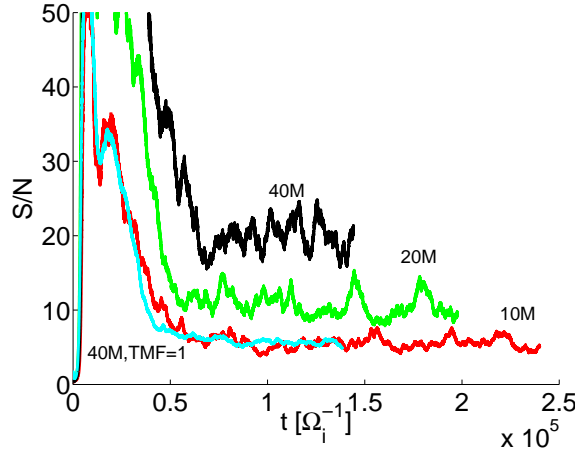


Figure 7.22: Signal (without the zonal component) to noise ratio vs time for different marker numbers and one simulation with all toroidal modes.

it seems that 20M markers is a reasonable marker number. Note that such a simulation requires 4 days with 2048 PEs on a BG/P machine, which is $2 \cdot 10^5$ CPU hours. It is therefore impossible to span the whole space of numerical parameters. A simulation with $\gamma_{Ki} = \gamma_{Ke} = 7 \cdot 10^{-5} \Omega_i$, i.e. 30% smaller than the original value has been performed. The lower value of the damping rates implies that the number of particles had to be doubled to have a satisfactory signal to noise ratio. The normalized temperature gradient for the $\gamma_{Ki} = \gamma_{Ke} = 7 \cdot 10^{-5} \Omega_i, N_i = N_e^t = 40M$ simulation is smaller by 0.1 and the heat flux is, on average, smaller by 15% compared to the simulation $\gamma_{Ki} = \gamma_{Ke} = 1 \cdot 10^{-4}, N_i = N_e^t = 20M$ which is analog to the intrinsic variability observed in ITG simulations [58]. It means that the value of the Krook damping rate should not be higher.

7.8.4 Analysis

Starting from the parameters described in the previous Section, four different simulations have been performed, for $\tau = T_e/T_i = 1, \tau = 3$ with and without zonal flows. The simulations "without zonal flows" mean that the $n = 0$ mode has been artificially filtered out. The number of markers is $N_i = N_e^t = 20M$. Note that a bug has been found in the code after the simulations were run. Unfortunately, due to the high CPU required there was not enough time to rerun all the simulations. However, the two simulations at $\tau = 3$ could be rerun and it was found that the simulations were qualitatively similar, and it is therefore expected that the same conclusions holds for the $\tau = 1$ cases. Because no

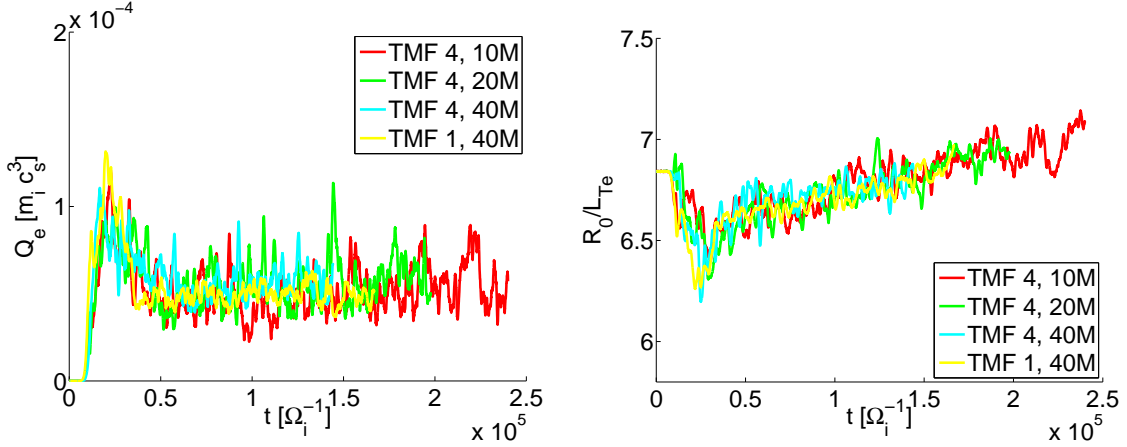


Figure 7.23: Time evolution of the electron heat flux (left) and normalized temperature gradient (right) for simulations with different marker numbers and one simulation with all toroidal modes. Profiles are radially averaged between $\tilde{\rho} = 0.4$ and $\tilde{\rho} = 0.6$.

quantitative analysis is presented, this bug does not modify any of the statements exposed in what follows. First, the linear phase of the simulations is examined. Fig. 7.24 shows the growth rates vs $k_{\theta}\rho_{Li}$ computed at the very start of the simulation (left plot) and at the end of the linear phase (right plot). Initially, the growth rate spectrum resembles the typical linear spectrum of TEM modes, with more unstable modes at large k . Note that the long wavelength approximation of the solver may affect the spectrum for $k_{\theta}\rho_{Li} > 0.6$. In the end of the linear phase, nonlinear effects are visible: first the zonal flow $k_{\theta}\rho_{Li} = 0$ mode has a high growth rate, approximately twice the growth rate of the bulk of spectrum. Also, low $k_{\theta}\rho_{Li}$ modes have become nonlinearly unstable. To understand this nonlinear coupling, consider the Vlasov equation:

$$\left. \frac{d\delta f}{dt} \right|_0 + \left. \frac{d\delta f}{dt} \right|_1 = \tau(\vec{E}) \quad (7.28)$$

$$\left. \frac{d\delta f}{dt} \right|_1 = \left. \frac{\partial\delta f}{\partial t} \right|_1 + \left. \frac{\partial\delta f}{\partial s} \frac{ds}{dt} \right|_1 + \left. \frac{\partial\delta f}{\partial\theta_*} \frac{d\theta_*}{dt} \right|_1 + \left. \frac{\partial\delta f}{\partial\varphi} \frac{d\varphi}{dt} \right|_1 + \left. \frac{\partial\delta f}{\partial v_{\parallel}} \frac{dv_{\parallel}}{dt} \right|_1 \quad (7.29)$$

The toroidal Fourier decomposition is:

$$\delta f(s, \theta_*, \varphi, v_{\parallel}, \mu, t) = \sum_n \widehat{\delta f}^{(n)}(s, \theta_*, v_{\parallel}, \mu, t) e^{in\varphi} \quad (7.30)$$

$$\langle \phi \rangle(s, \theta_*, \varphi, \mu, t) = \sum_n \langle \widehat{\phi} \rangle^{(n)}(s, \theta_*, \mu, t) e^{in\varphi} \quad (7.31)$$

If one looks at the relation between the R.H.S. $\tau(\vec{E})$ and, say, the part of the L.H.S. that contains the θ_* derivative, one has:

$$\sum_{n+n'=n''} \frac{F(\psi)}{J_{\theta_* s \varphi} B B_{\parallel}^*} \frac{\partial \langle \phi \rangle^{(n')}}{\partial s} \frac{\partial \delta f^{(n)}}{\partial \theta_*} + \dots = - \frac{F(\psi)}{J_{\theta_* \psi \varphi} B B_{\parallel}^*} \frac{\partial \langle \phi \rangle^{(n'')}}{\partial \theta_*} + \dots \quad (7.32)$$

$\delta f^{(n)}$ and $\langle \phi \rangle^{(n)}$ are directly coupled through the quasineutrality equation. There are no direct toroidal couplings in the quasineutrality equation due to axisymmetry, as they would for example appear in stellarator geometry. The true coupling mechanisms are complicated processes and are beyond the scope of this work. However, the last equation contains the basic idea of nonlinear couplings. First, the $n = 0$ zonal flow is produced nonlinearly by all the couplings ($n \leftrightarrow -n$). Recall that the zonal flow is linearly stable because this radial perturbation is advected perpendicularly to the profile gradients by the $\vec{E} \times \vec{B}$ velocity. The growth rate of the zonal flow should be approximately twice the maximum linear growth rate because the nonlinearity is the product of two terms with similar growth rates. The strength of the coupling is directly proportional to the product of the amplitudes of the n and n' components. It can be anticipated that the nonlinear coupling will be stronger for low n modes during the linear phase, as the dominant linear modes have contiguous n values. This is confirmed on Fig. 7.25. The mode $n = 36$ is the most dominant mode during the linear phase: its field energy is one order of magnitude higher than the other modes. This mode, as well as all the others, nonlinearly couple with themselves to induce the zonal flow. The second dominant linear mode $\pm n = 32$ couples with the $\mp n = 36$ modes to excite the $n = 4$ mode which is the lowest allowed in the simulation. This mode is very weakly linearly unstable, but starts to grow when nonlinear effects start to become important. Note also that the high- k modes are nonlinearly excited, notably through the nonlinear couplings of low n modes.

When the nonlinear terms become important, more and more couplings come into play: the simulation saturates. For ITG turbulence, an energy cascade towards long wavelength modes usually takes place. This is also the case for TEM turbulence as can be seen from Fig. 7.26. During the linear phase, one toroidal mode is dominating the simulation, but in the nonlinear phase the spectrum is peaked at $k_{\theta} \rho_{Li} \sim 0.2 - 0.4$. This phenomenon as well as the effect of zonal flow can be seen on the poloidal section of the potential (without the zonal component), displayed on Fig. 7.27. In the left plot, the linear mode consisting of streamers is clearly visible. After the saturation, these structures

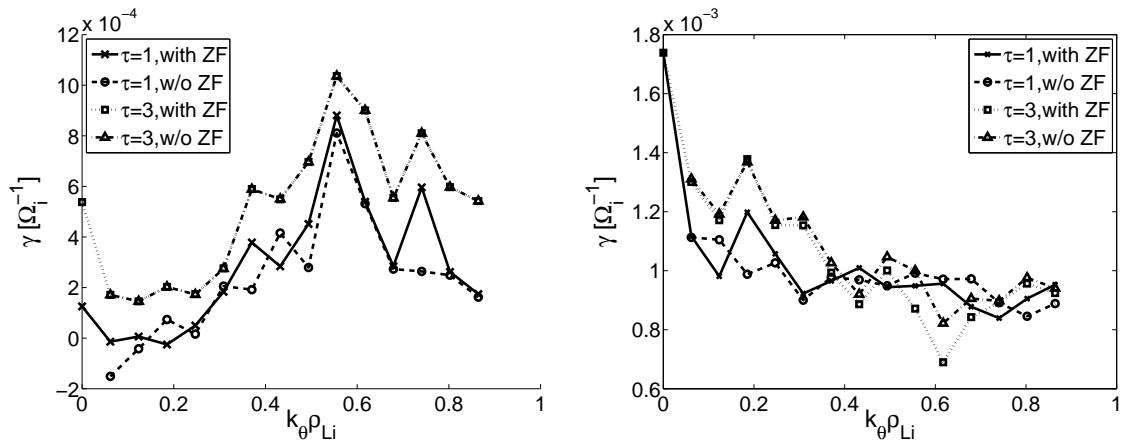


Figure 7.24: Growth rate vs $k_{\theta}\rho_{Li}$ for the simulations $\tau = 1$ with ZF (solid line, crosses), $\tau = 1$ without ZF (dashed line, circles), $\tau = 3$ with ZF (dotted line, squares) and $\tau = 3$ without ZF (dash-dotted line, triangles). The left plot shows growth rates computed between $t = 16.2$ and $t = 32.4a/c_s$ and the right plot shows growth rates computed between $t = 32.4a/c_s$ and $t = 48.7a/c_s$.

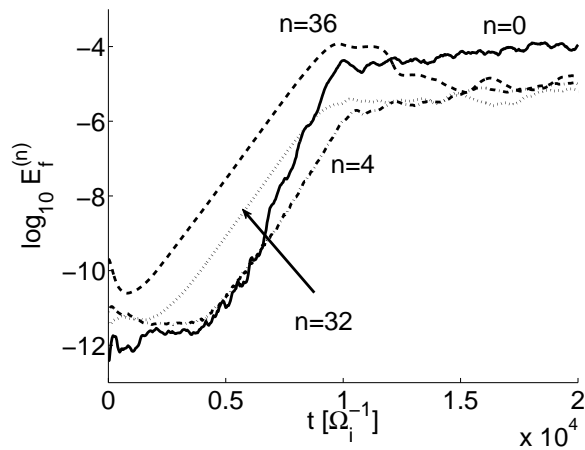


Figure 7.25: Time evolution of the field energy of the $n = 0$ (solid line), $n = 36$ (dashed line), $n = 32$ (dotted line) and $n = 4$ (dashed-dotted line) for the $\tau = 1$ simulation with zonal flow.

are progressively sheared by the zonal flow (middle plot). In the end of the simulation, the linear structure of the mode is completely destroyed, and the radial and poloidal wavelengths become comparable: the zonal flows tend to isotropize the perturbations in the direction perpendicular to \vec{B} . The same quantity is represented on Fig. 7.28 for the $\tau = 1$ simulation with zonal flows artificially filtered out from the simulation. In the linear phase, the structure of the potential is similar to the case with zonal flow, but in the nonlinear phase the streamers survive (right plot) and have even extended radially: in the linear phase, the logarithmic gradient of the temperature profiles is strong between $s = 0.4$ and $s = 0.8$ and rapidly decreases to 0 outside this interval. Therefore the instability is supposed to develop within this region. As nonlinear effects become important, heat is transported radially, modifying the temperature profile: the logarithmic gradient profile may extend and so could the streamers. This is represented on Fig. 7.29. After the saturation, the radial spreading of the temperature gradient is clearly visible (up to $s = 0.2$ and $s = 0.85$) and its width in the nonlinear phase corresponds well to the width of the streamers. However, near $s = 0.2$ and $s = 0.85$ the gradient is very small (right plot of Fig. 7.29) such that no linear instability could develop, but there is a very small heat flux. Therefore the presence of streamers in this region is the manifestation of a global nonlinear effect.

Next, the heat transport is analyzed. In these simulations, heat is transported by two species, ions and electrons. Passing electrons are passive but react to an electric field and can, in practice, transport heat. In theory, adiabatic electrons do not carry heat radially. Therefore, the passing electron contribution to the heat flux should be small. Fig. 7.30 shows that when the zonal flow is artificially removed from the simulation, the ratio between the passing and the trapped electron heat flux is 50% at the first saturation (overshoot) peak, while in the steady state this ratio goes down to 25%. When the zonal flow is included, this ratio is around 15%. At the saturation, the electric field is maximal and can be quite large. Therefore, according to Eq. (7.15), the distinction between passing and trapped particles becomes difficult to make. This is one of the drawbacks of the model. The heat flux instead of the heat diffusivity is further used to compare the heat transport quantitatively. This turns out to be more convenient as the ion and electron temperature gradient differ ($|\nabla T_e|/|\nabla T_i| = 3.12$): the use of χ_i and χ_e could be misleading. Moreover, because two species are involved, particle transport is no longer negligible. The transport

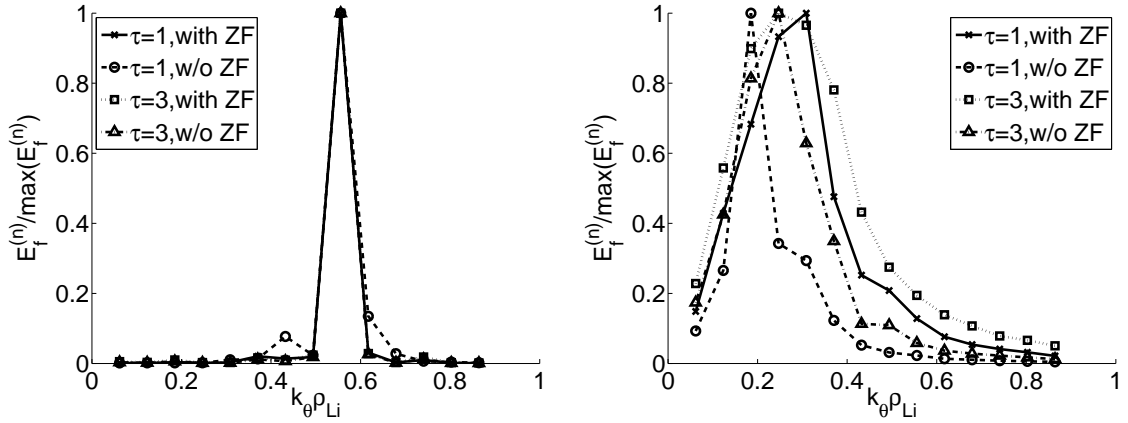


Figure 7.26: Field energy vs $k_{\theta}\rho_{Li}$ for the simulations $\tau = 1$ with ZF (solid line, crosses), $\tau = 1$ without ZF (dashed line, circles), $\tau = 3$ with ZF (dotted line, squares) and $\tau = 3$ without ZF (dash-dotted line, triangles). The left plot shows field energies computed between $t = 32.4a/c_s$ and $t = 48.7a/c_s$ (end of linear phase), and the right plot shows field energies time-averaged during the late nonlinear phase.

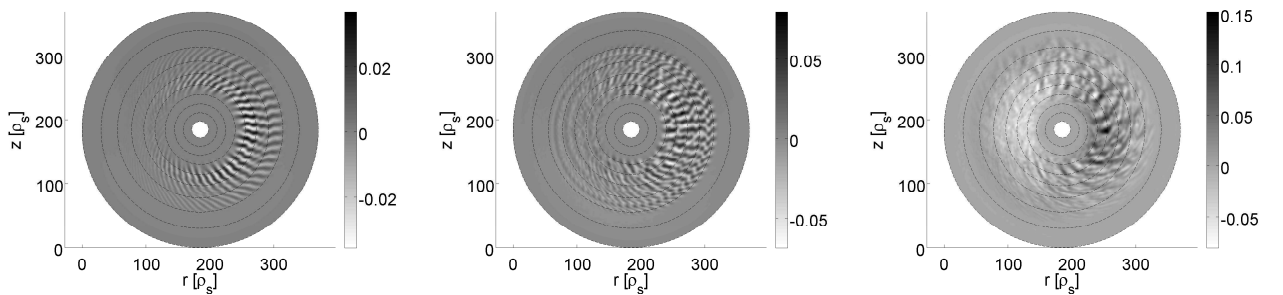


Figure 7.27: Electrostatic potential on the poloidal plane in the linear phase (left), just after the saturation (middle) and in the late nonlinear phase (right) for the $\tau = 1$ simulation with zonal flow. The zonal component has been removed.

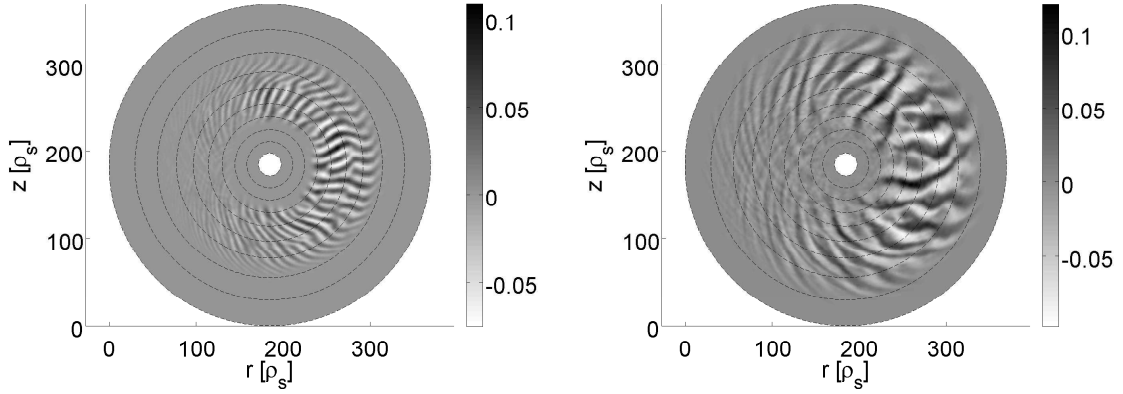


Figure 7.28: Electrostatic potential on the poloidal plane in the linear phase (left) and in the late nonlinear phase (right) for the $\tau = 1$ simulation without zonal flow.

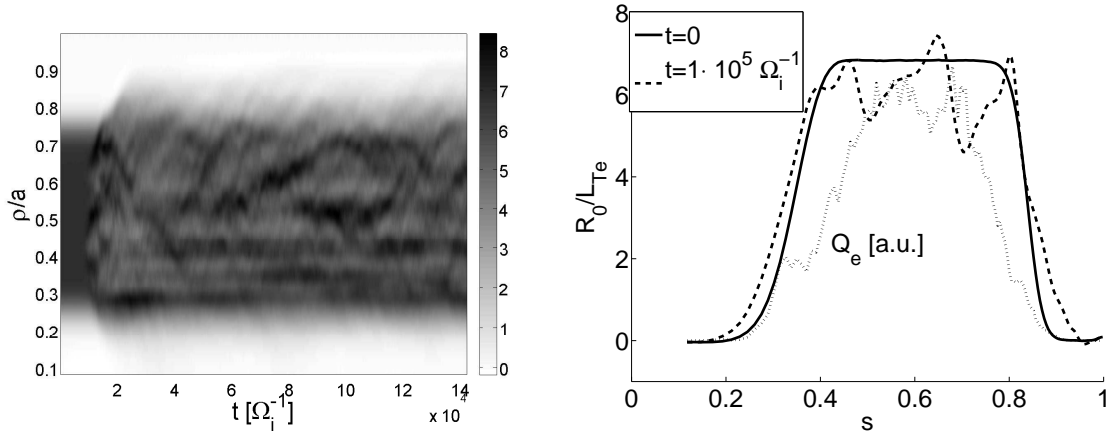


Figure 7.29: Left: radial and temporal evolution of R_0/L_{Te} for the $\tau = 1$ simulation without zonal flows. Right: radial profile of R_0/L_{Te} at $t = 0$ (solid line) and $t = 10^5 [\Omega_i^{-1}]$ (dashed line). The dotted line shows the radial profile of the heat flux in arbitrary units.

is then measured by looking at a matrix equation which relates for example the fluxes Q_i, Q_e, Γ_e (although parallel and impurity fluxes may also be taken into account) to the thermodynamical forces $\nabla T_i, \nabla T_e, \nabla n$ (the ion particle flux Γ_i is obtained through quasi-neutrality). The diagonal terms are the most important, but off-diagonal terms, leading to so-called pinches (neoclassical or anomalous), may play an important role [152]. Such kind of study is beyond the scope of this paper and consequently only the heat flux will be studied.

Figures 7.31 and 7.32 show the time evolution of the radial heat flux, averaged between $\bar{\rho} = 0.3$ and $\bar{\rho} = 0.7$, for ions and electrons and for the four different simulations. A common feature of all these curves is that the saturation of the heat flux occurs at a higher level when the zonal flows are artificially suppressed: the ion heat flux is increased by a factor 2 and the electron heat flux by a factor 3 for both the $\tau = 1$ and $\tau = 3$ cases. Then one can observe that the ion heat flux is always smaller than the electron one by approximately one order of magnitude, which is consistent with the fact that the instability is caused by the electron temperature gradient. Finally, one can see that the absence of zonal flows yields a higher electron heat flux (factor of 2) in the late nonlinear phase for the $\tau = 1$ case but the ion heat flux is less altered. For the $\tau = 3$ case, although the first burst is higher, the absence of zonal flows has no real impact on the level of heat flux. This is consistent with the observations in [146], where similar simulations (except for $R_0/L_{Te} = 6$) have been performed in flux tube geometry.

Next, the time evolution of the temperature gradient, Figs. 7.33 and 7.34, is analyzed. First, one can see that R_0/L_{Ti} is barely modified, due to the fact that the ion heat flux is much smaller. Also, the initial drop is always stronger when the zonal flows are suppressed, consistently with the higher heat fluxed observed for the first overshoot. For both $\tau = 1$ and $\tau = 3$, and for both ions and electrons, the gradients are consistently smaller when zonal flows are artificially suppressed. The role of zonal flows is often quantified by computing its shearing rate, which has been derived for cylindrical geometry [153], for high aspect ratio tokamak geometry [93], for arbitrary shaped tokamak plasmas [92], for quasisymmetric plasmas [154] and by taking the oscillatory behavior of the zonal flow into account [94]. In the following, this last effect will be neglected for simplicity. Here, an

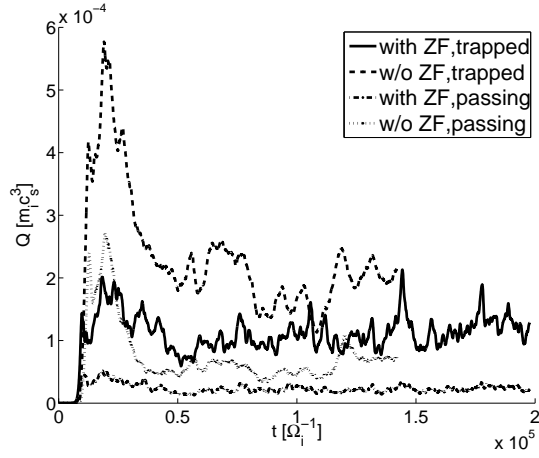


Figure 7.30: Time evolution of the volume-averaged trapped and passing electron heat flux (between $\tilde{\rho} = 0.3$ and $\tilde{\rho} = 0.7$) for the $\tau = 1$ simulations with and without zonal flow.

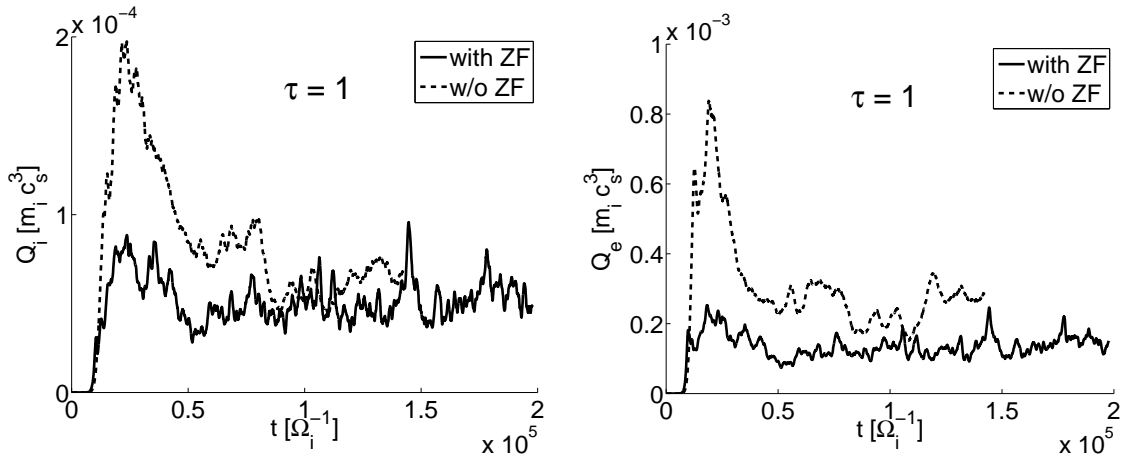


Figure 7.31: Time evolution of ion (left) and electron (right) heat flux for the $\tau = 1$ simulation with (solid line) and without (dashed line) zonal flow. All the curves are radially averaged between $\tilde{\rho} = 0.3$ and $\tilde{\rho} = 0.7$.

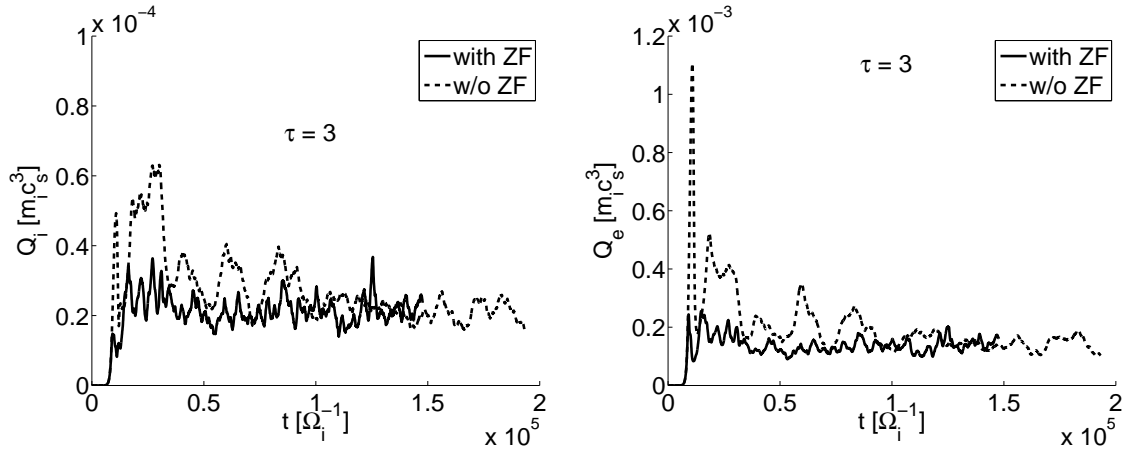


Figure 7.32: Time evolution of ion (left) and electron (right) heat flux for the $\tau = 3$ simulation with (solid line) and without (dashed line) zonal flow. All the curves are radially averaged between $\tilde{\rho} = 0.3$ and $\tilde{\rho} = 0.7$.

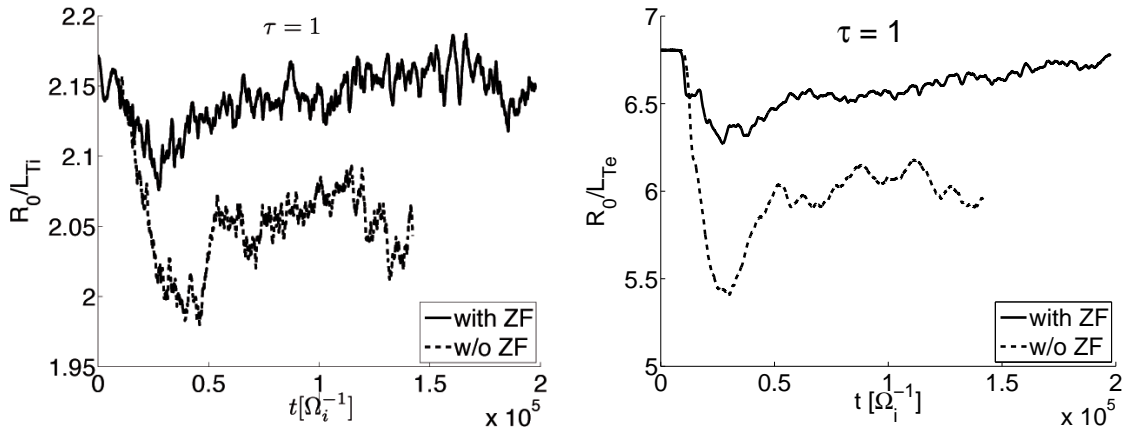


Figure 7.33: Time evolution of ion (left) and electron (right) normalized temperature gradient for the $\tau = 1$ simulation with (solid line) and without (dashed line) zonal flow. All the curves are radially averaged between $\tilde{\rho} = 0.3$ and $\tilde{\rho} = 0.7$.

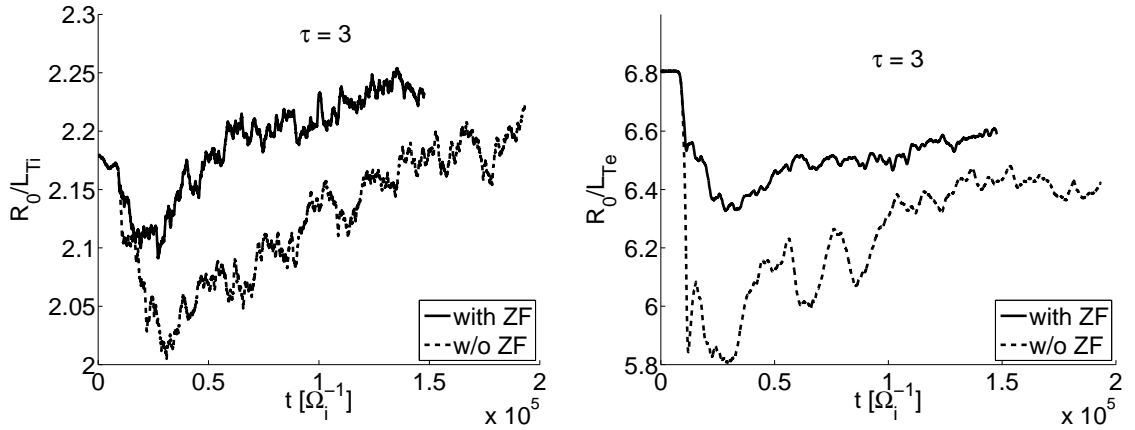


Figure 7.34: Time evolution of ion (left) and electron (right) normalized temperature gradient for the $\tau = 3$ simulation with (solid line) and without (dashed line) zonal flow. All the curves are radially averaged between $\tilde{\rho} = 0.3$ and $\tilde{\rho} = 0.7$.

approximation from [92], taken from [155], is used:

$$\omega_{E \times B} \cong \frac{s \frac{d\psi}{ds}}{q} \frac{d^2}{d\psi^2} \phi_0(\psi) \quad (7.33)$$

It is generally accepted that zonal flows suppress turbulence once their shearing rate exceeds the maximum linear growth rate. This is by no means an exact criterion but a rough estimate. Fig. 7.35 shows the time evolution of $|\omega_{E \times B}|$, averaged between $\tilde{\rho} = 0.4$ and $\tilde{\rho} = 0.6$ for two CYCLONE adiabatic ITG simulations with $R_0/L_{Ti} = 6.9$ and $R_0/L_{Ti} = 7.6$. On top of these curves, the linear growth rate of the most unstable linear mode as a function of the radially-averaged, time varying normalized temperature gradient is plotted. It has been obtained with a quadratic fit from linear simulations. One can observe a small drop of the growth rate, corresponding to a decrease in the temperature gradient at the same time where the shearing rate becomes comparable, thus validating the shearing criterion. In the nonlinear phase, the shearing rate is 1.5 to 2 times larger than the linear growth rate. Note also that the shearing rate is higher for the R_0/L_{Ti} case, reflecting a stronger, hence more difficult turbulence to suppress. The same curves for the two TEM simulations at $\tau = 1$ and $\tau = 3$ are represented on Fig. 7.36. For this case, the shearing rate value is on average comparable to the largest linear growth rate. For the $\tau = 3$ case, the linear growth rate is even slightly higher than the average shearing rate. From Figures 7.35 and 7.36, one can conclude that the shearing rate turbulence suppression criterion holds as well for the TEM simulations presented here. However,

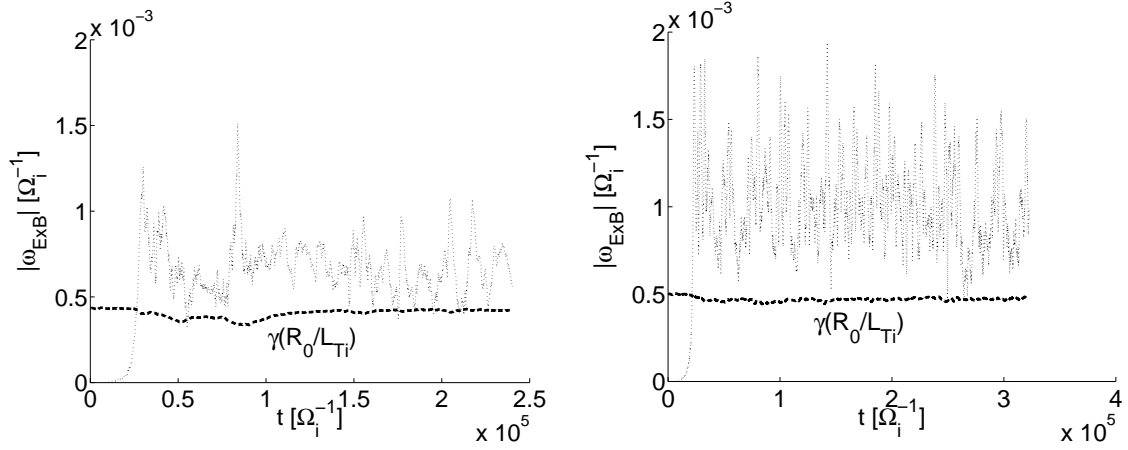


Figure 7.35: Time evolution of $|\omega_{ExB}|$, averaged between $\tilde{\rho} = 0.3$ and $\tilde{\rho} = 0.7$ for a CYCLONE ITG simulation with initial $R_0/L_{Ti} = 6.9$ (left) and $R_0/L_{Ti} = 7.6$ (right). The dashed line is $\gamma(R_0/L_{Ti}(t))$, where $R_0/L_{Ti}(t)$ is the radially-averaged value (between $\tilde{\rho} = 0.4$ and $\tilde{\rho} = 0.6$) at time t and $\gamma(x = R_0/L_{Ti})$ is obtained from a quadratic fit of the growth rate of the most unstable linear mode as a function of R_0/L_{Ti} .

in the ITG case, the shearing rate is approximatively twice the growth rate whereas for the TEM case it is comparable. This could be related to the fact that the heat flux for ITG turbulence is four times higher when zonal flows are filtered out, while this factor is strongly reduced for TEM turbulence. Therefore, another saturation mechanism may also be responsible for the turbulence suppression.

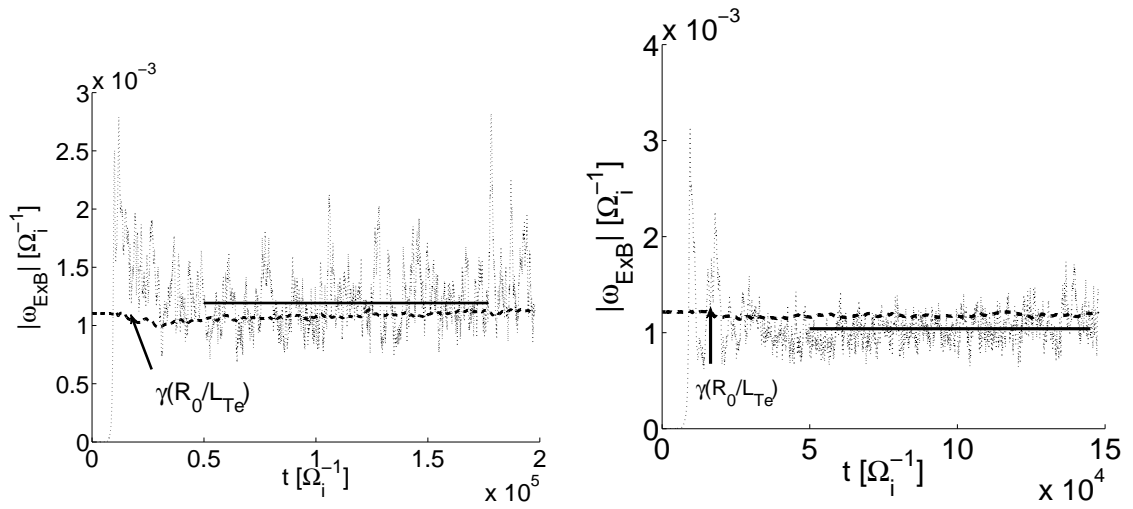


Figure 7.36: Time evolution of radial maximum of $|\omega_{ExB}|$ rate for TEM simulations with $\tau = 1$ (left) and $\tau = 3$ (right). The dashed line is $\gamma(R_0/L_{Te}(t))$, where $R_0/L_{Te}(t)$ is the radially-averaged value (between $\tilde{\rho} = 0.4$ and $\tilde{\rho} = 0.6$) at time t and $\gamma(x = R_0/L_{Te})$ is obtained from a quadratic fit of the growth rate of the most unstable linear mode as a function of R_0/L_{Te} . Horizontal solid lines are the time averages of $|\omega_{ExB}|$.

Chapter 8

Conclusions and future work

8.1 Conclusions

In this work, a 5D global gyrokinetic model aimed at studying microturbulence in Tokamaks has been presented and its implementation in a Particle-In-Cell code has been detailed. The originality lies in the use of the straight-field-line angle. The singularity at the magnetic axis is circumvented by using pseudo-cartesian coordinates. The straight-field-line angle is more adapted for this model because the turbulence is by assumption aligned with the magnetic field lines. It has led to a very efficient Fourier filtering technique. Its consequences have been thoroughly studied, both analytically and numerically. The weaknesses of the initial implementation (a rectangular Fourier filter and the implementation with the poloidal angle) have been identified. The great advantages of the new implementation have been clearly demonstrated. First, the energy conservation and the signal to noise ratio have been massively improved. Second, the time step of the simulation has been increased by one order of magnitude for the case of ITG turbulence. Third, a new field solver has been implemented which reduces the total memory by a factor 10. Altogether, a gain of CPU time of two to three orders of magnitude has been achieved for a given accuracy. Last but not least, the scaling of the code with respect to the plasma size, one of the most important parameter for future fusion devices, is now optimal. Coupled to the excellent parallel efficiency and other algorithms implemented in ORB5 by different persons during the time period of this work, this code is now able to simulate global ITG turbulence in ITER-size plasmas.

The new version of the code has been benchmarked in several ways. First, ORB5 has been compared to a simple toroidal ITG dispersion relation. The qualitative agreement is excellent. The quantitative comparison is of course delicate due to the numerous approximations done to obtain the dispersion relation. The code has also been linearly benchmarked against the global PIC code GT3D. The well-known CYCLONE nonlinear benchmark has been successfully performed.

Then, the code has been applied to two issues of the gyrokinetic theory. First, δf PIC codes are constantly criticized due to their inability to reach a thermodynamical steady state. Due to the linear growth of the numerical noise in time inherent to the δf PIC scheme, it is difficult, not to say inadequate, to make quantitative predictions based on this method. It has been theoretically argued that dissipation must be present in order to prevent this unphysical phenomenon. This thesis has shown for the first time that a Krook-based noise-control algorithm allows the simulations to reach a steady state. More specifically, the time evolution equation of the fluctuation entropy has been derived and examined, both analytically and numerically. A steady state is achieved because the fluctuation entropy is, on average, constant. For decaying turbulence, the steady state is temporary because the system gets closer and closer to the marginal state, with a turbulence decaying to zero, and therefore an unbounded signal to noise ratio. For driven simulations, the system remains in a turbulent state and the steady state is permanent. Second, the importance of the v_{\parallel} nonlinearity (VNL) has been re-examined with the optimized version of ORB5. While previous transient simulations with the old implementation of the model found a difference in the radial profile of the zonal flow, simulations using the field-aligned Fourier filter now prove that this difference was due to numerical noise, and that the VNL has in fact no significant impact on the heat transport and on the zonal flow structure for collisionless ITG simulations. This statement remains valid in the previously unexplored situation of driven simulations. These results show that although the noise issue is often discussed in the frame of ETG turbulence, it must be carefully diagnosed and measured in ITG turbulence as well.

The first part of this thesis has been devoted to the optimization of the code and has led to new contributions on ITG turbulence. However, these improvements are also aimed at developing the physical model beyond the usual ITG picture. To be specific, the adiabatic assumption employed in the ITG model is not able to capture the TEM instability,

caused by the precession drift of trapped electrons. From the computational point of view, simulating simultaneously electrons and ions at a kinetic level is a challenging task. The optimized version of ORB5 has been extended to include the drift-kinetic response of the trapped electrons, the passing ones being still adiabatic. The first stage of the model validation dealt with the convergence of several numerical parameters in the linear regime. The second stage included linear benchmarks against a dispersion relation and against the global PIC code GT3D. The third stage of the validation treated the nonlinear detrapping caused by turbulence. The passing-trapped boundary of the phase space is modified by the presence of an electric field. However, by invoking the gyrokinetic ordering it has been shown that the displacement of this boundary is indeed small. It has further been shown that the heat flux carried by detrapped electrons is small. Finally, long, driven nonlinear simulations of TEM turbulence have been performed and, in particular, the heat flux and the role of zonal flows have been studied. For the parameters considered, the shearing rate criterion seems to be valid for TEM simulations, although another saturation mechanism yet unknown might also play a role.

8.2 Future work

In a long term perspective, it is desirable that gyrokinetic codes contain as much physical effects as possible for two reasons. First, the fundamental understanding of microturbulence is not complete yet. The starting point of most of gyrokinetic codes is the collisionless, electrostatic ITG turbulence case for circular geometry. Many important features of turbulence have been discovered such as the Dimits shift and saturation through zonal flow shearing. These issues are currently re-examined with more physics included in the model. Second, the fundamental purpose of gyrokinetic codes would be to recover the experimentally measured transport, and in a further step to test the actual scaling laws in view of predicting the performance of future tokamaks. These predictions will obviously be more realistic if all the relevant physical effects are included.

In parallel with the physical model, there are still some numerical improvements to be made. In terms of CPU time, the code scales as $(\rho^*)^{-2}$ except for the Fourier transforms that are done on a $(N_s, N_{\theta_*}, N_\varphi) \sim (\rho^*)^{-3}$ grid. The Fourier transforms are rather fast compared to the markers pushing, but the parallel transpose operation (i.e. going from an

array parallelized in the φ direction to an array parallelized in the θ_* direction) becomes rapidly dominant for large system size $\rho_* \sim 1/1000$. Optimization of the whole Fourier transform/parallel transpose process is highly desirable for simulations of ITER-size plasmas.

Another necessary modification concerns the coefficients for MHD equilibria: they are interpolated on a (s, θ_*) grid from a (r, z) grid given by CHEASE. Because this code is able to provide the equilibrium directly in (s, θ_*) coordinate, it is possible to avoid these cumbersome interpolations.

Finally, the numerical noise problem is still a hot research topic. New methods like Proper Orthogonal Decomposition (POD) have been implemented in lower dimensional PIC codes [156] and showed promising results. The use of POD methods in a 5D gyrokinetic code could be useful for radial filtering, which is absent in ORB5, and collisions operators.

There are several essential physical effects missing in ORB5. One of the most important is collisions: even if the temperature in ITER will be extremely high, there remains a small but finite collisionality. Ion-ion collisions have a damping effect on the zonal flow [157] and are needed to retrieve neoclassical transport from gyrokinetic codes [158]. Electron-Ion collisions have a clear effect on TEM through the detrapping effect: this mode is often divided into a collisionless and a dissipative branch.

Another important effect presently missing in ORB5 is the impurities. The presence of impurities in the core can lead to radiative losses which will lower the power of fusion reactions. Burning plasmas will contain helium ashes which can dilute the deuterium and the tritium. In addition, the so-called impurity mode [159] can be driven unstable when the impurity density profile is outwardly peaked while the main ion species and the electrons density profiles are inwardly peaked. There has been some linear [160], [161] and nonlinear [162] studies on this topic.

This work has been done by assuming electrostatic turbulence, i.e. $\beta = 0$. However, at finite β a new electromagnetic mode can become unstable, the shear-Alfvénic ion temperature gradient (AITG) mode [163], [164], sometimes called Kinetic Ballooning Mode (KBM) [141]. It is very difficult to study nonlinear electromagnetic simulations with PIC codes due to the cancellation problem [132], [134]. A split-weight scheme [130] or a hybrid fluid-kinetic model [165] can suppress this problem. First global PIC electromagnetic gy-

gyrokinetic simulations have been published recently [166]. In ORB5, the development of electromagnetic perturbation is in progress, while a model for static magnetic islands has already been implemented [167].

Burning plasmas will contain energetic α -particles. These particles have extremely wide orbits and are very fast such that a special treatment is needed. For instance, energetic particles are treated as passive in the flux-tube code GENE [168].

These examples, as well as this work, show that plasma turbulence is a huge, relatively unexplored and extremely complex field. However, the massive development of analytical models and gyrokinetic codes will hopefully provide solid theoretical foundations for increasing the predictive capability for turbulent transport in future fusion devices.

Appendix A

Discretization with splines

This annex gives the detailed expressions of splines quantities computed with ORB5. These technical details are useful to understand the implementation of the quasi-neutrality equation in ORB5. In particular, they provide a solid basis for people who would like to add additional physics in the quasi-neutrality equation directly in ORB5.

A.1 Splines notations

B-splines are piecewise polynomial functions on a finite support. They are generated via the relation:

$$\Lambda_{n+1}(x) = \int \Lambda_0(x - x')\Lambda_n(x')dx' \quad (\text{A.1})$$

Where $\Lambda_0(x)$ is defined by:

$$\Lambda_0(x) = \mathcal{H}(x)\mathcal{H}(1 - x) = \begin{cases} 1 & \text{if } 0 < x < 1 \\ 0 & \text{else} \end{cases} \quad (\text{A.2})$$

where $\mathcal{H}(x)$ is the Heavyside function. A spline of order $p > 0$ is therefore composed of $p + 1$ contiguous piece-wise polynomials of order p , named $P_k^p(x)$, $k = 0, 1, \dots, p$, that can be reduced to the interval $[0 : 1]$. For cubic splines the P_k^3 are given by:

$$P_0^3(x) = \frac{1}{6}x^3 \quad (\text{A.3})$$

$$P_1^3(x) = \frac{1}{6} + \frac{1}{2}x + \frac{1}{2}x^2 - \frac{1}{2}x^3 \quad (\text{A.4})$$

$$P_2^3(x) = \frac{2}{3} - x^2 + \frac{1}{2}x^3 \quad (\text{A.5})$$

$$P_3^3(x) = \frac{1}{6} - \frac{1}{2}x + \frac{1}{2}x^2 - \frac{1}{6}x^3 = \frac{1}{6}(1 - x)^3 \quad (\text{A.6})$$

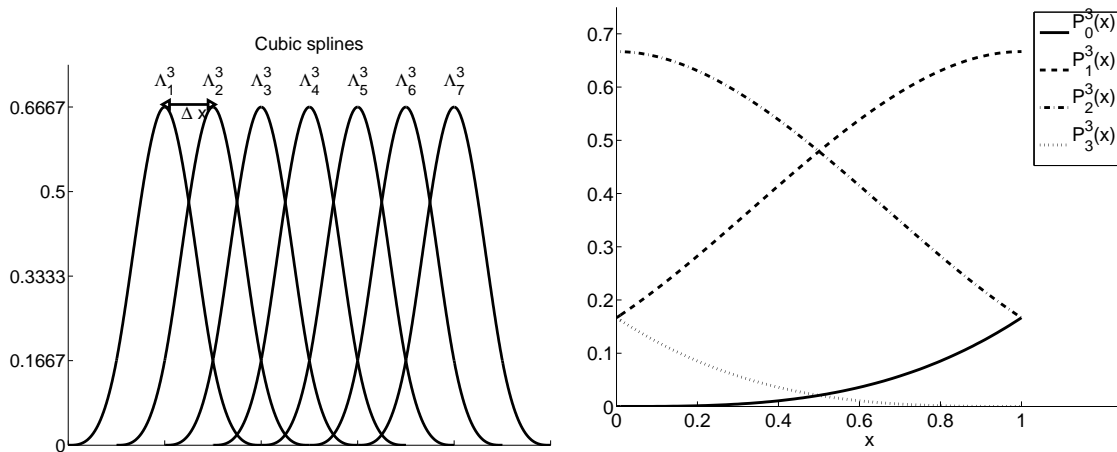


Figure A.1: Cubic splines (left) and $\{P_k^3(x)\}$ (right).

This polynomial decomposition is for example useful to compute the generic expression, valid for any spline order p , of $M^{(n)}$ (see Eq. (4.90) for $p = 1, 2, 3$):

$$M^{(n)} = \frac{2\pi}{N_\varphi} \left\{ \sum_{k=1}^p 2 \cos\left(\frac{2\pi}{N_\varphi} nk\right) C_k^p + C_0^p \right\} \quad (\text{A.7})$$

$$C_k^p = \sum_{j=0}^{p-k} \int_0^1 dx P_j^p(x) P_{j+k}^p(x) \quad (\text{A.8})$$

Cubic splines are displayed on Fig. A.1. Splines are very convenient to solve integro-differential equations because operators act on polynomial functions that are very easy to handle. It is obvious that the higher the order, the smoother the potential will be. B-splines have the important property that for any spline order:

$$\int_{-\infty}^{\infty} \Lambda_i(x) dx = 1 \quad \forall i \quad (\text{A.9})$$

ORB5 can use linear, quadratic or cubic splines. The splines are tensor products of B-splines:

$$\Lambda_\mu(\vec{x}) = \Lambda_j(s) \Lambda_k(\theta_*) \Lambda_l(\varphi) \quad (\text{A.10})$$

where N_s, N_{θ_*} and N_φ are the number of intervals in the s, θ_* and φ directions. The lengths of the intervals are $\Delta s = (s_{f,\max} - s_{f,\min})/N_s$, $\Delta\theta_* = 2\pi/N_{\theta_*}$ and $\Delta\varphi = 2\pi/N_\varphi$. The intervals are numbered from 0 to $N_s - 1, N_{\theta_*} - 1, N_\varphi - 1$, giving $N_s + 1, N_{\theta_*} + 1$ and $N_\varphi + 1$ grid points, numbered from 0 to N_s, N_{θ_*} and N_φ . In the periodic directions θ_* and φ , the first and the last grid points are the same. Therefore there are N_{θ_*} and

N_φ different splines, numbered from 0 to $N_{\theta_*} - 1, N_\varphi - 1$. In the radial direction, due to the non-periodicity p_l splines must be added to the left of the domain, numbered $\Lambda_{-p_l}, \Lambda_{-p_l+1}, \dots, \Lambda_{-1}$ and p_r splines must be added to the right of the domain, numbered $\Lambda_{N_s}, \Lambda_{N_s+1}, \dots, \Lambda_{N_s+p_r-1}$, with:

$$p_l = \text{floor}(p/2), \quad p_r = \text{ceiling}(p/2) \quad (\text{A.11})$$

In the radial direction there are $p_l + p_r = p$ additional splines. The following convention is used for the splines numbering. For odd spline order, a spline $\Lambda_j(s)$ is centered on point s_j . For even spline order, a spline $\Lambda_j(s)$ is centered on point $s_{j+1/2} = (s_j + s_{j+1})/2$. The sum over μ in (4.71) is in fact a sum over three indices:

$$\sum_{\mu} = \sum_{j=-p_l}^{N_s+p_r-1} \sum_{k=0}^{N_{\theta_*}-1} \sum_{l=0}^{N_\varphi-1} \quad (\text{A.12})$$

A.2 Discretization of Finite-Element-Matrices

The analytical form of the matrix is given by Eq. (4.87):

$$\begin{aligned} A_{\mu\nu} = & \int ds d\theta_* J_{\theta_* s \varphi}(s, \theta_*) \left\{ \frac{en_0(s)}{T_e(s)} \Lambda_\nu(s, \theta_*) \Lambda_\mu(s, \theta_*) \right. \\ & \left. + \frac{n_0(s)}{B\Omega_i} \nabla_{\text{pol}} \Lambda_\nu(s, \theta_*) \cdot \nabla_{\text{pol}} \Lambda_\mu(s, \theta_*) \right\} \end{aligned} \quad (\text{A.13})$$

First, the matrix is divided into $n_A = 5$ terms depending on the derivative order of the splines:

$$\begin{aligned} w = 1 & \rightarrow \Lambda_j(s) \Lambda_{j'}(s) \Lambda_k(\theta_*) \Lambda_{k'}(\theta_*) \\ w = 2 & \rightarrow \Lambda'_j(s) \Lambda'_{j'}(s) \Lambda_k(\theta_*) \Lambda_{k'}(\theta_*) \\ w = 3 & \rightarrow \Lambda_j(s) \Lambda'_{j'}(s) \Lambda'_k(\theta_*) \Lambda_{k'}(\theta_*) \\ w = 4 & \rightarrow \Lambda'_j(s) \Lambda_{j'}(s) \Lambda_k(\theta_*) \Lambda'_{k'}(\theta_*) \\ w = 5 & \rightarrow \Lambda_j(s) \Lambda_{j'}(s) \Lambda'_k(\theta_*) \Lambda'_{k'}(\theta_*) \end{aligned}$$

The matrix can therefore be decomposed as:

$$A_{\mu\nu} = \sum_{w=1}^{n_A} A_{\mu\nu}^w \quad (\text{A.14})$$

The integrals are performed with a Gaussian integration formula of order n_g :

$$\int_{s_{f,\min}}^{s_{f,\max}} ds f(s) \rightarrow \sum_{J=0}^{N_s-1} \sum_{q_s=1}^{n_g} g_{q_s} f(s_{Jq_s}) \Delta s \quad (\text{A.15})$$

$$\int_0^{2\pi} d\theta_* f(\theta_*) \rightarrow \sum_{K=0}^{N_{\theta_*}-1} \sum_{q_{\theta_*}=1}^{n_g} g_{q_{\theta_*}} f(\theta_{*Kq_{\theta_*}}) \Delta\theta_* \quad (\text{A.16})$$

where $s_{Jq_s} = (J + p_{q_s}) \Delta s$, $\theta_{*Kq_{\theta_*}} = (K + p_{q_{\theta_*}}) \Delta\theta_*$, $\{g_i, i = 1, \dots, n_g\}$ are the Gaussian weights and $\{p_i, i = 1, \dots, n_g\}$ are the Gaussian points: the integral is divided into intervals containing n_g Gauss points. For convenience, the derivation of the discretized form of the matrix $A_{\mu\nu}^1$ is presented, and then the complete form is easily generalized.

$$\begin{aligned} A_{j k, j' k'}^1 &= \int ds d\theta_* J_{\theta_* s \varphi}(s, \theta_*) \frac{e n_0(s)}{T_e(s)} \Lambda_j(s) \Lambda_{j'}(s) \Lambda_k(\theta_*) \Lambda_{k'}(\theta_*) \\ &= \Delta\theta_* \Delta s \sum_{J=0}^{N_s-1} \sum_{K=0}^{N_{\theta_*}-1} \sum_{q_s, q_{\theta_*}=1}^{n_g} g_{q_{\theta_*}} g_{q_s} J_{\theta_* s \varphi}(s_{Jq_s}, \theta_{*Kq_{\theta_*}}) \frac{e n_0(s_{Jq_s})}{T_e(s_{Jq_s})} \times \\ &\quad \Lambda_j(s_{Jq_s}) \Lambda_{j'}(s_{Jq_s}) \Lambda_k(\theta_{*Kq_{\theta_*}}) \Lambda_{k'}(\theta_{*Kq_{\theta_*}}) \end{aligned} \quad (\text{A.17})$$

According to the spline notation, i and i' go from $-p_l$ to $N_s - 1 + p_r$ and j, j' go from 0 to $N_{\theta_*} - 1$. The convention adopted is that global indices μ, ν are in $[1 : (N_s + p)N_{\theta_*}]$ and so:

$$\mu = (j + p_l)N_{\theta_*} + k + 1, \quad \nu = (j' + p_l)N_{\theta_*} + k' + 1 \quad (\text{A.18})$$

In order to get a convenient discretized form, the key point is to realize that all the splines have the same shape. Therefore the spline number can be shifted together with the evaluated location. Mathematically this is expressed as:

$$\Lambda_k(\theta_{*Kq_{\theta_*}}) = \Lambda_k((K + p_{q_{\theta_*}})\Delta\theta_*) = \Lambda_{\text{mod}(k-K, N_{\theta_*})}(p_{q_{\theta_*}} \Delta\theta_*) \quad (\text{A.19})$$

The same applies in the radial direction (without the modulo operation). If one assumes that each interval goes from 0 to 1, this property means that the matrix can be written in terms of the polynomials $\{P_k^p\}, k = 0, \dots, p$ evaluated at the Gauss points.

$$\begin{aligned} A_{j k, j' k'}^1 &= \Delta\theta_* \Delta s \sum_{J=0}^{N_s-1} \sum_{K=0}^{N_{\theta_*}-1} \sum_{q_s, q_{\theta_*}=1}^{n_g} g_{q_{\theta_*}} g_{q_s} J_{\theta_* s \varphi}(s_{Jq_s}, \theta_{*Kq_{\theta_*}}) \frac{e n_0(s_{Jq_s})}{T_e(s_{Jq_s})} \times \\ &\quad \Lambda_{j-J}(p_{q_s}) \Lambda_{j'-J}(p_{q_s}) \Lambda_{\text{mod}(k-K, N_{\theta_*})}(p_{q_{\theta_*}}) \Lambda_{\text{mod}(k'-K, N_{\theta_*})}(p_{q_{\theta_*}}) \end{aligned}$$

Note that the indexing of splines in the radial direction is slightly wrong in order to lighten the notations. However the final form of the discretized matrix will be correct. Once that the splines and the coefficient $J_{\theta_* s \varphi}(s, \theta_*) en_0(s)/T_e(s)$ have been computed at the Gauss points, one needs to add 4 loops containing $p + 1$ elements and to find the $p + 1$ values of j, j', k, k' that will have a non zero contribution. At this point it is important to know the indexing of the splines and the matrix. The indexing convention is such that for an interval J, K , there will be a contribution from splines $j, j' = J - p_l$ to $j, j' = J + p_r$, and splines $k, k' = K - p_l$ to $k, k' = K + p_r$, so $(p_l + p_r + 1)^4 = (p + 1)^4$ contributions in total. The final step to understand the matrix construction is the matrix indexing, which differs from the spline indexing. The matrix can be viewed as a $(N_s + p) \times (N_s + p)$ blocks of size $N_{\theta_*} \times N_{\theta_*}$. For a given interval J, K where $J \in [0 : N_s - 1], K \in [0 : N_{\theta_*} - 1]$, the indexes of the splines that will receive a non-zero contribution are the following:

$$\begin{aligned}
j &= J - p_l + u, u = 0, 1, \dots, p \\
j' &= J - p_l + u', u' = 0, 1, \dots, p \\
k &= \text{mod}(K - p_l + u, N_{\theta_*}), u = 0, 1, \dots, p \\
k' &= \text{mod}(K - p_l + u', N_{\theta_*}), u' = 0, 1, \dots, p
\end{aligned}$$

The matrix can be rewritten as:

$$\begin{aligned}
A_{jk, j'k'}^1 &= \Delta\theta_* \Delta s \sum_{J=0}^{N_s-1} \sum_{K=0}^{N_{\theta_*}-1} \sum_{q_s, q_{\theta_*}=1}^{n_g} g_{q_{\theta_*}} g_{q_s} J_{\theta_* s \varphi}(s_{Jq_s}, \theta_{*Kq_{\theta_*}}) \frac{en_0(s_{Jq_s})}{T_e(s_{Jq_s})} \\
&\quad \sum_{u_j, u_{j'}, u_k, u_{k'}=0}^p \Lambda_{j-J}(p_{q_s} \Delta\theta_*) \Lambda_{j'-J}(p_{q_s} \Delta s) \Lambda_{\text{mod}(k-K, N_{\theta_*})}(p_{q_{\theta_*}} \Delta\theta_*) \\
&\quad \Lambda_{\text{mod}(k'-K, N_{\theta_*})}(p_{q_{\theta_*}} \Delta\theta_*) \delta_{j, J-p_l+u_j} \delta_{j', J-p_l+u_{j'}} \delta_{k, \text{mod}(K-p_l+u_k, N_{\theta_*})} \\
&\quad \delta_{k', \text{mod}(K-p_l+u_{k'}, N_{\theta_*})}
\end{aligned} \tag{A.20}$$

Each spline of order p is composed of $p + 1$ polynomials $P_k^p(x), k = 1, \dots, p + 1$, which for simplicity are defined in the interval $[0 : 1]$. When the $(p + 1)$ different splines Λ_j are evaluated on a given interval J , it is in fact the $p + 1$ polynomials $P_k^p(x), k = 0, \dots, p$ that are evaluated at the different Gauss points. For a given spline, the polynomials are numbered from left to right, but on a given interval, the contribution from the left most spline $J - p_l$ is given by the right most polynomial P_{p+1}^p . In this way the splines Λ can

be replaced with the polynomials $P_k^p(x)$.

$$\begin{aligned}
A_{jk,j'k'}^1 &= \sum_{J=0}^{N_s-1} \sum_{K=0}^{N_{\theta_*}-1} \sum_{q_s, q_{\theta_*}=1}^{n_g} \Delta s \Delta \theta_* g_{q_s} g_{q_{\theta_*}} \frac{en_0(s_{Jq_s})}{T_e(s_{Jq_s})} \\
&\quad \sum_{u_j, u_{j'}, u_k, u_{k'}=0}^p P_{p-u_j}^p(p_{q_s}) P_{p-u_{j'}}^p(p_{q_s}) P_{p-u_k}^p(p_{q_{\theta_*}}) P_{p-u_{k'}}^p(p_{q_{\theta_*}}) \\
&\quad \delta_{j, J-p_l+u_j} \delta_{j', J-p_l+u_{j'}} \delta_{k, \text{mod}(K-p_l+u_k, N_{\theta_*})} \delta_{k', \text{mod}(K-p_l+u_{k'}, N_{\theta_*})}
\end{aligned}$$

Now the whole expression of A can be written. Because the polynomials $\{P_k^p\}$ are defined between 0 and 1, a derivative in the s direction will introduce a factor Δs^{-1} and a derivative in the θ_* direction will introduce a factor $\Delta \theta_*^{-1}$. The discretized form of the matrix is then:

$$\begin{aligned}
A_{jk,j'k'} &= \sum_{J=0}^{N_s-1} \sum_{K=0}^{N_{\theta_*}-1} \sum_{q_s, q_{\theta_*}=1}^{n_g} \sum_{w=1}^{n_A} \Delta s^{1-a_j^w - a_{j'}^w} \Delta \theta_*^{1-a_j^w - a_{j'}^w} g_{q_s} g_{q_{\theta_*}} C^w(s_{Jq_s}, \theta_{*Kq_{\theta_*}}) \\
&\quad \sum_{u_j, u_{j'}, u_k, u_{k'}=0}^p \frac{d^{a_j^w}}{dx^{a_j^w}} P_{p-u_j}^p(p_{q_s}) \frac{d^{a_{j'}^w}}{dx^{a_{j'}^w}} P_{p-u_{j'}}^p(p_{q_s}) \frac{d^{a_k^w}}{dx^{a_k^w}} P_{p-u_k}^p(p_{q_{\theta_*}}) \\
&\quad \frac{d^{a_{k'}^w}}{dx^{a_{k'}^w}} P_{p-u_{k'}}^p(p_{q_{\theta_*}}) \delta_{j, J-p_l+u_j} \delta_{j', J-p_l+u_{j'}} \delta_{k, \text{mod}(K-p_l+u_k, N_{\theta_*})} \delta_{k', \text{mod}(K-p_l+u_{k'}, N_{\theta_*})}
\end{aligned} \tag{A.21}$$

With:

$$C^1(s_{Jq_s}, \theta_{*Kq_{\theta_*}}) = J_{\theta_* s \varphi}(s_{Jq_s}, \theta_{*Kq_{\theta_*}}) \frac{en_0(s_{Jq_s})}{T_e(s_{Jq_s})} \tag{A.22}$$

$$C^2(s_{Jq_s}, \theta_{*Kq_{\theta_*}}) = J_{\theta_* s \varphi}(s_{Jq_s}, \theta_{*Kq_{\theta_*}}) \frac{n_0(s_{Jq_s})}{B(s_{Jq_s}, \theta_{*Kq_{\theta_*}}) \Omega_i(s_{Jq_s}, \theta_{*Kq_{\theta_*}})} \tag{A.23}$$

$$C^i(s_{Jq_s}, \theta_{*Kq_{\theta_*}}) = C^2(s_{Jq_s}, \theta_{*Kq_{\theta_*}}), i = 3, \dots, 5 \tag{A.24}$$

$$a_j^w = \{0, 1, 0, 1, 0\}, a_{j'}^w = \{0, 1, 1, 0, 0\}, a_k^w = \{0, 0, 1, 0, 1\}, a_{k'}^w = \{0, 0, 0, 1, 1\} \tag{A.25}$$

The construction of the matrix is parallelized: each processor has a fraction of the (J, K) intervals. The final matrix is obtained by summing the elements over all the processors. The code does not compute directly the coefficients, but loops over the intervals and progressively fills in the different matrix elements. The structure of A is show on Fig. A.2. The matrix can be viewed as $N_s + p$ blocks of size $N_{\theta_*} \times N_{\theta_*}$, The matrix is a band matrix whose bandwidth increases with the spline order.

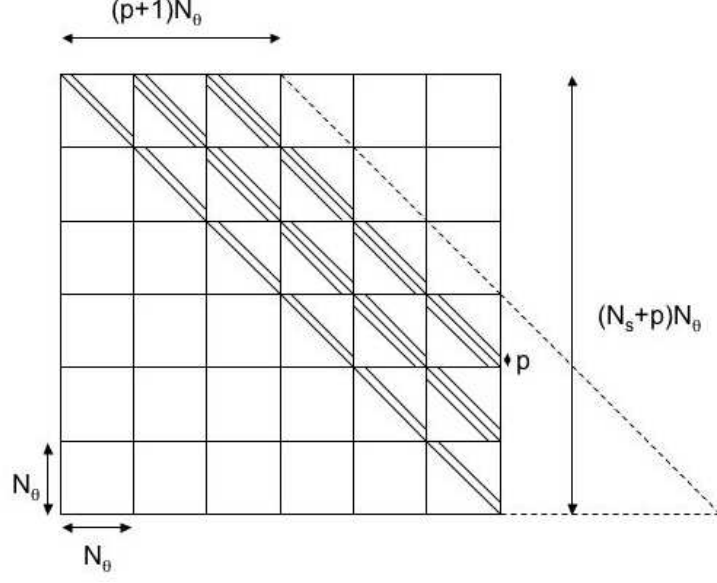


Figure A.2: Structure of A .

The zonal flow matrix is given by:

$$\begin{aligned} A_{\mu\nu}^{ZF} &= - \int ds d\theta_* J_{\theta_* s \varphi}(s, \theta_*) \frac{en_0(s)}{T_e(s)} \bar{\Lambda}_\mu(s) \Lambda_\nu(s, \theta_*) \\ &= - \int ds \frac{2\pi en_0(s)}{\Sigma(s) T_e(s)} \Lambda_j(s) \Lambda_{j'}(s) \tilde{\Lambda}_k(s) \tilde{\Lambda}_{k'}(s) \end{aligned} \quad (\text{A.26})$$

$$\tilde{\Lambda}_k(s) = \int d\theta_* \Lambda_k(\theta_*) J_{\theta_* s \varphi}(s, \theta_*) \quad (\text{A.27})$$

The expression for $\tilde{\Lambda}_k(s)$ can be obtained by using (A.19):

$$\tilde{\Lambda}_k(s) = \sum_{K=0}^{N_{\theta_*}-1} \sum_{q_{\theta_*}=1}^{n_g} \sum_{u_k=0}^p \Delta\theta_* g_{q_{\theta_*}} J_{\theta_* s \varphi}(s, \theta_{*Kq_{\theta_*}}) P_{p-u_k}^p(p_{q_{\theta_*}}) \delta_{k, \text{mod}(K-p_l+u_k, N_{\theta_*})} \quad (\text{A.28})$$

This expression can be simplified by noting that:

$$k = \text{mod}(K - p_l + u_k, N_{\theta_*}) \Leftrightarrow K = \text{mod}(k + p_l - u_k, N_{\theta_*}) \quad (\text{A.29})$$

The Kronecker function can be changed to give:

$$\tilde{\Lambda}_k(s) = \sum_{q_{\theta_*}=1}^{n_g} \sum_{u_k=0}^p \Delta\theta_* g_{q_{\theta_*}} J(s, \theta_{*\text{mod}(k+p_l-u_k, N_{\theta_*})q_{\theta_*}}) P_{p-u_k}^p(p_{q_{\theta_*}}) \quad (\text{A.30})$$

The discretized form of A^{ZF} can be written as:

$$\begin{aligned} A_{j k, j' k'}^{ZF} &= - \sum_{J=0}^{N_s-1} \sum_{q_s=1}^{n_g} \sum_{u_j, u_{j'}=0}^p \Delta s g_{q_s} C^{ZF}(s_{Jq_s}) \tilde{\Lambda}_j(s_{Jq_s}) \tilde{\Lambda}_{j'}(s_{Jq_s}) \times \\ &\quad P_{p-u_j}^p(p_{q_s}) P_{p-u_{j'}}^p(p_{q_s}) \delta_{j, J-p_l+u_j} \delta_{j', J-p_l+u_{j'}} \end{aligned} \quad (\text{A.31})$$

with:

$$C^{ZF}(s_{Jq_s}) = \frac{2\pi en_0(s_{Jq_s})}{T_e(s_{Jq_s})\Sigma(s_{Jq_s})} \quad (\text{A.32})$$

The zonal flow matrix has a different structure: the flux-surface-averaged operator couples all θ_* : all θ_* blocks are full.

A.3 Discretization of the perturbed density and electric field

Both the perturbed density and the electric field are splines quantities that depend on the markers position. The perturbed density is:

$$b_\nu^i = \frac{N_{\text{ph}}}{N_i} \sum_{r=1}^{N_i} \frac{1}{2\pi} \int d\alpha \Lambda_\nu(\vec{R}_r + \vec{\rho}_{Lir}) w_r(t) \quad (\text{A.33})$$

The integral is written as a finite sum:

$$b_{j,k,l}^i = \frac{N_{\text{ph}}}{N} \sum_{r=1}^N \frac{w_r(t)}{N_{gr}} \Lambda_l(\varphi_r) \sum_{\beta=1}^{N_{gr}} \Lambda_j(s_{r\beta}) \Lambda_k(\theta_{*r\beta}) \quad (\text{A.34})$$

With $s_{r\beta} = s_r \left(\frac{2\pi}{N_{gr}} (\beta - 1) \right)$ and $\theta_{*r\beta} = \theta_{*r} \left(\frac{2\pi}{N_{gr}} (\beta - 1) \right)$. The same procedure as in Sec. A.2 is used, with the difference that the polynomials $P_u^p(x)$, $u = 0, \dots, p$ are evaluated on $[0 : 1]$ depending on where the markers lie in their respective (s, θ_*, φ) intervals. One finds:

$$b_{j,k,l}^i = \frac{N_{\text{ph}}}{N_i} \sum_{r=1}^{N_i} \frac{w_r(t)}{N_{gr}} \sum_{\beta=1}^{N_{gr}} \sum_{u_j, u_k, u_l=0}^p P_{p-u_l}^p(\tilde{\varphi}_r) P_{p-u_j}^p(\tilde{s}_{r\beta}) P_{p-u_k}^p(\tilde{\theta}_{*r\beta}) \times \delta_{j, J_{r\beta} - p_l + u_j} \delta_{k, \text{mod}(K_{r\beta} - p_l + u_k, N_{\theta_*})} \delta_{l, \text{mod}(L_r - p_l + u_l, N_\varphi)} \quad (\text{A.35})$$

Where:

$$J_{r\beta} = \left[\frac{s_{r\beta} - s_{f,\min}}{\Delta s} \right], K_{r\beta} = \left[\frac{\theta_{*r\beta}}{\Delta \theta_*} \right], L_r = \left[\frac{\varphi_r}{\Delta \varphi} \right] \quad (\text{A.36})$$

$$\tilde{s}_{r\beta} = \frac{s_{r\beta} - s_{J_{r\beta}}}{\Delta s}, \tilde{\theta}_{*r\beta} = \frac{\theta_{*r\beta} - \theta_{*K_{r\beta}}}{\Delta \theta_*}, \tilde{\varphi}_r = \frac{\varphi_r - \varphi_{L_r}}{\Delta \varphi} \quad (\text{A.37})$$

The indexing of the RHS is slightly different from the matrix indexing. Instead of doing modulo operations in the poloidal and toroidal directions, p_l cells are added to the left and p_r cells are added to the right of the poloidal and toroidal domains. Applying modulo operations would require to send information between processors in the toroidal direction, and would slow down the computation in the poloidal direction. After the charge assignment, the following operations are done:

$$b_{j,k-1,l} = b_{j,k-1,l} + b_{j,N_{\theta_*}+k-1,l}, k = 1, \dots, p_r \quad (\text{A.38})$$

$$b_{j,N_{\theta_*}-k,l} = b_{j,N_{\theta_*}-k,l} + b_{j,-k,l}, k = 1, \dots, p_l \quad (\text{A.39})$$

$$b_{j,k,l-1} = b_{j,k,l-1} + b_{j,k,N_{\varphi}+l-1}, l = 1, \dots, p_r \quad (\text{A.40})$$

$$b_{j,k,N_{\varphi}-l} = b_{j,k,N_{\varphi}-l} + b_{j,k,-l}, l = 1, \dots, p_l \quad (\text{A.41})$$

The last two operations require communications between neighboring processors.

The electric field is obtained in a similar way except that a derivative must be applied on the splines:

$$\langle \vec{E} \rangle = \frac{1}{N_{gr}} \sum_{\beta=1}^{N_{gr}} \vec{E}_{s\beta} + \vec{E}_{\theta_*\beta} + \vec{E}_{\varphi\beta} \quad (\text{A.42})$$

$$\vec{E}_{s\beta} = \frac{1}{\Delta s} \sum_{u_j, u_k, u_l=0}^p \phi_{u_j, u_k, u_l} \frac{dP_{p-u_j}^p(\tilde{s}_{r\beta})}{dx} P_{p-u_k}^p(\tilde{\theta}_{*r\beta}) P_{p-u_l}^p(\tilde{\varphi}_r) \nabla s|_{s_{r\beta}, \theta_{*r\beta}}$$

$$\vec{E}_{\theta_*\beta} = \frac{1}{\Delta \theta_*} \sum_{u_j, u_k, u_l=0}^p \phi_{u_j, u_k, u_l} P_{p-u_j}^p(\tilde{s}_{r\beta}) \frac{dP_{p-u_k}^p(\tilde{\theta}_{*r\beta})}{dx} P_{p-u_l}^p(\tilde{\varphi}_r) \nabla \theta_*|_{s_{r\beta}, \theta_{*r\beta}}$$

$$\vec{E}_{\varphi\beta} = \frac{1}{\Delta \varphi} \sum_{u_j, u_k, u_l=0}^p \phi_{u_j, u_k, u_l} P_{p-u_j}^p(\tilde{s}_{r\beta}) P_{p-u_k}^p(\tilde{\theta}_{*r\beta}) \frac{dP_{p-u_l}^p(\tilde{\varphi}_r)}{dx} \nabla \varphi|_{s_{r\beta}, \theta_{*r\beta}}$$

$$\phi_{u_j, u_k, u_l} = \phi_{J_{r\beta}+p_l-u_j, K_{r\beta}+p_l-u_k, L_{r\beta}+p_l-u_l} \quad (\text{A.43})$$

The summation must be done in cartesian coordinates, yielding $\langle \vec{E} \rangle = \langle E_r \rangle \nabla r + \langle E_z \rangle \nabla z + \langle E_{\varphi} \rangle \nabla \varphi$. $\langle E_{\varphi} \rangle$ would need complicated parallel communications if the gyropoints were not lying in the poloidal plane. The electric field is then transformed back to $\langle \vec{E} \rangle = \langle E_s \rangle \nabla s + \langle E_{\theta_*} \rangle \nabla \theta_* + \langle E_{\varphi} \rangle \nabla \varphi$ via:

$$\langle E_s \rangle = \frac{\langle E_r \rangle \frac{\partial \theta_*}{\partial z} - \langle E_z \rangle \frac{\partial \theta_*}{\partial r}}{\frac{\partial s}{\partial r} \frac{\partial \theta_*}{\partial z} - \frac{\partial s}{\partial z} \frac{\partial \theta_*}{\partial r}}, \quad \langle E_{\theta_*} \rangle = \frac{\langle E_z \rangle \frac{\partial s}{\partial r} - \langle E_r \rangle \frac{\partial s}{\partial z}}{\frac{\partial s}{\partial r} \frac{\partial \theta_*}{\partial z} - \frac{\partial s}{\partial z} \frac{\partial \theta_*}{\partial r}} \quad (\text{A.44})$$

For drift kinetic electrons, the electric field is obtained by setting $N_{gr} = 1$ and by replacing the particle position by the guiding center position.

A.4 Boundary conditions

Boundary conditions are applied at $s = s_{f,\min}$ and $s = s_{f,\max}$. It is *a priori* not obvious to express any type of boundary conditions with splines, as the value of the potential at a given magnetic surface depends on $p + 1$ spline elements. For simplicity, the case $s = s_{f,\min}$ is presented. At any grid point there are p splines that are non zero. The idea is to introduce a new spline basis $\{\tilde{\Lambda}_\mu(x)\}$ on the first interval starting at $s = s_{f,\min}$ such that $\Lambda_{-p_l}(0) = 1$ and $\Lambda_i(0) = 0, i = -p_l + 1, -p_l + p$. In this way only one spline has a non-zero value at the first grid point and it becomes much easier to apply boundary conditions. The new basis can be found by writing that $\sum_\mu \phi_\mu \Lambda_\mu = \sum_\mu \tilde{\phi}_\mu \tilde{\Lambda}_\mu$ on the first p grid points. The new basis is $\tilde{\Lambda}_\mu = S_L \Lambda_\mu$, with:

$$S_L = \begin{pmatrix} \frac{1}{P_p^p(0)} & 0 \\ -\vec{w} & \mathbb{I} \end{pmatrix} \quad (\text{A.45})$$

$$\vec{w} = \begin{pmatrix} \frac{P_{p-1}(0)}{P_p^p(0)} & \frac{P_{p-2}(0)}{P_p^p(0)} & \dots & \frac{P_2(0)}{P_p^p(0)} \end{pmatrix} \quad (\text{A.46})$$

The same method applies for the right boundary of the domain. If S_L is the transformation matrix on the left side of the domain, then the transformation matrix on the right side of the domain, S_R is simply given by:

$$(s_r)_{ij} = (s_l)_{(-i+p+1)(-j+p+1)} \quad (\text{A.47})$$

For cubic splines, S_L and S_R are:

$$S_L = \begin{pmatrix} 6 & 0 & 0 \\ -4 & 1 & 0 \\ -1 & 0 & 1 \end{pmatrix}, S_R = \begin{pmatrix} 1 & 0 & -1 \\ 0 & 1 & -4 \\ 0 & 0 & 6 \end{pmatrix} \quad (\text{A.48})$$

On Fig. A.3, the new cubic spline basis is represented. The linear system in the new basis is:

$$\begin{pmatrix} S_L B S_L^t & S_L C & S_L D S_R^t \\ E S_L^t & F & G S_R^t \\ S_R H S_L^t & S_R I & S_R J S_R^t \end{pmatrix} \begin{pmatrix} \vec{u} \\ \vec{v} \\ \vec{w} \end{pmatrix} = \begin{pmatrix} S_L \vec{c} \\ \vec{d} \\ S_R \vec{e} \end{pmatrix} \quad (\text{A.49})$$

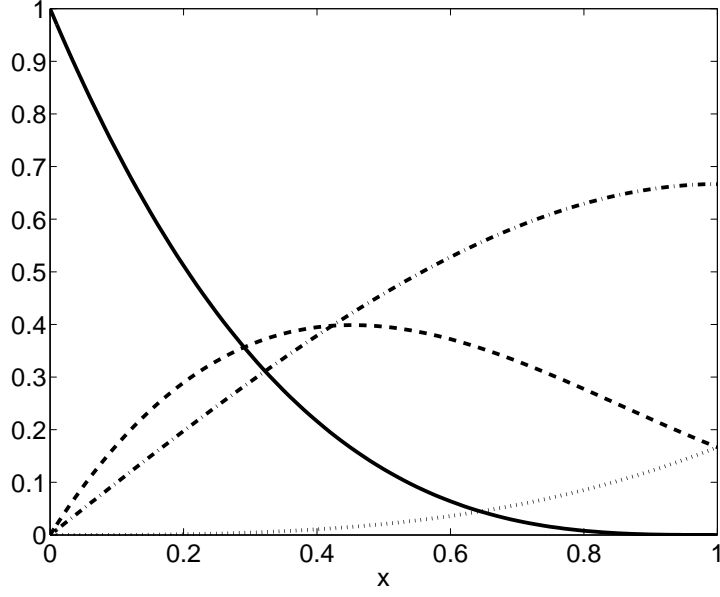


Figure A.3: Modification of cubic splines at $s = s_{f,\min}$.

Where the finite element matrix A and the charge assignment vector \vec{b} have been formally written as:

$$A = \begin{pmatrix} B & C & D \\ E & F & G \\ I & J & K \end{pmatrix}, \vec{b} = \begin{pmatrix} \vec{c} \\ \vec{d} \\ \vec{e} \end{pmatrix} \quad (\text{A.50})$$

When $s = 0$ is included in the simulation domain, unicity of the potential is applied: $\phi(s = 0, \theta_*, \varphi) = \phi_{axis} \forall \theta_*, \varphi$. The linear system is modified as follows:

$$\begin{pmatrix} 1 & 0 & \dots & 0 & 0 & 0 & \dots & 0 \\ 0 & 1 & \dots & 0 & 0 & 0 & \dots & 0 \\ \dots & \dots & \dots & \dots & \dots & \dots & \dots & \dots \\ 0 & 0 & \dots & 1 & 0 & 0 & \dots & 0 \\ 0 & 0 & \dots & 0 & \sum_{i,j=1}^{N_{\theta_*}} a_{i,j} & \sum_{i=1}^{N_{\theta_*}} a_{i,N_{\theta_*}+1} & \dots & \sum_{i=1}^{N_{\theta_*}} a_{i,N_{tot}} \\ 0 & 0 & \dots & 0 & \sum_{j=1}^{N_{\theta_*}} a_{N_{\theta_*}+1,j} & a_{N_{\theta_*}+1,N_{\theta_*}+1} & \dots & a_{N_{\theta_*}+1,N_{tot}} \\ \dots & \dots & \dots & \dots & \dots & \dots & \dots & \dots \\ 0 & 0 & \dots & 0 & \sum_{j=1}^N a_{N_{tot},j} & a_{N_{tot},N_{\theta_*}+1} & \dots & a_{N_{tot},N_{tot}} \end{pmatrix} \begin{pmatrix} \hat{\phi}_1 \\ \hat{\phi}_2 \\ \dots \\ \hat{\phi}_{N_{\theta_*}-1} \\ \hat{\phi}_{N_{\theta_*}} \\ \hat{\phi}_{N_{\theta_*}+1} \\ \dots \\ \hat{\phi}_{N_{tot}} \end{pmatrix} = \begin{pmatrix} 0 \\ 0 \\ \dots \\ 0 \\ \sum_{i=1}^{N_{\theta_*}} b_i \\ b_{N+1} \\ \dots \\ b_{N_{tot}} \end{pmatrix} \quad (\text{A.51})$$

Where N_{tot} is the total number of unknowns. It has been obtained after defining a matrix transformation that leaves the $\hat{\phi}_{N_{\theta_*}}$ coefficient unchanged and cancels the coefficients $\hat{\phi}_1$

to $\hat{\phi}_{N_{\theta_*}-1}$. After the solve the coefficient $\hat{\phi}_{N_{\theta_*}}$ is copied into the coefficients $\hat{\phi}_1$ to $\hat{\phi}_{N_{\theta_*}-1}$. At $s = s_{f,\max}$, the Dirichlet boundary condition $\phi(s_{f,\max}, \theta_*, \varphi) = 0$ is applied. The system is modified as follows:

$$\begin{pmatrix} B & 0 \\ 0 & \mathbb{I} \end{pmatrix} \begin{pmatrix} \vec{u} \\ \vec{v} \end{pmatrix} = \begin{pmatrix} \vec{c} \\ 0 \end{pmatrix} \quad (\text{A.52})$$

where \vec{v} contains the N_{θ_*} unknowns at $s = s_{f,\max}$ and \mathbb{I} is the $N_{\theta_*} \times N_{\theta_*}$ identity matrix.

A.5 Discretization of the FEM matrix for the field-aligned-solver

A general matrix $A = \{\{a\}_{jk}\}$ of size $N_{\theta_*} \times N_{\theta_*}$ reads in Fourier space:

$$\tilde{a}_{mm'} = \frac{1}{N_{\theta_*}} \sum_{j,k=0}^{N_{\theta_*}-1} a_{jk} \exp\left(-\frac{2\pi i}{N_{\theta_*}}(jm - km')\right) \quad (\text{A.53})$$

Using the decomposition (A.14), the derivation is presented for A^1 and will be generalized to the whole matrix A . The Fourier representation of A^1 is computed starting from Eq. (A.17):

$$\tilde{A}_{jm,j'm'}^{\text{lwa},1} = \frac{\Delta\theta_*\Delta s}{N_{\theta_*}} \sum_{J=0}^{N_s-1} \sum_{q_s, q_{\theta_*}=1}^{n_g} g_{q_{\theta_*}} g_{q_s} \Lambda_j(s_{Jq_s}) \Lambda_{j'}(s_{Jq_s}) \tilde{B}_{mm'}^1(s_{Jq_s}, q_{\theta_*}) \quad (\text{A.54})$$

$$\begin{aligned} \tilde{B}_{mm'}^1(s_{Jq_s}, q_{\theta_*}) &= \sum_{K=0}^{N_{\theta_*}-1} \sum_{k=0}^{N_{\theta_*}-1} \sum_{k'=0}^{N_{\theta_*}-1} J_{\theta_* s \varphi}(s_{Jq_s}, \theta_{*Kq_{\theta_*}}) \frac{en_0(s_{Jq_s})}{T_e(s_{Jq_s})} \Lambda_k(\theta_{*Kq_{\theta_*}}) \Lambda_{k'}(\theta_{*Kq_{\theta_*}}) \times \\ &\exp\left[-\frac{2\pi i}{N_{\theta_*}}(mk - m'k')\right] \end{aligned} \quad (\text{A.55})$$

By using Eq. (A.19), one has:

$$\begin{aligned} \tilde{B}_{mm'}^1(s_{Jq_s}, q_{\theta_*}) &= \sum_{K=0}^{N_{\theta_*}-1} \sum_{k=0}^{N_{\theta_*}-1} \sum_{k'=0}^{N_{\theta_*}-1} J_{\theta_* s \varphi}(s_{Jq_s}, \theta_{*Kq_{\theta_*}}) \frac{en_0(s_{Jq_s})}{T_e(s_{Jq_s})} \Lambda_{\text{mod}(k-K, N_{\theta_*})}(\Delta\theta_* p_{q_{\theta_*}}) \times \\ &\Lambda_{\text{mod}(k'-K, N_{\theta_*})}(\Delta\theta_* p_{q_{\theta_*}}) \exp\left[-\frac{2\pi i}{N_{\theta_*}}(mk - m'k')\right] \end{aligned} \quad (\text{A.56})$$

Now the index substitution $k \rightarrow k + K, k' \rightarrow k' + K$ is applied. The modulo can be removed:

$$\begin{aligned} \tilde{B}_{mm'}^1(s_{Jq_s}, q_{\theta_*}) &= \sum_{K=0}^{N_{\theta_*}-1} \sum_{k=0}^{N_{\theta_*}-1} \sum_{k'=0}^{N_{\theta_*}-1} J_{\theta_* s \varphi}(s_{Jq_s}, \theta_* K q_{\theta_*}) \frac{en_0(s_{Jq_s})}{T_e(s_{Jq_s})} \Lambda_k(\Delta\theta_* p_{q_{\theta_*}}) \Lambda_{k'}(\Delta\theta_* p_{q_{\theta_*}}) \times \\ &\exp \left[-\frac{2\pi i}{N_{\theta_*}} (mk - m'k' + mK - m'K) \right] \end{aligned} \quad (\text{A.57})$$

The J dependence in the splines has been removed. It is in fact the convolution theorem.

$$\begin{aligned} \tilde{B}_{mm'}^1(s_{Jq_s}, q_{\theta_*}) &= \sum_{K=0}^{N_{\theta_*}-1} J_{\theta_* s \varphi}(s_{Jq_s}, \theta_* K q_{\theta_*}) \frac{en_0(s_{Jq_s})}{T_e(s_{Jq_s})} \exp \left[-\frac{2\pi i}{N_{\theta_*}} K(m - m') \right] \times \\ &\sum_{k=0}^{N_{\theta_*}-1} \Lambda_k(\Delta\theta_* p_{q_{\theta_*}}) \exp \left[-\frac{2\pi i}{N_{\theta_*}} km \right] \times \\ &\sum_{k'=0}^{N_{\theta_*}-1} \Lambda_{k'}(\Delta\theta_* p_{q_{\theta_*}}) \exp \left[-\frac{2\pi i}{N_{\theta_*}} k'm' \right] \end{aligned} \quad (\text{A.58})$$

The construction of $\tilde{B}_{mm'}^1(s_{Jq_s}, q_{\theta_*})$ has been reduced to three separate Fourier transforms. The splines are evaluated at $\Delta\theta_* p_{q_{\theta_*}}$, which is in the first interval. Therefore the sums over k, k' reduce to $p + 1$ terms:

$$\begin{aligned} \tilde{B}_{mm'}^1(s_{Jq_s}, q_{\theta_*}) &= \sum_{K=0}^{N_{\theta_*}-1} J_{\theta_* s \varphi}(s_{Jq_s}, \theta_* K q_{\theta_*}) \frac{en_0(s_{Jq_s})}{T_e(s_{Jq_s})} \exp \left[-\frac{2\pi i}{N_{\theta_*}} K(m - m') \right] \times \\ &\sum_{k=0}^{N_{\theta_*}} \sum_{u_k=0}^p P_{p-u_k}^p(p_{q_{\theta_*}}) \exp \left[-\frac{2\pi i}{N_{\theta_*}} km \right] \delta_{k, \text{mod}(-p_l + u_k, N_{\theta_*})} \times \\ &\sum_{k'=0}^{N_{\theta_*}} \sum_{u_{k'}=0}^p P_{p-u_{k'}}^p(p_{q_{\theta_*}}) \exp \left[\frac{2\pi i}{N_{\theta_*}} k'm' \right] \delta_{k', \text{mod}(-p_l + u_{k'}, N_{\theta_*})} \end{aligned} \quad (\text{A.59})$$

which gives:

$$\tilde{B}_{mm'}^1(s_{Jq_s}, q_{\theta_*}) = \tilde{C}_{mm'}^1(s_{Jq_s}, q_{\theta_*}) \tilde{Z}_m^0(q_{\theta_*}) \tilde{Z}_{m'}^{0\dagger}(q_{\theta_*}) \quad (\text{A.60})$$

With:

$$\tilde{C}_{mm'}^w(s_{Jq_s}, q_{\theta_*}) = \sum_{K=0}^{N_{\theta_*}-1} C^w(s_{Jq_s}, \theta_* K q_{\theta_*}) \exp \left[-\frac{2\pi i}{N_{\theta_*}} K(m - m') \right] \quad (\text{A.61})$$

$$\begin{aligned} \tilde{Z}_m^a(q_{\theta_*}) &= \sum_{u_k=0}^p \frac{d^a}{dy^a} P_{p-u_k}^p(p_{q_{\theta_*}}) \times \\ &\exp \left[-\frac{2\pi i}{N_{\theta_*}} \text{mod}(-p_l + u_k, N_{\theta_*}) m \right] \end{aligned} \quad (\text{A.62})$$

It is now easy to generalize the discretized version of $\tilde{A}_{jm,j'm'}$:

$$\begin{aligned} \tilde{A}_{jm,j'm'} &= \sum_{w=1}^{n_A} \sum_{J=0}^{N_s-1} \sum_{q_s, q_{\theta_*}=1}^{n_g} \sum_{u_j, u_{j'}=0}^p \frac{\Delta s^{1-a_j^w - a_{j'}^w} \Delta \theta_*^{1-a_k^w - a_{k'}^w}}{N_{\theta_*}} g_{q_s} g_{q_{\theta_*}} \tilde{Z}_m^{a_k^w}(q_{\theta_*}) \tilde{Z}_{m'}^{a_{k'}^w \dagger}(q_{\theta_*}) \\ &\quad \frac{d^{a_j^w}}{dx^{a_j^w}} P_{p-u_j}^p(p_{q_s}) \frac{d^{a_{j'}^w}}{dx^{a_{j'}^w}} P_{p-u_{j'}}^p(p_{q_s}) \tilde{C}_{mm'}^w(s_{Jq_s}, q_{\theta_*}) \delta_{j, J-p_l+u_j} \delta_{j', J-p_l+u_{j'}} \end{aligned} \quad (\text{A.63})$$

Where the $\{a_j^w\}$, $\{a_{j'}^w\}$, $\{a_k^w\}$, $\{a_{k'}^w\}$ coefficients are defined in (A.25). The zonal flow matrix $\tilde{A}_{jm,j'm'}^{ZF}$ is obtained in a similar way:

$$\begin{aligned} \tilde{A}_{jm,j'm'}^{ZF} &= -\frac{\Delta s \Delta \theta_*^2}{N_{\theta_*}} \sum_{J=0}^{N_s-1} \sum_{q_s, q_{\theta_*}, r_{\theta_*}=1}^{n_g} \sum_{u_k, u_{k'}=0}^p g_{q_s} g_{q_{\theta_*}} g_{r_{\theta_*}} \frac{2\pi e n_0(s_{Jq_s})}{\Sigma(s_{Jq_s}) T_e(s_{Jq_s})} \times \\ &\quad P_{p-u_k}^p(p_{q_s}) P_{p-u_{k'}}^p(p_{q_s}) \tilde{J}_{m'}^\dagger(s_{Jq_s}, q_{\theta_*}) \tilde{J}_m(s_{Jq_s}, r_{\theta_*}) \tilde{Z}_{m'}^{0\dagger}(q_{\theta_*}) \tilde{Z}_m^0(r_{\theta_*}) \times \\ &\quad \delta_{j, J-p_l+u_k} \delta_{j', J-p_l+u_{k'}} \end{aligned} \quad (\text{A.64})$$

$$\tilde{J}_m(s_{Jq_s}, r_{\theta_*}) = \sum_{K=0}^{N_{\theta_*}-1} J_{\theta_* s \varphi}(s_{Jq_s}, \theta_* K q_{\theta_*}) \exp \left[-\frac{2\pi i}{N_{\theta_*}} K(m-m') \right] \quad (\text{A.65})$$

Both matrices \tilde{A} and \tilde{A}^{ZF} are hermitian and positive definite. In practice ORB5 computes and stores the poloidal modes inside a field-aligned filter of width $2\widetilde{\Delta m} + 1$: \tilde{A} depends on the toroidal mode number.

A.6 Boundary conditions for the field-aligned solver

The boundary conditions must be revisited when the matrix is expressed in Fourier space. In fact, the spline transformations using S_L and S_R matrices (see Annex A.4) remain valid because they act in the radial direction, which is not affected by the poloidal Fourier transform. The boundary conditions at the plasma edge are also not modified. One must however express the unicity at the magnetic axis in Fourier space. In real space, the

system must be modified according to Eq. (A.51):

$$\begin{pmatrix}
1 & 0 & \dots & 0 & 0 & 0 & \dots & 0 \\
0 & 1 & \dots & 0 & 0 & 0 & \dots & 0 \\
\dots & \dots & \dots & \dots & \dots & \dots & \dots & \dots \\
0 & 0 & \dots & 1 & 0 & 0 & \dots & 0 \\
0 & 0 & \dots & 0 & \sum_{i,j=1}^{N_{\theta_*}} a_{i,j} & \sum_{i=1}^{N_{\theta_*}} a_{i,N_{\theta_*}+1} & \dots & \sum_{i=1}^{N_{\theta_*}} a_{i,N_{tot}} \\
0 & 0 & \dots & 0 & \sum_{j=1}^{N_{\theta_*}} a_{N_{\theta_*}+1,j} & a_{N_{\theta_*}+1,N_{\theta_*}+1} & \dots & a_{N_{\theta_*}+1,N_{tot}} \\
\dots & \dots & \dots & \dots & \dots & \dots & \dots & \dots \\
0 & 0 & \dots & 0 & \sum_{j=1}^N a_{N_{tot},j} & a_{N_{tot},N_{\theta_*}+1} & \dots & a_{N_{tot},N_{tot}}
\end{pmatrix}
\begin{pmatrix}
\hat{\phi}_1 \\
\hat{\phi}_2 \\
\dots \\
\hat{\phi}_{N_{\theta_*}-1} \\
\hat{\phi}_{N_{\theta_*}} \\
\hat{\phi}_{N_{\theta_*}+1} \\
\dots \\
\hat{\phi}_{N_{tot}}
\end{pmatrix}
=
\begin{pmatrix}
0 \\
0 \\
\dots \\
0 \\
\sum_{i=1}^{N_{\theta_*}} b_i \\
b_{N+1} \\
\dots \\
b_{N_{tot}}
\end{pmatrix}
\quad (\text{A.66})$$

The term $\sum_{i,j=1}^{N_{\theta_*}} a_{i,j}$ is equal to $N_{\theta_*} \tilde{a}_{00}$ and the term $\sum_{i=1}^{N_{\theta_*}}$ is equal to $N_{\theta_*} b^{(0)}$: imposing unicity on the axis means retaining only the $m = 0, m' = 0$ component of the matrix and the $m = 0$ component of the perturbed density at $m = 0$ at $s = 0$. Then, the unicity boundary conditions introduce additional terms of the form

$$\sum_{k'=0}^{N_{\theta_*}-1} A_{jk,j'k'} = \sum_{m=0}^{N_{\theta_*}-1} \exp \left[-\frac{2\pi i}{N_{\theta_*}} km \right] A_{jm,j'0} \quad (\text{A.67})$$

The Fourier transform of this vector is $A_{jm,j'0}$, therefore the linear system must be modified as follows:

$$\begin{pmatrix}
\tilde{a}_{0,0} & 0 & \dots & 0 & \tilde{a}_{0,N+1} & \dots & \tilde{a}_{0,N_{tot}} \\
0 & 1 & \dots & 0 & 0 & \dots & 0 \\
\dots & \dots & \dots & \dots & \dots & \dots & \dots \\
\dots & 0 & \dots & 1 & 0 & \dots & 0 \\
0 & 0 & \dots & 0 & 1 & \dots & 0 \\
\tilde{a}_{N+1,0} & 0 & \dots & 0 & 0 & a_{N+1,N+1} & \dots & a_{N+1,N_{tot}} \\
\dots & \dots & \dots & \dots & 0 & \dots & \dots & \dots \\
\tilde{a}_{N_{tot},0} & 0 & \dots & 0 & 0 & a_{N_{tot},N+1} & \dots & a_{N_{tot},N_{tot}}
\end{pmatrix}
\begin{pmatrix}
\hat{u}_1 \\
\hat{u}_2 \\
\dots \\
\hat{u}_{N-1} \\
\hat{u}_N \\
\hat{u}_{N+1} \\
\dots \\
\hat{u}_{N_{tot}}
\end{pmatrix}
=
\begin{pmatrix}
\tilde{b}_0 \\
0 \\
\dots \\
0 \\
0 \\
b_{N+1} \\
\dots \\
b_{N_{tot}}
\end{pmatrix}
\quad (\text{A.68})$$

This is true only if $m = 0$ is included in the field-aligned filter. If it is not, then $\tilde{a}_{0,0}$ must be replaced by 1 and $\tilde{a}_{0,N+1}, \dots, \tilde{a}_{0,N_{tot}}$ as well as $\tilde{a}_{N+1,0}, \dots, \tilde{a}_{N_{tot},0}$ must be replaced by 0. The conclusion is that the unicity condition in real space is equivalent to retaining only the $m = 0$ component in Fourier space.

Bibliography

- [1] J. D. Lawson, Proceedings of the Physical Society B **70**, 6 (1957).
- [2] ITER website, <http://www.iter.org>.
- [3] M. Greenwald *et al.*, Nucl. Fusion **28**, 2199 (1988).
- [4] ITER Physics Group on Confinement and Transport and Confinement Modelling and Database and ITER Physics Basis Editors, Nucl. Fusion **39**, 2175 (1999).
- [5] X. Garbet, Plasma Phys. Control. Fusion **43**, A251 (2001).
- [6] W. Horton, Rev. Modern Phys. **71**, 735 (1999).
- [7] W. M. Tang, Nucl. Fusion **20**, 1439 (1980).
- [8] B. Coppi, A. Ferreira, J.-K. Mark, and J. J. Ramos, Nucl. Fusion **19**, 715 (1979).
- [9] P. H. Rutherford, Phys. Fluids **16**, 1903 (1973).
- [10] A. Hasegawa and K. Mima, Phys. Fluids **21**, 87 (1978).
- [11] P. W. Terry and W. Horton, Phys. Fluids **26**, 106 (1983).
- [12] B. B. Kadomstev, Sov. J. Plasma Phys. **1**, 295 (1975).
- [13] Z. Lin, S. Ethier, T. Hahm, and W. M. Tang, Phys. Rev. Lett. **88**, 195004 (2002).
- [14] R. Waltz, J. Candy, and M. N. Rosenbluth, Phys. Plasmas **9**, 1938 (2002).
- [15] J. Candy and R. Waltz, Phys. Rev. Lett. **91**, 045001 (2003).
- [16] J. Candy, R. Waltz, and W. Dorland, Phys. Plasmas **11**, L25 (2004).

- [17] P. H. Diamond and Y. B. Kim, Phys. Fluids B **3**, 1626 (1991).
- [18] Y. Idomura, M. Wakatani, and S. Tokuda, Phys. Plasmas **7**, 3551 (2001).
- [19] K. Hallatschek and D. Biskamp, Phys. Rev. Lett. **86**, 1223 (2001).
- [20] P. H. Diamond, S. I. Itoh, K. Itoh, and T. Hahm, Plasma Phys. Control. Fusion **47**, R35 (2005).
- [21] L. Garcia and B. A. Carreras, Phys. Plasmas **12**, 092305 (2005).
- [22] J. F. Drake, P. N. Guzdar, and A. B. Hassam, Phys. Rev. Lett. **61**, 2205 (1988).
- [23] F. Jenko, W. Dorland, M. Kotschenreuter, and B. N. Rogers, Phys. Plasmas **7**, 1904 (2000).
- [24] W. Horton, R. D. Estes, and D. Biskamp, Phys. Plasmas **22**, 662 (1980).
- [25] B. Labit and M. Ottaviani, Phys. Plasmas **10**, 126 (2003).
- [26] M. A. Beer, Ph.D. thesis, Princeton University, 1995.
- [27] G. W. Hammett and F. W. Perkins, Phys. Rev. Lett. **64**, 3019 (1990).
- [28] W. Dorland and G. W. Hammett, Phys. Fluids B **5**, 812 (1993).
- [29] R. Waltz, R. Dominguez, and G. W. Hammett, Phys. Fluids B **4**, 3138 (1992).
- [30] B. D. Scott, Plasma Phys. Control. Fusion **39**, 1635 (1997).
- [31] B. D. Scott, Phys. Plasmas **12**, 102307 (2005).
- [32] W. W. Lee, Phys. Fluids **26**, 256 (1983).
- [33] T. Hahm, Phys. Fluids **31**, 2670 (1988).
- [34] E. A. Frieman and L. Chen, Phys. Fluids **25**, 502 (1982).
- [35] A. J. Brizard, Phys. Plasmas **7**, 4816 (2000).
- [36] R. G. Littlejohn, J. Plasma Physics **29**, 111 (1983).

- [37] M. Kotschenreuter, G. Rewoldt, and W. M. Tang, *Comp. Phys. Commun.* **88**, 128 (1995).
- [38] F. Jenko, *Comp. Phys. Commun.* **125**, 196 (2000).
- [39] J. Candy and R. Waltz, *Journ. Comp. Phys.* **186**, 545 (2003).
- [40] C. Z. Cheng and G. Knorr, *Journ. Comp. Phys.* **22**, 330 (1976).
- [41] M. Brunetti *et al.*, *Comp. Phys. Commun.* **163**, 1 (2004).
- [42] V. Grandgirard *et al.*, *Journ. Comp. Phys.* **217**, 395 (2006).
- [43] V. Grandgirard *et al.*, *Plasma Phys. Control. Fusion* **49**, B173 (2007).
- [44] T. M. Tran *et al.*, in *Theory of fusion Plasmas*, edited by E. Compositori (Società italiana di Fisica, Bologna, 1999), p. 45.
- [45] S. E. Parker, C. Kim, and Y. Chen, *Phys. Plasmas* **6**, 1709 (1999).
- [46] A. M. Dimits, T. J. Williams, J. A. Byers, and B. I. Cohen, *Phys. Rev. Lett.* **77**, 71 (1996).
- [47] R. D. Sydora, V. C. Decyck, and J. M. Dawson, *Plasma Phys. Control. Fusion* **38**, A281 (1996).
- [48] Z. Lin *et al.*, *Science* **281**, 1835 (1998).
- [49] Y. Idomura, *Nucl. Fusion* **43**, 234 (2003).
- [50] G. Jost *et al.*, *Phys. Plasmas* **8**, 3321 (2001).
- [51] V. Kornilov *et al.*, *Phys. Plasmas* **11**, 3196 (2004).
- [52] M. Kotschenreuter, *Bull. Am. Phys. Soc.* **33**, 2107 (1988).
- [53] R. Hatzky *et al.*, *Phys. Plasmas* **9**, 898 (2002).
- [54] P. Angelino *et al.*, *Plasma Phys. Control. Fusion* **48**, 557 (2006).
- [55] A. Bottino *et al.*, in *Theory of fusion Plasmas*, edited by E. Compositori (Società italiana di Fisica, Bologna, 2004), p. 75.

- [56] T. Dannert and F. Jenko, *Phys. Plasmas* **12**, 072309 (2005).
- [57] J. Lang, Y. Chen, and S. E. Parker, *Phys. Plasmas* **14**, 082315 (2007).
- [58] B. F. McMillan *et al.*, *Phys. Plasmas* **15**, 052308 (2008).
- [59] S. Brunner, Ph.d. thesis no 1701, Ecole Polytechnique Federale de Lausanne, 1997.
- [60] I. S. Gradshteyn and I. M. Ryzik, *Table of integrals, series, and products* (Academic Press, London, 1980).
- [61] J. W. Connor, R. J. Hastie, and J. B. Taylor, *Phys. Rev. Lett.* **40**, 396 (1978).
- [62] R. D. Hazeltine and W. A. Newcomb, *Phys. Fluids B* **2**, 7 (1990).
- [63] H. Luetjens, A. Bondeson, and O. Sauter, *Comp. Phys. Commun.* **97**, 219 (1996).
- [64] L. S. Solovév, *Soviet Physics JETP* **26**, 400 (1968).
- [65] D. H. E. Dubin, J. A. Krommes, C. Oberman, and W. W. Lee, *Phys. Fluids* **26**, 3524 (1983).
- [66] G. Dif-Pradalier *et al.*, *Phys. Plasmas* **15**, 042315 (2008).
- [67] P. Angelino *et al.*, *Phys. Plasmas* **13**, 052304 (2006).
- [68] S. J. Allfrey and R. Hatzky, *Comp. Phys. Commun.* **154**, 98 (2003).
- [69] A. Y. Aydemir, *Phys. Plasmas* **1**, 822 (1994).
- [70] P. Angelino *et al.*, *Phys. Plasmas* **15**, 062306 (2008).
- [71] J. A. Krommes, *Phys. Plasmas* **6**, 1477 (1999).
- [72] M. N. Rosenbluth and F. L. Hinton, *Phys. Rev. Lett.* **80**, 724 (1998).
- [73] P. Angelino, Ph.d. thesis no 3559, Ecole Polytechnique Federale de Lausanne, 2006.
- [74] A. Bottino, Ph. d. thesis no 2938, Ecole Polytechnique Federale de Lausanne, 2004.
- [75] R. Hatzky, *Parallel Computing* **32**, 325 (2006).
- [76] A. Bottino *et al.*, *Phys. Plasmas* **14**, 010701 (2007).

- [77] C. K. Birdsall and A. B. Langdon, *Plasma physics via computer simulations* (Adam Hilger, Bristol, 1989).
- [78] W. W. Lee, *Journ. Comp. Phys.* **73**, 243 (1987).
- [79] S. P. Hirshman *et al.*, *Phys. Plasmas* **1**, 2277 (1994).
- [80] S. Jolliet *et al.*, in *Theory of fusion Plasmas*, edited by E. Compositori (Società italiana di Fisica, Bologna, 2005).
- [81] K. J. Bowers, *Journ. Comp. Phys.* **173**, 393 (2001).
- [82] E. Rafajlowicz and R. Schwabe, *Stat. Prob. Lett.* **76**, 803 (2006).
- [83] M. P. I. Forum, MPI: A Message-Passing Interface standard (version 1.1), *www.mpi-forum.org*, 1995.
- [84] P. C. Liewer and V. C. Decyck, *Journ. Comp. Phys.* **85**, 302 (1989).
- [85] C. C. Kim and S. E. Parker, *Journ. Comp. Phys.* **161**, 589 (2000).
- [86] K. Höllig, *Finite Element Methods with B-Splines* (Society for Industrial and Applied Mathematics (SIAM), Philadelphia, 2003).
- [87] M. Fivaz *et al.*, *Comp. Phys. Commun.* **111**, 27 (1998).
- [88] E. Anderson *et al.*, *LAPACK Users' Guide*, 3 ed. (Society for Industrial and Applied Mathematics (SIAM), Philadelphia, PA, 1999).
- [89] L. S. Blackford *et al.*, *ScaLAPACK Users' Guide* (Society for Industrial and Applied Mathematics (SIAM), Philadelphia, PA, 1997).
- [90] A. M. Dimitis *et al.*, *Phys. Plasmas* **7**, 969 (2000).
- [91] W. M. Nevins *et al.*, *Phys. Plasmas* **12**, 122305 (2005).
- [92] T. S. Hahm and K. H. Burrell, *Phys. Plasmas* **2**, 1648 (1995).
- [93] T. S. Hahm, *Phys. Plasmas* **1**, 2940 (1994).
- [94] T. S. Hahm *et al.*, *Phys. Plasmas* **6**, 922 (1999).

- [95] R. Waltz, J. C. DeBoo, and M. N. Rosenbluth, *Phys. Rev. Lett.* **65**, 2390 (1990).
- [96] N. Winsor, J. L. Johnson, and J. M. Dawson, *Phys. Fluids* **11**, 2448 (1968).
- [97] A. Bottino *et al.*, in *Theory of fusion Plasmas*, edited by E. Compositori (Societá italiana di Fisica, Bologna, 2001), p. 327.
- [98] A. Mishchenko, A. Koenies, and R. Hatzky, *Phys. Plasmas* **12**, 062395 (2005).
- [99] A. Bottino *et al.*, in *33rd EPS Conference on Plasma Phys.* (IOP, Rome, 2006), No. O-3.001.
- [100] C. M. Greenfield *et al.*, *Nucl. Fusion* **37**, 1215 (1997).
- [101] G. L. Falchetto *et al.*, *Plasma Phys. Control. Fusion* **50**, 124015 (2008).
- [102] J. Candy and R. E. Waltz, *Phys. Plasmas* **13**, 032310 (2006).
- [103] Y. Chen and S. E. Parker, *Journ. Comp. Phys.* **189**, 463 (2003).
- [104] X. Q. Xu and M. N. Rosenbluth, *Phys. Fluids B* **3**, 627 (1991).
- [105] Y. Chen and R. B. White, *Phys. Plasmas* **4**, 3591 (1997).
- [106] S. Brunner, E. Valeo, and J. A. Krommes, *Phys. Plasmas* **6**, 4504 (1999).
- [107] J. L. V. Lewandowski, *Phys. Plasmas* **12**, 052322 (2005).
- [108] J. Denavit, *Journ. Comp. Phys.* **9**, 75 (1972).
- [109] S. Vadlamani, S. E. Parker, Y. Chen, and C. Kim, *Comp. Phys. Commun.* **164**, 209 (2004).
- [110] Y. Chen and S. E. Parker, *Phys. Plasmas* **14**, 082301 (2007).
- [111] T.-H. Watanabe and H. Sugama, *Phys. Plasmas* **9**, 3659 (2002).
- [112] T.-H. Watanabe and H. Sugama, *Phys. Plasmas* **11**, 1476 (2004).
- [113] X. Garbet *et al.*, *Phys. Plasmas* **12**, 082511 (2005).
- [114] H. Sugama and M. Okamoto, *Phys. Plasmas* **3**, 2379 (1996).

- [115] Y. Idomura, M. Ida, S. Tokuda, and L. Villard, *Journ. Comp. Phys.* **226**, 244 (2007).
- [116] L. Villard *et al.*, *Plasma Phys. Control. Fusion* **46**, B51 (2004).
- [117] J. C. Kniep, J. N. G. Leboeuf, and V. C. Decyck, *Comp. Phys. Commun.* **164**, 98 (2004).
- [118] Z. Lin *et al.*, *J. Phys. Conf. Ser.* **16**, 16 (2005).
- [119] S. Jolliet *et al.*, in *Theory of fusion Plasmas* (American Institute of Physics, Melville, New York, 2006), Vol. 871, p. 124.
- [120] J. Candy, R. E. Waltz, S. E. Parker, and Y. Chen, *Phys. Plasmas* **13**, 074501 (2006).
- [121] L. Villard *et al.*, *Nucl. Fusion* **44**, 172 (2004).
- [122] N. J. L. Cardozo, *Plasma Phys. Control. Fusion* **37**, 799 (1995).
- [123] F. Ryter *et al.*, *Plasma Phys. Control. Fusion* **43**, A323 (2001).
- [124] F. Wagner *et al.*, *Phys. Rev. Lett.* **56**, 2187 (1986).
- [125] F. Ryter *et al.*, *Phys. Rev. Lett.* **95**, 085001 (2005).
- [126] F. Jenko and W. Dorland, *Phys. Rev. Lett.* **89**, 225001 (2002).
- [127] Z. Lin, L. Chen, and F. Zonca, *Phys. Plasmas* **12**, 056125 (2005).
- [128] W. M. Nevins *et al.*, *Phys. Plasmas* **13**, 122306 (2006).
- [129] W. M. Nevins *et al.*, *Phys. Plasmas* **14**, 084501 (2007).
- [130] W. W. Lee, J. L. V. Lewandowski, T. S. Hahm, and Z. Lin, *Phys. Plasmas* **8**, 4435 (2001).
- [131] S. Sorge and R. Hatzky, *Plasma Phys. Control. Fusion* **44**, 2471 (2002).
- [132] Y. Chen and S. E. Parker, *Phys. Plasmas* **8**, 2095 (2001).
- [133] R. Hatzky, A. Koenies, and A. Mishchenko, *Journ. Comp. Phys.* **225**, 568 (2007).
- [134] A. Mishchenko, R. Hatzky, and A. Koenies, *Phys. Plasmas* **11**, 5480 (2004).

- [135] B. H. Fong and T. S. Hahm, *Phys. Plasmas* **6**, 188 (1999).
- [136] Y. Idomura, S. Tokuda, and Y. Kishimoto, *J. Plasma Fusion Res.* **6**, 17 (2004).
- [137] G. Rewoldt, Z. Lin, and Y. Idomura, *Comp. Phys. Commun.* **177**, 775 (2007).
- [138] A. Bottino *et al.*, *Phys. Plasmas* **11**, 198 (2004).
- [139] X. Lapillonne *et al.*, To be published in *Phys. Plasmas* (2008).
- [140] G. Rewoldt, W. M. Tang, and M. S. Chance, *Phys. Fluids* **25**, 480 (1982).
- [141] G. Rewoldt, W. M. Tang, and R. J. Hastie, *Phys. Fluids* **30**, 807 (1987).
- [142] H. Sugama and T.-H. Watanabe, *Phys. Rev. Lett.* **94**, 115001 (2005).
- [143] H. Sugama and T.-H. Watanabe, *J. Plasma Physics* **72**, 825 (2006).
- [144] D. W. Ross and W. Dorland, *Phys. Plasmas* **9**, 5031 (2002).
- [145] S. E. Parker *et al.*, *Phys. Plasmas* **11**, 2594 (2004).
- [146] J. Lang, S. E. Parker, and Y. Chen, *Phys. Plasmas* **15**, 055907 (2008).
- [147] F. Merz and F. Jenko, *Phys. Rev. Lett.* **100**, 035005 (2008).
- [148] D. R. Ernst *et al.*, *Phys. Plasmas* **11**, 2637 (2004).
- [149] R. E. Waltz, J. Candy, and M. Fahey, *Phys. Plasmas* **14**, 056116 (2007).
- [150] J. Candy, R. E. Waltz, M. R. Fahey, and C. Holland, *Plasma Phys. Control. Fusion* **49**, 109 (2007).
- [151] T. Göerler and F. Jenko, *Phys. Rev. Lett.* **100**, 185002 (2008).
- [152] X. Garbet *et al.*, *Phys. Rev. Lett.* **91**, 035001 (2003).
- [153] H. Biglari, P. H. Diamond, and P. W. Terry, *Phys. Fluids B* **2**, 1 (1990).
- [154] T. S. Hahm, *Phys. Plasmas* **4**, 4074 (1997).
- [155] L. Villard, A. Bottino, O. Sauter, and J. Vaclavik, *Phys. Plasmas* **9**, 2684 (2002).

- [156] D. del Castillo-Negrete, D. A. Spong, and S. P. Hirshman, *Phys. Plasmas* **15**, 092308 (2008).
- [157] Z. Lin *et al.*, *Phys. Rev. Lett.* **83**, 3645 (1999).
- [158] Z. Lin, W. M. Tang, and W. W. Lee, *Phys. Rev. Lett.* **78**, 456 (1997).
- [159] B. Coppi, H. P. Furth, M. N. Rosenbluth, and R. Z. Sagdeev, *Phys. Rev. Lett.* **17**, 377 (1966).
- [160] J. Q. Dong, W. Horton, and W. Dorland, *Phys. Plasmas* **1**, 3635 (1994).
- [161] J. Q. Dong and W. Horton, *Phys. Plasmas* **2**, 3412 (1995).
- [162] C. Estrada-Mila, J. Candy, and R. E. Waltz, *Phys. Plasmas* **12**, 022305 (2005).
- [163] F. Zonca, L. Chen, J. Q. Dong, and R. A. Santoro, *Phys. Plasmas* **6**, 1917 (1999).
- [164] G. L. Falchetto, J. Vaclavik, and L. Villard, *Phys. Plasmas* **10**, 1424 (2003).
- [165] Z. Lin and L. Chen, *Phys. Plasmas* **8**, 1447 (2001).
- [166] Y. Nishimura, Z. Lin, and W. X. Wang, *Phys. Plasmas* **14**, 042503 (2007).
- [167] E. Poli, A. Bottino, A. G. Peeters, and O. Sauter, *Theory of fusion Plasmas* (American Institute of Physics, Melville, New York, 2006), Vol. 871, p. 400.
- [168] T. Dannert *et al.*, *Phys. Plasmas* **15**, 062508 (2008).

Acknowledgements

This thesis is the accomplishment of four and a half years of work. It would not have been possible without the valuable help of many people who have become friends and to whom I am deeply grateful.

First, I really would like to thank my thesis supervisor Laurent Villard who has led me with an amazing enthusiasm during all these years. His continuous support as well as his numerous ideas and advices have given me a great motivation through all these years. I am extremely thankful for his constant availability and his willingness to share his physics knowledge.

I owe my gratitude to Alberto Bottino who has taught me the mysteries of gyrokinetic theory, has answered my never-ending questions on ORB5, and has helped me through the debugging of the code. It was a true honor to work with you and I hope that we will have the opportunity to collaborate in the future. Grazie!

Special thanks go to Paolo Angelino. I have very much appreciated our collaboration during the entire time of this thesis which has given rise to many ideas in this work. Grazie!

I would like to like to thank Ben McMillan for the fruitful collaboration, and for sharing your brilliant and innovative look on gyrokinetic simulations.

I am in debt with Trach-Minh Tran and Roman Hatzky for their patience towards my ignorance of computers and for guiding me through many, if not all the numerical and technical aspects of this work. Thank you for teaching me the rigor of programming.

I am also in debt with Stephan Brunner, who has provided me a Matlab script which solves the dispersion relations used in this work. This was a very interesting physics exercise!

A sincere acknowledgement goes to Yasuhiro Idomura. His valuable help and his pertinent advices have significantly improved the quality of this work. It was a pleasure to

share your office during the first three months of my thesis. I am looking forward to the forthcoming collaboration in Japan.

During all these years, I have had the opportunity to discuss my work with many people from CRPP. Therefore I would like to thank Olivier Sauter, Kurt Appert, Rajamaran Ganesh, Tony Cooper, Thibaut Vernay, Xavier Lapillonne, Yann Camenen, Nicolas Mellet, Mattia Albergante, Martin Jucker, Simon Allfrey, Jonathan Graves, Maura Brunetti for the stimulating discussions. A special thought goes to Anja Mücke, Vielen Dank für Deine Geduld und Mühe meine Deutschkenntnisse aufgebessert zu haben. Es war sehr nett und angenehm mit Dir das Büro geteilt zu haben.

Unfortunately I do not have the space to mention all my other colleagues, but I do not forget you. You've really made my life more enjoyable. Merci à tous!

This work has also gained from the collaboration with many scientists from other laboratories. I would like to express my gratitude to Bruce Scott, Emanuele Poli, Arthur Peeters, Gloria Falchetto, Virginie Grandgirard, Ralf Kleiber, Axel Koënies, Frank Jenko, William Tang and T. S. Hahm for stimulating discussion.

I would like to thank Xavier Garbet, Fulvio Zonca, Antoine Pochelon and Olivier Schneider, together with Laurent Villard for being a member of my thesis jury. I also would like to acknowledge Laurent Villard, Alberto Bottino and Roman Hatzky for the careful reading of the manuscript.

I would like to deeply thank Costanza Zucca for the sincere friendship and the amazing time spent in our office. You've really supported me during the ups and downs of my life. Grazie mille!

Enfin je tiens à remercier toute ma famille et tout particulièrement ma mère pour m'avoir constamment et inconditionnellement soutenu.

All the ORB5 simulations presented in this work were performed on the parallel

Pleiades, Pleiades2 and BG/L clusters of the Ecole Polytechnique Fédérale de Lausanne and on the BG/P cluster of the Forschungszentrum of Jülich, Germany. This work was partly supported by the Swiss National Science Foundation.

Curriculum Vitae

Personal Data:

Name: Sébastien JOLLIET
Date of birth: February 16th, 1982
Place of birth: Morges, Switzerland
Nationality: Swiss

Educational background:

Jul 1999 Maturité scientifique, Gymnase de Chamblandes, Pully
Mar 2004 Master of Science in Physics at the Ecole Polytechnique Fédérale de Lausanne, Thesis title="Resolution of gyrokinetics equations in curvilinear coordinates"
Feb 2005 Course attended: "MPI, Introduction à la programmation parallèle" at SIC/EPFL, Lausanne, Switzerland

Professional experience:

Aug - Sep 2002 Trainee at Asulab SA, Marin, Switzerland: calibration and integration of a humidity sensor in a watch, mechanical drawings, measurements in a vapour-bath.
2003 - 2004 Teaching Assistant at the Physics Department, Ecole Polytechnique Fédérale de Lausanne.
Aug - Sep 2003 Trainee at CFS Engineering SA, Parc Scientifique de l'Ecole Polytechnique Fédérale de Lausanne: implementation of incompressible flows using the artificial compressibility method in the CFD code NSMB, development of turbulence models.
Jun 2004 - Present Assistant and Doctoral Student at de Centre de Recherches en Physique des Plasmas (CRPP), Ecole Polytechnique Fédérale de Lausanne (EPFL), Lausanne, Switzerland.

Language skills:

French mother tongue. Fluent English, Good knowledges German.

Refereed publications

- P. Angelino, A. Bottino, R. Hatzky, **S. Jolliet**, O. Sauter, T. M. Tran and L. Villard, *On the definition of a kinetic equilibrium in global gyrokinetic simulations*, Physics of Plasmas 13, 052304 (2006).
- P. Angelino, A. Bottino, R. Hatzky, **S. Jolliet**, O. Sauter, T. M. Tran and L. Villard, *Effects of plasma current on nonlinear interactions of ITG turbulence, zonal flows and geodesic acoustic modes*, Physics of Plasmas 48, 557 (2006).
- A. Bottino, A. G. Peeters, R. Hatzky, **S. Jolliet**, B. F. McMillan, T. M. Tran and L. Villard, *Nonlinear low noise particle-in-cell simulations of electron temperature gradient driven turbulence*, Physics of Plasmas 14, 010701 (2007).
- **S. Jolliet**, A. Bottino, P. Angelino, R. Hatzky, T. M. Tran, B. F. McMillan, O. Sauter, K. Appert, Y. Idomura and L. Villard, *Nonlinear low noise particle-in-cell simulations of electron temperature gradient driven turbulence*, Computer Physics Communication 177, 409 (2007).
- V. Grandgirard, Y. Sarazin, P. Angelino, A. Bottino, N. Crouseilles, G. Darmet, G. Dif-Pradalier, X. Garbet, P. Gendrih, **S. Jolliet**, G. Latu, E. Sonnendrücker and L. Villard, *Global full-f gyrokinetic simulations of plasma turbulence*, Plasma Physics and Controlled Fusion 49, B173 (2007).
- B. F. McMillan, S. Jolliet, T. M. Tran, L. Villard, A. Bottino and P. Angelino, *Long global gyrokinetic simulations: Source terms and particle noise control*, Physics of Plasmas 15, 052308 (2008).
- P. Angelino, X. Garbet, L. Villard, A. Bottino, **S. Jolliet**, P. Gendrih and V. Grandgirard, *The role of plasma elongation on the linear damping of zonal flows*, Physics of Plasmas 15, 062306 (2008).
- G. L. Falchetto, B. D. Scott, P. Angelino, A. Bottino, T. Dannert, V. Grandgirard, S. Janhunen, F. Jenko, **S. Jolliet**, A. Kendl, B. F. McMillan, V. Naulin, A. H. Nielsen, M. Ottaviani, A. G. Peeters, M. J. Pueschel, D. Reiser, T. Ribeiro and M. Romanelli, *The European turbulence code benchmarking effort: turbulence*

driven by thermal gradients in magnetically confined plasmas, Plasma Physics and Controlled Fusion 50, 124015 (2008).

- B. F. McMillan, **S. Jolliet**, T. M. Tran, L. Villard, A. Bottino and P. Angelino, *Avalanche-like bursts in global gyrokinetic simulations*, accepted for publication in Phys. Plasmas, 2009.

Invited participations to conferences

- **S. Jolliet**, A. Bottino, P. Angelino, T. M. Tran, B. F. McMillan, R. Hatzky, A. G. Peeters, E. Poli, O. Sauter and L. Villard, *Ion and Electron Dynamics in Nonlinear PIC Simulations*, Theory of fusion Plasmas, Int. Workshop, American Institute of Physics, Melville New York, 2006, p. 124.

Conferences proceedings

- A. Bottino, P. Angelino, S. J. Allfrey, S. Brunner, R. Hatzky, Y. Idomura, **S. Jolliet**, O. Sauter, T. M. Tran and L. Villard, *Recent advances in nonlinear gyrokinetic PIC simulations in tokamak geometry*, Theory of fusion Plasmas, Int. Workshop, Editrice Compositori, Società italiana di Fisica, Bologna, 2004, p. 75.
- **S. Jolliet**, P. Angelino, A. Bottino, Y. Idomura and L. Villard, *A linear gyrokinetic model in magnetic coordinates*, Theory of fusion Plasmas, Int. Workshop, Editrice Compositori, Società italiana di Fisica, Bologna, 2004, p. 345.
- A. Bottino, A. G. Peeters, R. Hatzky, T. M. Tran, P. Angelino, **S. Jolliet**, E. Poli, O. Sauter and L. Villard, *Global Nonlinear Gyrokinetic Simulations of ETG turbulence using particles*, Proceedings of the 33rd EPS Conference on Plasma Physics, Roma, 2006, 301, O-3.001.
- P. Angelino, A. Bottino, R. Hatzky, **S. Jolliet**, O. Sauter, T. M. Tran and L. Villard, *Plasma elongation and magnetic shear effects in nonlinear simulations of ITG-zonal flow turbulence*, Proceedings of the 33rd EPS Conference on Plasma Physics, Roma, 2006, 301, P1.195.

- L. Villard, P. Angelino, A. Bottino, R. Hatzky, S. Jolliet, B. F. McMillan, O. Sauter and T. M. Tran, *Plasma Shape Effects on Geodesic Acoustic Oscillations*, Theory of Fusion Plasmas, Int. Workshop, American Institute of Physics, Melville New York, 2006, p. 424.
- S. Saarelma, R. Akers, M. Reshko, C. M. Roach, M. Romanelli, A. Thyagaraja and MAST team, A. Peeters, A. Bottino and **S. Jolliet**, *Global Turbulence Simulations of CYCLONE Base Case and MAST Plasmas*, Theory of Fusion Plasmas, Int. Workshop, American Institute of Physics, Melville New York, 2008, p. 200.
- X. Lapillonne, T. Dannert, S. Brunner, A. Marinoni, **S. Jolliet**, L. Villard, F. Jenko, T. Goerler and F. Merz, *Effects of geometry on linear and non-linear gyrokinetic simulations, and development of a global version of the GENE code*, Theory of Fusion Plasmas, Int. Workshop, American Institute of Physics, Melville New York, 2008, p. 289.

Contributions to conferences (as first author)

- **S. Jolliet**, A. Bottino, P. Angelino, R. Hatzky, O. Sauter, T. M. Tran and L. Villard, *Recent advances in non-linear PIC simulations in magnetic coordinates*, 11th European Fusion Theory Conference, Aix-en-Provence, 2005.
- **S. Jolliet**, A. Bottino, B. F. McMillan, P. Angelino, T. M. Tran, X. Lapillonne, Y. Idomura, L. Villard, *Nonlinear global gyrokinetic PIC simulations of Collisionless TEM turbulence*, 49th APS Conference, Orlando, 2007.
- **S. Jolliet**, B. F. McMillan, T. M. Tran, X. Lapillonne, L. Villard, A. Bottino and P. Angelino, *Global Nonlinear Simulations of Ion and Electron Turbulence Using a Particle-In-Cell Approach*, 22nd IAEA Fusion Energy Conference, Geneva, 2008.
- **S. Jolliet**, T. M. Tran, B. F. McMillan, L. Villard, X. Lapillonne, A. Bottino, P. Angelino and Y. Idomura, *Nonlinear global PIC simulations of collisionless trapped electron mode turbulence*, NEXT Workshop, Kyoto, 2008.

Seminars

- **S. Jolliet**, A. Bottino, P. Angelino, R. Hatzky, T. M. Tran, B. F. McMillan, O. Sauter, K. Appert, Y. Idomura and L. Villard, *A global collisionless PIC code in magnetic coordinates*, Talk given at IPP, Garching, 11th December 2006.
- **S. Jolliet**, T. M. Tran, B. F. McMillan, L. Villard, X. Lapillonne, A. Bottino, P. Angelino and Y. Idomura, *Nonlinear global gyrokinetic PIC simulations of Collisionless TEM turbulence*, Talk given at PPPL, Princeton, 19th November 2007.